Probing Molecular Dynamics using Novel Light Sources

ISBN: 978-90-77209-47-9

Cover: *A light*.
Photograph by Wing Kiu Siu

Probing Molecular Dynamics using Novel Light Sources

EEN WETENSCHAPPELIJKE PROEVE OP HET GEBIED VAN
DE NATUURWETENSCHAPPEN,WISKUNDE EN INFORMATICA

PROEFSCHRIFT

ter verkrijging van de graad van Doctor
aan de Radboud Universiteit Nijmegen,
op gezag van de rector magnificus
prof. mr. S.C.J.J. Kortmann,
volgens besluit van het college van decanen
in het openbaar te verdedigen op maandag 27 juni 2011
om 10.30 uur precies

door

Wing Kiu Siu

Geboren op 27 augustus 1982
te Hong Kong

Promotor:	Prof. dr. M. J. J. Vrakking
Manuscriptcommissie:	Prof. dr. H. J. Bakker (Universiteit van Amsterdam) Prof. dr. M. Y. Ivanov (Imperial College London) Prof. dr. W. J. van der Zande

FOM Institute
AMOLF

Nederlandse titel: Het bestuderen van moleculaire dynamica met nieuwe lichtbronnen

The work described in this thesis was performed at the FOM-institute AMOLF, Science Park 104, 1098 XG, Amsterdam, The Netherlands.

This work is part of the research programme of the 'Stichting voor Fundamenteel Onderzoek der Materie (FOM)', which is financially supported by the 'Nederlandse Organisatie voor Wetenschappelijk Onderzoek (NWO)'.

Het was zo donker dat ik allemaal lichtpuntjes zag

Loesje

CONTENTS

1

Introduction

The sun has been our primary light source since millions of years. In the course of time, other sources of light have been developed to enlighten places were the sun cannot reach or at times after sunset. Probably the very first application of a light source beyond enlightening dark moments was the use of fire as a means of communication. Nowadays, light has found applications in signalling devices, electronic multimedia devices, telecom communications and medical applications and has become a part of everyday life.

Light has intrigued researchers for centuries. It has been the object of investigation and finally led to the realization of the wave-particle duality of light by Einstein in the early 1900's. Light-matter interaction has provided great insight into the properties of light and matter itself. In the field of atomic and molecular physics, the field of research that we are concerned with in this thesis, light has been a very important tool in the investigation of the structure and dynamics of atoms and molecules.

A enormous variety of light sources has been used, that varied in wavelength, intensity, power and pulse duration. Different part of the electromagnetic spectrum can be used to investigate different structural properties of matter. Insight into the rotational and vibrational spectra of atoms and molecules can for example be obtained using absorption of light in the microwave and infrared regime [1, 2]. Whereas ultraviolet/visible light absorption spectroscopy is often used in analytical chemistry for a quantitative determination of chemical components [3]. Structural studies of matter based on diffraction, requires that the wavelength of the light is is smaller than the object under investigation and has motivated the development of sources with wavelengths in the X-ray regime to study atomic structure. In 1947, the first radiation from a synchrotron source was reported and nowadays these sources, with variable wavelengths from the extreme-ultraviolet (XUV) to the X-ray regime are used to investigate the spatial, electronic and magnetic structure of matter.

In 1960 the laser (light amplification by stimulated emission) was invented [4, 5] and 50 years later, we can state that lasers are a vital tool in many areas of fundamental and applied research. A major step forward for the study of light-matter interaction has been the development of pulsed laser sources. Shortly after the demonstration of the first continuous laser, lasers with nanosecond (1 ns = 10^{-9} s) pulse durations were developed. Nature could now be studied directly on the timescales of these fast laser pulses. Further advances came with the generation of picosecond (10^{-12} s) and femtosecond (10^{-15} s) pulses laser pulses, based on mode-locking techniques.

These lasers with pulse durations on the time-scale of the rotations and vibrations of molecules have made it possible to study these dynamics in real-time. One finds an analogy to photography of fast-moving objects, where the shutter time should be on the time-scale of the movement of the photographed object to avoid a blurred image.

In parallel with shortening the laser pulse durations to the femtosecond time-domain, amplifiers were developed that increased the laser intensity. In 1986 Ti:Sa was introduced as a lasing medium [6], with wavelengths in the infrared regime (IR). This increased the laser intensities to levels where the field strength becomes comparable to the Coulomb field of the ion that is felt by electrons. The interaction of these strong laser fields with atoms gives rise to novel physical phenomena.

Advancing the limits of light sources has in the past opened up new research areas in atomic, molecular and the condensed matter sciences. In the past decade three novel light sources have been developed that opened up new exciting research directions in atomic and molecular physics.

First, continuous shortening of femtosecond IR laser pulses led to the generation of few-cycle IR pulses. The carrier-envelope-phase, which is the difference between the phase of the fast oscillating electric field called the carrier wave and the envelope position, now becomes an important parameter in the light-matter interaction [7]. Second, the non-linear interaction of atoms with strong laser fields has led to the generation of light pulses based on high harmonic generation (HHG). These HHG sources offer tablet-top extreme-ultraviolet laser pulses with pulse durations that are in the attosecond (10^{-18} s) time-domain [8]. Third, going from lab-scale to facility-scale lasers, accelerator based free electron lasers with wavelengths in the XUV to X-ray regime offer unprecedented intensities at these wavelengths. In this thesis, these three novel light sources have been used to study the structure and dynamics of diatomic molecules.

1.1 High-intensity infrared femtosecond lasers

The ionization mechanism of atoms using high-intensity lasers, with a photon energy that is lower than the ionization potential I_p of the target atom, is markedly different from the explanation of the photoelectric effect described by Einstein in 1905. For high-intensity lasers, the field strength becomes comparable to the ion Coulomb field and ionization occurs via the absorption of multiple photons (multi-photon ionization). In a classical picture, the ionization occurs via a 'vertical' transition of the electron from the potential well into the continuum and is most conveniently described in the frequency domain. Under certain conditions, multiphoton ionization is more conveniently described in the time-domain and the multiphoton ionization looks like a tunneling of the electron through a potential energy barrier, that is formed by the distortion of the Coulomb field by the oscillating electric field of the laser. The potential energy barrier is considered to be static during the time the electron tunnels through the barrier. The distinction between these two pictures is conveniently indicated by the Keldysh parameter: $\gamma = \sqrt{\frac{I_p}{2U_p}}$, where $U_p = \frac{I_{laser}}{4\omega^2}$ (with e=m=$\hbar$=1 in atomic units) is the ponderomotive energy of an electron in an

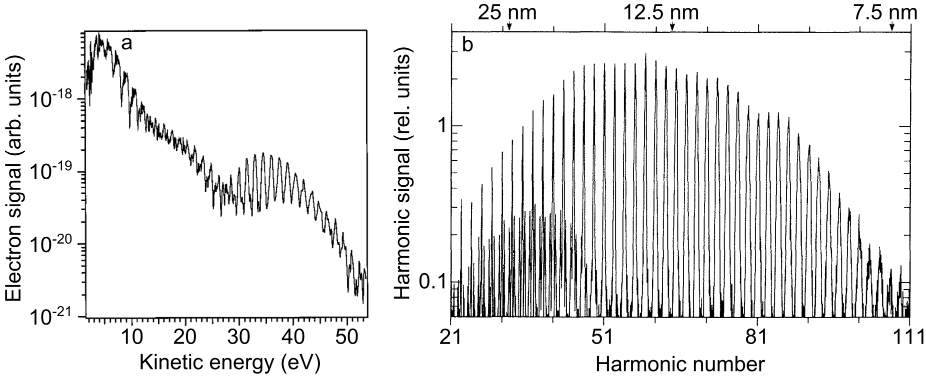

Figure 1.1: a) Photoelectron spectrum of xenon for ionization with a short infrared laser pulse (120 fs, 800 nm) at an intensity of 1.51 × 10^{14} W/cm^2. Figure is taken from P. Hansch *et al.* [11]. There are clearly two parts in the spectrum. First, there is a rapid decrease of the photoelectron peak intensities with kinetic energy, due to direct tunneling (i.e. no return of the electron to the nucleus) and second, there is a plateau region where the intensity of the peaks varies less rapidly and extends to $\sim 10\ U_p$. b) High harmonic spectrum generated in neon with an infrared laser (800 nm, 125 fs) at an intensity of 1.3 × 10^{15} W/cm^2. Figure is taken from J.J. Macklin *et al.*[12]. The first increase is due to the response of the grating of the detector. The decrease at higher harmonics is due to the harmonic cutoff and extends up to the 111th harmonic.

oscillating field [9]. For $\gamma < 1$ a quasi-static picture of the ionization mechanism, in which the electron tunnels through the barrier, is more applicable. Whereas for $\gamma > 1$ the ionization mechanism is more accurately described by a 'vertical' transition of the electron to the continuum.

If the target atom absorbs more photons than necessary to promote an electron to the continuum, a photoelectron spectrum is observed that contains a series of peaks that are separated by the photon energy. This has been called above-threshold ionization (ATI) and an ATI spectrum is shown in Figure 1.1a [10]. The maximum kinetic energy that an electron can gain from the laser field is 2 U_p and the intensity of the photoelectron peaks decreases rapidly in this regime.

Once the electron has entered the continuum following multi-photon ionization, various types of laser-mediated electron-ion interactions can occur that lead to the observation of a variety of phenomena. A semiclassical three-step model has been highly successful in providing an intuitive description of the various interactions that can occur [13]. In the first step of this model, the electron is tunnel-ionized by the laser field and is subsequently accelerated away from the ion by the oscillating field (second step). When the electron returns to the vicinity of the ion core, it can interact with the parent ion and can either scatter elastically, inelastically or recombine with the parent ion (third step). The three-step model is illustrated in Figure 1.2a for recombination of the electron.

Elastic scattering of the continuum electron with the parent ion, mediated by the oscillating laser field, leads to the observation of a plateau in the photoelectron spectrum that spans from $E_k = 2$ to 10 U_p [14]. This is also observed in the ATI spectrum of xenon that is shown in Figure 1.1a. Inelastic scattering of the continuum electron can promote a bound electron to the continuum, ionizing the parent ion. This is known as non-sequential double ionization (NSDI) and is the mechanism responsible for the unexpected high ionization rates of multiply charged atoms at high laser intensities [15].

In 1987, the first observation of a third type of electron-ion interaction was made. The interaction of an intense laser pulse with a gaseous medium (Figure 1.2b) led to the observation of a photon spectrum that consists of the high-order harmonics of the frequency of the driving laser and has been called high harmonic generation [16, 17]. A high harmonic spectrum, taken in neon is shown in Figure 1.1b. The emission of high-order harmonics can be understood as the result of the the recombination of the electron with the parent ion. This process is illustrated in Figure 1.2a. The recombination process takes place during a fraction of the optical cycle of the driving IR laser ($\tau = 2.5$ fs) and the emission is in the attosecond time-domain [8].

From the semiclassical model, effects of the intensity and frequency on the described strong-field phenomena can be interpreted. Effects of the pulse duration have been observed in above-threshold ionization [18] and high harmonic generation [19] and become increasingly important for pulse durations that enter the few-cycle regime.

Waveform-controlled few-cycle IR pulses

In the past three decades considerable progress has been made in shortening the pulse durations of femtosecond IR pulses to the few-cycle regime [20–22]. The electric field of few-cycle pulses is influenced by a shift of the carrier wave with respect to the pulse envelope and the carrier-envelope-phase (CEP) becomes important in characterizing the laser field (Fig. 1.3a). In 2001 stabilization of the carrier-envelope phase of femtosecond oscillators [23] was demonstrated and was extended to amplifiers in 2003 [24]. Control over the waveform of few-cycle pulses has been a major step forward in studying effects of the instantaneous electric field on strong-field phenomena [7].

The control over the CEP can now be used as an additional parameter in light-matter interaction with few-cycle IR pulses. For example, ionization is predicted to have a non-linear dependence on the field strength [25] and to occur at the maxima of the electric field. As such, the ionization yield is predicted to increase in a step-wise manner as a function of time. As the electric field is influenced by a shift of the CEP, phase effects are expected to be observed in the time-dependent ionization of atoms by few-cycle pulses [7]. The step-wise increase in the ionization has indeed experimentally observed [26].

This non-linear dependence of the ionization on the electric field strength is exploited in the 'attoscond double-slit experiment' [27]. Depending on the CEP either one or two half-cycles contributed to the photoemission in xenon atoms. Interference of electrons ionized at a similar vector potential during two consecutive half-cycles, led to the observation of interference fringes in the photoelectron spectrum. These short bursts of ionization can be viewed as the temporal slits in the famous double-

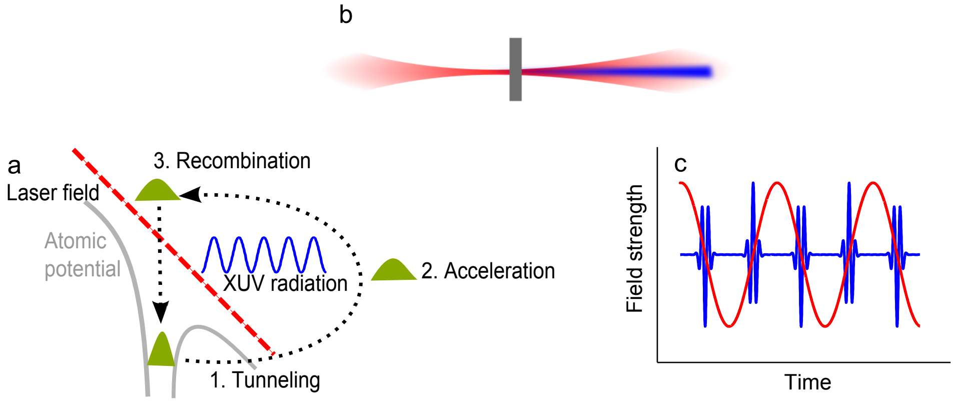

Figure 1.2: a) Semiclassical three-step model for high harmonic generation. (1) Tunnel ionization through the potential barrier releases an electron in the continuum. Following acceleration by the laser field (2), the electron can return to the vicinity of the parent ion. (3) Recombination of the electron with the ion leads to the emission of light that are the higher order harmonics of the driver laser. b) Schematic illustration of an experimental setup for HHG in a gaseous medium using an intense laser field. c) HHG with a multicycle driver laser (red line) results in the generation of an attosecond pulse train (APT).

slit experiment.

In addition to interference effects in the above-threshold-ionization spectra [28], effects of the CEP can be observed in the cut-off energy in the photoelectron spectra [29]. This can be related to the maximum energy the electron can gain in the continuum between ionization and recollision and after recollision, as a function of the CEP. In HHG, the energy of the re-colliding electron is mapped onto the energy of the emitted photons. The phase that the electron acquires in the continuum is responsible for the harmonic emission and is strongly dependent on intensity [30] and likewise the CEP. HHG is predicted to depend on the CEP [31] and indeed has experimentally been observed in the cut-off part of the high harmonic spectrum [32, 33].

CEP effects in light-matter interaction have first been reported for atoms [7] and then extended to molecules in 2006 [34]. D_2 molecules were ionized by few-cycle CEP-stabilized IR pulses. Recollision excitation by the continuum electron led to the dissociation of D_2^+ molecules, forming $D^+ + D$ fragments with a high kinetic energy ($E_k \sim$ 3-10 eV). It was observed that the remaining electron in the D_2^+ molecule could be steered, as a function of CEP, to either the 'left' or 'right' D^+ ion with respect to the laser polarization. This was observed as an asymmetric ejection of D^+ fragment ions in the laboratory frame (Fig. 1.3b). Such an asymmetric ejection of D^+ fragments requires a breaking of the symmetry of the electron localization in the dissociating D_2^+ molecule. This symmetry breaking is provided by the asymmetric electric field of the few-cycle IR pulse. The IR-field forms a coherent superposition of the 'gerade' and ungerade' electronic states of the dissociating

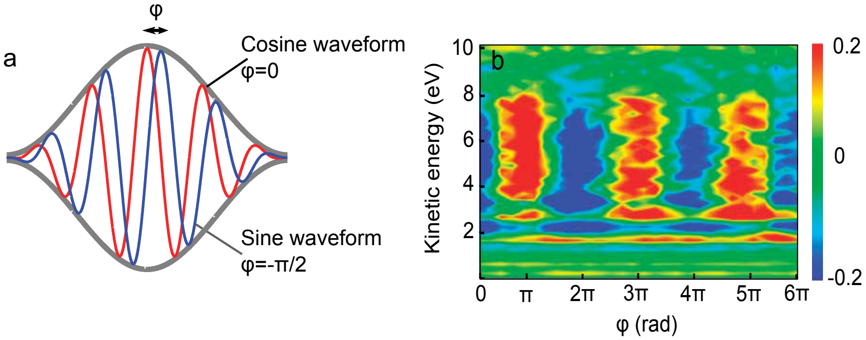

Figure 1.3: sa) The electric field for a few-cycle laser pulse shows a dependence on the carrier-envelope-phase (ϕ). For a cosine waveform (ϕ=0, red line), the maximum of the electric field and pulse envelope (gray line) coincide. For a sine waveform ($\phi = -\pi/2$, blue line) there are two electric field maxima. b) The asymmetric ejection of D^+ fragments in the laboratory frame is quantified by the asymmetry parameter $= \frac{D^+_{\text{left}} - D^+_{\text{right}}}{D^+_{\text{left}} + D^+_{\text{right}}}$ and is plotted as a function of ϕ and the kinetic energy of the D^+ fragments.

molecular ion, which localizes the electron on the 'left' or 'right' nucleus depending on the CEP.

1.2 Extreme ultraviolet radiation generated by high harmonic generation

After the discovery of HHG it was soon realized that it can potentially form a very powerful new light source. Femtosecond laser based HHG sources provide light with photon energies in the extreme-ultraviolet to soft X-ray regime [35] with spatial and temporal coherence, owing to the nature of the generation process. As such they can be a table-top light source with excellent peak brilliance and photon energies that traditionally have only been available at large scale synchrotron light sources. Moreover, it provides a light source with pulse durations in the attosecond time-domain [8]. In case of a multi-cycle laser pulse, the HHG takes place twice per optical cycle and results in the generation of an attosecond pulse train [8] (Fig 1.2c). Conversely an isolated attosecond pulse can be generating by limiting the HHG process to only one half-cycle in the laser pulse. The harmonic emission is dependent on the return and recombination of the continuum electron with the parent ion, which can be controlled by the ellipticity of the driving laser pulse. Isolated attosecond pulsed can be generated by making use of a time-dependent ellipticity of the laser pulse to suppress the harmonic emission to only one event and has been termed polarization gating [36].

XUV pulses generated by HHG for studying molecular structure and dynamics

The short pulse duration of the XUV pulses generated by HHG can be used in time-resolved studies of the dynamics of atoms and molecules that take place on the femtosecond time-scale. The foundations of time-resolved studies of molecular dynamics are in the area of femtochemistry and Achmed Zewail received the Nobel Prize in chemistry for his contribution to this field in 1999 [37]. The study of atomic and molecular motions on these ultrafast timescales requires the configuration of a pump-probe set-up, in which one pulse (pump) initiates the dynamics under investigation and a second time-delayed pulse (probe) measures it. In femtochemistry, an absorption spectrum is measured that serves as a fingerprint of the intermediate products that are involved in a chemical reaction [37].

The XUV/soft X-ray pulses generated by HHG with pulse durations down to the attosecond time-domain can be used in experiments that are complementary to the femtochemistry methods. These methods are based on the measurement of the products that are the result from a photodissociative ionization reaction (ions or electrons). The measurement of the ion products can elucidate the dynamics of photodissociation reactions and the transient species that are involved. For example, the delay-dependent kinetic energy distribution of ion fragments, measured using XUV/soft X-ray femtosecond pump-probe spectroscopy, gave insight into the dynamics of molecular ion dissociation [38] or the fastest molecular vibrations of H_2^+ [39].

The measurement of the photoelectron kinetic energy is used in time-resolved femtosecond photoelectron spectroscopy (TRPES) and follows the electronic distributions that accompany the nuclear dynamics. Early TRPES experiments, using light in the visible wavelength regime, have for example shown that the dissociation of $(NO)_2^+$ is likely to proceed via a two-step mechanism, not revealed in time-resolved studies of the photoion fragments [40].

HHG light sources now allow to extend time-resolved photoelectron spectroscopy to the XUV/soft X-ray regime. First results include the study of the dissociation of neutral Br_2 molecules, initiated by a photoexcitation process with visible light. Time-resolved soft X-ray photoelectron spectroscopy revealed an extremely fast dissociation time of 40 femtosecond [41]. It demonstrated that the femtosecond soft X-ray pulses are sensitive to a changing electron distribution, accompanying the dissociating molecule and that is reflected in a delay-dependent photoelectron spectrum. This technique has been extended to chemical reactions taking place at the surface [42].

Attosecond time-resolved studies of electron dynamics

The short pulse duration of these XUV light pulses have proven their use in the study of molecular dynamics using time-resolved photoion or photoelectron spectroscopy. The pulse duration of these laser pulses is on the time-scale of the motion of electrons and can be used to study electron dynamics in real-time. Attosecond spectroscopy strives to develop techniques to follow the electron motion on its natural timescale. Excited by this prospect, the development of attosecond pulses has opened up a new research field encompassing the dynamics of electrons in atoms, molecules and condensed matter [43].

Following the example set by the femtochemistry, one would try to use a pump-probe set-up, with attosecond XUV pump and probe pulses. However, the low cross-section for two photon XUV absorption, combined with the low intensity of the HHG sources make such experiments extremely difficult. Attosecond resolution can still be obtained by using a pair of IR and XUV pulses, where the XUV pulse is synchronized with the oscillations of the intense IR field. This synchronization provides a natural sub-femtosecond clock for all processes that are sensitive to the oscillations of the electric field and not only to the pulse envelope. Given that the IR field strength changes by several V/m in a matter of a femtosecond, most of the IR-field induced processes are very sensitive to the oscillations of the IR electric field.

For example, attosecond streaking uses the relation between the electron momentum at the detector and the phase of the IR optical cycle at which the electron enters the continuum [44]. It has been used to map out the electric field of a waveform-controlled few-cycle pulse [45]and measure photoemission in atoms [46] and in condensed matter [47] in a time-resolved way.

Conversely, one can measure the transmitted photons, similar to the femtochemistry experiments. In attosecond transient absorption spectroscopy a delay-dependent XUV absorption spectrum is measured, which reflects the evolution of the electronic wavepacket. This method has successfully characterized coherence between different electronic states of the ion, produced by strong-field ionization, and measured the real-time motion of valence electrons in Kr [48].

Another method exploits the high non-linearity of the ionization process by intense IR laser pulses. Theory predicts that the ionization is confined to sub-femtosecond intervals centered at the peaks of the oscillating IR field [25] and this has also experimentally been observed [26]. The sub-femtosecond duration of the ionization process can thus be used as the starting trigger for a wide range of dynamics, which can be probed by a synchronized attosecond XUV pulse.

A major part of these attosecond experiments have been performed in atoms [43]. The relevancy of an attosecond timescale to the molecular physics is inferred from the fact that the interactions of molecules with incident light is of electronic nature. Interaction of a molecule with incident light can promote the molecule to excited electronic states, where the subsequent nuclear dynamics takes place on a femtosecond timescale, which can be probed with time-resolved XUV/soft X-ray photoelectron or photoion spectroscopy. The presence of an attosecond time-scale in large biomolecules has theoretically been predicted. The rearrangement of electrons following excitation by an attosecond light pulse was found to take place on a sub-femtosecond timescale [49].

The first experimental observation of attosecond electron dynamics in molecules was presented in 2010. Electron localization in dissociating D_2^+ molecules could be probed with attosecond precision by measuring laboratory frame asymmetries in the ejection of D^+ ions, reflecting the localization of the electron [50].

1.3 Extreme Ultra-violet/X-ray Free Electron Lasers

Accelerator based free electron lasers (FELs) are being built on various locations in the world, amongst which are the LCLS in the USA, the SCSS in Japan and the XFEL in Germany. These FELs are based on self-amplified spontaneous emission (SASE) of free electrons with relativistic energies (Figure 1.4a). They generate coherent light with femtosecond pulse durations and photon energies in the XUV to the hard X-ray regime [51, 52]. Light at these energies has, until the operation of X-ray FELS, only been available at synchrotrons. However, the FELs offer much higher intensity and shorter pulse durations.

The combination of the short pulse duration with the high photon flux of the FEL allows one to reach unprecedented light intensities in this wavelength regime. One of the research interests using these FELs, is to investigate the aforementioned strong-field ionization mechanisms in the XUV/X-ray regime and thereby testing the validity of the Keldysh parameter for strong-field processes at these wavelengths [53–55].

Structural studies using photon diffraction

One of the motivations for the construction of these XUV/X-ray FELs is the prospect of performing structural studies of matter. Insight into the structure of matter on the atomic scale has mainly been obtained by X-ray diffraction of homogeneous crystalline samples by synchrotron sources or lab-scale X-ray tubes. The regular arrangement of the atoms in a crystalline sample allows for coherent addition of the scattered photons, reducing the X-ray flux required to measure a high-resolution diffraction pattern.

Structural determination has been severely limited for samples that cannot be crystallized, like bio-molecules, requiring many photons to record a high resolution diffraction pattern. Photon absorption causes sample damage, which forms a major problem in the structural determination. The Absorption of a photon results in the creation of a hole in a deep-lying orbital and the electronically unstable ion will relax through fluorescence or Auger processes, inducing movement in the sample, thereby limiting the time in which a diffraction pattern can be recorded.

X-ray FELs potentially offer photon fluxes within a short pulse duration that allows one to record a high resolution diffraction pattern before the sample is destroyed. This has been confirmed by simulations of femtosecond X-ray scattering on single protein molecules [58]. Experimental proof-of-principle was given by the measurement of a single-shot diffraction pattern of a micro-meter sized object at the free electron laser in Hamburg (FLASH) at a wavelength of 32 nm [59]. Meanwhile, the first diffraction experiment on nanocrystals of a membrane protein was performed at the LCLS in Stanford and the single-shot diffraction patterns contain structural information of the protein complex [60]. This experimental proof is a major step forward for the determination of bio-molecules, which otherwise would have been inaccessible.

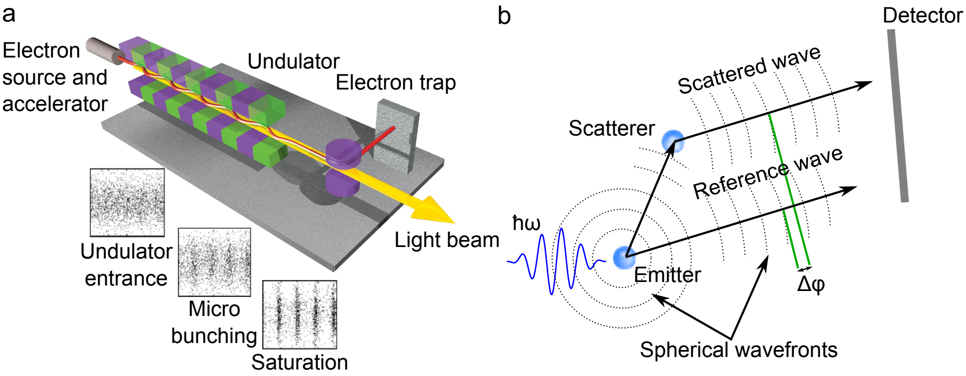

Figure 1.4: a) Schematic illustration of the free electron laser in Hamburg (FLASH). Pulses of electrons are accelerated by an accelerator to velocities close to the speed of light and enter the undulator which has an alternating magnetic structure. The time-evolution of the electron beam is numerically simulated as a function of the propagation distance in the undulator. The result of the simulation is shown in the three panels under the undulator structure. The interaction between the electrons and the spontaneously emitted radiation by the electrons will cause a microbunching of the electrons into slices that are shorter than the wavelength of the light. The electrons within a microbunch will radiate like a single particle of high charge, generating light with temporal and spatial coherence [56].
b) Schematic illustration of the principle of electron holography [57]. Ionization by a light pulse emits an electron from one of the atoms, which now acts as a source of electron waves with spherical wavefronts. There are two possible pathways towards the detector, an undistorted reference wave and a wave that is scattered by a second atom. The phase difference $\Delta\phi$ between the waves results in the measurement of an interference pattern that reflects the internuclear distance between the emitting and scattering atom.

Following molecular dynamics using photoelectron diffraction

The cross-section for diffraction of photons with a swavelength of 1 Å is about 10 times smaller than the photoabsorption cross-section [58]. The larger cross-section for photoabsorption, which induces sample damage, can actually be used to the experimentalist's advantage, by using diffraction by the photoelectrons.
This principle of 'illuminating the molecule from within' was demonstrated by Landers *et al.* in 2001 [61]. In the experiment, the angle-resolved momentum distribution of coreshell ionized electrons, using a synchroton light source, showed a modulation in the angular distribution, related to the diffraction of the photoelectrons on one of the atomic nuclei. This principle of electron holography, illustrated in Figure 1.4b, van be used to follow molecular dynamics in real-time by extending the experiment of Landers *et al.*, using a continuous light source, to the femtosecond X-ray FELs [57]. This method potentially provides a major advantage over femtochemistry techniques as it does not rely on the interpretation of the absorption spectrum and comparison to simulations.

An important prerequisite of diffraction experiments on molecules is that the experiment is performed in the molecular frame (the photoelectron angular distribution is measured in a frame that is defined by the orientation of the molecule). In the experiment by Landers *et al.* [61] the ion fragments resulting from dissociation and the diffracted electrons were recorded in coincidence. The molecular frame in the reaction microscopes is determined by the ejection direction of the ion fragments, provided that the axial recoil approximation is valid. The disadvantage of these reaction microscopes [62] is that they are limited to channels that dissociate. Another drawback is that the count rates are limited to less than one count per laser shot to completely kinematically resolve the system.

An attractive alternative method is the velocity map imaging spectrometer (VMIs) [63], which measures the angular resolved momentum distribution of either electrons or ions. VMIs offers a 100% collection efficiency and therefore makes optimal use of the high photon flux of the FELs. Measuring the photoelectron distribution in the molecular frame can be realized by aligning the molecules in the laboratory frame using impulsive [64] or adiabatic alignment by a synchronized laser pulse and recording the photoelectron angular distribution using VMIs.

1.4 Outline of this thesis

The research described in this thesis is strongly motivated by the prospect of making progress in the study of molecular dynamics. The aim of this thesis was to explore methods that bring new insight into the electronic and nuclear dynamics of molecules, using the novel light sources described here. The experiments presented in this thesis have either provided new insights into molecular dynamics were an important step in developing methods that realize this goal.

The goal of the first part of this thesis was to explore the use of XUV pulses generated by HHG in probing nuclear and electron dynamics in molecules. First, the elements that are needed to configure a stable attosecond XUV-femtosecond IR pump-probe set-up are described in chapter 2. The experimental set-up at AMOLF in Amsterdam is described in detail, together with the tailored velocity map imaging spectrometer that is used in the experiments described in Chapter 4 and 6.

In chapter 3 we used XUV light pulses generated by HHG or the fundamental or second harmonic of a Ti:Sapphire laser, to directly probe the sign of the permanent dipole moment of NO molecules. The experiment eliminated a possible error in the sign of the NO dipole moment as the cause of a long-standing sign discrepancy between experimental and theoretical results in collision experiments of NO with other atoms or molecules. The experiment was my first encounter with generating XUV light pulses by HHG and I am very satisfied with the result. In addition, the experiment was a combination of techniques to orient molecules in the laboratory frame and of short laser pulses to probe this orientation. Such a combination of aligning and orienting molecules in the laboratory frame with short light pulses is a prerequisite in experiments where structural and dynamical information is obtained by 'illuminating the molecule from within', as described in the section concerning free electron lasers.

The interest in HHG as a source of XUV light pulses is also motivated by the

attosecond pulse durations of these sources, which are on the timescale at which electron motion takes place. A major part of attosecond experiments have elucidated electron dynamics in atoms. In chapter 4 we explore the application of attosecond light pulses as a probe for electron dynamics in molecules. As mentioned previously, XUV - XUV attosecond pump-probe experiments are extremely challenging due to the low intensity of HHG sources. Therefore, as a proof-of-principle, we induced a time-dependent polarization in O_2 molecules by a moderately strong IR laser field and ionized these polarized O_2 molecules by an XUV attosecond pulse train. The fragment ion yield and angular distributions were found to depend on the phase of the IR field at the time of the XUV + IR ionization. The observations are understood in terms of an IR-field induced coupling between electronic states in the molecular ion. The experiment shows that dissociative ionization by the APT is sensitive to a time-dependent polarization induced by the IR field and that attosecond pulses can be used to probe these dynamics. The explanation of the observed dynamics in terms of a simplified model of the molecule provided an intuitive view of the dynamics. Unfortunately, dynamical models to completely describe the O_2 molecules are still under development and to our disappointment could not be included yet in the interpretation of the results. The analysis of the experimental data illustrated for us the challenges one encounters in an attempt to provide a complete description of the observed dynamics in slightly more complex molecules than H_2, such as O_2.
The experiment was performed at the new attosecond pump-probe setup at AMOLF, described in chapter 2. This result was one of the first that have been obtained at this setup and the high quality of the experimental data was therefore very satisfying and demonstrated the potential of our experimental setup.

A unique facility is the soft X-ray free electron laser in Hamburg (FLASH). In chapter 5 we describe the first velocity map imaging (VMI) experiment at FLASH, where we used FLASH to ionize a range of rare gas atoms and small molecules. The experiment was an important step in developing a novel method that uses free electron lasers to study molecular dynamics by recording the photoelectron angular distributions of aligned molecules. The experiment was a necessary step to implement the VMIs at FLASH and has led to experiments where FLASH was used to probe the time-dependent alignment of CO_2 molecules [65] and the dissociation of aligned Br_2 molecules. The uniqueness of a facility such as FLASH combined with exploring a novel method to directly probe molecular dynamics, made the long hours of beamtime at FLASH a rewarding experience. Although experimental proof of the use of FLASH in probing molecular dynamics based on diffraction by photoelectrons has yet to come, we think that this is a promising method in directly probing the motion of the atomic nuclei.

Gaining insight into molecular dynamics does not always require the configuration of a pump-probe setup. The control over the waveform of few-cycle IR pulses has led to the observation of sub-cycle effects in the interaction of light with atoms and molecules. In chapter 6 we used CEP-stabilized few-cycle pulses to study electron localization in the dissociative ionization of H_2 and D_2 molecules. The experiment was an extension of the pioneering work presented in [34], which is described in section 1.1. To gain a qualitative understanding of the experimental results we performed numerical simulations of the dissociation of the molecular ion in the presence of the few-cycle IR pulse. A semiclassical model was developed that allowed us to include the electron-electron interaction, leading to excitation of the molecular ion, in the numerical calculations. I am particularly excited about this chapter, as the experiments were performed at a unique experimental setup in Milano and the combination of the experimental results, the numerical simulations and the semiclassical model provided a fantastic playground for me to gain insight into the physics of recollision electron dynamics.

2 Experimental techniques for XUV-IR pump-probe experiments

Since the first observation of attosecond pulses in 2001 [8], the physics community has been excited about the prospect of following electronic processes in atoms, molecules and solids on the relevant time-scales. Attosecond science is a very rapidly developing research areas and has studied electronic processes in atoms [46], molecules [50] and solids [47]. The aim of this chapter is to describe the techniques that are used by experimentalists to configure successful attosecond experiments. These methods are found in attosecond laboratories around the world. Emphasis is put to the attosecond laboratory at the AMOLF-institute, at which the results of chapter 4 were obtained.

2.1 Introduction

Measuring time-resolved dynamics in atoms, molecules and solids requires the configuration of a set-up in which two laser pulses initiate (pump pulse) and detect (probe pulse) dynamics, similar to the pump-probe setups that have in the past been successfully applied in femtochemistry experiments [37]. Measuring time-resolved electron dynamics requires one to extend these approaches to the domain of the atomic unit of time, i.e. the attosecond domain (1 a.u. = 24 as). This requires the availability of novel light sources capable of generating pulses in the attosecond domain, and imposes very stringent requirements on the stability of the experimental setups involved. Time-resolved applications of attosecond laser pulses have so far been limited to two-color experiments, where the attosecond laser pulses are used either in the pump or probe step, and where attosecond time-resolution is achieved by using the optical cycle of a near-infrared (near-IR) laser as a clock. This clock has been based on the sub-cycle dependence of strong-field ionization rates [26] and on sub-cycle dependent acceleration of continuum electrons (so-called 'streaking') [66, 67].

First the essential elements, that are part of an attosecond XUV-IR setup, are described. As an illustration, a detailed description of the attosecond pump-probe setup at the FOM Institute AMOLF in Amsterdam is given (see Figure 2.1). The starting point of every attosecond experiment is an intense femtosecond (1 fs = 10^{-15} s) near-IR or IR laser pulse. This laser pulse is either used directly to drive a high-harmonic generation (HHG) process in order to generate the attosecond (1 as = 10^{-18} s) pulses, or first tailored to meet special needs for the generation of, for

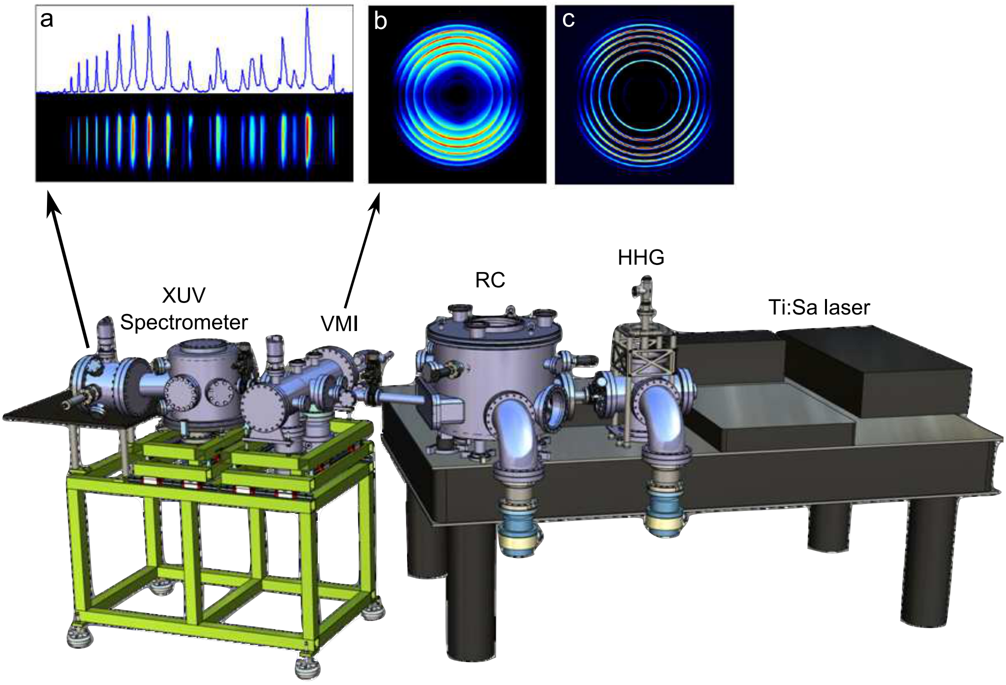

Figure 2.1: The attosecond pump-probe setup at AMOLF. The output of the Ti:Sa laser is split into the two arms of a Mach-Zehnder interferometer. In one arm the laser is focused into a HHG gas cell and recombined with the other arm in the recombination chamber (RC) after filtering out the fundamental and low order harmonics. The beams are collinearly focused by a toroidal mirror into the center of a velocity-map imaging spectrometer (VMIS), where charged particles arising from interaction with the two laser pulses are detected on a two-dimensional detector. After the VMIS a XUV spectrometer is connected to monitor the harmonic spectrum. b) An example of a recorded velocity map image is shown for photoelectrons from ionization of Ar atoms with HHG radiation generated in Ar. The rings correspond to the different harmonic orders. The image was recorded in 5 s using 15000 laser shots. The 3D photoelectron velocity distribution can be reconstructed from the measured image by an Abel inversion. A slice through this distribution is shown in (c). A typical XUV spectrum from HHG in Ar measured with the XUV spectrometer is shown in (a).

example, tailored attosecond pulse trains or isolated attosecond pulses. Successful attosecond experiments require that the XUV pulse is recombined and locked with an IR pulse with interferometric stability. Most experiments rely on the detection of charged particles (electrons and ions) resulting from the interaction of the target under investigation with the two pulses, and different choices can be made in the type of detector that is applied. The majority of the experiments up to date have been carried out in gas-phase targets in a molecular beam or at the exit of a gas-jet. A smaller number of experiments have been performed with solid-state targets, which often calls for a different detector approach. Recently, several groups have reported on all-optical experiments in which one measures two-colour absorption or enhancement of the harmonic spectrum. For these experiments an XUV spectrometer is a necessary tool, which in many labs also functions as a convenient diagnostic to monitor the XUV spectrum. The components described above will now be discussed in more detail.

2.2 Femtosecond driver laser

With very few exceptions, attosecond experiments depend on amplified Ti:Sapphire femtosecond lasers as the driver light-source since in order to efficiently drive the HHG process, laser pulse energies on the order of a milli-Joule (mJ) are required. Typical HHG conversion efficiencies are 10^{-6} which leads to $\sim 10^6$ XUV photons for a pulse energy of 1 mJ.

Using the approaches described in this section it is then possible to configure XUV experiments where as many as 10^3 photoelectrons or photoions can be recorded per laser shot. Amplified Ti:Sa lasers produce pulses around a central wavelength of 780 nm, and typically start with a mode-locked Ti:Sa oscillator, producing pulses with a duration of 5-50 fs full-width-half-maximum (FWHM) and pulse energies of several nJ at a repetition rate of 80 MHz. These pulses are subsequently amplified using a chirped pulse amplification (CPA) scheme that operates at a reduced repetition rate of typically one to several kHz, generating pulses of typically 30 fs FWHM and pulse energies of 1-10 mJ. For reference material on ultrashort pulse lasers and high power ultrafast laser amplification we refer the reader to [68–70] and the references therein.

At AMOLF, a multi-pass amplifier is used that delivers 30 fs FWHM pulses with an energy of 2.3 mJ at a repetition rate of 3 kHz. Although amplified Ti:Sa lasers have been very successful in the emergence of attosecond science it is likely that lasers based on optical parametric amplification (OPA) will gradually replace Ti:Sa-based systems. The most important advantage that OPA has over Ti:Sa is the larger gain bandwidth so that shorter pulses can be generated. For example in a non-collinear OPA sub-5 fs have been generated in the visible wavelength regime [71]. For a review of OPAs we refer the reader to [72]. In order to reach the XUV intensities of 10^{13}-10^{14} W/cm^2 that are necessary for the observation of non-linear XUV ionization (a pre-requisite for XUV pump - XUV probe spectroscopy), higher driver pulse energies and intensities are needed. Current developments to accomplish this are aimed at increasing the pulse energy of Ti:Sa CPA systems and at the development of OPAs. In combination with chirped pulse amplification (non-collinear optical parametric chirped pulse amplification (NOPCPA), 8 fs pulses with an energy of 130 mJ at 10 Hz have already been achieved [73]. Finally, OPA systems also form a viable route towards substantially higher repetition rate attosecond sources which will be greatly beneficial for certain experiments. Pulse energies of several tens of J at 60 kHz [74] and more than 1 J at repetition rates at 143 kHz [75] have been reported.

2.2.1 Carrier-envelope-phase (CEP) stabilized pulses

The electric field of a linearly polarized laser can be described by $E_L(t) = E_0(t)\cos(\omega_L(t)t + \phi)$. Here, $E_0(t)$ is the laser pulse envelope, $\omega_L(t)$ is the instantaneous frequency of the electric field and ϕ is the carrier envelope phase (CEP). In the case of a transform-limited pulse, this simplifies to $E_L(t) = E_0(t)\cos(\omega_L t + \phi)$. The response of atoms and molecules to few-cycle pulses is strongly affected by the CEP, ϕ [34, 76]. Most importantly, as will be described later, the generation of single attosecond pulses (SAPs) depends crucially on the stabilization of the CEP of the driver laser. Standard pulse diagnostics like an autocorrelator, SPIDER or FROG cannot measure the CEP.

Measurement, control and stabilization of the relative CEP change was demonstrated in 2000 [23]. The output of a mode-locked laser oscillator corresponds in the frequency domain to a comb of frequencies, separated by the repetition rate f_{rep}. The comb frequencies are integer multiples of the repetition rate with an offset frequency δ. The pulse-to-pulse change in the CEP $\Delta\phi$ is related to this offset frequency by

$$\delta = (\frac{\Delta\phi}{2\pi})f_{rep} \tag{2.1}$$

A so-called $f-2f$ interferometer makes use of an octave-spanning frequency comb to determine and stabilize the offset frequency δ. Although oscillators exist that generate octave spanning spectra, generally the laser pulse spectrum needs to be broadened, e.g. in a photonic crystal fiber. The long wavelength end of the spectrum is frequency doubled, generating a second frequency comb with twice the CEP offset frequency. The frequency-doubled light is overlapped with the original spectrum at the same wavelength on a photodiode. The beat note between the high frequency components in the original comb ($f_f = nf_{rep}+\delta$) and the low frequency components in the frequency-doubled comb ($f_{2f} = 2mf_{rep}+2\delta$), then immediately reveals δ and hence the pulse-to-pulse change in the CEP phase $\Delta\phi$ [23]. The measured pulse-to-pulse phase slip can be used to drive an electronic feed-back loop which controls the pump power in the oscillator with an Acoustic Optical Modulator (AOM) or by the tilt of a mirror in the cavity at a position where the frequencies are dispersed, which both impact $\Delta\phi$. Since it is in general not possible to zero δ, because in that case the beat note disappears, δ is usually stabilized to $\frac{1}{4}$ of the repetition rate of the laser oscillator. This means that every 4^{th} pulse from the oscillator has the same CEP, and the lower repetition rate of the amplifier can then be chosen so that every amplified pulse has the same CEP.

An important step for attosecond science was realized in 2003 when CEP phase measurement and stabilization was realized for an amplified Ti:Sa laser system [24].

CEP-stabilized Ti:Sa amplified lasers utilize a second $f - 2f$ interferometer to stabilize the CEP of the amplifier and, as mentioned above, it is ensured that only pulses with identical CEP are selected for amplification. The reduced repetition rate and the absence of a pulse-to-pulse phase slip calls for a different design of the $f - 2f$ interferometer. An octave spanning bandwidth is generated by self-phase modulation in a medium like sapphire. The long wavelength end of the spectrum is frequency doubled and overlapped on a spectrometer. The interference of the frequency doubled light and the fundamental results in a fringe pattern in the spectrum that is dependent on the CEP, and can therefore be used to stabilize the CEP. Typically the feedback loop runs at a repetition rate of a few to tens of Hz and is therefore commonly referred to as the slow loop, as opposed to the fast loop of the oscillator.

Correcting CEP drifts in the slow loop can be done by superimposing the error onto the fast loop, supplying a correction to the grating or prism spacing in the amplifier stretcher/compressor [77], changing the path length through a pair of wedges or by an acousto-optic programmable dispersive filter [78, 79].

Recently, Steinmeyer and co-workers have introduced the possibility to correct the CEP of a non-stabilized oscillator using a feed-forward applied to an acousto-optic frequency shifter (AOFS) [80]. Supplementing these improvements in the control of the CEP, recent work has also advanced measurement of the CEP, notable through the use of stereo-ATI (Above-Threshold Ionization) measurements [81]. This method allows for the determination of the CEP itself, in contrast to $f - 2f$ interferometers which only determine relative changes in the CEP.

Most schemes for the generation of isolated attosecond pulses require pulse durations of the driver field that are significantly shorter than amplified Ti:Sa lasers can deliver. Two pulse compression techniques have been developed for the generation of few-cycle pulses.

2.2.2 Generation of few-cycle pulses in a hollow core waveguide

Compression of multi-cycle IR pulses by spectral broadening in a hollow-core fused silica waveguide was first time reported by Nisoli [20, 21]. In this scheme multi-cycle laser pulses are loosely focused in a hollow-core waveguide filled with noble gases at high pressures (1-2 bar). Spectral broadening due to self-phase modulation by non-linear interaction with the noble gas and subsequent pulse compression by e.g. chirped mirrors can shorten the pulses down to a sub-5 fs FWHM duration, close to the fundamental limit of a single optical cycle [22]. The wave propagation occurs through multiple grazing incidence reflections with accompanying losses at the inner surface. Only the fundamental mode propagates with high efficiency in a long waveguide resulting in a single mode output. Output pulses therefore exhibit excellent uniform beam profiles after compression. Typical input pulse energies are limited to 1 mJ, due to self-focusing and ionization at the entrance of the fiber, resulting in a degraded coupling of the beam and the waveguide for higher pulse energies. Using a pressure gradient in the hollow fiber, input pulses with an energy of 5 mJ (pulse duration 25 fs FWHM) have been used, which resulted in the generation of pulses with 5.4 fs FWHM pulse duration and 2.7 mJ pulse energy [82]. Chen *et al.* recently reported the production of 4.5 fs pulses with 1 mJ pulse energy [83].

2.2.3 Generation of few-cycle pulses through filamentation

A potentially simpler technique to generate few-cycle laser pulses is through filamentation [84]. The guiding effects of the hollow wave guide are substituted by the self-guiding effects that can arise when a laser propagates through a transparent medium. The self-guiding is the result of interplay between two effects: self-focusing due to an intensity-dependent refractive index of the medium (Kerr effect) and defocusing of the beam due to plasma formation. In certain conditions the two effects can be balanced resulting in a filament with a length of tens of centimeters. In the filament self-phase modulation broadens the spectrum, as in a hollow core waveguide.

The first demonstration of filamentation employed a sequence of two gas cells filled with Argon at pressures of 840 and 700 mbar [84]. The input pulses (43 fs, 0.84 mJ) were loosely focused in the gas cells and formed filaments of 10-15 cm. Pulse compression with chirped mirrors generated pulses of 5.4 fs (0.38 mJ). A comparison between hollow core waveguides and filamentation methods is described in [85]. Hollow-core waveguides generate box-like spectra, better suited for chirped mirror based compression and produce beams with excellent spatial profiles over a wide range of gas pressures. Disadvantages of hollow core waveguides are the coupling losses introduced by the fiber and the sensitive dependence on alignment, causing possible thermal drifts over time. Filamentation shows a sensitive dependence on gas pressure due to the dependence of the guiding effects on the plasma formation. In the absence of a waveguide, filamentation provides less homogeneous beams, but offers a potentially higher throughput compared to hollow core fibers.

2.3 Generation of attosecond pulses by high-harmonic generation

In 1987 two research groups observed, that the interaction of a high-intensity laser pulse with a gas, resulted in the emission of photons with a spectrum that consisted of high-order odd harmonics of the driving laser pulse [16, 17]. The harmonic spectrum is characterized by three regions: 1) low-order harmonics, showing a rapid decrease in intensity, 2) a plateau region and 3) a cut-off region beyond which the intensity of the high-order harmonics rapidly becomes negligible. Existing models that explained the production of low-order harmonics failed to reproduce the plateau region and cut-off. In 1993 the introduction of the semi-classical three-step model gave a rationale for the observed effects, described in section1.1 [13, 86]. The model predicts a cut-off energy of $3.17U_p + I_P$, which is exactly what was seen experimentally. U_p is the ponderomotive energy of the electron in the laser field and I_P the ionization potential of the atom. The HHG process is repeated for every half-cycle of the laser pulse and therefore generates a sequence of XUV bursts in the time-domain, and a spectrum that consists of peaks with frequencies that are odd multiples of that of the driving laser (the frequencies are odd rather than even multiples since the driving laser field changes sign between consecutive half-cycles). The time-structure of HHG radiation was experimentally revealed in 2001 by measuring the relative phase of the harmonics [8]. This was possible using a two-color cross correlation measurement known as the RABITT (Reconstruction of Attosecond Beating by Interference of Two-photon Transitions) technique. The photoelectron spectra resulting from ionization by the harmonics are measured as a function of the delay between the harmonics and a moderately strong IR field. Photoelectrons at an energy E_n in between the odd harmonic peaks E_{n-1} and E_{n+1} are generated through two paths, one that involves harmonic order $n-1$ plus an IR photon and the other that involves harmonic order $n+1$ minus an IR photon. From the interference of the two paths the relative phase between the contributing harmonics can be determined. Using the determined relative phases it could be inferred that the radiation consisted of a train of attosecond pulses, with an average duration of 250 as [8].

Shortly after the semi-classical three-step model was introduced, a quantum mechanical model for HHG was developed. In this model, each harmonic is the sum of interfering contributions, corresponding to different trajectories of the electron in the continuum [87, 88]. Two groups of - short and long - quantum paths can be distinguished, referring to the time spent by the electron in the continuum. This is also illustrated in 2.2 where the kinetic energy of the continuum electron is plotted as a function of the time of return to the ion. As one can see, the same energy is emitted twice in time, once by electrons following the short trajectory and once by electrons following the long trajectory. The generation of attosecond pulses therefore requires the selection of either the short or long trajectories. The intrinsic phase of the harmonic dipole moment is different for the two trajectories and can be approximated as $\Phi_q \sim -U_p\tau$, where $U_p = \frac{I_{laser}}{4\omega_{laser}^2}$ and τ is the travel time of the electron.

2.3.1 Macroscopic phase-matching of high-harmonic generation

The three-step model and other single atom pictures of HHG cannot account for all effects that are found experimentally, since in practice HHG is always the result of a coherent addition of radiation from a number of atoms, so that propagation and dispersion effects also play an important role. Each atom can be considered as an emitter of XUV radiation, with amplitudes and phases depending on the local IR intensity. The coherent properties of the XUV radiation, emerging collinearly with the fundamental beam, are the result of a constructive interference of radiation from atoms in an extended medium, where phase matching is achieved when the following condition is fulfilled [89]

$$k_q = qk_1 + \nabla\Phi_q \tag{2.2}$$

where q is the harmonic order and k_q and k_1 are the wavevectors of the q^{th} harmonic and of the fundamental wave. Phase matching in HHG can be realized by balancing atomic, electronic and geometric dispersion [90, 91]

$$k_q = qk_1 + \Delta k_{atom} + \Delta k_{electron} + \Delta k_{geo} + \nabla\Phi_q \tag{2.3}$$

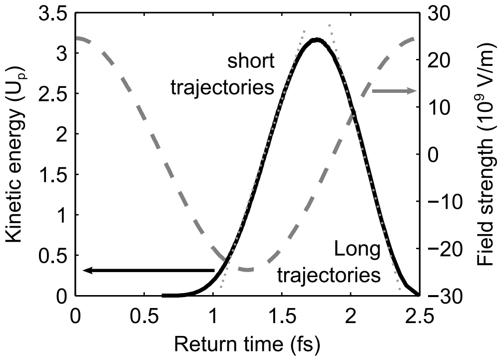

Figure 2.2: The kinetic energy of the continuum electron, upon return to the ion, as a function of the time of return (black line). The IR field is plotted in dashed gray lines. Each energy is emitted twice in HHG by electrons following the short and long trajectories. These two groups are schematically indicated by the dotted gray lines.

Atomic dispersion Δk_{atom} from the linear atomic polarizability plays a limited role in phase matching for low gas densities, but becomes important for higher gas densities.

When ionization of target gas atoms produces free electrons, electronic dispersion Δk_{elec} due to the wavelength dependence of the refractive index is significant. Laser beam focusing in the target gas introduces geometric dispersion Δk_{geo} by the Gouy phase shift, which is π for a Gaussian beam going through a focus.

Experimental parameters that control the phase-matching are the gas density (free electron dispersion), focusing conditions (geometric and free electron dispersion) and gas jet position (geometric dispersion). In general, loose focusing conditions will minimize phase mismatch due to the dipole phase and the Gouy phase shift and reduce ionization (free electron dispersion).

When the laser beam is focused before the gas medium, conditions can be created where the dipole phase mismatch is compensated by the geometric dispersion. In this on-axis phase matching configuration, short trajectories are favored over the long trajectories [92, 93]. The intensity-dependence of the dipole phase is smaller for the short trajectories compared to the long trajectories and due to this difference, the phase matching conditions are different for the short and long trajectories. For the generation of attosecond pulses, the short trajectories are favored for their smaller intensity dependence. The contributions from long trajectories can be spatially filtered out by a pinhole, due to their larger divergence [94].

The choice of the target gas in HHG is a trade-off between efficiency and maximum photon energy. Gas targets with a higher ionization potential can be exposed to higher laser intensities, increasing U_p and the cut-off energy, although at the expense of the HHG efficiency. For the rare gas atoms for example, Xe and Kr have a lower ionization potential and higher conversion efficiency and the opposite is true for He and Ne. As a guideline for designing gas targets, $L_{med} > 3L_{abs}$ and $L_{coh} > 5L_{abs}$ [95], where L_{med} is the gas medium length, $L_{abs} = 1/(\rho\sigma)$ is the absorption length, ρ is the gas density and σ the ionization cross-section. The coherence length $L_{coh} = \pi/|\Delta k_{tot}|$ where $\Delta k_{tot} = k_q - qk_l$ is the phase mismatch between the fundamental and harmonic wave. As an example the absorption length for Ar (12 mbar) for H15 is 885 µm and for Xe (6 mbar) is 1.8 mm.

Phase matching conditions can also be achieved in a gas-filled hollow capillary waveguide [35, 95, 96]. The waveguide propagation eliminates defocusing and the longitudinal dependence of the dipole phase. Phase matching is realized by changing the gas pressure (atomic and electronic dispersion) and capillary diameter (waveguide dispersion). Limitations on the gas pressure due to phase mismatch from electronic dispersion can be overcome by using a waveguide with a modulated inner diameter, with a periodicity of twice the coherence length ($\sim$ 1 mm) [97, 98].

Recent work suggests that HHG in hollow capillary waveguides also provides an avenue towards the generation of harmonics in the hard x-ray regime. Significant extension of the cut-off energy at near constant (or even slightly improving) efficiencies have been predicted and partially experimentally demonstrated when scaling the driver laser wavelength for a HHG process in a hollow waveguide towards the mid-infrared [99].

In the AMOLF setup (see Figure 2.1) the harmonic generation is performed in a static cell. The medium length is 3 mm and typical backing pressures are 20 mbar for Xe and 25 mbar for Ar. The steel tube assembly is mounted on a translation stage, movable along the laser propagation direction. Phase matching conditions are found by adjusting the position of the gas cell with respect to the laser focus, changing the gas pressure and adjusting the beam size with a variable iris prior to the focusing mirror.

In the right configuration a multi-cycle laser pulse leads to the generation of an attosecond pulse train (APT). For many pump-probe experiments one actually needs to generate a single attosecond pulse (SAP). Several routes have been developed to realize this goal.

In one method, the harmonics in the cut-off region are only generated by the center half-cycle of a very short laser pulse ($<$ 5 fs FWHM). By spectrally filtering out this part of the HHG spectrum one obtains a SAP [100]. Other methods make use of the fact that the efficiency of the HHG process strongly depends on the ellipticity of the generating field. In the semi-classical model it can be intuitively shown that a small degree of ellipticity will prevent the electron from returning to the core and will suppress the recombination process. By changing the ellipticity within the generating pulse in such a way, that only a single half-cycle is linearly polarized, a SAP can be generated. What follows is a closer look at the experimental conditions that are needed to generate attosecond pulse trains and single attosecond pulses.

2.3.2 Generation of attosecond pulse trains

High-harmonic generation using multi-cycle driving pulses leads to the generation of a harmonic spectrum characterized by a region of low-order harmonics with a rapidly decreasing intensity as function of harmonic order, a plateau and a cut-off region. A train of attosecond pulses can be obtained provided that the spectrum

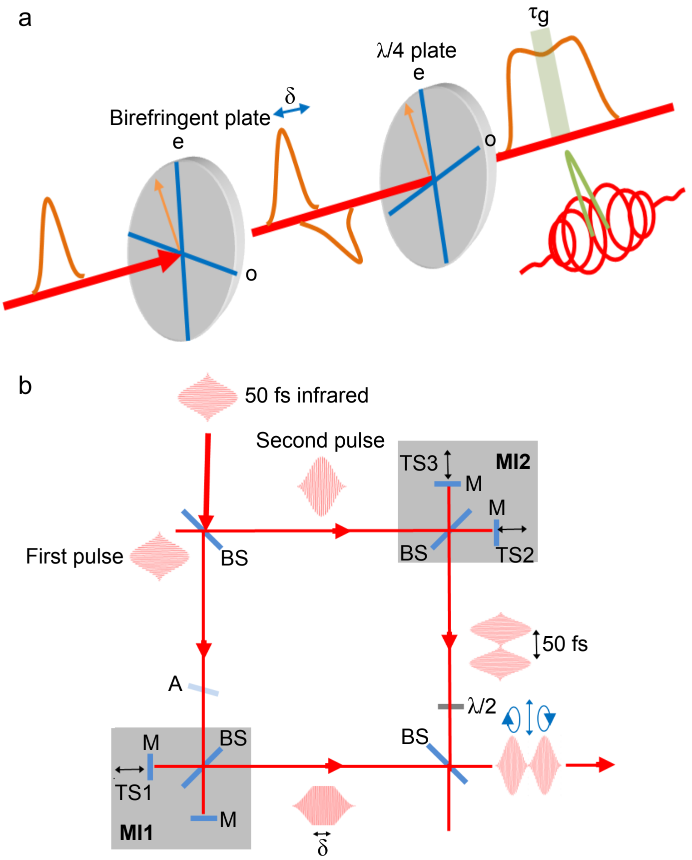

Figure 2.3: Methods for the generation of isolated attosecond laser pulses: a) Polarization gating using few-cycle CEP-stabilized laser pulses [101]: the pulses (5 fs) are split by a 181 µm multiple-order birefringent waveplate into two orthogonal, linearly polarized pulses, separated by $\delta = 5.8$ fs. A second zero-order quarter waveplate ($\lambda/4$ plate) transforms the linear polarization to circular polarization with an opposite helicity on the front and back parts of the pulse. The polarization-modulated pulse has linear polarization in the center (green line), where the two pulses overlap and circular polarization in the wings of the pulse. The time-gate τ_g with linear polarization is shorter than a half-cycle of the IR pulse, allowing the generation of isolated attosecond pulses. b) Interferometric polarization gating [102]: BS: beam splitters. M: flat mirrors. TS1,2,3 piezoelectric translation stages. A: intensity attenuator. δ variable time-delay. The two interferometers (MI1 and MI2) produce two linearly polarized pulses with orthogonal polarization. One pulse has a minimum in its temporal profile. Recombination of these pulses leads to the generation of a pulse with a polarization that rapidly changes from elliptical-to-linear-to-elliptical, with the linearly polarized temporal gate having a duration that is dependent on the chosen delay δ and attenuation A.

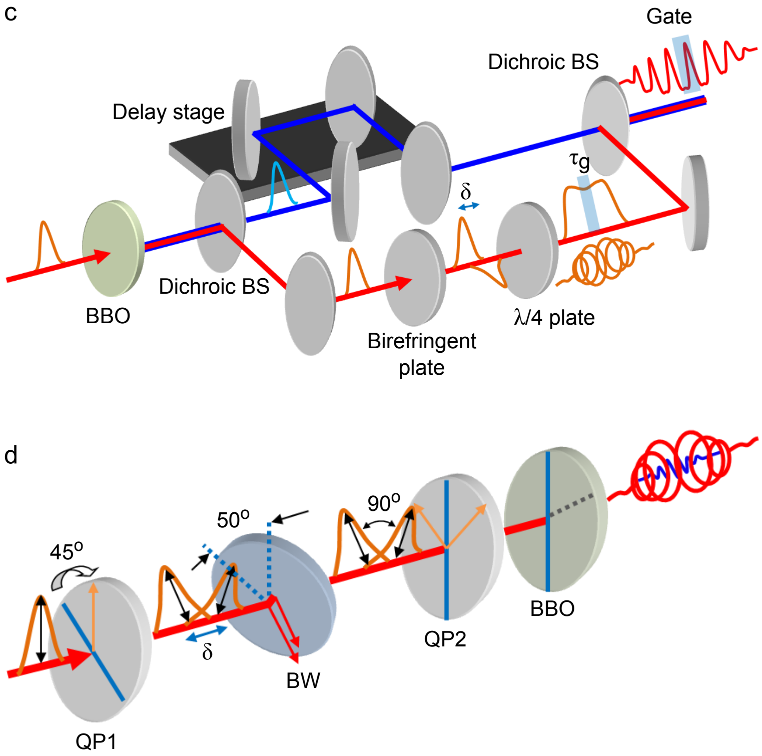

c) Double Optical Gating (DOG) [103]: The driving laser pulse, from the output of a hollow-core fiber compressor is incident on a barium-borate crystal (BBO, d = 250 µm). The fundamental and second harmonic field are separated by a dichroic beam splitter (BS) and propagate in the two arms of a Mach-Zehnder interferometer. The fundamental beam is used to make the polarization gate using a sequence of a birefringent quartz plate (0.4 mm) and an achromatic quarter-waveplate (2 mm). The resulting polarization gate width is 2 fs. d) Generalized Double Optical Gating (GDOG) [104]: A linearly polarized laser pulse is incident on the first quartz plate (QP1), with an optical axis orientation of 45° to the linear polarization of the input pulse. This creates two orthogonally polarized pulses with a certain time-delay. Depending on the input pulse duration, the thickness of the first quartz plate has to be changed to set an appropriate time-delay. A combination of a second quartz plate (QP2) and a type I barium borate (BBO) crystal functions, both with an optical axis in the plane of the input polarization, act as a quarter wave plate. This creates two counter-rotating fields with a second harmonic field with a polarization in the plane of the input pulse. A fused silica Brewster window (BW) is used to set the relative intensities of the driving field and the gating field, thereby allowing for shorter gate durations.

contains sufficient bandwidth, that the low-order harmonics are removed as well as contributions from the long trajectories. Through spectral filtering by metallic filters [105] and/or the wavelength dependence of the photo-absorption/ionization where the harmonics are used (where processes may be studied that cannot be initiated by low-order harmonics) [8, 106] the contributions from the low-order harmonics (< 15 eV) can be eliminated. As mentioned before, the long trajectories are more divergent compared to the short trajectories [94], allowing spatial filtering by placing a fixed aperture downstream from the HHG interaction region. The resulting spectrum after spectral and spatial filtering has an intrinsic attosecond chirp, which is positive for the short trajectories and negative for the long trajectories [93]. Using an aluminum filter with negative group delay dispersion, which also acts as a filter for the residual IR field, the positive attosecond chirp associated with the short trajectories can be compensated, resulting in a train of pulses, each with a duration of less than two-hundred attoseconds [105].

APTs are attractive for their relatively high photon numbers (compared to a SAP) and the simplicity of the generation scheme. Interpretation of time-resolved data can however be more straightforward with isolated attosecond pulses. For example, if in an experiment one is sensitive to the electric field of the IR at the arrival time of the attosecond pulse, rather than the absolute value of the field, this can lead to averaging out of the effect in normal pulse trains since consecutive pulses in the train see an opposite field. This problem can be partly circumvented by generating an APT with a single pulse per optical cycle by using two-color driving fields consisting of a fundamental infrared field and its second harmonic. This breaks the inversion symmetry of subsequent infrared half-cycles and ionization from half of the cycles can be suppressed. This creates a harmonic spectrum of odd and even harmonics and the corresponding attosecond pulse train consists of only one pulse per infrared cycle, with consecutive pulses exhibiting the same CEP [107, 108]. However this does not mean that isolated attosecond pulses are not needed at all, on the contrary, a lot of efforts have been going into the development of these sources.

2.3.3 Generation of isolated attosecond pulses

Isolated attosecond pulses can be generated by confining the HHG to a single half cycle of the driving laser field. Several methods have been developed that allow to do this. Because the emission time of the attosecond pulse is locked to the electric field of the IR pulse, the phase of the field within the envelope of the pulse needs to be controlled and therefore the use of CEP-stabilized laser pulses is essential.

The first experimental demonstration of isolated attosecond pulses was reported shortly after attosecond pulse trains were demonstrated [100]. This experiment exploits that the highest photon energies that are generated in HHG, by a few-cycle IR pulse, originate from the center half-cycle. Therefore it is possible to pick out an isolated attosecond pulse by spectrally selecting the highest energy part of the spectrum, which instead of exhibiting harmonic peaks is a continuum spectrum. In [100] a band pass filter (Zr) at ~ 90 eV selected the high energy region from HHG radiation in Ne by a 7 fs FWHM pulse, thereby confining 90% of the photons within one isolated attosecond pulse of ~ 650 as duration.

Following the development of the first CEP-stable femtosecond laser amplifier this work was significantly improved [24], and pulses with a duration of 250 attoseconds were reported. More recently, using single-cycle CEP-stabilized driving pulses of 3.3 fs, isolated attosecond pulses with a pulse duration of 80 as were generated, the current world record [109]. Because of the single-cycle nature of these pulses, ionization is dominated by half-cycles near the peak of the pulse envelope and is nearly absent in the wings of the pulse. For a large range of CEP values the single-cycle pulses lead effectively to emission of isolated attosecond pulses. The CEP now merely acts as a control parameter for the field intensity and hence the cut-off energy.

A family of methods to generate isolated attosecond pulses exploits the HHG efficiency dependence on ellipticity. By employing an ellipticity-modulated driver pulse, HHG can be restricted to a single half-cycle where the polarization is linear. Whereas HHG is suppressed in the wings of the pulse where the polarization is circular or elliptical [110].

A comparison and explanation of the different implementations of this principle is shown in Figure 2.3. Using only birefringent plates a pulse can be created for which the polarization changes from circular to linear to circular with opposite helicity. In this way 130 as FWHM isolated attosecond pulses were generated with CEP stable 7 fs FWHM driver pulses [36, 101]. This method, however, becomes highly inefficient if the pulses become much longer than 7 fs, therefore it does not provide a way to produce isolated attosecond pulses directly from a Ti:Sa laser. This problem was partly resolved by the realization that if one chooses elliptical polarization in the wings of the pulse, instead of circular polarization, this can lead to a much more efficient production of isolated attosecond pulses. The first experimental demonstration of this used interferometers to achieve the desired pulse shape and the technique was dubbed Interferometric Polarization Gating (IPG) [102]. A comparison between IPG and the 'traditional' polarization gating techniques was given in ref [111].

Another way to improve the efficiency of polarization gating for multi-cycle driver fields is the combination of polarization gating and two-color generation in a technique called double optical gating (DOG) [103]. As was discussed before, the addition of a weak second harmonic field can reduce the number of attosecond pulses per optical cycle to one and therefore allows a temporal gate of 1 optical cycle. Additionally it has the advantage of limiting ionization (ground state depletion) in the leading edge of the pulse. An XUV supercontinuum supporting 130 as was generated in neon gas using 9 fs laser pulses [112].

The last step that has been made in this line of improvements is the combination of the ideas of the IPG and the DOG techniques and was given the name generalized double optical gating (GDOG) [104]. This all co-linear scheme uses two birefringent plates, a second harmonic crystal and a brewster window. It is compatible with the use of pulse durations of tens of femtoseconds. Using GDOG, the generation of isolated attosecond pulses via HHG with input pulses of 20 fs (the output of a hollow core fiber) and 28 fs (the output of a Ti:Sa amplified laser system) was demonstrated. This technique is the most efficient route available for the production of isolated attosecond pulse from multi-cycle drivers, and is mainly interesting because currently sources of few-cycle laser pulses are limited in pulse energy. For a given pulse energy generation of a isolated attosecond pulse from a few-cycle pulse is obviously significantly more efficient since a much larger fraction of the laser pulse is used in the HHG process. This makes the development of high power OPCPA systems that deliver few-cycle pulses very important.

A potentially simpler technique for the generation of isolated attosecond pulses is the ionization gating technique [113], which relies on the loss of macroscopic phase matching on the leading edge of the driving pulse. First, due to the rising intensity in the leading edge of the pulse, the ionization rises above a critical ionization level. The negative dispersion resulting from free electrons can no longer be compensated by the positive atomic dispersion and thereby quenching the HHG process [33]. Second, a new spectral range with an increasing cut-off energy, is generated during subsequent half-cycles in the pulse. By spectral selection of a range of frequencies that correspond to HHG during only one half-cycle (by suppressing the lower-energy harmonics, generated during earlier half-cycles), one can produce a continuum spectrum and generate an isolated attosecond pulse. This method was demonstrated using driving pulses of 15 fs and 7 fs pulses. The latter was shown to generate pulses with a duration of 430 as using HHG in Ne and spectral selection with a Zr filter [113, 114].

2.4 XUV-IR pump-probe setup

Attosecond time-dependent studies require the configuration of an extremely stable pump-probe setup, in which one of the pulses is time-delayed with respect to the second pulse. For example, a drift of a mirror position of only 100 nm will result in a delay change of 0.6 fs rendering it impossible to obtain attosecond resolution. On top of the temporal stability, spatial stability of a small fraction of the laser focus (i.e. $\ll$ 100 µm) is required.

Two types of pump-probe setups are commonly used in attosecond experiments, namely setups where the XUV and IR are collinear throughout the entire optical path and setups based on a Mach-Zehnder interferometer configuration.

In a collinear setup, the full output of the IR driver laser is focused into the HHG medium [115]. The generated XUV radiation exhibits a smaller divergence than the IR beam, allowing for spatial separation of the two wavelengths downstream from the HHG medium. Any IR light that overlaps with the XUV can be filtered out using a metal filter. The XUV and IR beams are focused into the experimental region using a two-part mirror consisting of a central XUV multilayer mirror to focus the XUV beam and an annular mirror to focus the IR beam. The XUV mirror is mounted on a piezo-electric stage, to allow the two pulses to be varied temporally (with attosecond time-resolution) with respect to each other. In this type of setup, temporal stability is generally good because only a single mirror is used. Active stabilization can be used for long-term stability [116].

As an alternative approach, a Mach-Zehnder type interferometer can be used for the configuration of the pump-probe setup [93] which is the chosen configuration at AMOLF. (see Figure 2.4). The input beam is split into two parts by a beam splitter mounted on a long-range delay stage with a minimum step size of 6.7 fs and a maximum scan range of 0.7 ns. In the XUV arm, the IR is focused into the HHG setup by an f = 50 cm concave mirror. After the HHG process, the remaining IR field

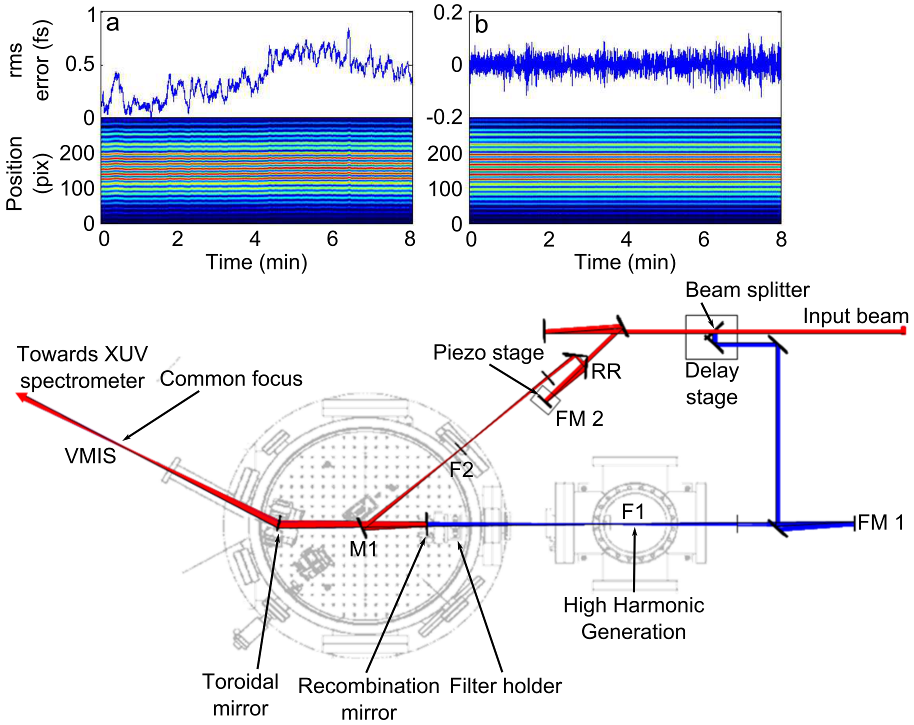

Figure 2.4: The Mach-Zehnder interferometer in the AMOLF attosecond setup. The input beam is split into two arms by a 50/50 beamsplitter mounted on a long-range delay stage. The reflected part (blue line) is focused by a mirror FM1 (f = 50 cm) into the HHG chamber. The transmitted part (red line) is focused by a mirror FM2 (f = 50 cm) to match the XUV divergence. F1 and F2 are the focii (in vacuum) of the XUV and IR paths, respectively. The retro-reflector (RR) is mounted on a delay stage to allow for adjustment of the longitudinal IR focus position to match the focus position of the XUV in the VMIS. The two beams are recombined in the recombination chamber using a flat holey mirror. The IR beam is reflected by a Ag mirror M1 onto the recombination mirror. From there the two beams collinearly propagate and are focused by a toroidal mirror into the center of the velocity map imaging spectrometer (VMIS). RR and the recombination mirror are motor-controlled to overlap the beams and ensure a collinear propagation. A co-propagating He-Ne beam (not shown here) is used to compensate slow drifts in the relative path lengths of the two arms. A CCD camera is used to measure an interference pattern from which changes in the relative path lengths can be extracted and stabilized. Recorded interference patterns as a function of time are plotted in a) using no stabilization and b) using active stabilization. The resulting rms stability in case of active stabilization is 20 as.

is filtered out by an aluminum filter (200-300 nm) held in a vertically translatable filter holder. The XUV radiation propagates through a hole in a drilled mirror, conveniently filtering out contributions from the long trajectories. The IR beam to be used in the experiment is reflected via various Ag mirrors to match the XUV and IR path lengths. The IR beam is focused in vacuum by a focusing mirror (FM2: f = 50 cm) that is mounted on a piezo-electric delay-stage to control the XUV-IR delay with attosecond precision. In addition, a retro-reflector (RR) is mounted on a delay stage allowing for adjustment of the longitudinal focus position of the IR beam to overlap with the focus of the XUV beam. In the recombination chamber, the IR beam is reflected on the recombination mirror via M1. The XUV and IR pulses are focused by a toroidal mirror (f = 40 cm) into the interaction region of a velocity map imaging spectrometer.

Collinearity of the XUV and IR beams is ensured by imaging the XUV-IR spatial overlap at two points along the beam path. The first point is the reflection of the IR beam on the recombination mirror. The beam is positioned such that the beam hits the mirror in the center using mirror M1. The second point is the focus of the XUV and IR beams in the interaction region. The focus of the IR beam in the XUV arm is imaged by removing the aluminum filter and the recombination mirror is used to overlap the two beams.

To ensure spatial and temporal stability of the interferometer care must be taken in the design of all the components of the setup. It has proven essential to prevent the vibrations from fore-line pumps and turbo pumps from interfering with the optical components. This can be accomplished by decoupling the vacuum-chambers from the optical table while attaching the breadboard inside the vacuum chamber rigidly to the optical table. In a similar fashion the fore-line pumps can be de-coupled from the turbopumps. However even when the greatest care is taken, when the Mach-Zehnder interferometer is partly placed outside the vacuum and contains very long path lengths (~ 3 m), active stabilization is required to achieve the highest temporal stability [117].

A He-Ne laser is co-propagated with the XUV and IR beams slightly below the main beam path allowing to pick it off. Propagation through the HHG gas cell and metal filter is not possible and therefore in this part of the interferometer the He-Ne laser propagates parallel to the XUV arm. The two paths are recombined under a small angle and the resulting interference pattern is measured by a digital camera at a repetition rate of 30 Hz. By software the actual delay and error are determined and fed back through a PID feedback loop on a piezo-electric stage. The resulting rms stability is 20 as, as illustrated by Figure 2.4, which is sufficient to perform experiments with attosecond resolution.

2.5 Charge particle detection

The XUV and IR beams are focused into the interaction region, onto an ensemble of target gas molecules introduced by effusive sources or pulsed valves. The charged particles arising from interaction with the XUV and IR pulses can be detected by various types of spectrometers.

2.5.1 Time-of-Flight spectroscopy

Two types of time-of-flight (TOF) spectroscopy can be distinguished. In ion time-of-flight spectroscopy, ions created in a static electric field are accelerated towards a field-free flight tube and impinge on a detector, e.g. an electron multiplier tube. The time of flight is inversely proportional to the velocity of the ion when it enters the field-free region and is proportional to square root of the ion mass/charge ratio. The time-dependent detector signal thus offers the separation of ions with different mass/charge ratios and a quantification of their abundance. In electron TOF spectroscopy, electrons created in a field-free region are captured by the detector and their time-of-flight is inversely proportional to their initial velocity. The absence of an accelerating static field enables a very high energy resolution ($\sim 0.1\%$). Obtaining angular distributions is however time-consuming as it requires measurements where the polarization of the laser(s) is systematically varied with respect to the time-of-flight axis.

2.5.2 Magnetic Bottle Electron Spectroscopy

In magnetic bottle electron spectroscopy (MBES), the ionization takes place in a strong magnetic field (~1 T) parallel to the flight tube direction [118]. The magnetic field decreases smoothly towards the flight tube where it is constant (~1 mT). The electrons spiral around the magnetic field line on which they are created while the initial velocity of the electrons is converted into a velocity in the direction parallel to the flight tube axis. The electrons are detected by a stack of microchannel plates (MCPs) which converts the time-dependent electron current into a measurable TOF spectrum. The great advantage of a magnetic bottle electron spectrometer over a conventional TOF spectrometer is its higher collection efficiency, typically being 50% or even 100% depending on the exact magnetic field configuration in the spectrometer.

2.5.3 COLd Target Recoil Ion Momentum Spectroscopy

COLd Target Recoil Ion Momentum Spectroscopy (COLTRIMS) [62] allows measuring the complete fragmentation dynamics of a few-body system. All the charged particles (ions and electrons) are projected onto two two-dimensional position sensitive detectors, consisting of delay line detectors which are able to measure both the position and the time of impact of impinging particles. From the measured time-of-flights and the arrival position on the detector, the full three-dimensional momentum distributions can be measured in coincidence. A COLTRIMS detector provides the most complete information possible and is therefore a very powerful technique, but is limited to very low count rates ($\ll$1 hits/laser shot) in order to avoid so called "false coincidences" in the data analysis.

2.5.4 Velocity Map Imaging Spectrometer

The velocity map imaging spectrometer (VMIS) in the AMOLF attosecond setup is shown in Figure 2.5. In velocity map imaging [63], electrons or ions resulting from interaction of atoms or molecules with a laser pulse are projected onto a two-dimensional (2D) detector by a static electric field. The 2D detector consists of a stack of micro-channel plates (MCPs) followed by a phosphor screen and a digital camera. The static electric field is formed by a repeller and extractor electrode. Provided the ion optics are properly tuned, the positions of the electrons/ions impinging on the 2D detector depend on their velocity and hardly at all on the position of ionization. If the initial three-dimensional (3D) velocity distribution is cylindrically symmetric, it can be retrieved from the 2D projection via an Abel inversion [119], as long as the symmetry axis (laser polarization) is in the plane of the detector.

The ability to measure angularly-resolved velocity distributions with 100% collection efficiency are major advantages of the VMIS. In addition, using a phosphor screen that is read out optically rather than electronically (as for the delay-line detectors), allows for very high count rates ($10^4 - 10^5$ events/shot are feasible). Similar to the TOF technique, the time-of-arrival of ionic particles at the detector depends on the mass/charge ratio. The momentum distribution of a single ion species can be measured by gating the detector at the corresponding time delay.

Tailoring velocity map imaging to attosecond experiments

In a conventional velocity map imaging spectrometer, the target gas is introduced by a skimmed atomic/molecular beam. This provides rotationally and possibly vibrationally cooled atoms/molecules and can in many cases be advantageous. However, the use of dilute skimmed beams is disadvantageous when the ionizing light source is relatively weak, as is the case with current attosecond sources based on HHG. To increase the signal level the AMOLF attosecond setups uses a velocity map imaging spectrometer with an integrated gas injection system in the repeller electrode [120]. An illustration of this injection system is shown in Figure 2.5. The flat repeller electrode in a conventional VMIS is replaced by a repeller electrode with an integrated laser-drilled capillary (d = 50 µm, l = 200 µm). The shape of the electrode includes a flat part of 1 mm to realize a curved equipotential field line profile, similar to the open electrode geometry in a conventional VMI [63]. From the flat part, the repeller electrode has a conical shape with a 154^o angle to accommodate the laser focus in front of the capillary. Introduction of the target gas directly at the interaction region increases the gas density by 2-3 orders of magnitude. A further increase in the gas density in the interaction region has been realized by integrating a pulsed piezoelectric valve into the repeller electrode.

The mechanical design of the integrated pulsed valve is shown in Figure 2.6. A series bimorph piezo (PXE5) with a free length of 8 mm (resonance frequency is 3.6 KHz) is clamped between 2 metal sheets for electrical contact and is mounted on a movable vespel piece for fine-adjustment. Due to the coned shape of the repeller, the nozzle is closed by a viton plate (d = 0.5 mm) glued on a vespel pillar. The piezo valve is operated at the repetition frequency of the laser (3 KHz) with driving pulses of 10-30 µs. The gas pulse duration, measured with a fast ion gauge, is 20 µs FWHM. Compared to a continuous flow, this translates to ∼15 times higher gas density in the interaction region, when the chamber pressure is the limiting factor. Meanwhile, we have improved the mechanical design of the pulsed valve, the details

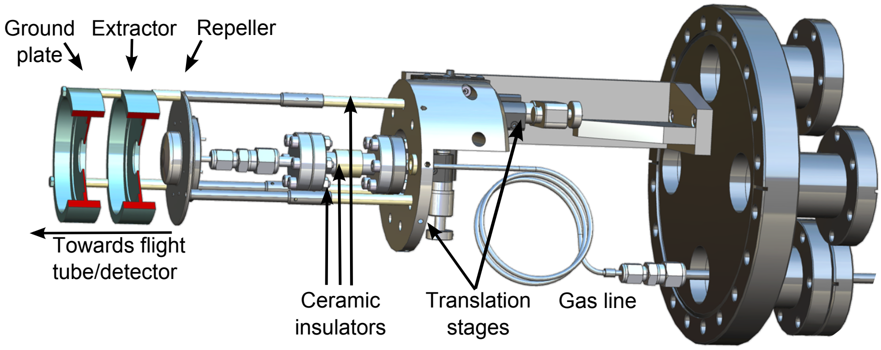

Figure 2.5: Ion optics of the velocity map imaging spectrometer with an integrated effusive gas jet in the repeller optics. The ion optics exists of a repeller and extractor electrode and a ground plate. The repeller electrode is electrically isolated from the housing by ceramic isolators. The laser beam propagates in between the repeller and extractor electrodes and is polarized in the plane of the detector (not shown). The position of the ion optics can be moved in vertically and horizontally by motor controlled translation stages to ensure a good overlap of the gas beam and laser foci. Positioning of the ion optics along the laser propagation axis is done by translation of the entire vacuum chamber.

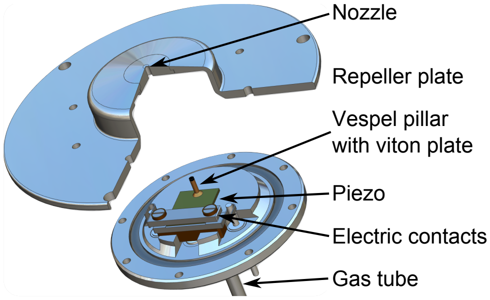

Figure 2.6: Pulsed piezo valve integrated in the effusive repeller. The effusive repeller comprises a flat part of 1 mm with a laser-drilled nozzle in the center. The repeller takes a conical shape from the flat part on to accommodate the laser focus. The nozzle is closed off by a viton plate mounted on a vespel pillar, glued onto the piezo crystal. The piezo valve is operated at a repetition frequency of 3 KHz by driving pulses with a duration of 10-30 µs, generating a gas pulse with a full-width-half-maximum of ~20 µs.

of which are described in appendix A.

Isolating the repeller electrode from the vacuum chamber is realized by a ceramic isolator. The ion optics, and thus the gas-jet, is positioned with respect to the laser foci by translating the ion optics assembly. Translation in two directions perpendicular to the laser propagation direction adjusts the height and distance from the laser focus. The position of the VMIS along the laser propagation direction can easily be adjusted by moving the VMIS on a translation stage. Apart from tuning the ion optics to image the velocity of the charged particles, the spectrometer can also be operated in a so-called spatial imaging mode. We note that the use of ion optics where the XUV laser beam is focused close to a conically shaped repeller electrode necessitates the introduction of measures to reduce stray XUV light without affecting the probe beam. In the AMOLF setup a drilled silica plate is placed close to the velocity map imaging spectrometer that transmits XUV light, and blocks XUV photons that deviate from the optical axis (e.g. as a result of diffuse scattering from the toroidal mirror).

2.6 XUV spectrometer

The spectrum of the radiation resulting from HHG can be characterized using an XUV spectrometer, providing an independent tool to characterize and optimize the harmonic spectrum. Typically XUV spectrometers are based on a grazing incidence grating in order to get a high enough reflection efficiency [121, 122]. Focusing in the plane of diffraction can be obtained by a concave grating. Variable line spacing (VLS) gratings are available (e.g. Hitachi) to compensate aberrations and generate a flat-field spectrum, meaning that the foci of the entire wavelength range are lying in a plane. An MCP-phosphor screen combination together with a CCD camera can be used as a detector, alternatively XUV-CCD cameras are available for direct detection.

2.6.1 XUV optics

Where dielectric or metallic coatings provide good reflection efficiencies at all desired incoming angles, this is far from straightforward for wavelengths that are shorter than 150 nm. Moreover radiation at XUV and soft X-Ray wavelengths is absorbed in nearly all solid materials. This makes that the availability of standard optical components for HHG radiation, like mirrors, filters, gratings and beamsplitters is limited or absent. The role of beamsplitters is commonly replaced by drilled mirrors where the XUV radiation transmits through the hole of the mirror as was described for the AMOLF attosecond setup.

Filters that transmit XUV and soft X-ray radiation can be made from thin metal foils, where different metals have different transmission spectra [123]. An additional advantage is the chirp compensation of the attosecond pulses due to the negative dispersion of the metals. Such chirp compensation can also be pursued using specially designed chirped mirrors [124, 125]. Metallic coatings like gold or platinum exhibit good reflection efficiency at grazing incidence angles. To be able to make use of this fact in a focusing mirror, one has to use a toroidally shaped mirror to avoid an astigmatic focus. The disadvantage of these mirrors is that they are difficult to align and expensive. Meanwhile a lot of efforts have been put into developing coating technology to reflect XUV wavelengths at zero or 45 degrees, where the first one is a requirement in the earlier described co-linear attosecond setup. An important requirement in this is the reflection bandwidth which has to be wide enough to support the short attosecond pulses. Mo/Si multilayer mirrors provide a reflection efficiency of $\sim 50\%$ around 90 eV at zero degrees. This relies on coatings that have been developed for the lithography industry. Coatings for other incoming angles and wavelengths do exist but are not generally available.

3 Direct determination of the sign of the NO dipole moment

We report a novel approach for determining the sign of permanent dipole moments, using nitric oxide [NO(ν=0)] as an example. State-selected NO (j= $|m|$ = $|\Omega|$ =1/2) molecules are focused using a hexapole and oriented in a strong dc electric field. The angular distributions of ionic fragments resulting from extreme ultraviolet single-photon and multiphoton dissociative ionization at 400 and 800 nm are measured and indicate that the dipole moment is negative (corresponding to $N^{-}O^{+}$). The experiments thus rule out an error in the sign of the dipole of NO as the possible source of a remarkable discrepancy between previous theoretical and experimental work on orientation effects in bimolecular collisions involving oriented NO.

3.1 Introduction

As a result of extensive fundamental research, molecular ionization and dissociation in intense laser fields are now quite well understood [126]. Studies of atomic and molecular dynamics in intense laser fields have led to important spinoffs such as coherent light sources in the extreme ultraviolet (XUV) by high-order harmonic generation (HHG) [7] and new methods for measuring molecular structures [127] and wave functions [128, 129]. Here, we present a study where HHG and recently acquired understanding on the alignment and orientation of molecules in strong laser and dc fields are used to determine the sign of the permanent dipole moment of NO in its ground state. This dipole moment has been the subject of a recent controversy [130], due to an unresolved sign discrepancy between measurements and calculations of the steric asymmetry for He- NO, Ar-NO, and D_2-NO rotationally inelastic collisions [130–133]. The steric asymmetry describes the orientation dependence of the (final state-dependent) collision cross section σ and is defined as:

$$S = \frac{\sigma^{Head} - \sigma^{Tail}}{\sigma^{Head} + \sigma^{Tail}} \tag{3.1}$$

For NO, a collision onto the N-end is considered to be a head collision. If S > 0, head collisions contribute more to a specific final rotational state NO(j') than tail collisions. Experiment and theory agree that for Ar-NO, He-NO, and D_2-NO collisions S oscillates and changes sign as a function of final rotational state. However, while the absolute values of the experimental and theoretical steric asymmetry agree very well, their sign is opposite. The discrepancy would be resolved if the dipole moment of NO would be opposite to it's ab initio value – i.e., N^+O^- instead of N^-O^+, inverting the NO orientation in the experiment [130]. The absolute value of the electric dipole of NO($\nu = 0$, $X\,^2\Pi$) was measured with high precision by Hoy *et al.*: μ_{NO}=0.15740.014 D [134]. This value slightly deviates from the ab initio value of 0.1732 D calculated by Langhoff *et al.* [135]. The latter authors predicted a negative dipole moment, i.e., N^-O^+, which is supported by additional ab initio calculations [136–138]. The sign of a molecular dipole moment can in principle be obtained experimentally from the isotopic dependence of magnetic susceptibility factors [139]. However, for N_2O, this technique led to a sign opposing a theoretical calculation [140]. So far, even the highest precision measurements have been unable to determine the sign of the NO dipole moment experimentally [141]. In this chapter, we present a new approach towards measuring the sign of molecular dipole moments and apply it to NO.

3.2 Experimental methods

The experimental measurements were carried out in four steps: namely (1) full state-selection of NO in the low-field seeking component of the rotational ground state using a hexapole focusing field, (2) orientation in a strong dc field, (3) dissociative ionization of the oriented NO using an XUV, a UV (400 nm), or a near-infrared (800 nm) light source, and (4) measurements of the angular distribution of ionic fragments using the velocity map imaging technique [63]. The interaction energy W for NO in relatively high dc fields is approximated by the first order Stark effect:

$$W^{(1)} = - < \mu \cdot E >= -\mu E \frac{m\Omega}{j(j+1)} = -\mu E < \cos\theta > \tag{3.2}$$

Here, m and Ω are the projections of total angular momentum j onto the space-fixed z-axis (defined along electric field $\mathbf{E}$) and on the internuclear axis, respectively, μ is the permanent dipole moment, and θ is the angle between the permanent dipole and the laser polarization axis. In Equation 3.2, the internuclear axis points along the permanent dipole moment, i.e., from the negative towards the positive end of the molecule. In a hexapole [consisting of six hexagonally-assembled rods to which alternating negative and positive dc voltages are applied (see Figure 3.1) [142], molecules with $m\Omega > 0$ are in high-field seeking states and are pulled towards the hexapole rods, while molecules with $m\Omega < 0$ are in low-field seeking states and are pushed towards the center of the hexapole. Without any dc electric field present, each rotational state of NO consists of a Λ-doublet, i.e., a symmetric or antisymmetric linear combination of symmetric top wave functions. In a dc field, the two components of the λ-doublet are mixed and turn into a high-field seeking and a low-field seeking state. In Hunds case (a), the orientation probability distribution of these states in a relatively high dc electric field is given by

$$W(\theta) = |\Psi_{j,m,\Omega}|^2 = |d^j_{m,\Omega}(\theta)|^2 \tag{3.3}$$

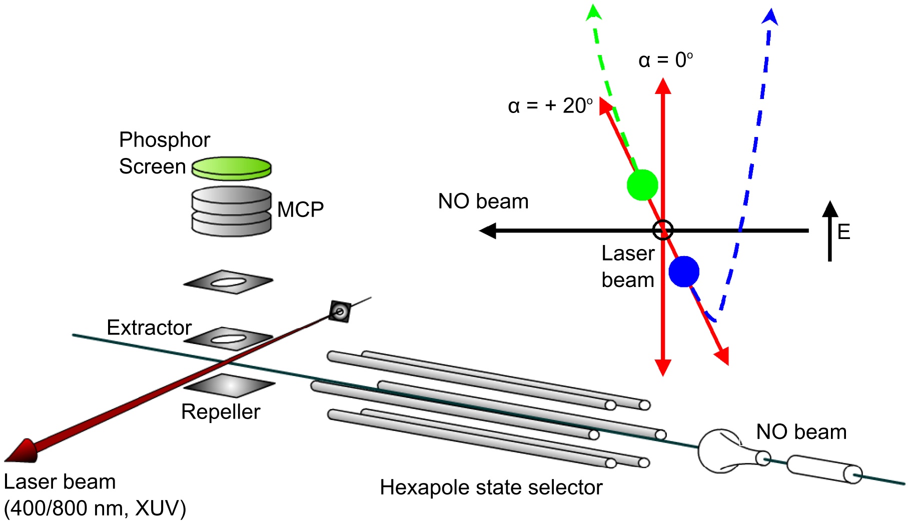

Figure 3.1: Schematic representation of the experiment. NO molecules are state-selected using a hexapole and oriented in the 13 kV/cm extraction field of a velocity map imaging spectrometer. They are dissociatively ionized using femtosecond XUV radiation or 400/800 nm radiation from an intense femtosecond Ti:Sa laser. The laser polarization is tilted with respect to the detector axis, so that ions moving upwards or downwards after the dissociation can be distinguished.

For low- and high-field seeking states with j=1/2, it follows that

$$\begin{aligned} W(\cos\theta) &= \frac{1-\cos\theta}{2} \quad \mathrm{for\ j = 1/2, m = \pm 1/2, \Omega = \mp 1/2, low-field\ seeking} \\ W(\cos\theta) &= \frac{1+\cos\theta}{2} \quad \mathrm{for\ j = 1/2, m = \pm 1/2, \Omega = \pm 1/2, high-field\ seeking} \end{aligned} \tag{3.4}$$

Molecules in the low-field seeking state that are placed in a dc orientation field orient with their negative end towards the negative electrode. To determine which side of the molecule this corresponds to, dissociative ionization in combination with angular-resolved mass-spectrometric detection can be used (see Figure 3.1), provided that the orientation is not altered by the laser and that the dissociation process occurs on a time scale that is much shorter than the rotational period of the molecule (10 ps). In the experiment (see Figure 3.1), a mixture of 10% of NO in Ar (1.6 bar) expanded from a General Valve operated at 15 – 25 Hz. Following a d=1 mm collimator placed at 5 cm from the nozzle, the beam entered a hexapole state selector, placed 25 cm further downstream. The inscribed radius and the diameter of the 1 m long hexapole rods [143] were both 4 mm. Using a 10 kV voltage difference between the hexapole rods, selected NO molecules were focused into a velocity map imaging spectrometer (VMIS) [63], placed 30 cm downstream. The VMIS consisted of an extraction region, a drift region, and a dual microchannel

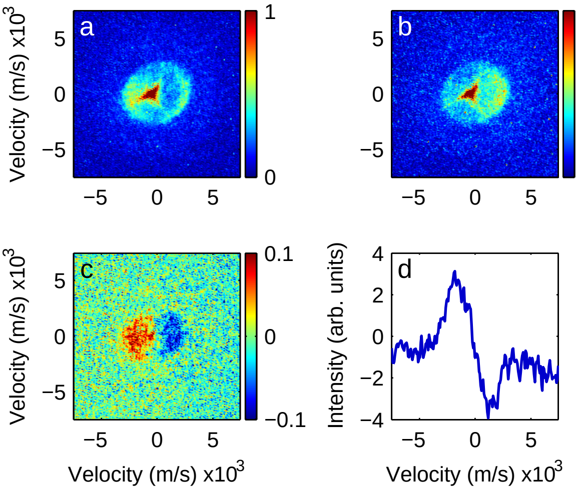

Figure 3.2: 2D Velocity maps for N^+ fragments from dissociative ionization of oriented NO by a fs XUV pulse, with a) $\alpha = +45°$ and b) $\alpha = -45°$. The difference between a) and b) is shown in c). Figure d) results from integration along the y axis of c). For $\alpha > 0$, the N^+ fragments are more abundant in the left part of a), indicating that in the oriented NO sample, the N-atoms face the negative electrode. This is consistent with the negative charge of the dipole being on the N-atom. The central dot in the images is due to partial detection of NO^+ caused by the DC component of the time dependent voltage applied to the MCP.

plate detector (MCP) followed by a phosphor screen and a camera system to record the positions of ion impact. In the VMIS, the NO molecules were oriented by the applied 13 kV/cm extraction field and dissociatively ionized. The polarization axis of the laser was tilted with respect to the detector axis. Consequently, an asymmetry in the recoil velocity distribution of the fragment ions caused by orientation of the parent molecule (with respect to the detector axis) leads to an asymmetry in the fragment velocity distribution in the plane of the velocity map imaging detector (see Figure 3.1). We note that the measured 2D distribution is determined both by the degree of orientation and by the dependence of the dissociative ionization process on the angle of the internuclear axis of the molecule with the laser polarization. Our temporal resolution did not allow determination of the molecular orientation from flight time differences ($\sim$ 1 ns) for fragments initially moving towards or away from the detector. To distinguish N^{q+} and O^{q+} (with q being the charge state), a fast Kentech SPSV (12 ns, -1 kV into 50 Ω) pulse-generator was used to gate the frontside of the MCP detector. A positive dc voltage was applied to the backside of the MCP detector. Hence, for a duration of (at most) 12 ns, the detector operated at full gain, whereas outside this time window, the detector operated at a gain that was reduced by approximately 3 orders of magnitude, allowing selective detection of N^{q+} or O^{q+}.

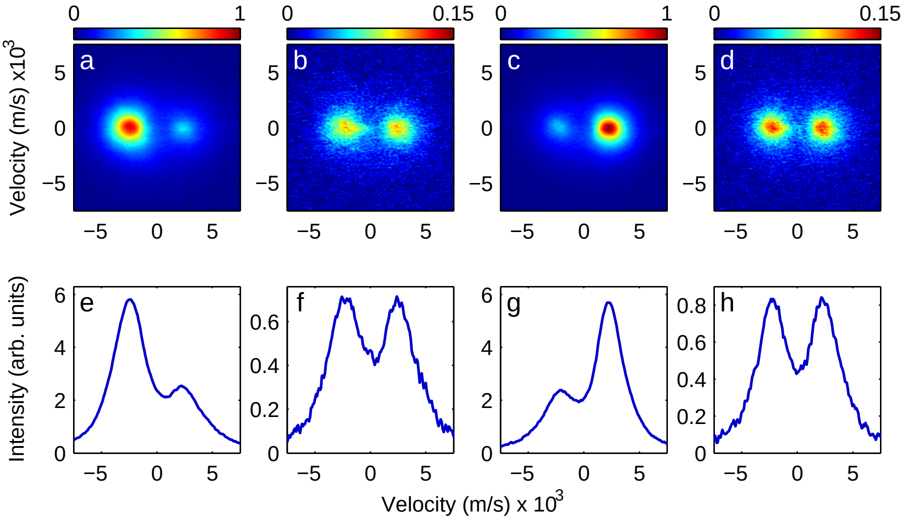

Figure 3.3: 2D Velocity maps for detection of N^{2+} and O^{2+} fragments resulting from dissociative ionization of NO by an intense 50 fs 800 nm pulse with $\alpha = +20°$. Figures a) and b) show N^{2+} results with the hexapole on a) and off b), while c) and d) show this information for O^{2+}. Figures e), f), g), and h) result from integration along the y-axis of the velocity maps shown above. With the hexapole off, the N^{2+} and O^{2+} fragments are symmetrically distributed. With the hexapole on, N^{2+} appears predominantly on the left and O^{2+} predominantly on the right. This indicates (see Figure 3.1) that in the oriented NO sample, the N-atom faces the negative electrode and is consistent with the negative charge of the dipole being on the N-atom.

3.3 Probing the orientation of NO molecules using infrared, visible and XUV light

In Figure 3.2, 2D velocity maps are shown for detection of N^+ resulting from XUV dissociative ionization. To generate the XUV, a 2 mJ 50 fs Ti:Sa laser was focused onto a pulsed Ar jet using a 1 m lens. The divergent XUV beam, containing a superposition of harmonics, intersected the NO beam at right angles. The intensity of the Ti:Sa laser at the interaction region was 3-4 $\times 10^{10}$ W/cm^2, i.e., too low to influence the dissociation. Velocity maps were recorded with the XUV polarization at $\alpha = \pm\ 45^o$ with respect to the dc electric field axis and show that the N^+ ions favor an ”upward” recoil, consistent with the N-end of the molecule being negative and the O-end being positive (N^-O^+). The absence of detectable O^+ fragments suggests that $N^+ + O$ and $N^+ + O^-$ were predominantly formed. O^- ions were observed, but not in sufficient quantities to allow measurement of a velocity map. Experiments were also performed using intense 400 and 800 nm light from the same fs Ti:Sa laser. Figure 3.3 shows N^{2+} and O^{2+} velocity maps obtained by Coulomb explosion of NO at 800 nm, using $\leq$ 4 mJ 50 fs Ti:Sa laser pulses focused with a

20 cm lens. The 800 nm experiments show the effect of geometric and/or dynamic alignment [126]. Strong field ionization processes tend to favor molecules that are aligned along the polarization axis of the ionizing laser ("geometric alignment"). In addition, molecules experience a torque and are dynamically aligned [144, 145]. While dynamic alignment facilitates the visibility of the orientational asymmetry, it is a possible source of error if the laser system contains prepulses. Given that the production of N^{2+} and N^{2+} ions by Coulomb explosion requires intensities of $O(10^{15}\text{W/cm}^2)$, prepulses with an intensity of $\sim 0.1\%$ of the main peak are sufficient to alter the molecular orientation before it is probed [146, 147]. Indeed, we have observed that at 800 nm, the observed asymmetry disappears when the peak intensity at the focus of the laser becomes too high.

In Figure 3.3, a comparison is presented of N^{2+} and O^{2+} velocity maps at 800 nm with the voltage on the hexapole rods turned on or off. In the former case, the NO molecules are state-selected and the experiment uses an oriented sample, while in the latter case, equal numbers of high-field seeking and low-field seeking NO molecules are present in the laser focus which orient in opposite directions. Consequently, no net orientation is expected and no asymmetry is observed. Conversely, when the hexapole state-selector selects low-field seeking states, the signal increases by an order of magnitude, and a pronounced asymmetry is observed, which confirms the orientation of the NO molecules with the N-side towards the negative electrode. To alleviate the problem of dynamic alignment by prepulses, further experiments were performed using the 2^{nd} harmonic of the fs Ti:Sa laser at 400 nm, generated by using a 1 cm KDP crystal ($\tau_{UV} \approx 750$ fs $\ll T_{rot}$). Figure 3.4 shows N^{2+} and O^{2+} velocity maps from experiments where the 400 nm polarization was at $\alpha = +30°$ and $\alpha = -30°$ with respect to the dc electric field axis. The influence of dynamic and/or geometric alignment is again visible. However, since 2^{nd} harmonic generation is a nonlinear process, the influence of prepulses no longer needs to be considered. The results in Figure 3.4 show once more that the low-field seeking states selected by the hexapole orient with the N-side towards the negative electrode, confirming our conclusion that in the dipolar NO molecule the negative charge is on the N-end and the positive charge is on the O-end. Hence, all three experiments rule out that an error in the sign of the dipole moment of NO is responsible for the long-standing discrepancy between experimental and theoretical results on the orientation dependence of Ar-NO, He-NO and D_2-NO collision experiments.

3.4 Conclusion

Our experiments open a new chapter in experimental work on strong field manipulation of the external degrees of freedom of molecules. In the last decade, significant progress has been made on strong field molecular alignment, where the state-of-the-art is now 3D alignment of cold molecules under field-free conditions [148]. Sakai and co-workers have so far obtained the only results on molecular orientation [149]. However, their method is only suited for relatively heavy molecules that orient in low electric fields and a very modest degree of orientation was observed. In our experiment, the use of a hexapole introduces the possibility to perform strong field alignment and orientation experiments with a state-selected molecular beam,

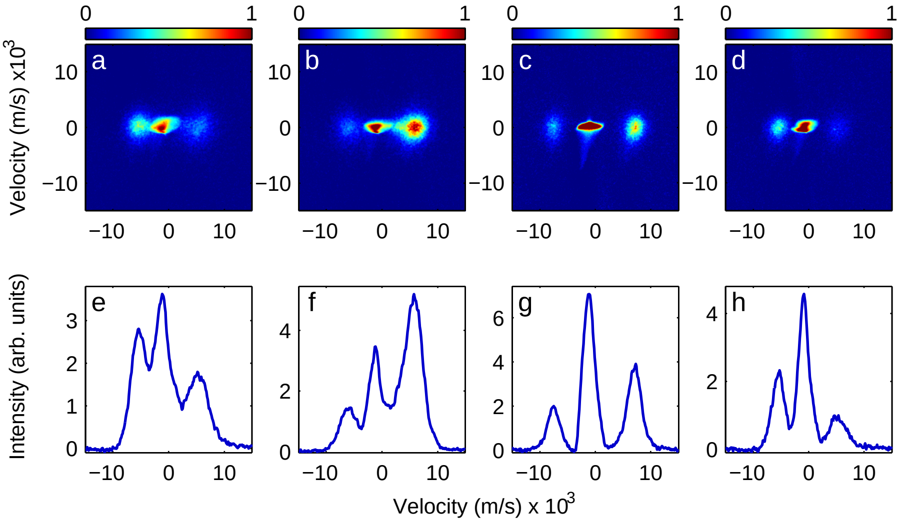

Figure 3.4: 2D Velocity maps for N^{2+} and O^{2+} fragments resulting from dissociative ionization of oriented NO by an intense 750 fs 400 nm pulse. Figures a) and b) show N^{2+} results for a) $\alpha = +30°$ and b) $\alpha = -30°$, while (c) and (d) show this information for O^{2+}. Figures e), f) g), and h) result from integration along the y-axis of the results shown above. For $\alpha > 0$, the N^{2+} fragments appear predominantly on the left and the O^{2+} fragments predominantly on the right, while for $\alpha < 0$, the situation is reversed. This indicates (see Figure 3.1) that in oriented NO molecules, the N-atom faces the negative electrode and is consistent with the negative charge of the dipole being on the N-atom. Similar to Figure 3.2, the central dot in the images is due to partial detection of NO^+ caused by the DC component of the time dependent voltage applied to the MCP.

thereby improving the degree of alignment and orientation that can be achieved and providing experimental access to the full quantal information of an alignment or orientation process. [148].

4

Attosecond ionization of O_2 molecules in the presence of an IR-field

O_2 molecules are ionized by an attosecond pulse train in the presence of a moderately strong IR-field. The ionization by the attosecond pulse train occurs into various dissociative ionization pathways. A dependence of the yield and angular distributions of the ion fragments on the phase of the IR field at the time of ionization is observed. The experimental observations are understood in terms of an IR-field induced coupling between electronic states in the molecular ion. The observed dependence of the fragment ion yield is explained in terms of a constructive or destructive interference of two ionization pathways that involve two molecular ion states, that are coupled by the IR field.

4.1 Introduction

The instantaneous response of matter to incident light in the visible to ultra-violet wavelength region occurs on the attosecond timescale [150]. Hence electronic excitation processes such as the removal of an electron can lead to ultrafast charge re-arrangement and migration processes. The occurrence of ultrafast charge migration in mid-size molecules of chemical and biological interest on the attosecond to few-femtosecond timescale has been theoretically predicted [49, 151]. A crucial task that lies ahead is the experimental validation of these predictions, by probing the electron dynamics in real time. So far all available evidence for ultrafast charge migration processes has been indirect. Charge migration has, for example, been implicated in experiments where peptide ions dissociated in a bond-selective manner after ionization [152], as well as in high-harmonic generation (HHG) experiments where the measured extreme ultra-violet (XUV) spectrum as a function of the alignment of the molecule with respect to the laser polarization axis reveals an interference between contributions involving different ionic electronic states [153, 154].
In the past decade, two experimental techniques have emerged in the ultrafast laser community that allow one to address rapid electron dynamics in molecules. On the one hand, attosecond pump-probe spectroscopy based on the formation of attosecond light pulses by means of HHG has been developed [8]. Attosecond laser pulses

have been applied in pioneering experiments on atoms, molecules and condensed matter [26, 47, 50]. On the other hand, the emergence of free electron laser (FEL) facilities like FLASH in Hamburg [51] and the LCLS at Stanford [55, 155], opens new opportunities to address molecular dynamics with XUV & X-ray pulses with a duration that can be as short as a few femtoseconds.

In the context of these developments, it becomes of crucial importance to address the question how, in an attosecond or few-femtosecond time-resolved experiment, electron dynamics can be revealed. Previously we have reported on a measurement of laboratory frame fragment asymmetries (i.e. an in-balance between the number of fragment ions that fly upward or downward along the laser polarization axis) that arises in a two-color XUV + IR pump-probe experiment on H_2 and D_2, and that is indicative of electron localization [50]. More recently the effect of the IR field on the XUV ionization of H_2 and D_2 molecules was measured. The fragment ion yield was observed to depend on the delay between the XUV and IR pulses and was explained by IR-induced coupling of two ionic states.

We report in this chapter on experiments where O_2 molecules were exposed to a moderately strong infrared field and ionized by a synchronized attosecond pulse train (APT). Angle- and kinetic energy resolved measurements of O^+ fragments that resulted from dissociative ionization of O_2 revealed a sensitivity of both the fragment ion yield, the fragment ion kinetic energy distribution and the fragment ion angular distribution to the IR field strength at the time of ionization. This shows that the ionization by the attosecond pulse train was sensitive the time-dependent polarization induced by the IR-field and that they can be used to probe such dynamics. Our results support the notion that attosecond pulses can be used to monitor prompt electron dynamics following photo-excitation and/or photo-ionization [49, 150, 151].

4.2 Experimental methods

In the experiment the output of a 3 KHz Ti:Sa laser, producing 2 mJoule/pulse with a full-width-at-half-maximum (FWHM) duration of 30 fs (linear polarization, $\lambda = 780$ nm) was equally split into two beams. One beam was used to generate an XUV attosecond pulse train (APT) by high-harmonic generation in Xe. The IR field and lower-order harmonics were filtered out using a 200 nm aluminium filter. The resulting spectrum consisted of harmonics 11-21 of the driving laser frequency and the spectrum extended from 17.5 eV-33.4 eV. The other beam was time-delayed with attosecond precision and co-linearly recombined with the XUV using a drilled mirror. The XUV and IR beams were focused into the interaction region of a velocity map imaging spectrometer, [63] where O_2 molecules are introduced by a pulsed valve that was integrated into the repeller electrode [120]. Fragment ions resulting from (two-color) dissociative ionization were projected onto a two-dimensional detector consisting of a stack of microchannel plates (MCPs), a phosphor screen and a camera system. The three-dimensional momentum distribution of O^+ fragments was determined using an inversion procedure. The IR intensity was chosen such that no ionic fragments are detected in the presence of the IR pulse only and estimated to be on the order of $5 \times 10^{12} \mathrm{W/cm}^2$.

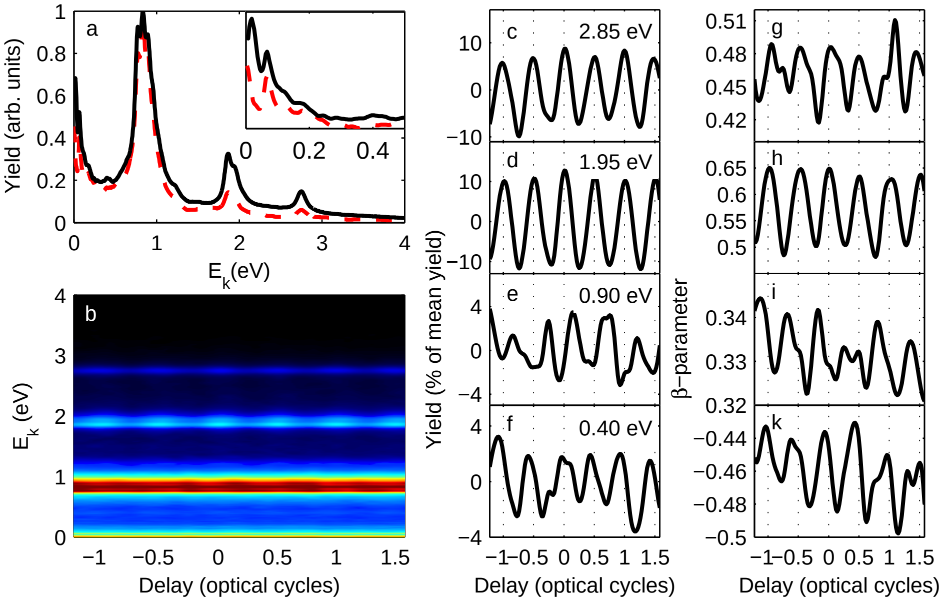

Figure 4.1: a) O^+ kinetic energy spectrum, resulting from XUV only ionization (red dashed line), along with the kinetic energy spectrum for XUV + IR ionization, averaged over one full period of the XUV + IR delay (solid black line). The kinetic energy spectrum for $E_k < 0.5$ eV is plotted in the inset and shows various sharp features on top of a broad contribution. b) Dependence of the angle-integrated kinetic energy spectrum on the time delay between the XUV and IR pulses. The fragment yield oscillations for the individual channels, resulting from an energy integration ($\Delta E = 0.2$ eV) of b) are shown for $E_k =$ c) 2.9 eV d) 1.9 eV, e) 0.9 eV and f) 0.4 eV. The accompanying time-dependence of the $\beta(E_k, t)$, describing the fragment ion angular distribution is shown in g-j). In the experiment it is found that the period of half the IR-cycle did not exactly match the periodicity of the yield oscillations, due to thermal drifts in the interferometer. The delay-axis is adjusted to accommodate two yield oscillations within one optical cycle of the IR field. The dotted lines are spaced by a half period of the IR cycle and coincide with the maxima in the fragment ion yield in the $E_k = 1.9$ and $E_k = 2.9$ eV channels.

4.3 Results

4.3.1 XUV ionization of O_2

Prior to discussing the two-color results, a basic understanding of the XUV only ionization of O_2 molecules is useful. The angle-integrated kinetic energy spectrum of O^+ fragments, resulting from ionization with only the XUV pulse is shown in Figure 4.1a (red dashed line). The relevant potential energy curves of the O_2^+ molecular ion are shown in Figure 4.2.

The photoion spectrum in Figure 4.1a contains four main contributions around E_k = 0-0.1, 0.9, 1.9 and 2.9 eV. Based on available literature [156, 157] the contribution

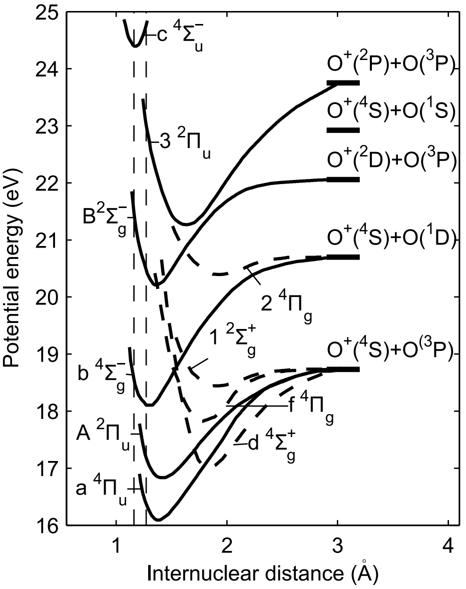

Figure 4.2: Potential energy curves for the O_2^+ molecular states. The energy scale refers to the O_2 ground state and the Franck-Condon region is indicated by vertical dashed lines. Data taken from [156].

at $E_k = 0.9$ eV is assigned to dissociative ionization pathways (DPI) via the $\mathrm{B}\,^2\Sigma_g^-$ state and the contributions at $E_k = 1.9$, 2.9 eV are assigned to DPI via the $\mathrm{c}\,^4\Sigma_u^-$ state of the molecular ion. Zooming in on details in the photoion spectrum, we observe sharp subfeatures around $E_k = 0.9$ and 1.9 eV and these are attributed to dissociation from specific vibrational states of the $\mathrm{B}\,^2\Sigma_g^-$ (v = 0-3) state and the $\mathrm{c}\,^4\Sigma_u^-$ (v = 0,1) state.

When we concentrate on the lower-energy region of E_k = 0-0.2 eV, which is shown in the inset in Figure 4.1a, we observe sharp features that can be associated with DPI from the O_2^* ($3^2\Pi_u, 4s\sigma_g$) [156, 158], $\mathrm{b}\,^4\Sigma_g^-$ and $\mathrm{B}\,^2\Sigma_g^-$ states [156]. In addition, a broad contribution in kinetic energy (E_k ~0-1 eV) is due to DPI from the $3\,^2\Pi_u$ state [156]. We note that minor contributions to the fragment ion kinetic energy spectrum may be due to additional dissociative ionization pathways involving higher-lying ionic states and/or the excitation of excited neutral states followed by dissociation and autoionization [159].

4.3.2 XUV + IR ionization of O_2

The O^+ kinetic energy spectrum for XUV + IR ionization, resulting from averaging over a range of delays corresponding to a full cycle of the IR field, is shown in Figure 4.1a (solid black line). The photoion spectrum shows an increase in the fragment ion yield over a large range of kinetic energies. This increase is maximal for the contributions centered at $E_k = 1.9$ and 2.9 eV ($\mathrm{c}\,^4\Sigma_u^-$ state), which are enhanced by a factor of 2.

The sub-cycle dependence of the effects introduced by the IR field can be observed Figure 4.1b, where the angle-integrated kinetic energy spectra are plotted as a function of the XUV-IR delay. Clear oscillations in the yield of various DPI pathways are observed. We will now concentrate on a selection of contributing DPI pathways. Figure 4.1c-e show the delay-dependence of the angle-integrated yields of the fragment ion channels involving the $\mathrm{B}\,^2\Sigma_\mathrm{g}^-$ ($E_k = 0.9$) and $\mathrm{c}\,^4\Sigma_\mathrm{u}^-$ ($E_k = 1.9$ and 2.9 eV) states. In addition an energy-integration around $E_k = 0.4$ eV is shown, which predominantly contains contributions involving the $3\ ^2\Pi_\mathrm{u}$ state.

In all of the chosen DPI channels, the oscillations in the fragment ion yields have a period that is half the period of the IR cycle. The experiments therefore suggests that the fragment ion distributions are sensitive to the instantaneous IR intensity/field strength at the moment of ionization by the XUV pulses. Since the experiment is performed with an APT that contains two attosecond pulses per optical cycle, a possible dependence on the sign of the laser electric field cannot be revealed in these measurements since consecutive pulses in the train are overlapped with the same instantaneous IR intensity but with an opposite sign of the electric field. Interestingly, the fragment ion yield for XUV + IR ionization is higher than for XUV only ionization, independent of the XUV-IR delay. This suggests that additional dissociative photoionization pathways that are induced by the IR-field may play an important role.

To explain the observed IR-induced effects on the ionization by the XUV one needs to consider whether the effect of the electric field of the IR is primarily affecting the neutral (initial) or the ionic (final) state. By analogy with the existing literature on Rydberg wavepacket dynamics [160], we expect that the formation of coherent superposition of states in the neutral molecule (which in ions leads to charge migration [49, 151]) might show up in the experiment through time-dependent variations in the *total* O^+ and O_2^+ ion yields. At the same time, we expect that couplings that are induced between ionic states may lead to time-dependent variations in the ion yield from specific fragmentation channels. In the present experiment, measurements of the O_2^+ yield showed no delay dependence in excess of the existing experimental fluctuations of $1-2\%$. The experimental data therefore seem to support the latter interpretation.

We will concentrate the analysis on the four selected channels. The contributions related to the $\mathrm{c}\,^4\Sigma_\mathrm{u}^-$ ($E_k = 1.9$ and 2.9 eV) and the $3\ ^2\Pi_u$ ($E_k = 0.4$ eV) molecular ion states, oscillate in phase with each other. The delay dependence of the contribution related to the $\mathrm{B}\,^2\Sigma_\mathrm{g}^-$ state ($E_k = 0.9$ eV) shows a hint of an oscillation. However, the small modulation depth ($\sim \pm 2\%$) precludes a clear resolution of this oscillation against the inherent experimental fluctuations ($\pm\ 1-2\%$). To the extent that it can be determined, the data of the $E_k = 0.9$ eV channel seems to be out-of-phase with the oscillations in the $E_k = 0.4$, 1.9 and 2.9 eV channels.

Following the interpretation that a coupling of ion states can result in the observation of yield oscillations in the different fragmentation channels, we will concentrate on possible couplings induced by the IR-field.

In considering possible couplings between molecular ion states by the IR-field, it is important to realize that these IR-induced couplings occur during the ionization by the XUV field. Therefore couplings between molecular ion states with different

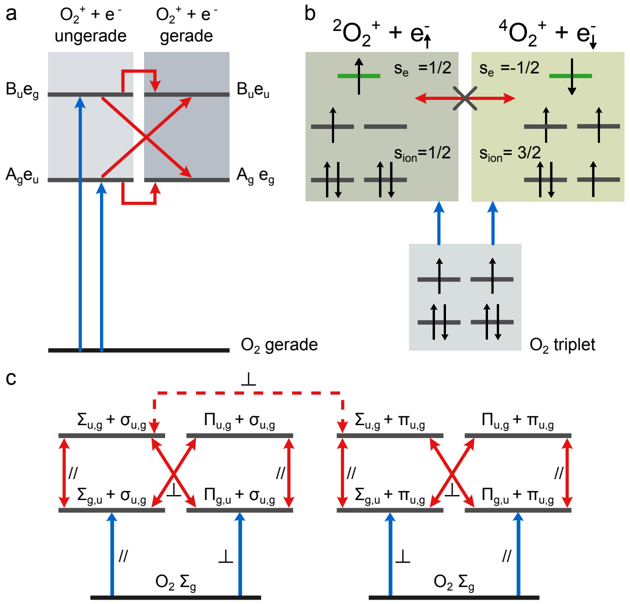

Figure 4.3: a) Schematic illustration of XUV + IR ionization of neutral O_2 with *gerade*-parity to two molecular ion states (A, B) with an accompanying electron e. XUV ionization (blue arrows) can lead to a O_2^+ + e^- state with total *ungerade* parity. The O_2^+ + e^- state with total *gerade* parity can be accessed by the IR-induced coupling, by a change in the parity of the molecular ion (diagonal red arrows) or the continuum electron (horizontal red arrows). b) XUV + IR ionization of O_2 molecules with a triplet $(s_{O_2} = 1)$ ground state. XUV ionization of an electron in the highest occupied orbital (HOMO) can lead to a molecular ion state with doublet spin multiplicity $(s_{ion} = \frac{1}{2})$ and a continuum electron (green bar) with parallel spin $(s_e = \frac{1}{2})$. XUV ionization of an electron in the HOMO-1 orbital can lead to an ion state with quartet spin multiplicity $(s_{ion} = \frac{3}{2})$, accompanied by a continuum electron with an opposite spin $(s_e = -\frac{1}{2})$. IR-induced couplings between molecular ion states with different spin symmetry are excluded as this would require a spin flip of a bound and a continuum electron. c) Schematic illustration of the symmetry of the neutral → molecular ion + electron transition for XUV + IR ionization. In the left panel, the ionization of the O_2 Σ_g state to the molecular ion states, accompanied by an electron wave with $\sigma_{u,g}$ symmetry, is respectively a parallel or perpendicular transition if the ionic state has $\Sigma_{g,u}$ or $\Pi_{g,u}$ symmetry. Ionization from the neutral Σ_g to the $\Sigma_{g,u}$ or $\Pi_{g,u}$ molecular ion state, but accompanied by a $\pi_{u,g}$ wave (right panel), is respectively a perpendicular or parallel transition. IR-induced couplings between molecular ion states with different electron wave symmetries are not taken into account (red dotted arrow).

continuum electrons cannot be excluded. This is illustrated in Figure 4.3a where we consider that in a dipole transition, the parity of the initial and final state should be opposite [161]. In other words, only transitions between *gerade* ↔ *ungerade* states are allowed. In the schematic diagram in Figure 4.3a XUV ionization of the neutral

O_2 molecule with a *gerade* ground state can form an O_2^+ + e^- state with total *ungerade* parity. The molecular ion state (indicated by A or B) can have *gerade* or *ungerade* parity accompanied by a continuum electron with respectively *ungerade* or *gerade* parity. When we consider couplings induced by the IR field in the molecular ion, couplings between molecular ion states with opposite parity are allowed when the parity of the continuum electron is preserved (red diagonal arrows). Conversely, couplings between ion states with similar parity (red horizontal arrows) are only allowed when the continuum electron undergoes a parity change.

Likewise, we can apply the selection rules to the spin multiplicity of the neutral → O_2^+ + e^- transition and to the coupling of molecular ion + e^- states by the IR field. By selection rules, the total spin of the system needs to be conserved ($\Delta S = 0$) [161]. A schematic diagram is shown in Figure 4.3b. The neutral O_2 molecule has two unpaired electrons with parallel spins in the highest occupied molecular orbital (HOMO) and 4 paired electrons in the HOMO-1 orbital. The neutral O_2 molecule therefore has a triplet spin multiplicity ($s_{O_2} = 1$). XUV ionization (blue arrows in Figure 4.3b) can lead to an O_2^+ + e^- state with total $s = 1$ and where the molecular ion has doublet spin multiplicity ($s_{ion} = \frac{1}{2}$, dark grey bars) and the continuum electron is in a parallel spin state ($s_e = \frac{1}{2}$) (green bar). XUV ionization can also lead to an O_2^+ ion with quartet spin multiplicity ($s_{ion} = \frac{3}{2}$), accompanied by a continuum electron with an opposite spin ($s_e = -\frac{1}{2}$). When we consider possible couplings of molecular ion states by the IR field we exclude couplings that would require a spin change of two electrons. This means that couplings between molecular ion states with different spin symmetry by the IR-field are excluded (red arrow).

Summarizing, couplings between molecular ion states with similar and opposite parity are possible when the continuum electron is taken into account and is allowed to undergo a change in parity. On the other hand, only couplings between molecular ion states with similar spin multiplicity are allowed. Applying these rules to the current experiment, we can expect that the $\mathrm{c}\,{}^4\Sigma_\mathrm{u}^-$ state is coupled to a state with a quartet spin multiplicity, for which the $\mathrm{b}\,{}^4\Sigma_\mathrm{g}^-$ and $\mathrm{a}\,{}^4\Pi_\mathrm{u}$ states are possible candidates [156]. Likewise, the $\mathrm{B}\,{}^2\Sigma_\mathrm{g}^-$ and $3\,{}^2\Pi_\mathrm{u}$ states are expected to couple to a molecular ion state with doublet spin multiplicity. Interestingly, the yield oscillations in the channels related to these states oscillate out-of-phase with each other and therefore suggest a coupling of the $\mathrm{B}\,{}^2\Sigma_\mathrm{g}^-$ and $3\,{}^2\Pi_\mathrm{u}$ states. However, a coupling of these states to the bound $\mathrm{X}\,{}^2\Pi_\mathrm{g}$ or $\mathrm{A}\,{}^2\Pi_\mathrm{u}$ states cannot be ruled out.

Delay-dependent angular distributions

In addition to the IR-induced effects in the fragment ion yield, delay-dependent changes are also observed in the O^+ fragment angular distributions. The fragment ion angular distribution is well described by $\mathrm{P}(\mathrm{E}, \cos(\theta), \mathrm{t}) \sim 1 + \beta(\mathrm{E}, \mathrm{t})\, \mathrm{P}_2(\cos(\theta))$, as higher-order terms in $\mathrm{P}(\mathrm{E}, \cos(\theta))$ are found to be negligible. The β-parameters for the previously selected DPI channels are plotted as a function of delay in Figure 4.1g-j. Similar to the delay-dependence of the fragment ion yields, oscillations in the β-parameter are observed for all the selected channels with a period of half the IR period.

From the delay-dependence of the β-parameter additional information about the molecular ion states that are involved in possible couplings by the IR-field can be extracted. In the axial recoil approximation, the β-parameter of the ion angular distribution is directly related to the symmetry of the neutral $\rightarrow$ ion + e^- transition. A dominant contribution of a parallel transition is reflected by an ion angular distribution that is peaked along the laser polarization, which corresponds to a $\beta > 0$. Likewise, a dominant contribution of a perpendicular transition will be reflected by an ion angular distribution that is peaked perpendicular to the laser polarization, which corresponds to $\beta < 0$.

The symmetry of the transition depends on the symmetries of the initial and final state, which in the case of photoionization are the neutral state and the molecular ion + electron state. The total symmetry of the final state therefore also includes the symmetry of the continuum electron. This is schematically illustrated in Figure 4.3c.

The O_2 ground state is a Σ_g-state. If the ionic state under consideration is a Σ_g or Σ_u-state then the $\Sigma_g^{neutral} \rightarrow \Sigma_{g,u}^{ion}$ transition will be a parallel transition when the accompanying continuum electron is a wave with $\sigma_{u,g}$ symmetry. If the continuum electron is however a wave with $\pi_{u,g}$ symmetry, then the $\Sigma_g^{neutral} \rightarrow \Sigma_{g,u}^{ion}$ transition is a perpendicular transition. Note that in this discussion we restricted ourselves to electron waves with σ or π symmetry for reasons of brevity. The contribution of δ electron waves in the photoionization of O_2 has also been reported [162]. For the δ electron waves, the same argument holds as for the σ electron waves, i.e. a transition from the neutral to the $\Sigma_{g,u}^{ion}$, accompanied by a $\delta_{u,g}$ is a parallel transition. The electron waves can be described by their partial waves in terms of their l quantum numbers. Electron waves with *gerade* parity are described by the $l = even$ orders (s and d partial waves) and electron waves with *ungerade* parity are described by the $l = odd$ orders (p and f waves) [162].

When the ionic state under consideration is a $\Pi_{g,u}$-state, then the $\Sigma_g^{neutral} \rightarrow \Pi_{g,u}^{ion}$ transition will be a perpendicular transition when the accompanying continuum electron is an electron wave with $\sigma_{u,g}$ symmetry and will be a parallel transition when the electron wave has $\pi_{u,g}$ symmetry.

Calculations on single-photon ionization of O_2 molecules with energies $\hbar\nu <$30 eV [163] show that the $\Sigma_g^{neutral} \rightarrow \Sigma_{g,u}^{ion}$ transitions are characterized by a positive β-parameter and hence are parallel transitions. For the $\Sigma_g^{neutral} \rightarrow \Pi_{g,u}^{ion}$ transitions, calculations yield a negative β-parameter which reflects the dominant contribution of a perpendicular transition [162, 163].

However in the current experiment, the XUV photoionization takes place in an IR field, which can induce couplings among the molecular ion + electron states. Similar to the case of XUV ionization, one can deduce the symmetry of the coupling by the IR-field from the symmetry of the initial and final molecular ion + electron state. This is schematically illustrated in Figure 4.3c, where the coupling by the IR-field between different states is shown by red arrows.

Let us consider the coupling between two molecular ion states which we indicate by A and B. The coupling between the A $\Sigma_{g,u}$ + $\sigma_{u,g}$ molecular ion + electron state to the molecular ion state B $\Sigma_{g,u}$, accompanied by a $\sigma_{u,g}$ partial wave, will be a parallel transition. Conversely a coupling of the A $\Sigma_{g,u}$ + $\sigma_{u,g}$ molecular ion + electron state to the same B $\Sigma_{u,g}$ ionic state, but now accompanied by a $\pi_{u,g}$ partial wave will be a perpendicular transition (dotted red arrow). In the following discussion, we assume that couplings that involve both a change of the molecular ion state and of the outgoing electron partial wave are less important compared to couplings that only require a change in the state of the molecular ion. We therefore only take couplings between molecular ion states into account that have the same symmetry of the electron partial wave. It is important to note that for increasingly high IR intensities, multiple IR-induced dipole transitions start to contribute and this assumption becomes invalid.

In our picture, a coupling between molecular ion states with the same symmetry by the IR field is favored for molecules aligned parallel to the laser polarization. Then an increase in the ion fragment yield, as a result of the IR-coupling, is expected to be accompanied by an increase in the β-parameter. Conversely couplings between molecular ion states with different symmetry will be favored for molecules aligned perpendicular to the laser polarization. In this case an increase in the fragmentation yield is thus expected to be accompanied by a decrease in the β-parameter.

In the experimental results, we find for the $E_k = 0.4$ eV channel, the oscillations in the fragment yield and $\beta(E,t)$ are in-phase (Fig. 4.1f,j). Following the previous assignment of this channel to dissociative ionization of the $3\,^2\Pi_\mathrm{u}$ state and including only states with doublet spin multiplicity based on selection rules, implies a coupling to a state with a $^2\Pi$ symmetry. The X $^2\Pi_\mathrm{g}$ and A $^2\Pi_u$ states meet these requirements. These are bound ionic states and therefore do not show up in our O^+ spectrum. On the other hand, the fragment yield and β-parameter oscillations for the $E_k = 0.9$ eV channel, related to DPI from the $\mathrm{B}\,^2\Sigma_\mathrm{g}^-$ state appear to be out-of-phase (Fig. 4.1e,i), although a clear phase relation between the two cannot be determined. Accordingly, the data suggests that the $\mathrm{B}\,^2\Sigma_\mathrm{g}^-$ state is coupled to a state with $^2\Pi$ symmetry. Based on the in-phase oscillations of the yield and β-parameter of the $3\,^2\Pi_\mathrm{u}$ state, we regard that a coupling of the $\mathrm{B}\,^2\Sigma_\mathrm{g}^-$ state to the $3\,^2\Pi_\mathrm{u}$ state is not a dominant contribution. The $\mathrm{B}\,^2\Sigma_\mathrm{g}^-$ is possibly coupled to the bound X $^2\Pi_\mathrm{g}$ or $\mathrm{A}\,^2\Pi_\mathrm{u}$ states.

The oscillations in the fragment yield and β-parameter for the $E_k = 1.9$ and 2.9 eV channels are clearly in-phase (Fig. 4.1c,d,g,h). This suggests a coupling of the $\mathrm{c}\,^4\Sigma_\mathrm{u}^-$ state to a state of $^4\Sigma$-symmetry. The $\mathrm{b}\,^4\Sigma_\mathrm{g}^-$ state meets this condition and dissociates only to a minor degree, forming fragment ions with $E_k < 0.2$ eV. An integration in this kinetic energy region did not reveal a well resolved oscillation, which is attributed to overlapping contributions from different DPI pathways.

XUV + IR ionization in a 3-level system

In the previous paragraph, we suggested that the selected dissociative molecular ion states are coupled to bound molecular ion states by the IR-field. In this section we now concentrate on developing an intuitive understanding of the mechanism, responsible for the observed oscillations in the fragment ion yield. A simplified model is used that is based on a model used in the work on D_2 molecules [164] and explains the dependence of the XUV + IR ionization on the delay between these two pulses.

The molecular system is described by a neutral ground state ψ_0 and two ionization continua with ionization thresholds of $I_{p,1}$ and $I_{p,2}$.

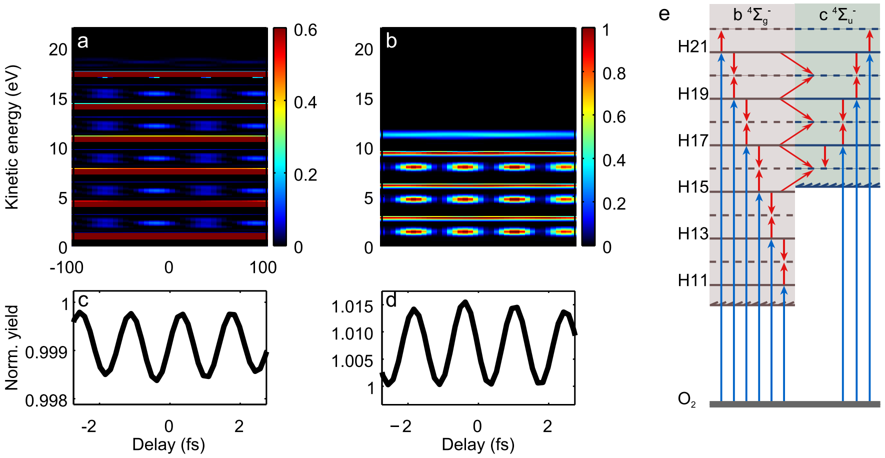

Figure 4.4: Results for calculating the photoelectron spectra for two-color ionization in a simplified three-level system. Photoelectron spectrum as a function of the XUV - IR delay for the a) first ionization continuum, related to the b $^4\Sigma_g^-$ state and b) the second ionization continuum, related to the c $^4\Sigma_u^-$ state. The spectrum resulting from XUV only ionization was subtracted to illustrate the sidebands more clearly. The residual straight lines are due to a small difference in the kinetic energy of the photoelectrons that are the result of XUV only ionization and XUV + IR ionization. The difference in kinetic energy is attributed to a change in the ionization potential in a moderately strong IR field. Total ionization yield for the c) b $^4\Sigma_g^-$ and d) c $^4\Sigma_u^-$ ionization continuum, obtained by summing over the full photoelectron energy range. e) A schematic illustration of XUV + IR ionization in a system that contains the O_2 neutral ground state and two ionization continua that are related to the b $^4\Sigma_g^-$ and c $^4\Sigma_u^-$ states. The diagram explains the appearance of sidebands in the second ionization continuum (shown in Fig 4.4b). XUV ionization (blue arrows) by the odd harmonics yields the straight lines in the photoelectron spectra shown in a) and b). Couplings *between* the two ionization continua by the IR field (diagonal red arrows) results in the sidebands at positions in between the lines that arise from ionization by the odd harmonics. Couplings within the same continuum by the IR field (vertical red arrows) will also result in the observation of sidebands, as observed in RABBITT experiments, but does not lead to a delay-dependence of the total yield.

The wavefunction $\Psi(t)$ is written as:

$$\Psi(t) = G(t)\psi_0 + \int d\epsilon A_1(\epsilon,t)\psi_{1,\epsilon} + \int d\epsilon A_2(\epsilon,t)\psi_{2,\epsilon} \tag{4.1}$$

ψ_0 is the ground state of the neutral molecule and $\psi_{1,\epsilon}, \psi_{2,\epsilon}$ are continuum states with photoelectron energy ϵ belonging to the first and second ionization continua with $I_{p,1}$ and $I_{p,2}$. $A_1(\epsilon,t)$ and $A_2(\epsilon,t)$ are the time-dependent amplitudes of the above mentioned continuum states. The time-dependent population in the continuum states are calculated by inserting the wavefunction in equation 4.1 into the time-dependent Schrödinger equation (TDSE). The model calculates the ionization probability to the two continuum states as a function of the photoelectron energy and the XUV - IR delay, resulting in a delay-dependent photoelectron spectrum. The yield of a particular molecular ion state equals the total yield in the photoelectron spectrum related to the ionization continuum that belongs to the ionic state. The calculation is done for fixed nuclei and therefore does not include the dissociation of the molecule.

In the TDSE calculation XUV-induced couplings between the ground state ψ_0 and the two ionization continua $\psi_{1,\epsilon}, \psi_{2,\epsilon}$ are included in the Hamiltonian. IR-induced couplings are considered to be present between the two ionization continua $\psi_{1,\epsilon}$ and $\psi_{2,\epsilon}$. Couplings within the same ionization continuum and couplings between continuum states $\psi_{1,\epsilon}, \psi_{2,\epsilon'}$ with $\epsilon \neq \epsilon'$ are neglected, to simplify the calculation.

The model therefore only includes two molecular ion states and we restrict the following discussion to one of the selected dissociative molecular ion states. We previously suggested that the $\mathrm{B}\,^2\Sigma_\mathrm{g}^-$ and $3\,^2\Pi_\mathrm{u}$ dissociative molecular ion states were coupled to the bound $\mathrm{X}\ ^2\Pi_\mathrm{g}$ or $\mathrm{A}\,^2\Pi_\mathrm{u}$ states. In addition, the experimental data also suggested a coupling of the $\mathrm{c}\,^4\Sigma_\mathrm{u}^-$ state to the dominantly bound $\mathrm{b}\,^4\Sigma_\mathrm{g}^-$ state. As the yield and β-parameter oscillations, related to the $\mathrm{c}\,^4\Sigma_\mathrm{u}^-$ state, were clearly resolved in the experimental data, we chose the simulate the coupling of this state to the $\mathrm{b}\,^4\Sigma_\mathrm{g}^-$ state. Correspondingly, the ionization thresholds for the ionization continua $\psi_{1,\epsilon}, \psi_{2,\epsilon}$ are chosen to simulate the $\mathrm{b}\,^4\Sigma_\mathrm{g}^-$ and $\mathrm{c}\,^4\Sigma_\mathrm{u}^-$ states. For the couplings between the ground state and the two ionization continua, the cross-sections for ionization in this photon energy range are used [163]. Unfortunately, the coupling strength between the $\mathrm{b}\,^4\Sigma_\mathrm{g}^-$ and $\mathrm{c}\,^4\Sigma_\mathrm{u}^-$ states was not available. As a first estimation we chose the coupling strength to be similar to the transition dipole moment of the two lowest electronic states in the H_2^+ molecular ion, which can be approximated by eR/2.

The results of this simple model are plotted in Figure 4.4. The simulated photoelectron spectra as a function of delay between the XUV and IR pulse are respectively plotted for the first ($\mathrm{b}\,^4\Sigma_\mathrm{g}^-$ state) and second ionization ($\mathrm{c}\,^4\Sigma_\mathrm{u}^-$ state) continuum in Figure 4.4a and 4.4b. Two sets of horizontal lines can be distinguished. The most intense set of lines corresponds to direct ionization from the neutral ground state to the first or second ionization continuum by the XUV pulse. Ionization to the $\mathrm{b}\,^4\Sigma_\mathrm{g}^-$ is possible for harmonics H11-21 and these lines in the photoelectron spectrum (Fig. 4.4a) are therefore observed at $\epsilon = (11 + 2n)\omega_{IR} - I_{p,1}$ with $n = 0 - 5$. The $\mathrm{c}\,^4\Sigma_\mathrm{u}^-$ state has a higher ionization potential than the $\mathrm{b}\,^4\Sigma_\mathrm{g}^-$ state and ionization is possible for harmonics H17-H21. These lines in the photoelectron spectra (Fig. 4.4b) are thus observed at $\epsilon = (17 + 2n)\omega_{IR} - I_{p,2}$. In addition a second set of weaker lines is observed in the photoelectron spectra that shows a modulation with the XUV - IR delay. The origin of this second set of lines in the second ionization continuum $\mathrm{c}\,^4\Sigma_\mathrm{u}^-$ comes from a two-color ionization process and is schematically illustrated in Figure 4.4e. The XUV excites (blue arrows) the molecule to the first continuum and the IR field (de)-excites it to the second continuum (diagonal red arrows). These sidebands are observed at $\epsilon = (16+2n)\omega_{IR} - I_{p,2}$ with $n = 0-2$. A set of sidebands is also observed in the first continuum ($\mathrm{b}\,^4\Sigma_\mathrm{g}^-$ state) at $\epsilon = (12+2n)\omega_{IR} - I_{p,1}$ with $n = 0 - 4$ and is similarly attributed to a two-color ionization process, involving

XUV excitation to the second ionization continuum and (de)-excitation by the IR-field to the first continuum (not illustrated in Figure 4.4e for reasons of clarity of the schematic diagram).

The set of sidebands in the first and second ionization continuum are modulated with a periodicity of half the IR optical cycle. The origin of this modulation comes from the interference of two possible ionization paths for a specific sideband, namely by absorption or stimulated emission of an IR photon from a direct ionization process to the other continuum by a harmonic order below and above the sideband. Constructive or destructive interference of the two pathways, depending on the relative phases of the XUV and IR pulses, leads to a delay-dependence of the sidebands. Because of depletion also the yield of the direct ionization channels are modulated. Further evidence for this mechanism is given by the presence of a delay-independent sideband, observed at $\epsilon = (22)\omega_{IR} - I_{p1,p2}$ for both the first and second ionization continuum. This line is not modulated as there is only one XUV + IR pathway that contributes to H21 + IR, since the harmonic spectrum does not contain H23.

By integrating over all photoelectron energies ϵ the total yield of the corresponding molecular ion state is obtained. The total yields in the ψ_1 and ψ_2 continua, which can respectively be related to the ion yields from the bound $\mathrm{b}\,^4\Sigma_\mathrm{g}^-$ and dissociative $\mathrm{c}\,^4\Sigma_\mathrm{u}^-$ states, are respectively plotted in Figures 4.4c and 4.4d. A clear modulation of the total yield is observed with a periodicity of half the IR optical cycle. The oscillations of the total ionization to the first continuum and second continuum are out of phase with each other. The small modulation depth of 0.04 % prevents the measurement of yield oscillations that are related to the $\mathrm{b}\,^4\Sigma_\mathrm{g}^-$ state.

Similarities to the well-known RABBITT [8] technique are easily recognized. However a RABBITT experiment involves just a single ionization continuum. When only a single ionization continuum is present, the couplings within the continuum result in the appearance of sidebands, which merely leads to a redistribution of the energy of the photoelectrons. Conversely, in the simple model considered here, the two interfering pathways involve *two* ionization continua, i.e. the IR couples two different ionization continua and a modulation in the total ionization yield into both of the two continuum states is observed as a function of delay.

A closer inspection of the yield related to the ψ_1 continuum shows that the dominant contribution of the delay-dependence is attributed to the photoelectron lines located at $\epsilon = (11 + 2n)\omega_{IR} - I_{p,1}$, i.e. the direct ionization channels. At the same time the modulations in the yield in the ψ_2 continuum come from the modulations of the sidebands in this continuum. The IR field therefore predominantly transfers population from the first to the second continuum and to a lesser extent from the second to the first ionization continuum. In other words, the modulations in the total yields are related to depletion or population of the two continuum states as a function of delay. An increase in the ratio between the cross-sections for XUV ionization to the two ionization continua will therefore result in a larger modulation depth of the oscillations. Another factor that influences the modulation depth of the total yield is the strength of the IR-induced coupling between the two ionization continua. As can be expected, increasing this coupling strength will increase the modulation depth.

The calculated modulation depth in Figure 4.4d, related to the yield oscillations in the $\mathrm{c}\,^4\Sigma_\mathrm{u}^-$ state is $\sim \pm 1\%$ and is smaller than the experimentally observed modulation depth in Figure 4.1c,d. A possible reason for this is the underestimation of the IR coupling strength between the $\mathrm{b}\,^4\Sigma_\mathrm{g}^-$ and $\mathrm{c}\,^4\Sigma_\mathrm{u}^-$ states.

In reality couplings within a single ionization continuum are present. This means that the model does not provide a realistic description of the photoelectron spectrum. Including the couplings within the individual continua, in addition to couplings between continuum states, leads to a decreased contrast of the delay-dependent total photoelectron yield, but qualitatively retains the delay-dependent total photoelectron yield [165].

Despite the simplifications in the present model it provides a rationale for the modulations in the fragment ion yield observed in the experiment.

4.4 Conclusion

Ionization of O_2 molecules by an APT is shown to be affected by the presence of a moderately strong IR field. Various dissociative ionization channels show oscillations in the yield as a function of the delay between the APT and the IR with a period that is half the period of the IR. Besides the yield also the angular distributions of these fragment ions are found to oscillate with the delay. These oscillations can be understood in terms of an IR induced coupling between ionic states. A simple model of the ionization can qualitatively explain the experimental result. The electronic states that are involved in the coupling can be deduced from the phase-relation between the yield oscillations of different channels and from the phase-relation between the oscillations in the yield and the angular distribution (characterized by a β-parameter) of a single channel. In addition, applying selection rules to the XUV and IR transitions exclude couplings between molecular ion states with different spin multiplicities and simplify the analysis. The oscillations that arise due to the coupling between molecular ion states can be explained in terms of an interference of two XUV + IR ionization pathways, involving two ionization continua. In a time dependent picture, one can view the IR-induced coupling of molecular ion states as a time-dependent change in the orbitals of the ion. In this picture ionization by the APT can be seen as a probe of this time-dependence with the fragment ion yield and angular distributions as observables. This is the first time that such effects are observed in multi-electron molecules.

5 Velocity map imaging of atomic and molecular processes at the free electron laser in Hamburg (FLASH)

Velocity map imaging was implemented at the free electron laser in Hamburg (FLASH). Atomic and molecular photoionization processes were imaged at a photon energy of 45.55 eV. High quality momentum distributions were recorded for a range of rare gases (He, Ne, Ar, Kr and Xe) and small molecules (H_2, D_2, O_2, N_2, CO_2). This proof-of-principle experiment illustrates the potential for using velocity map imaging (VMI) in order to study non-linear ionization and/or dissociation processes at free-electron laser sources that recently have become available.

5.1 Introduction

The development of extreme ultraviolet (XUV)/x-ray free electron lasers (FELs), like the free electron laser in Hamburg (FLASH), offers exciting prospects for atomic and molecular physics research. Free electron lasers like FLASH offer high frequency radiation with a short pulse duration (down to 10 fs [166]) and a high flux/intensity (several tens of μJ/pulse that can be focussed down to intensities of $\sim 10^{16}$ W/cm^2). A tunability of FLASH down to 13.7 nm, with harmonics extending down to 2.75 nm, has already been demonstrated [166]. This allows for an extremely wide range of novel dynamical and structural studies. Published examples already include a first demonstration of diffractive imaging [167] and studies of atomic and molecular ionization and dissociation at high intensities [53, 168].

In this paper we present experimental results that were obtained in a campaign where a velocity map imaging spectrometer [169] was installed on the BL2 beamline of FLASH. The velocity map imaging spectrometer was placed approximately 1 meter downstream from a COLTRIMS apparatus [170] in which the FEL was brought to a focus. Thus, while being able to make use of the high photon flux of the FEL (up to 3×10^{12} photons/pulse at a photon energy of 45.55 eV), the present experiments do not yet make use of the high peak intensity that can be generated. Nevertheless, the experiments are a first demonstration of the utility of velocity map imaging spectrometers at free electron lasers and pave the way for experiments involving non-linear ionization and/or dissociation, which will be attempted shortly.

The velocity map imaging technique provides a 100% collection efficiency and allows for high count rates. It thus provides detection characteristics that combine very favorably with the high brilliance of FLASH.

One of the main opportunities provided by a facility like FLASH is that it readily

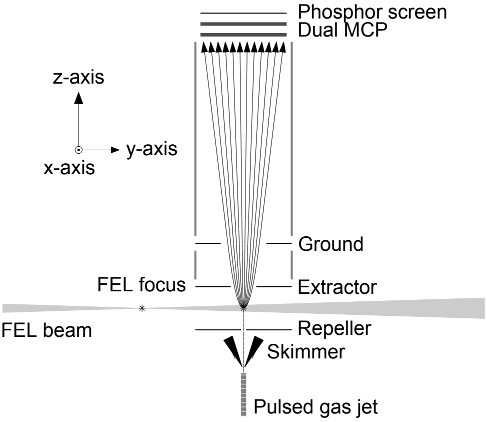

Figure 5.1: A schematic illustration of the experimental set-up. The focus of FLASH was approximately 1 m before the center of the interaction region. Photoelectrons or ionic fragments formed at the crossing point of the laser beam and the molecular beam were accelerated by the static electric field towards a dual MCP/phosphor screen assembly, where their impact was registered by a CCD camera.

allows to perform ionization and dissociation experiments involving non-linear photoabsorption. Ionization in strong laser fields has traditionally been investigated using low-frequency laser sources [7] where the laser frequency $\omega \ll$ the ionization potential I_p of the target atom/molecule. Ionization then proceeds by multi-photon ionization or by means of tunneling. Both involve the removal of multiple photons from the laser field. The transition between multi-photon ionization and tunneling occurs around conditions satisfying $\gamma = (I_\mathrm{p}/2U_\mathrm{p})^{1/2} \cong 1$, where γ is the Keldysh parameter, and where $U_\mathrm{p} = {E_\mathrm{laser}}^2/4\omega^2$ (a.u.) is the ponderomotive energy. For $\gamma \ll 1$ the ionization occurs by means of tunneling. A facility like FLASH allows to extend studies of non-linear ionization to a regime where $\omega \gg I_\mathrm{p}$. Under this condition significant changes in the dynamics of strong field ionization are anticipated. The ω^{-2} scaling of the ponderomotive energy suggests a greatly diminished role of field ionization in favor of a multi-photon ionization mechanism. Furthermore, stationary phase arguments dictate that the radial momentum of the electron before and after photoabsorption is the same, favoring photoabsorption at small distances of the electron from the nucleus, and hence, of inner-shell electrons. One of the first experiments at FLASH where optical non-linearities were observed, was ionization of single xenon atoms. Wabnitz *et al.* used intensities of $\sim 10^{13}\mathrm{W/cm}^2$ at a photon energy of ~12.7 eV and observed multiple charged ions up to Xe^{6+} by multiphoton sequential ionization [171]. By using a description in terms of rate equations, which take into account the simulated FEL pulses and multiphoton cross-sections, Santra *et al.* [172] were able to understand the high degree of ionization compared to ionization in the infrared domain. In a recent experiment, where FLASH (operating at a photon energy of 98 eV) was focused to intensities of $\sim 10^{16}\mathrm{W/cm}^2$, even higher degrees of ionization, up to Xe^{21+}, were observed [53]. Similarly, Makris *et al.* [54] used rate equations to describe these observations, where the spatiotemporal structure of FLASH and multiphoton cross-sections were the necessary components. Whereas no multi-electron ejection was observed in the former experiment, it was necessary to take multiphoton single electron as well as multi-electron ejection processes into account to explain the remarkable high degree of ionization.

The existence of non-linearities in ionization or dissociation processes is a precondition for being able to study these processes in the time-domain. In time-domain pump-probe experiments, dynamical processes are commonly initiated by the absorption and/or emission of one or more pump photons, and evaluated after a given delay by means of a second interaction involving one or more probe photons. At present there is considerable excitement in the ultrafast laser community about the development of XUV attosecond pulses [100, 173]. In the coming years investigations of electron dynamics on ultrafast time-scales will be possible [22, 26, 174] providing unique insights into the nature of photo-excitation processes, electron correlation and the interaction of electronic and nuclear degrees of freedom in photochemistry. The common technique for generating attosecond laser pulses is high harmonic generation, where atoms/molecules are exposed to an intense femtosecond laser, and where harmonics are formed by means of a three-step process consisting of ionization of the medium, acceleration of the electron in the oscillatory laser field, and emission of photons in the course of a recombination process [175, 176]. One drawback of present-day attosecond sources is that they are very weak, typical pulse energies for isolated attosecond laser pulses being on the order of 1 pJ. Free electron lasers like FLASH provide an attractive alternative, although the pulse durations achieved in high harmonic generation remain for the time being unsurpassed. Nevertheless, we consider that there exists an important complementarity between the emergence of attosecond laser pulses in table-top laboratory-scale experiments and the emergence of free electron laser facilities, where a joint user community may be able to accomplish significant progress on both sides.

A technique that has - in the last few years - become very popular in chemical physics [177] (and in attosecond science) is velocity map imaging [169]. In VMI, ions or electrons are formed at the crossing point of an atomic/molecular beam and one or more laser beams. The ions or electrons are accelerated towards a two-dimensional detector that usually consists of a dual micro-channel plate followed by a phosphor screen and a camera system. Since the extraction ion optics are designed so that the position on the camera is almost exclusively dependent on the velocity of the ion or electron, and hardly on the position where the ionization event took place. Hence, velocity map imaging measures a 2D projection of the 3D electron or ion velocity distribution that is formed in the experiment. If the experiment contains an axis of symmetry in the plane of the detector, as is usually the case, the 3D distribution can be retrieved from the 2D projection. Following the emergence of XUV attosecond pulses generated by means of high-order harmonic generation, velocity map imaging has been used to characterize the duration of attosecond pulses [106], to develop a new type of electron interferometry [129] and to observe interference in two-color attosecond XUV + few-cycle infrared (IR) ionization [178]. At FLASH we performed a series of proof-of-principle experiments where we used VMI to study atomic and molecular single-photon ionization processes. In this chapter results for a range of small molecules will be discussed.

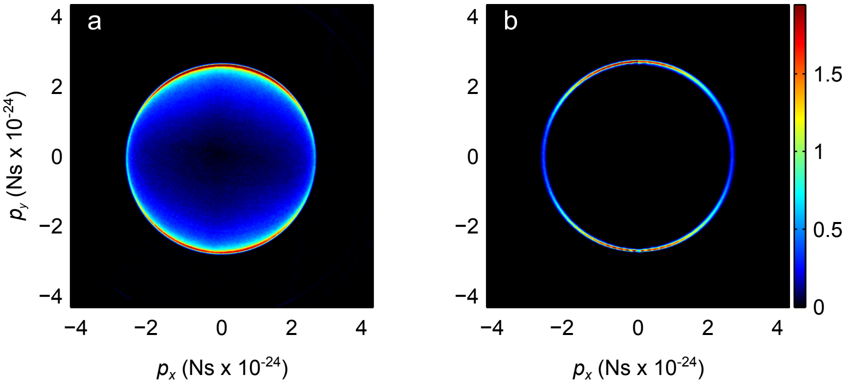

Figure 5.2: a) The measured projection of the momentum distribution of electrons resulting from photoionization of Neon. b) A slice (p_z= 0) through the retrieved 3D momentum distribution from the measured projection.

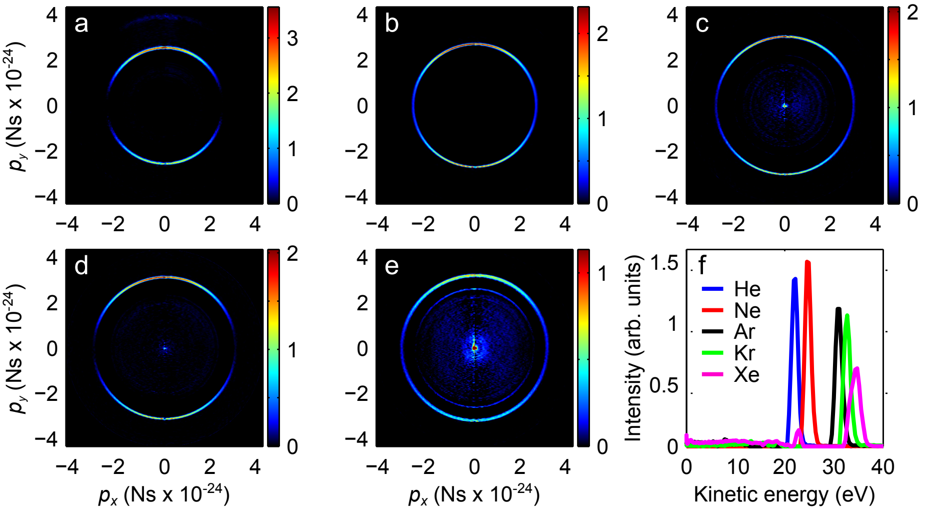

Figure 5.3: a) A slice (p_z= 0) through the 3D momentum distribution of electrons resulting from ionization of a) Helium, b) Neon, c) Argon, d) Krypton and e) Xenon. f) The electron kinetic energy spectra resulting from angular integration of the 3D momentum distributions.

5.2 Methods

5.2.1 Experimental setup

During the measurements, the laser was tuned to operate around 46 eV ($\lambda \sim 27$ nm) and delivered pulse trains with a repetition rate of 5 Hz. Each train consisted of 30 micropulses spaced by 4 μs. The pulses had an average energy of 10 μJ and a pulse duration of 25 fs.

A skimmed atomic or molecular beam was formed by supersonic expansion in a pulsed gas jet operated at 5 Hz. The target beam intersected the laser beam at right angles (see Figure 5.1). From here we consider that the laser propagated along the y-axis and was polarized along the x-axis, while the gas jet moved along the z-axis. The partial pressure of the molecular beam in the interaction region was estimated to be on the order of 10^{-9} mbar, low enough to guarantee that space-charge effects are avoided. Ions or electrons created at the crossing point were accelerated towards the detector by a static electric field. The ion optics consisted of a repeller and extractor electrode. For photoelectrons an extraction field of -1.09 kV/cm was used (V_{repeller} = -9.00 kV, $V_{\text{extractor}}$ = -7.15 kV) and the maximum kinetic energy that could be measured was 60 eV. For the extraction of ionic fragments, a field of typically 0.37 kV/cm was used ($V_{\text{repeller}} = 3$ kV, $V_{\text{extractor}} = 2.43$ kV). The maximum kinetic energy was then limited to 19 eV. The impact of the photoelectrons or ionic fragments were registered by a dual micro-channel plate/phosphor screen assembly, followed by a CCD camera. By applying a 200 ns gate to the back of the MCP/phosphor detector we were able to select ion masses and decrease background signals. The gate was synchronized with the last pulse in the train. In addition an on-line background subtraction was performed by measuring a background image for each second laser shot.

5.2.2 Retrieving the initial 3D angular and momentum distribution

In our experiment the laser polarization was in the plane of the detector, providing a symmetry axis. The measured 2D projection can therefore be used in a numerical inversion procedure, to retrieve the initial 3D momentum distribution [179]. To illustrate the result of this procedure, the measured 2D projection of electrons resulting from photoionization of Neon is shown in Figure 5.2a and a slice through the retrieved 3D distribution is shown in Figure 5.2b. A sharp ring is observed at 6.7×10^{-15} Ns and corresponds to ionization to the ground state of Ne^{+}.

A calibration of the photon energy and detector settings was performed to determine the kinetic energy of the fragments. A slice through the momentum distributions of the electrons resulting from ionization of a range of rare gases (He, Ne, Ar, Kr and Xe) is shown in Figure 5.3a-e. The electron kinetic energy spectra, resulting from an angular integration of the momentum distributions, are shown in Figure 5.3f. In the momentum distributions of argon, krypton and xenon, several rings are observed that are attributed to inner-shell processes. The photon energy $\hbar\omega$ and the calibration of the momentum scale in the 2D projection, was determined by minimizing the differences between the observed and theoretical kinetic energies:

$$\Delta = \sum_{\mathrm{He,Ne,Ar,Kr,Xe}} \left[\hbar\omega - I_{\mathrm{p}} - \frac{\mathrm{pixels}^2}{\alpha} \right]^2 \tag{5.1}$$

I_{p} is the first ionization potential and α is a calibration parameter that provides the conversion from the measured position on the detector (in pixels^2) to the energy of the photoelectron. During the experiments, FLASH was operated around a photon energy of 46 eV and the photon energy that was determined by this procedure is 45.55 ± 0.06 eV. The small standard deviation indicates excellent agreement between the measurements obtained using the different rare gases. The high accuracy is at first sight in contrast with the strong shot to shot fluctuations of FLASH [166]. The photon energy is however determined using the peak positions. Fluctuations in the photon energy will manifest themselves in the width of the peak. The mean value of the photon energy was therefore determined with an accuracy of 0.06 eV.

5.3 Results

5.3.1 H_2 and D_2

A slice through the 3D momentum distribution for electrons resulting from photoionization of D_2 is shown in Figure 5.4a. In the momentum distribution a ring with maxima along the laser polarization is observed at a kinetic energy of 30.08 ± 0.17 eV. This corresponds to ionization to the D_2^+ ground state (binding energy 15.47 eV).

A slice through the 3D momentum distribution for the D_2^+ ions is shown in Figure 5.4b. Noting that the momentum distributions of the electrons (Figure 5.4a) and that of the ions are plotted on the same absolute momentum scale, Figure 5.4b reveals that the departure of the electron is accompanied by a matching recoil momentum of the D_2^+. Remarkably the high fluence of FLASH allowed to observe this recoil momentum distribution within a single laser shot, while a high-quality image like Figure 5.4b was obtained in a few minutes.

Information about dissociative ionization processes is obtained from a slice through the D^+ 3D momentum distribution, shown in Figure 5.4c. The ion kinetic energy spectrum, resulting from angular integration of the momentum distribution, is shown in Figure 5.4d and shows the presence of two contributions. First, the peak at zero kinetic energy corresponds to D^+ ions produced by dissociative ionization to the $1s\sigma_g^+$ ground state. Second a broad distribution is present for E_k = 3.6-9 eV. These D^+ ions are predominantly ejected perpendicular to the laser polarization. They are attributed to a perpendicular transition to the repulsive $2p\pi_u$ state. This state has a potential energy of 35-44 eV in the Franck-Condon region and dissociates to $D^+ + D$ (28.2 eV), so that D^+ ions formed in this dissociative ionization process are expected to have a kinetic energy of 3.4-7.9 eV. Similar results were obtained by Ito *et al.* [180], who observed that for a photon energy of 45 eV, D^+ ions have a broad kinetic energy distribution around 6 eV and are mainly ejected perpendicular to the laser polarization. The results obtained for H_2 are similar to D_2 and are not shown here.

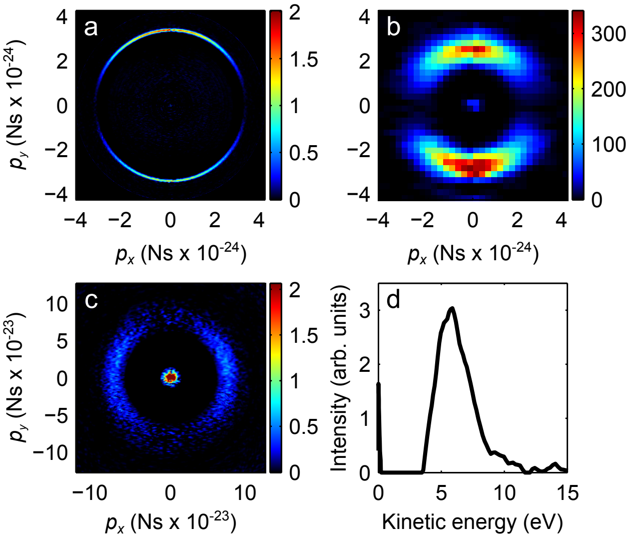

Figure 5.4: a) A slice (p_z= 0) through the retrieved 3D momentum distribution electrons resulting from ionization of D_2. The momentum distribution is peaked along the laser polarization and is maximum for E_k = 30.08 ± 0.17 eV. b) A slice (p_z= 0) through the retrieved 3D momentum distribution for b) D_2^+ ions. c) Idem, for D^+ ions. d) The D^+ kinetic energy spectrum, resulting from an angular integration. The momentum distribution for the D^+ ions is maximal at $E_k = 6$ eV.

5.3.2 O_2

A slice through the 3D momentum distribution of electrons resulting from photoionization of O_2 is shown in Figure 5.5a. The corresponding electron kinetic energy spectrum is shown in Figure 5.5b. The spectrum resulting from an integration ±5° perpendicular to the laser polarization is shown in red and shows additional peaks, that were not resolved in the fully angle-integrated blue spectrum. The electron kinetic energy spectrum was calibrated by associating the highest kinetic energy peak with ionization to the X $^2\Pi_g$ ground state and using the previously determined photon energy of 45.55 eV. The kinetic energies of the various peaks and the corresponding experimental binding energies are summarized in Table 5.1. The angular distribution of the data are fitted to Legendre polynomials P_l to extract the β-parameter:

$$P_{3D}(p_{3D}, \cos\theta_{3D}) = 2\pi \sum_l a_l \, P_l(\cos\theta_{3D}) \qquad (5.2)$$

P_{3D} is the 3D momentum distribution. β is the ratio of the second order and zeroth order Legendre polynomial coefficients ($\beta = a_2/a_0$). The β parameters are summarized in Table 5.1. The states marked with a ▲ were only resolved in an integration perpendicular to the laser polarization and the fit included therefore neighboring states as well.

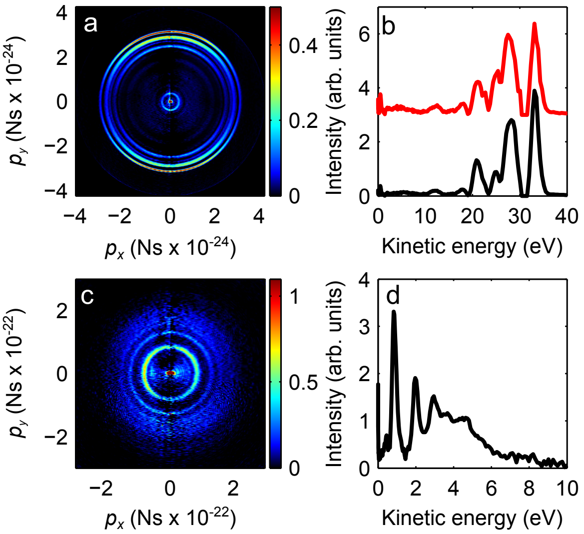

Figure 5.5: a) A slice ($p_z = 0$) through the 3D momentum distribution for the electrons resulting from ionization of O_2. b) The corresponding electron kinetic energy spectrum, from an angular integration of the momentum distribution. The electron kinetic energy spectrum resulting from an integration ±5° perpendicular to the laser polarization axis is shown in red and shows additional peaks not resolved in the fully angle-integrated blue spectrum. c) A slice ($p_z = 0$) through the 3D momentum distribution for O^+ ions resulting from ionization of O_2. d) The corresponding O^+ ion kinetic energy spectrum.

A slice through the O^+ 3D momentum distribution is shown in Figure 5.5c. The corresponding ion kinetic energy spectrum is shown in Figure 5.5d. An intense peak is present for zero kinetic energy and corresponds to the detection of O_2^{2+} ions, which did not gain a recoil velocity and/or to the formation of zero kinetic energy O^+ ions. Furthermore, various sharp peaks are present in the spectrum at 0.44, 0.86, 1.99 and 2.94 eV. For kinetic energies up to ∼ 7 eV, a broad distribution is present.

In what follows, a discussion of the peaks in the electron kinetic energy spectrum is presented. The experimental binding energies are compared to values from literature and a tentative assignment of the peaks is performed. Possible dissociative ionization pathways of these states will be discussed in connection with the experimental ion kinetic energy spectrum.

Our data show good correspondence with the electron kinetic energy spectrum measured by Baltzer *et al.* [181], using He IIα radiation at 40.8 eV. Below the peak at 33.24 eV, that was already assigned to the X $^2\Pi_g$ ground state, a relative intense peak is present for a kinetic energy of ∼ 29 eV. From Baltzer *et al.* [181] and Ellis *et al.* [186] it is known that the a $^4\Pi_u$, A $^2\Pi_u$ and b $^4\Sigma_g^-$ states contribute in this binding energy range. Predissociation of the b $^4\Sigma_g^-$ state to the first dissociation limit at 18.73 eV [182] can form zero kinetic O^+ fragments.

Table 5.1: Kinetic energies and binding energies of the peaks in the O_2 electron kinetic energy spectrum. The angular distributions were fitted to extract the β parameter. For the states marked with a ▲, the fit included both states. The fragmentation pathways to the dissociation limits L_D are cited to illustrate the dissociative ionization process. The dissociation limits L_D and the dissociation products are separately shown in Table 5.4, in the appendix at the end of this chapter.

	Exp. E_k (eV)	Exp. E_B (eV)	β	State	Vertical E_B (eV)	Fragmentation pathway	O^+ E_k (eV)
1	33.24 ± 0.17	12.31	1.3	X $^2\Pi_\mathrm{g}$	12.307 [181]	-	
2	29.99 ± 0.17	15.56	1.1▲	a $^4\Pi_\mathrm{u}$	16.703 [181]	-	
3	27.84 ± 0.17	17.71	1.1▲	A $^2\Pi_\mathrm{u}$	17.643 [181]	-	
				b $^4\Sigma_\mathrm{g}^-$	18.171 [181]	L_1 [182]	~ 0
4	25.18 ± 0.17	20.37	0.3	B $^2\Sigma_\mathrm{g}^-$	20.35 [181]	L_1 [182]	~ 0.81
5	22.60 ± 0.17	22.95	1.1▲	3 $^2\Pi_\mathrm{u}$	23.9 [181]	-	
6	21.15 ± 0.17	24.40	1.1▲	c $^4\Sigma_\mathrm{u}$	24.564 [181]	L_1 [182, 183]	~ 2.92
						L_2 [182, 183]	~ 1.93
						L_5 [184]	~ 0.42
7	17.90 ± 0.17	27.65	-	C $^2\Sigma_\mathrm{u}^-$	27.3 [181]	-	
8	12.15 ± 0.17	33.40	-	$^2\Pi_\mathrm{u}$, 3 $^2\Sigma_\mathrm{u}$	33.3	L_3 [185]	~ 5-6
						L_5 [185]	~ 4
						L_6 [185]	~ 4
9	0.53 ± 0.17		-	-	-	-	-

The peak at E_k = 25.18 eV, in the electron kinetic energy spectrum, is assigned to the B $^2\Sigma_\mathrm{g}^-$ state. Predissociation of this state to the first dissociation limit at 18.73 eV was reported in [182] and forms O^+ ions with a kinetic energy of 0.8 eV. This is in good agreement with the first intense peak in the ion kinetic energy spectrum.

In an integration perpendicular to the laser polarization axis, a small peak at E_k = 22.60 eV is observed. The binding energy of this state is close to the one of the 3 $^2\Pi_\mathrm{u}$ state [181][186]. The deviation of our experimental value from the literature value, is attributed to the finite resolution of our spectrometer, preventing us to separate the contributions of the c $^4\Sigma_\mathrm{u}^-$ and the 3 $^2\Pi_\mathrm{u}$ state.

The peak at E_k = 21.15 eV is assigned to the c $^4\Sigma_\mathrm{u}^-$ state. This state predissociates to the first, second and fifth dissociation limit (i.e L_1, L_2 and L_5 in Table 5.1), forming fragments with a kinetic energy of 3, 2 and 0.4 eV respectively (see [182, 183] and references therein). This is in excellent agreement with the peaks at E_k = 0.44, 1.99 and 2.94 eV in our ion kinetic energy spectrum.

The broad peak at E_k = 12.15 eV was assigned by Baltzer *et al.* [181] to the $^2\Pi_\mathrm{u}$ state. Based on the theoretical threshold photoelectron spectrum, Hikosaka *et al.* [185] attributes this peak also to the 3 $^2\Sigma_\mathrm{u}^-$ and the 5 $^2\Sigma_\mathrm{g}^-$ states. Threshold photoelectron-photoion coincidence studies (TPEPICO) [185] showed that dissociation of the $^2\Pi_\mathrm{u}$, 3 $^2\Sigma_\mathrm{u}$ and 5 $^2\Sigma_\mathrm{g}$ states to the third, fifth and sixth dissociation limit (i.e L_3, L_5 and L_6 in Table 5.1) produced ions with a kinetic energy of respectively 5-6 eV (L_3) and 4 eV (L_5 and L_6). The higher kinetic energy ions in our photoion spectrum may be due to dissociation from these states.

For binding energies higher than 36.13 eV [187, 188], single photon double ionization events should be taken into account. For the kinetic energy range < 9 eV however, the intensity is low and only one sharp ring at 0.5 eV is observed. It was found by Bolognesi *et al.* [189] that the dominant mechanism for single-photon double ionization is fast dissociation of a singly charged ion, followed by autoionization.

- $O_2 + \mathrm{hv} \rightarrow O_2^{*+} + e_1^-$
- $O_2^{*+} \rightarrow O^+ + O^*$
- $O^* \rightarrow O^+ + e_2^-$

The first electron (e_1^-) has a near zero kinetic energy, while autoionization of the excited O* leads to the formation of electrons (e_2^-) with $E_k \sim 0.4$-2 eV [190].

5.3.3 N_2

In Figure 5.6a a slice through the 3D momentum distribution of electrons resulting from photoionization of N_2 is shown. The corresponding electron kinetic energy spectrum is shown in Figure 5.6b. The kinetic energies of the various peaks and the corresponding binding energies are summarized in Table 5.2. The electron kinetic energy spectrum was calibrated by associating the highest kinetic energy peak with ionization to the $\mathrm{X}\,^2\Sigma_g^+$ ground state and using the previously determined photon energy of 45.55 eV. The angular distributions were, when possible, fitted to extract the β parameter (formula 5.2). The β parameters are summarized in Table 5.2 as well. Based on the experimentally determined binding energies, a tentative assignment of the states can be performed and is given in Table 5.2. The latter also contains state assignments and binding energies found in previous experiments [191, 192] and calculations [193]. Fragmentation pathways that are known from literature, are summarized in Table 5.2, together with the expected N^+ kinetic energy.

A slice through the N^+ 3D momentum distribution is shown in Figure 5.6c. The corresponding ion kinetic energy spectrum is shown in Figure 5.6d. In the ion kinetic energy spectrum, three main contributions can be distinguished. First, an intense peak at zero kinetic energy, corresponding to the intensity in the center of the image, is attributed to the detection of stable N_2^{2+} ions which did not gain a recoil velocity. Second, a peak around 1.38 eV is associated with the formation of N^+ ions via dissociative ionization channels ($N_2 \longrightarrow N^+ + N$). Third, a broad asymmetric peak is present around 4 eV and is attributed to dissociative ionization and Coulomb explosion channels. A discussion of the various states and their fragmentation pathways and products is presented.

The peak at $E_k \sim 29$ eV, in the electron kinetic energy spectrum, corresponds to ionization to the three lowest states $\mathrm{X}\,^2\Sigma_g^+$, $\mathrm{A}\,^2\Pi_u$ and $\mathrm{B}\,^2\Sigma_u^+$. Branching ratios for these three states were already measured in the late seventies by Plummer *et al.* [191] and Hammet *et al.* [194] for a range of photon energies. For a photon energy of 45 eV the ratios were approximately 33, 55 and 12% for the $\mathrm{X}\,^2\Sigma_g^+$, $\mathrm{A}\,^2\Pi_u$ and $\mathrm{B}\,^2\Sigma_u^+$ states respectively. In our spectrum, the relative peak intensities of these states are 34, 52 and 14 %, in good agreement with the previous results [191, 194].

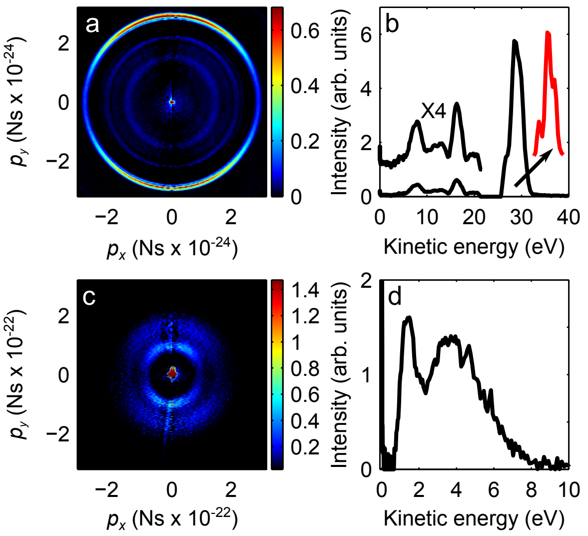

Figure 5.6: a) A slice (p_z= 0) through the 3D momentum distribution for electrons resulting from ionization of N_2. b) The corresponding electron kinetic energy spectrum, resulting from an angular integration. The inset in red, is a result from an integration ± 10° along the laser polarization axis and shows that the highest intensity peak actually consists of three peaks. The lower kinetic energy region was scaled by a factor to show the peaks more clearly. c) A slice (p_z= 0) through the N^+ 3D momentum distribution. d) The corresponding N^+ kinetic energy spectrum, resulting from an angular integration of the momentum distribution.

For a kinetic energy of 19.18-20.45 eV three small peaks can be distinguished in the electron kinetic energy spectrum. In this energy range Baltzer *et al.* [192] reported the presence of three states of which two states ($2\,{}^2\Pi_g$ and $C\,{}^2\Sigma_u^+$ states) exhibited vibrational progressions. In the electron kinetic energy spectrum, a relatively intense peak can be identified at E_k = 16.38 eV and corresponds to the $F\,{}^2\Sigma_g^+$ state. Fragmentation to the second and third dissociation limit (i.e L_2 and L_3 in Table 5.2) has been reported in [193, 195]. In the N^+ kinetic energy spectrum a broad peak is present at 1.35 eV and is predominantly attributed to dissociation of the $F\,{}^2\Sigma_g^+$ state to the former (i.e L_2) dissociation limit.

A relatively weak contribution is present for E_k = 11-14 eV in the electron kinetic energy spectrum. Fragments produced from dissociation of this state, are expected to have a kinetic energy of 2.66-3.16 eV.

The last peak in the electron kinetic energy spectrum (E_k = 7.71 eV) is associated with transitions to the $5\ {}^2\Sigma_g^+$ and $6\ {}^2\Sigma_g^+$ states [193]. The potential energy curves of these states correlate adiabatically to the sixth dissociation limit (i.e L_6 in Table 5.2) at 28.757 eV [193]. Fragmentation via this pathway produces fragments with E_k = 4.7 eV. Non-adiabatic transitions to the third and seventh dissociation limits (L_3 and L_7 in Table 5.2) were identified by Aoto *et al.* [193] and produce fragments with a kinetic energy of 5.7 and 4.1 eV respectively. All these features

Table 5.2: Kinetic energies and binding energies of the peaks in the N_2 electron kinetic energy spectrum. The angular distributions were fitted to extract the β parameter. For the states marked with a ▲, the fit included both states. The N_2^+ states can dissociate to the dissociation limits L_D, which are separately shown in Table 5.5 in the appendix together with the dissociation products.

	Exp. E_k (eV)	Exp. E_B (eV)	β	State	Vertical E_B (eV)	Fragmentation pathway	N^+ E_k (eV)
1	29.95 ± 0.17	15.60	1.1	X $^2\Sigma_\mathrm{g}^+$	15.6 [191]	-	
2	28.65 ± 0.17	16.90	1.3	A $^2\Pi_\mathrm{u}$	17.0 [191]	-	
3	26.67 ± 0.17	18.88	1.4	B $^2\Sigma_\mathrm{u}^+$	18.8 [191]	-	
4	20.45 ± 0.17	25.10	-	2 $^2\Pi_\mathrm{g}$	24.788 [192]	L_1 [195]	∼ 0.27
5	19.74 ± 0.17	25.81	-	C $^2\Sigma_\mathrm{u}^+$	25.51 [192]	L_1 [195]	∼ 0.61
						L_2 [195]	∼ 0.09
						L_3 [192, 196]	∼ 0.13
6	19.18 ± 0.17	26.37	-	D $^2\Pi_\mathrm{g}$	26.0 [192]	L_1 [192]	∼ 0.85
7	16.38 ± 0.17	29.17	0.3	F $^2\Sigma_\mathrm{g}^+$	28.8 [192]	L_2 [193, 195]	∼ 1.30
						L_3 [193, 195]	∼ 1.06
8	12.94 ± 0.17	32.61	-	(E) 3 $^2\Sigma_\mathrm{u}^+$	∼32 [193]	L_3 [193, 195]	∼ 2.66
9	11.55 ± 0.17	34.00	-	(E) 3 $^2\Sigma_\mathrm{g}^+$	∼33 [193]	L_3 [193, 195]	∼ 3.16
10	7.71 ± 0.17	37.84	0.0	(H) $5^2\Sigma_\mathrm{g}^+$ /$g^2\Sigma_\mathrm{g}^+$	∼38 [193]	L_3 [193]	∼ 5.7
						L_6 [193]	∼ 4.7
						L_7 [193]	∼ 4.1

are consistent with the broad kinetic energy distribution extending from 2 to 7 eV as observed in the measurements.

In addition to dissociative ionization channels, Coulomb explosion channels also play a role for this photon energy. Coulomb explosion channels were studied by Besnard *et al.* [197] using photoion-photoion coincidence spectroscopy (PIPICO) in the range of 45-60 eV. For a photon energy of 45-46 eV, the N_2^{2+} $^1\Pi_\mathrm{u}$ (the α state) and the $^3\Sigma_\mathrm{g}^-$ (the β state) with vertical binding energies of 45.2 ±0.5 eV and 46.1 ±0.3 eV, should be considered. Dissociation to the first fragmentation threshold N^+ (^{3}P) + N^+ (^{3}P) at 38.8 eV forms N^+ ions with a kinetic energy of 3.2 ± 0.3 eV and 3.7 ± 0.2 eV. These kinetic energies fall into the most intense part of the broad asymmetric peak.

5.3.4 CO_2

A slice through the 3D momentum distribution of electrons resulting from photoionization of CO_2 is shown in Figure 5.7a. The corresponding electron kinetic energy spectrum is shown in Figure 5.7b. The photoelectron spectrum was calibrated by associating the highest kinetic energy peak with ionization to the X $^2\Pi_\mathrm{g}^+$ ground state and using the previously determined photon energy of 45.55 eV. The kinetic energies of the various peaks and the corresponding binding energies are summarized in Table 5.3. Based on the experimental binding energies a tentative assignment of the states can be performed. The binding energies of the assigned states as found in previous experiments [198] are summarized in Table 5.3. The β parameters were, when possible, extracted from the data and are listed in Table 5.3 as well.

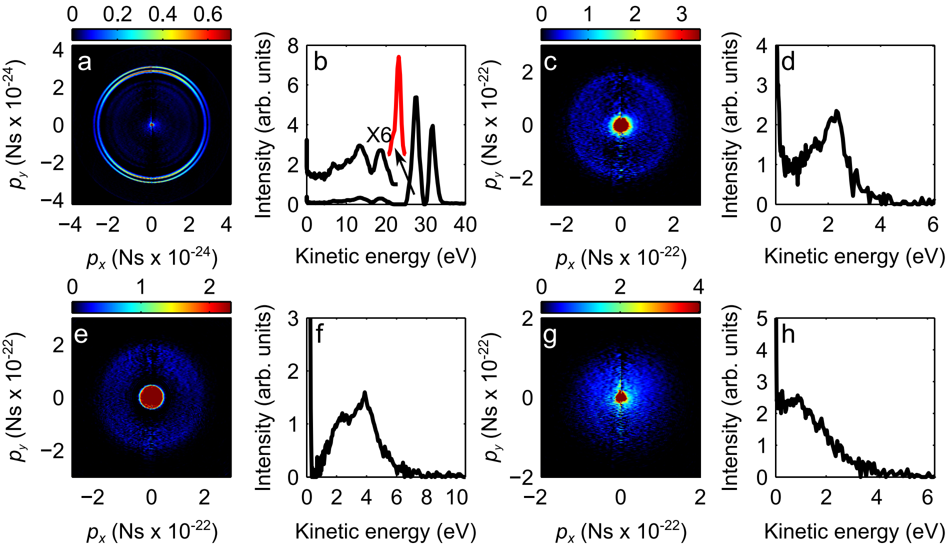

Figure 5.7: a) A slice (p_z= 0) through the 3D momentum distribution for electrons resulting from ionization of CO_2. b) The corresponding electron kinetic energy spectrum. The peak in red, resulted from an integration ± 5 ° along the laser polarization axis and shows that the second peak at E_k = 27.74 eV has an asymmetric feature at E_k = 26.31 eV, not observed in the fully angle-integrated blue spectrum. The lower kinetic energy region was scaled with a factor to show the features more clearly. c), e), g) A slice (p_z= 0) through the 3D momentum distributions of CO^+, O^+ and C^+ ions respectively. The corresponding ion kinetic energy spectra, from angular integration of the momentum distributions, are shown in d), f) and h).

A slice through the CO^+ and O^+ 3D momentum distribution is shown in Figure 5.7c and 5.7e respectively. The corresponding ion kinetic energy spectra are shown in Figure 5.7d and 5.7f. In the kinetic energy spectra of CO^+ and O^+ two main features can be distinguished, namely intense peaks at zero kinetic energy and broad asymmetric distributions at higher kinetic energies that are suggestive of multiple contributions. The distributions of CO^+ and O^+ ions seem to be momentum matched, suggesting that they may arise through a common fragmentation pathway. A slice through the 3D momentum distribution of the C^+ ions is shown in Figure 5.7g. The corresponding kinetic energy spectrum is shown in Figure 5.7h. In the spectrum an intense peak at zero kinetic energy is present, as well as a broad asymmetric distribution with an energy up to 3 eV.

In what follows a discussion of the assigned states in the electron kinetic energy spectrum and possible fragmentation pathways from the assigned states is given.

In the electron kinetic energy spectrum, the peak at E_k = 31.79 eV is associated with ionization of an essentially non-bonding electron localized on an O atom and corresponds to ionization to the $X\,^2\Pi_g^+$ state.

The next peak is observed at E_k = 27.74 eV. From previous experiments [201,

Table 5.3: Kinetic energies and binding energies of the peaks in the CO_2 electron kinetic energy spectrum. The angular distributions were fitted with a β parameter. The fragmentation pathways from literature, together with the dissociation limit are separately summarized in Table 5.6.

	Exp. E_k (eV)	Exp. E_B (eV)	β	State	Vertical E_B (eV)	Fragmentation pathway
1	31.79 ± 0.17	13.79	1.2	$\mathrm{X}\ ^2\Pi_g^+$	13.79 [198]	-
2	27.74 ± 0.17	17.81	$1.1^\blacktriangle$	$\mathrm{A}\ ^2\Pi_u^+$	17.59 [198]	-
3			$1.1^\blacktriangle$	$\mathrm{B}\ ^2\Sigma_u^+$	18.077 [198]	-
	26.31 ± 0.17	19.24	0.7	$\mathrm{C}\ ^2\Sigma_g^+$	19.36 [198]	A
						B
4	18.57 ± 0.17	26.98	0.7	MET II	26.5 ±0.5 [199]	C
				MET II'	29.0 ±0.5 [200]	D
				MET III	30.0 ±0.5 [199]	E
						F
5	13.56 ± 0.17	31.99	0.1	MET IV	32.0 ±0.5 [199]	-
6	10.35 ± 0.17	35.20	-	MET V	35.5 ±0.5 [199]	-
7	7.10 ± 0.17	38.45	-	MET VI	38.0 ±0.5 [199]	-

202] it is known that two states contribute in this binding energy region, namely the $\mathrm{A}\,^2\Pi_u^+$ and $B\,^2\Sigma_u^+$ states. Due to vibrational excitation these peaks overlap and are not resolved in our experiment.

From an integration ±5° along the laser polarization axis (shown in red in Figure 5.7b), an asymmetric feature on the left side of the second peak can be distinguished at $E_k = 26.31$ eV. This peak is associated with ionization to the $\mathrm{C}\,^2\Sigma_g^+$ state. It was found that the molecule dissociates via the pathways A and B, summarized in Table 5.6 in the appendix. Predissociation to $O^+\,(^4S_u) + CO\,(X\,^1\Sigma^+)$ at 19.07 eV [203] and to $CO^+\,(X\,^2\Sigma^+) + O\,(^3P)$ at 19.465 eV was reported to produce near zero kinetic energy O^+ ions [203, 204] and CO^+ ions [203].

For lower kinetic energies, various peaks are observed that were previously associated with multi-electron transitions (MET) [199, 205]. The binding energies of these states from Brion *et al.* [199] are listed in Table 5.3. A dissociative electroionization study by Locht *et al.* [200] identified a series of fragmentation pathways, producing C^+, O^+ and CO^+, for a couple of these MET states. The relevant pathways, indicated by C-F, are shown in Table 5.6 together with the measured kinetic energies of the ionic fragments by Locht *et al.* Our measured kinetic energies for the C^+ ion are in good agreement with these results.

The threshold for single-photon double ionization is at 37.34 ± 0.01 eV [206]. The threshold value for the formation of CO^+ and O^+ ions was found to be 39.2 ± 0.3 eV [207]. For this energy, two states should be considered: $\mathrm{X}\,^3\Sigma_g^-$ and $\mathrm{a}\,^1\Delta_g$. Fragmentation pathways of these states together with the expected kinetic energies of the fragment ions, are summarized in Table 5.7 in the appendix.

The kinetic energy distribution of the CO^+ ions in Figure 5.7d is centered around 2.3 eV. Its asymmetric shape is suggestive of multiple contributions, with a small maximum at 1.5 eV. In the O^+ ion kinetic energy spectrum (Figure 5.7f), two maxima are observed at 2.3 and 3.7 eV. Comparison with the kinetic energy values listed in Table 5.7 suggests that dissociation to the first limit, forming CO^+ ions with an energy of 2.2 eV and O^+ ions with an energy of 3.9 eV is an important contribution. Our kinetic energy release of 6 eV is in good agreement with the results from Curtis *et al.* [208]. In addition, dissociation to the third limit is in good agreement with the maximum at 2.3 eV in the O^+ photoion spectrum and the feature at 1.5 eV in the CO^+ photoion spectrum.

We note that, although the agreement suggested by the analysis presented above is quite good, additional electronic states exist between the 39.2 eV threshold and our 45.55 eV photon energy, which could have contributed to our experiment. Furthermore the importance of contribution from dissociative ionization in the relative kinetic energy range cannot be ruled out.

5.4 Discussion

In this paper we have reported on experiments where the velocity map imaging technique was for the first time implemented at the free electron laser in Hamburg. We have imaged single-photon ionization processes of a range of small molecules (H_2, D_2, O_2, N_2 and CO_2), allowing us to test the capabilities of the velocity map imaging technique. Our results demonstrate both the strengths and weaknesses of the implemented spectrometer in combination with FLASH.

In the discussion of the results, it became evident that the resolution of our spectrometer was limiting (typically 1-2%), compared to i.e time-of-flight spectrometers or electrostatic analyzers. However, while these techniques provide superior energy resolution over the velocity map imaging technique, they lack angular resolution. Previous high intensity IR experiments have shown that the angular distribution contains a large part of the information about non-linear ionization processes and are essential in the interpretation of high-intensity experiments.

The interpretation of dissociative ionization processes can be complicated when several states contribute in the same kinetic energy range. Indeed definite fragmentation pathways could not always be identified. A commonly used technique to study dissociation processes is COLTRIMS. While providing coincidence, this technique is limited to low count rates, making it a challenging technique in combination with the low repetition rate of FLASH. The velocity map imaging technique allows for high count rates and thus makes optimal use of the high brilliance and intensity of FLASH.

A type of experiments that makes use of the high fluence *and* the time-resolution of the FLASH are pump-probe experiments. These experiments provide a wealth of information about the dynamics of photoexcitation processes, but require that measurements at a given pump-probe delay are completed in a short time. For example, FLASH can be used to dissociatively ionize molecules that have been dynamically aligned by an intense femtosecond IR laser pulse. By synchronizing FLASH with the time of an alignment revival, angle-resolved photoelectron momentum distributions can be obtained from aligned molecules. These distributions provide information about the photoemission process in the molecular frame, not measured before due to the intensity of the current XUV sources. Dynamic alignment has been successfully probed by velocity map imaging in the past [64]. Velocity map imaging is thus a promising technique for studying dynamic alignment, as well as (dissociative) ionization processes at FLASH, providing accessibility to high count rates and angular resolution. The first promising results have already been obtained with the aforementioned VMIs setup, where CO_2 molecules were dynamically aligned in the laboratory frame and probed by FLASH [65] and meanwhile have been extended to three-pulse experiments on Br_2 molecules.

5.5 Appendix

Table 5.4: Dissociation limits L_D of O_2^+, their potential energies E_D and the fragmentation products [156].

L_D	Products			E_D (eV)
L_1	O (^3P)	+	O^+ (^4S)	18.73
L_2	O (^1D)	+	O^+ (^4S)	20.70
L_3	O (^3P)	+	O^+ (^2D)	22.06
L_4	O (^1S)	+	O^+ (^4S)	22.92
L_5	O (^3P)	+	O^+ (^2P)	23.75
L_6	O (^1D)	+	O^+ (^2D)	24.02
L_7	O (^1D)	+	O^+ (^2P)	25.72
L_8	O (^1S)	+	O^+ (^2D)	26.25
L_9	O (^5S)	+	O^+ (^4S)	27.88
L_{10}	O (^1S)	+	O^+ (^2P)	27.94

Table 5.5: Dissociation limits L_D of N_2^+, their dissociation energies E_D and the fragmentation products [193].

L_D	Products			E_D(eV)
L_1	N (^4S)	+	N^+ (^3P)	20.293
L_2	N (^4S)	+	N^+ (^1D)	26.192
L_3	N (^2D)	+	N^+ (^3P)	26.676
L_4	N (^2P)	+	N^+ (^3P)	27.869
L_5	N (^4S)	+	N^+ (^1S)	28.345
L_6	N (^2D)	+	N^+ (^1D)	28.575
L_7	N (^2P)	+	N^+ (^1D)	29.768
L_8	N (^2D)	+	N^+ (^1S)	30.728
L_9	N (^2P)	+	N^+ (^1S)	31.921

Table 5.6: Fragmentation pathways for CO_2 with dissociation limits E_D for pathways A and B. The dissociation from pathways C-F is due to fragmentation from the MET states.

Label	Products			E_D (eV)	CO^+, O^+, C^+ E_k(eV)
A	O^+ (^4S_u)	+	CO ($X^1\Sigma^+$) [203, 204]	19.07	$O^+ \sim$ 0-0.5
B	O^+ (^3P)	+	CO ($X^2\Sigma^+$) [203]	19.47	$CO^+ \sim 0$
C	C^+ (^2P)	+	O_2 ($b^1\Sigma_u^+$) [200]		$C^+ \sim$ 0.6-0.8
D	C^+ (^4P)	+	O_2 ($a^1\Delta_g$) [200]		$C^+ \sim$ 0-0.5
E	C^+ (^2P)	+	O_2 ($a^1\Delta_g$) [200]		$C^+ \sim$ 1.6-3.6
F	C^+ (^4P)	+	O_2 ($X^3\Sigma_g^-$) [200]		$C^+ \sim$ 2.4-3.6

Table 5.7: Dissociation limits E_D and expected kinetic energies of the CO^+ and O^+ fragments for dissociation from the threshold of 39.2 eV. The range given for the third dissociation limit is due to vibrational excitation of the CO^+ in the $A^2\Pi_u$ state [207].

Products			E_D (eV)	CO^+ E_k (eV)	O^+ E_k (eV)
O^+ (^4S_u)	+	CO^+ ($X^2\Sigma_g^+$)	33.09 [207]	2.2	3.9
O^+ (^2D_u)	+	CO^+ ($X^2\Sigma_g^+$)	36.41 [207]	1	1.8
O^+ (^4S_u)	+	CO^+ ($A^2\Pi_u$)	35.51-36.93 [207]	0.8-1.3	1.5-2.3

6

Electron localization in recollision excitation induced dissociation of H_2^+ and D_2^+ molecules

H_2 and D_2 molecules are dissociatively ionized by waveform-controlled few-cycle laser pulses. The formation of fragments with E_k=3-9 eV is attributed to dissociation induced by recollision excitation. An asymmetry in the fragment ion ejection, indicative of electron localization is observed and shows a dependence on the fragment kinetic energy, previously not observed in [34]. Interestingly, the carrier-envelope-phase dependence of this asymmetry shows a π-phase difference between H_2 and D_2. The experimental results are an ideal test ground to investigate the role of the recollision electron dynamics in electron localization during molecular dissociative ionization.

A semiclassical approximation is presented that captures the electron-electron interaction, responsible for recollision excitation, in an effective optical field. This field is obtained by using classical electron trajectories in a laser field. The simulations indicate the importance of multiple returns of the electron in the recollision excitation. This is in contrast to numerical simulations [209, 210] of electron localization in dissociative ionization of D_2, where only the first return is considered.

6.1 Introduction

The dynamics of atoms and molecules in strong laser fields has led to the observation and the understanding of a variety of physical phenomena. Control of the waveform of few-cycle laser pulses [211] was a major step forward, leading to the direct measurement of light pulses [45] and control of electron motion in the continuum [66]. A further advance was the first demonstration of the control of electron motion in molecular dissociation of D_2 [34] and motivated a series of theoretical [209, 210] and experimental studies [50, 212], including studies on H_2 [213]. A crucial element in the pioneering experiment in [34] is excitation of the molecular ion, by recollision of the continuum electron, leading to the molecular dissociation.

Recollision electron dynamics is an important phenomenon in strong-field laser physics. As described in Chapter 1, the laser-mediated electron interaction with the parent ion leads to a variety of phenomena, like above-threshold-ionization (ATI)[10], non-sequential double-ionization (NSDI) [15] and high-harmonic generation (HHG), which is the basis for the generation of attosecond pulses [8].

The recollision electron can also be used as a probe, which constitutes a very active area of research. High-harmonic emission from recombining electrons contains information about the structure and dynamics of the system under investigation. Key results include the tomographic reconstruction of the highest-occupied orbitals of N_2 [128], the measurement of multi-electron dynamics in CO_2 [153] and the measurement of the internuclear distance of dissociating Br_2 molecules [214]. This route towards imaging molecular dynamics via in-situ electrons promises sub-femtosecond time-resolution and angstrom spatial resolution.

The sensitivity of molecular dynamics to the recollision electron dynamics is presented in [215]. The molecular motion of a H_2^+ vibrational wavepacket is probed by bunches of electrons returning to the ion at certain time intervals. The recollision electron excites the molecular ion to a dissociative state and maps the vibrational motion in the ground-state to a kinetic energy distribution.

In the current experiment results, electron localization in molecular dissociative ionization of D_2 and H_2 is measured. During the dissociation of the H_2^+ and D_2^+ the remaining electron localizes on one of the protons. The electron could be steered towards the 'left' or 'right' proton by changing the carrier-envelope-phase (CEP) of the few-cycle laser pulse. As a result an asymmetry in the ejection of H^+ or D^+ fragment ions is observed as a function of CEP. The formation of a coherent superposition of the gerade $1s\sigma_g$ and ungerade $2p\sigma_u$ states in the molecular ion by the IR laser field is the responsible mechanism for localizing the electron on the left- or right-ion.

An asymmetry in the D^+ ejection was previously observed in [34]. In contrast with the results in [34], the asymmetry measured in the current experiment shows a dependence on the kinetic energy. In addition a π phase-shift of the CEP-dependence is observed between H_2 and D_2. The discrepancy between the experimental results needs to be sought in the slightly longer pulse duration and lower intensity of the laser pulse that was used in the current experiment.

The comparison between H_2 and D_2 and the sensitive dependence of the kinetic energy dependence of the asymmetry on the time of excitation of the molecular ion, provide an ideal testing ground to gain a better understanding of the role of the recollision electron dynamics in the electron localization during dissociative ionization and motivates the development of a semiclassical model of recollision excitation. The chapter is organized as follows: the experimental data are presented in paragraph 6.2. The semi-classical model and numerical methods are explained in paragraph 6.3. The results of the numerical simulations are presented in paragraph 6.4 and compared to the experimental data.

6.2 Experimental results

6.2.1 Experimental setup

The linearly polarized output pulses from a 1 kHz CEP-controlled Ti:Sapphire laser system (25 fs, 0.7 mJ), are spectrally broadened by self-phase modulation in a 60-cm long tapered hollow fiber [36] filled with argon and compressed to $\approx$ 6-7 fs pulses using ultra-broadband chirped mirrors. The IR pulses are focused with a spherical mirror into a velocity-map imaging spectrometer (VMIS) with an effusive gas jet integrated into the repeller electrode [120]. H^+ and D^+ ions resulting from disso-

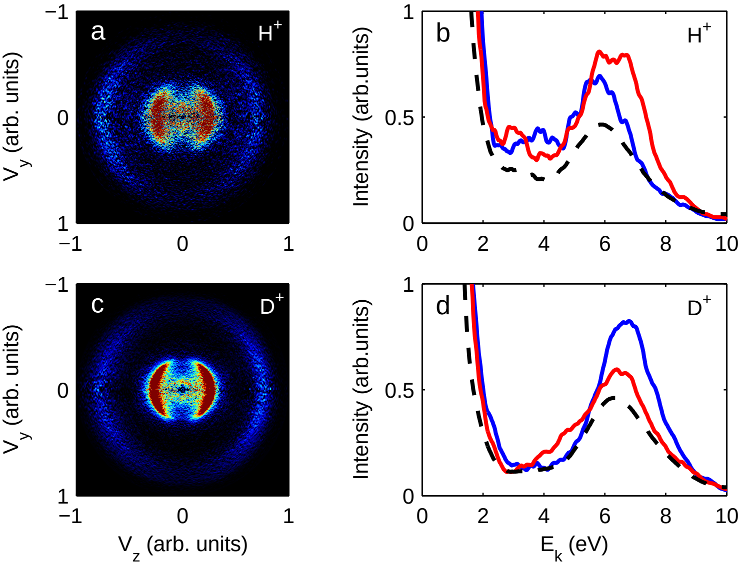

Figure 6.1: Cut through the 3D momentum distribution for a) H^+ and c) D^+ ions formed by dissociative ionization of H_2 and D_2 by the IR pulse. The momentum distributions are measured for one particular ϕ. Photoion spectra for b) H^+ and d) D^+, resulting from a full angular integration and averaged over ϕ are shown in black dotted lines. Photoion spectra for ions ejected 'left' and 'right' along the laser polarization are shown in red and blue solid lines. These spectra were measured at one particular ϕ and are the result from a partial integration along the laser polarization. The photoion spectra are smoothed by a moving average method, i.e. each element is averaged with N neighboring elements.

ciative ionization of H_2 and D_2 molecules by the IR pulses are projected onto a MCP+phosphor screen detector. From the two-dimensional ion images, acquired using a low-noise CCD camera, the three-dimensional momentum distributions are retrieved using an Abel inversion [119]. The angular resolved momentum distributions of the H^+ and D^+ ions are recorded as a function of the CEP ϕ, in steps of $\Delta\phi = \frac{\pi}{8}$. The experimental results of H_2 and D_2 are measured with identical ϕ, allowing for a direct comparison between H_2 and D_2.

6.2.2 Dissociative ionization of H_2 and D_2 by few-cycle IR pulses

A cut through the retrieved three-dimensional (3D) momentum distributions of H^+ and D^+ ions, resulting from dissociative ionization by the CEP-controlled IR pulses are respectively shown in figure 6.1a,c. The momentum distributions are shown for one particular ϕ. The laser polarization is along the z-axis.

Photoion spectra for H^+ and D^+, resulting from a full angular integration of the

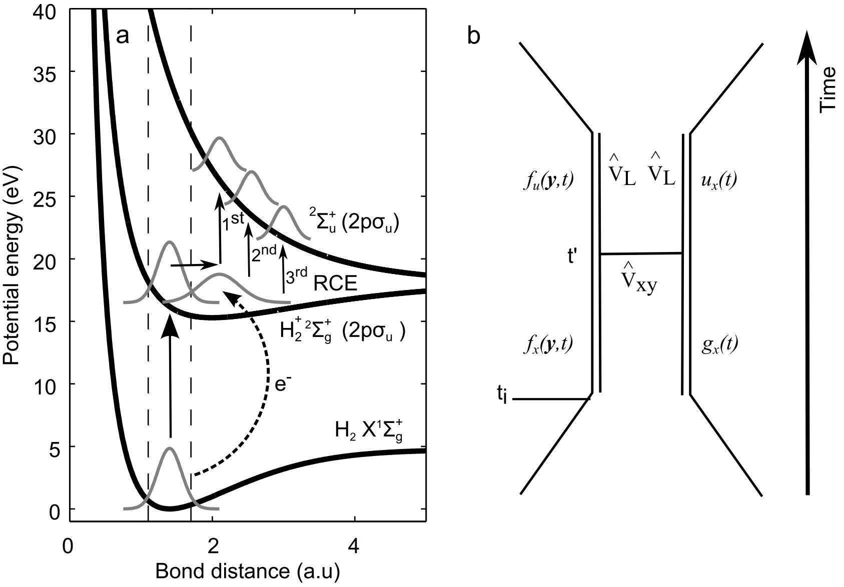

Figure 6.2: Simplified potential energy diagram for field-free H_2 and H_2^+, including only the ground state of the neutral $(^1\Sigma_g^+)$ and ion $(1s\sigma_g^+)$ and the first excited state $(^2p\sigma_u^+)$ of the ion. Recollision excitation (RCE) can excite the molecular ion in the ground state to the excited state, by the 1^{st},2^{nd} or 3^{rd} recollision of the continuum electron. b) Feynman diagram for RCE. Ionization at time t_i creates a molecular ion in the ground state $g(\mathbf{x}, t)$ and a correlated electron wavepacket $f_g(\mathbf{y}, t)$. $\mathbf{x}$ and $\mathbf{y}$ respectively are the coordinates of the bound and active continuum electron. Recollision at time t' excites the ion to the $u(\mathbf{x}, t)$ state with a correlated $f_u(\mathbf{y}, t)$ electron wavepacket.

momentum distributions, are shown in black dotted lines in figure 6.1 b and 6.1d. The photoion spectra are averaged over the CEP. For both the H^+ and D^+ ions, a strong contribution at low kinetic energies ($\leq$ 1 eV) is observed along the laser polarization. A weaker contribution is observed at higher kinetic energies ($\sim$ 7 eV). A simplified potential energy diagram of H_2 is shown in figure 6.2a. The potential energy curves of the ground-state of the neutral molecule $(^1\Sigma_g^+)$ and the ground state $1s\sigma_g$ and the first excited state $2p\sigma_u$ of the molecular ion are shown.
Fragments with a low kinetic energy ($\leq$ 1 eV) are most likely formed by strong-field ionization of neutral H_2, D_2 molecules to the $1s\sigma_g$ ground-state of H_2^+, D_2^+, followed by dissociation via a process called bond-softening [39]. The potential energy curves are modified in the presence of the laser field. In these field-dressed potential energy curves the potential energy barrier for the bound molecular ion is lowered resulting in a strong enhancement of the dissociation.
A weaker contribution between E_k = 4-10 eV is observed and several dissociation mechanisms can be considered. Recollision excitation by the continuum electron and ionization followed by laser excitation can both excite the molecular ion to the excited dissociative $2p\sigma_u$ state, forming $H^+ + H$ and $D^+ + D$ with $E_k \geq 3$ eV. The

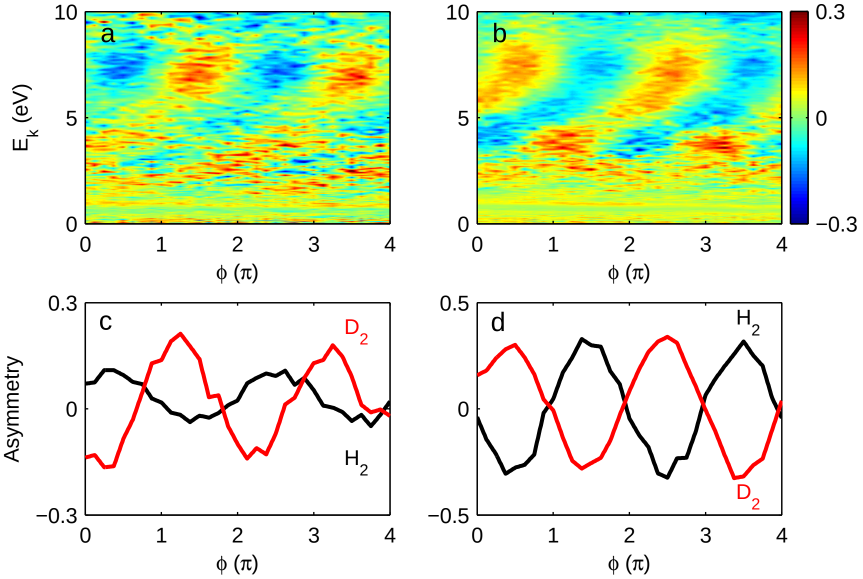

Figure 6.3: Asymmetry as a function of kinetic energy E_k and ϕ for a) H^+ and b) D^+ ions. There is a π phase-difference of the ϕ-dependence between H^+ and D^+ and this is illustrated in an energy integration of $A(E_k, \phi)$ for c) E_k = 3-5 eV and d) E_k = 5-9 eV.

recollision excitation is illustrated in Figure 6.2a. Ionization of the neutral molecule by the intense IR laser pulse forms H_2^+ and D_2^+ molecular ions in the $1s\sigma_g$ ground state. Subsequent recollisions of the continuum electron with the parent ion can excite it to the dissociative $2p\sigma_u$ state.

6.2.3 Electron localization in dissociative ionization of H_2 and D_2

In the cut through the 3D momentum distributions (Figure 6.1 a,c), an asymmetry in the number of fragment ions dissociating along the laser polarization to the 'left' and 'right' is observed in the kinetic energy region E_k = 5-10 eV. Photoion spectra for fragments ejected to the 'left' and right' ($P_{left}(E_k, \phi), P_{right}(E_k, \phi)$) are obtained from a ±30° angular integration along the polarization axis and are respectively plotted in Figure 6.1b,d in red and blue solid lines.

For the H^+ (D^+) ions, relatively more ions are ejected in the left- (right-) direction and an asymmetry in the fragment ion ejection with respect to the laser polarization is observed, indicating electron localization during the dissociation of H_2^+ and D_2^+. The ϕ-dependence of the asymmetry in the H^+, D^+ fragment ejection is defined as:

$$A(E_k, \phi) = \frac{P_{left}(E_k, \phi) - P_{right}(E_k, \phi)}{P_{left}(E_k, \phi) + P_{right}(E_k, \phi)} \tag{6.1}$$

The asymmetry A as a function of E_k and ϕ are respectively plotted for H^+ and D^+ in Figure 6.3a and 6.3b. Regions of positive and negative asymmetry are now observed to extend from the top right to the bottom left and will in the remainder of this chapter be referred as a 'tilted' kinetic energy dependence. This kinetic energy dependence is more clearly illustrated in an energy integration of $A(E_k, \phi)$ for $E_k =$ 3-5 eV and $E_k =$ 5-9 eV, respectively shown in Figure 6.3c and 6.3d. A clear π-phase difference is observed between these two kinetic energy regions. This kinetic energy dependence is in contrast to the results reported in [34], where regions of positive and negative asymmetry did not show a dependence on the kinetic energy (Figure 1.3). The reason for this discrepancy needs to be sought in the different experimental conditions. The current experimental results are measured with slightly longer laser pulses ($t_p \sim$ 6-7 fs *vs.* 5 fs FWHM) and lower laser intensities (4×10^{13} W/cm^2 *vs.* 1×10^{14} W/cm^2).

Interestingly, Figure 6.3c,d show a clear π phase-difference between H_2 (black solid line) and D_2 (red solid line) over the full kinetic energy range. The observed π-phase difference of $A(E_k, \phi)$ between H_2 and D_2 has not been observed previously.

The tilted kinetic energy dependence of $A(E_k, \phi)$ and the π-phase difference of $A(E_k, \phi)$ between H_2 and D_2 motivate numerical simulations to understand the role of the laser conditions and recollision excitation in the ϕ-dependence of electron localization.

6.3 Numerical simulations of electron localization in the dissociative ionization of H_2 and D_2

6.3.1 Motivation

Recollision excitation is the result of an electron-electron interaction and the correlated nature of the process poses a challenge for theoretical models. Two-electron quantum calculations, including all electron-electron interactions are nowadays available for H_2 [50]. The calculations presented in [50] are however limited to moderately strong laser fields, due to the demanding nature of the simulations and cannot be used to simulate the experimental results presented here. It is therefore desirable to develop lower-dimensional methods that capture the electron-electron interaction, responsible for recollision excitation.

A number of models exist [210, 215, 216] in which the continuum electron motion is classical. In these models one estimated the excitation probability to the dissociative $2p\sigma_u$-state from excitation cross-sections. In [215] the electron trajectories are classically calculated in two-dimensions in the laser field and the molecular ion field. The electron trajectories are started as a Gaussian distribution with initial conditions [217] corresponding to tunnel ionization.

In these models, the use of excitation cross-sections requires that the kinetic energy of the continuum electron is above the excitation energy of the transition. In the current experiment, this condition is not fulfilled. Therefore we need a model in which the interplay of the electron-electron interaction and the laser field is together considered and is treated on an equal footing.

A quantummechanical model of recollision excitation, including the electron correlation is presented in [209], in which the electron-electron interaction is described by an effective optical field. Numerical simulations including this effective optical field of H_2 are able to reproduce the asymmetric ejection of H^+ fragments for dissiociative ionization with waveform-controlled few-cycle pulses.
The present model combines the simplified quantum description of the electron-electron interaction and the laser field, on an equal footing, following [209]. The quantum description of the ion is essential since the recollision electron energy is significantly below the $1s\sigma_g \to 2p\sigma_u$ excitation energy. However, unlike [209], it uses the ensemble of electron trajectories for the continuum electron to generate the Coulomb interaction acting on the electron in the molecular ion. This approach allows one to develop an intuitive understanding of the role of different recolliding electron trajectories in inducing the localization of the bound electron. The model calculates the effective 'correlation' acting on the bound electron and captures it into an effective field, which is used in simulations of electron localization during the dissociative ionization of H_2 and D_2. The time-dependent Schrödinger equation (TDSE) is solved for H_2^+ and D_2^+ in the presence of a few-cycle pulse and the effective field. The solution of the TDSE yields fragment ion spectra for ejection 'left' and 'right' with respect to the laser polarization and allows calculating the asymmetry as a function of kinetic energy.

For the interested reader, the quantum analysis to replace the electron-electron interaction by an effective field is explained in section 6.3.2, this part is described previously in [209]. The approximations that are made using classical considerations to calculate the effective field are described in section 6.3.3. The derivation finally leads to equation 6.34 and the remainder of the chapter can be comprehended when the derivation is skipped.

6.3.2 Quantum analysis

The following analysis leads to an expression for an effective interaction potential $V_{eff}(t)$ and is defined as the interaction potential responsible for excitation of the molecular ion from the $1s\sigma_g$ to the $2p\sigma_u$ state. $V_{eff}(t)$ includes the electron-electron interaction responsible for recollision excitation and the correlation of the electron wavepacket before and after recollision. The expression for an effective field $E_{eff}(t)$ is easily obtained from $V_{eff}(t)$.
The total H_2, D_2 molecular system includes two protons with two electrons x and y. The two-electron Hamiltonian $\hat{H}$ can be written as:

$$\hat{H} = \hat{H}_x^{(0)} + \hat{H}_y^{(0)} + \hat{V}_{ee} + \hat{V}_L(t) \tag{6.2}$$

$\hat{H}_x^{(0)}$ and $\hat{H}_y^{(0)}$ include the kinetic energy and the interaction of the two electrons x and y with the nuclei. The electron-electron interaction is represented by $\hat{V}_{ee}$ and the interaction of the two electrons with the laser field is described by $\hat{V}_L(t) = (\mathbf{x} + \mathbf{y}) \cdot \mathbf{E}(t)$.
$\mathbf{x}$,$\mathbf{y}$ are the vector coordinates of the two electrons. For the derivation of the effective field, the internuclear coordinate R is assumed to be frozen and is omitted in the notation for brevity. The spatial part of the two-electron wave function $\Phi(x, y, t)$ is

symmetric (i.e. spins are opposite):

$$\Phi(\mathbf{x},\mathbf{y},t) = \Psi(\mathbf{x},\mathbf{y},t) + \Psi(\mathbf{y},\mathbf{x},t) \tag{6.3}$$

The two-electron wavefunction $\Psi(\mathbf{x},y,t)$ can be written as:

$$\begin{aligned}\Psi(\mathbf{x},\mathbf{y},t) &= \Psi_{cont}(\mathbf{x},\mathbf{y},t) + \Psi_0(\mathbf{x},\mathbf{y},t)\\ \Psi_{cont}(\mathbf{x},\mathbf{y},t) &= c_g(t)g(\mathbf{x},t)f_g(\mathbf{y},t) + c_u(t)u(\mathbf{x},t)f_u(\mathbf{y},t)\end{aligned} \tag{6.4}$$

$\Psi_0(\mathbf{x},\mathbf{y},t)$ is the neutral two-electron wavefunction. $\Psi_{cont}(\mathbf{x},\mathbf{y},t)$ is the wavefunction for the $H_2^+ + e^-$ system. From here on, the x-electron is considered to be the bound and the y-electron to be the 'active' continuum electron. $g(\mathbf{x},t)$ and $u(\mathbf{x},t)$ describe the bound electron in the ground and excited quasi-static states. For reasons of brevity, $g(\mathbf{x},t)$ and $u(\mathbf{x},t)$ will be written as $g_x(t)$ and $u_x(t)$. These states are different from the field-free ground and excited states of the molecular ion, since ionization of the neutral molecule creates the ion in the presence of a strong laser field. Thus, these states must include polarization of the ion by the field. We do this using the quasi-static approximation [218], which takes into account that the laser frequency is small compared to the excitation energy of H_2^+ near the equilibrium distance of $H_2$2, which is where H_2^+ is produced by ionization. To find the quasi-static (polarized) electronic states, we diagonalize the field-free Hamiltonian in the presence of a laser field, described by E$\dot{c}$os(ωt), with time treated as a parameter. The new ground and excited states are associated with the the field-free ground and excited states $1s\sigma_g$ and $2p\sigma_u$ in Figure 6.2a. $f_g(\mathbf{y},t)$ and $f_u(\mathbf{y},t)$ describe the continuum electron, respectively correlated to the ground $g_x(t)$ and excited $u_x(t)$ quasi-static states. $c_g(t), c_u(t)$ are the corresponding amplitudes of $f_g(\mathbf{y},t), f_u(\mathbf{y},t)$, i.e. the square roots of the populations, ensuring that the complex wavepackets $f_g(\mathbf{y},t)$ and $f_u(\mathbf{y},t)$ are normalized to unity. The time-evolution of the ion, without the impact of electron-electron interaction, is given by the complex time-dependence of the $g_x(t)$ and $u_x(t)$ quasi-static states.

The time-evolution of the x- and y-electron, in the presence of a laser field and an electron-electron interaction, is captured by a Feynman diagram shown in Figure 6.2b. Strong-field ionization at time t_i creates a molecular ion in the ground state $g(\mathbf{x},t)$ with a bound electron and a correlated continuum electron wavepacket $f_g(\mathbf{y},t)$. Recollision at time t' excites the molecular ion to the excited state $u(\mathbf{x},t)$ and creates the correlated wave packet $f_u(\mathbf{y},t)$.

In the Feynman diagram, the interaction with the laser field is fully included and is described by $\hat{V}_L$. $\hat{V}_{xy}$ is the part of the electron-electron interaction $\hat{V}_{ee}$ that causes excitation of the x-electron from the $g_x(t)$ to the $u_x(t)$ state. $\hat{V}_{xy}$ is only included to the first order which is justified by the low-recollision probability, de-excitation by $\hat{V}_{xy}$ is ignored.

We will now rewrite the time-dependent Schrödinger equation in integral form. To this end, the Hamiltonian is separated in parts (so-called partitioning). The electron-electron interaction potential $\hat{V}_{ee}$ in equation 6.2, is separated in a part that causes and a part that does not cause excitation:

$$\hat{V}_{ee} = \hat{V}_{xy} + \langle g_x(t)|\, \hat{V}_{ee}(\mathbf{x},\mathbf{y})\, |g_x(t)\rangle \tag{6.5}$$

$\langle g_x(t)|\,\hat{V}_{ee}(x,y)\,|g_x(t)\rangle$ is integrated over the $\mathbf{x}$-coordinate and is thus independent of the x-electron. This part does therefore not excite the x-electron and is called the self-consistent field of the ion acting on the active y-electron.
The Hamiltonian can be written as:

$$\hat{H} = \hat{H}_x^{(0)} + \hat{H}_y^{(0)} + \hat{V}_{xy} + \langle g_x(t)|\,\hat{V}_{ee}(x,y)\,|g_x(t)\rangle + \hat{V}_L(t) \tag{6.6}$$

In the next step the Hamiltonian is partitioned into parts that concern the x and y-electron:

$$\hat{H}_x^{(+)} = \hat{H}_x^{(0)} + \mathbf{x}\cdot\mathbf{E}(t) \tag{6.7a}$$

$$\hat{H}_y^{(SC)} = \hat{H}_y^{(0)} + \mathbf{y}\cdot\mathbf{E}(t) + \langle g_x(t)|\,\hat{V}_{ee}(\mathbf{x},\mathbf{y})\,|g_x(t)\rangle \tag{6.7b}$$

$\hat{H}_y^{(SC)}$ now contains the part of the electron-electron interaction that does not excite the bound electron: $\langle g_x(t)|\,\hat{V}_{ee}(x,y)\,|g_x(t)\rangle$. Defining:

$$\hat{H}_1 = \hat{H}_x^{(+)} + \hat{H}_y^{(SC)} \tag{6.8}$$

The Hamiltonian can be separated in a part $\hat{H}_1$, that contains all the interactions of the x, y electrons and the self-consistent field and a part $\hat{V}_{xy}$ that excites the x-electron:

$$\hat{H} = \hat{H}_1 + \hat{V}_{xy} \tag{6.9}$$

The time-dependent Schrödinger equation is written in integral form [219] and yields for $c_g(t')f_g(\mathbf{y},t')g_x(t')$ at the time of recollision t':

$$c_g(t')f_g(\mathbf{y},t')|g_x(t')\rangle = -i\int_0^{t'} dt_i\, e^{-i\int_{t_i}^{t'}\hat{H}_1(\tau)\,d\tau}|g_x(t_i)\rangle\langle g_x(t_i)|\,\hat{V}_{L,y}\,|\Psi_0(t_i)\rangle \tag{6.10}$$

The wavefunction of the neutral ground-state at the time of ionization t_i is given by $\Psi_0(t_i)$. Ionization at time t_i from the neutral ground state $\Psi_0(t_i)$ to the ground quasi-static state $g_x(t_i)$ is described by $\langle g_x(t_i)|\,\hat{V}_{L,y}\,|\Psi_0(t_i)\rangle$. Subsequent time-evolution of the x and y electrons up to t' is described by $e^{-i\int_{t_i}^{t'}\hat{H}_1(\tau)\,d\tau}$.
Analogous, $c_u(t)f_u(\mathbf{y},t)u_x(t)$ created by inelastic scattering at time t', is described by:

$$\begin{aligned}
c_u(t)f_u(\mathbf{y},t)|u_x(t)\rangle \approx -\int_0^t dt_i \int_{t_i}^t dt' e^{-i\int_{t'}^{t}\hat{H}_1(\tau)\,d\tau}|u_x(t')\rangle \\
\times \langle u_x(t')|\,\hat{V}_{xy}\,e^{-i\int_{t_i}^{t'}\hat{H}_1(\tau)\,d\tau}\,|g_x(t_i)\rangle \\
\times \langle g_x(t_i)|\,\hat{V}_{L,y}\,|\Psi_0(t_i)\rangle
\end{aligned} \tag{6.11}$$

The expression includes three terms and represents the three stages in forming $c_u(t)f_u(\mathbf{y},t)u_x(t)$ at time t after recollision at time t'. The last term describes ionization from the neutral ground state $\Psi_0(t_i)$ to the ground quasi-static state $g_x(t_i)$. The second term describes the time-evolution of the ground $g_x(t_i)$ from

$t_i \rightarrow t'$ and excitation by $\hat{V}_{xy}$ to the excited quasi-static state $u_x(t')$. The first term includes time evolution of the excited quasi-static state $u_x(t')$ and the continuum electron to time t by $e^{-i\int_{t'}^{t}\hat{H}_1(\tau)\,d\tau}$. Electron-electron interaction after recollision is neglected.
Using equation 6.10, equation 6.11 can be rewritten to:

$$\begin{aligned} c_u(t) f_u(\mathbf{y},t)|u_x(t)\rangle| \approx & -i\int_0^t dt'\; e^{-i\int_{t'}^{t}\hat{H}_1(\tau)\,d\tau}|u_x(t)\rangle \\ & \times \langle u_x(t')|\,\hat{V}_{xy}\,|g_x(t')\rangle f_g(\mathbf{y},t')\,c_g(t') \end{aligned} \tag{6.12}$$

$\langle u_x(t')|\,\hat{V}_{xy}\,|g_x(t')\rangle$ describes the excitation from the $|g_x(t')\rangle \rightarrow |u_x(t')\rangle$ at time t'. Multiplication of equation 6.12 with $f_u^*(\mathbf{y},t)\langle u_x(t)|$ and backwards propagation from t to t' gives:

$$c_u(t) \approx -i\int_0^t dt'\;\langle u_x(t')|f_u^*(\mathbf{y},t')\,\hat{V}_{xy}\,f_g(\mathbf{y},t')|g_x(t')\rangle\,c_g(t') \tag{6.13}$$

In equation 6.12 excitation from the $u_x(t') \leftarrow g_x(t')$ is recognized. Recalling that $V_{eff}(x,t)$ is defined as the interaction potential that is responsible for the excitation of the molecular ion from $g_x(t') \rightarrow u_x(t')$; $V_{eff}(t)$ is written as:

$$V_{\text{eff}}(\mathbf{x},t) = \int d\mathbf{y}\; f_u^*(\mathbf{y},t)\,\hat{V}_{xy}\,f_g(\mathbf{y},t) \tag{6.14}$$

Integration over the $\mathbf{y}$-coordinate of the continuum electron gives an effective interaction potential that is dependent on $\mathbf{x}$. The effective potential is in first order given by the electron-electron correlation $\hat{V}_{xy}$, which couples the continuum electron wavepackets. Note that the expression for the effective interaction potential is derived from the correlated two-electron wavefunction and includes the phase relationship between the continuum wavepackets $f_g(\mathbf{y},t)$ and $f_u(\mathbf{y},t)$.
Multipole expansion of $\hat{V}_{xy}$ up to the dipole term, yields an expression for the effective field that can excite the bound x-electron to the excited state:

$$E_{eff}(t) = -\int d\mathbf{y}\; f_u^*(\mathbf{y},t)\,\nabla_x\hat{V}_{xy}|_{x=0}\,f_g(\mathbf{y},t) \tag{6.15}$$

Gräfe *et al.* [209] calculates the effective field by propagating the Schrödinger equation for the x and y-electrons and the internuclear distance R in one dimension. Propagation of the Schrödinger equations yields the average internuclear distance $R(t)$, which is then used to calculate the two-electron wavefunction $\Phi(x,y,t)$. The continuum part of the two-electron wavefunction is obtained by projecting out the first 4 bound states. Subsequently only the continuum part of the two-electron wave function is propagated for $t > t'$. The correlated electron wave packets $f_g(\mathbf{y},t)$, $f_u(\mathbf{y},t)$ are calculated by projecting the continuum wavefunction onto $g_x(t)$ and $u_x(t)$. The effective field can then be calculated using $f_g(y,t)$ and $f_u(y,t)$.

6.3.3 Analytical approximations

The approach followed in [209] calculates the exact $f_{g,u}(\mathbf{y},t)$ in the presence of the laser field and nuclear dynamics. This method is however numerically demanding and does not provide much insight into the role of the recollision dynamics in the excitation of the molecular ion and the resulting asymmetry. This motivates a semiclassical approach in which the effective field is calculated by combining the fully correlated quantum mechanical analysis with a classical description of the electron in the laser field. In doing so, approximations about the wavepackets $f_g(\mathbf{y},t), f_u(\mathbf{y},t)$ and $\hat{V}_{xy}$ need to be made [220]. In the following the approximations made will be described.

First, recalling equation 6.5, $\hat{V}_{xy} = \hat{V}_{ee} - \langle g_x(t)| \hat{V}_{ee}(\mathbf{x},\mathbf{y}) |g_x(t)\rangle$. The electrostatic electron-electron interaction is by definition written as: $\hat{V}_{ee} = \frac{1}{|\mathbf{x}-\mathbf{y}|}$. The self-consistent part is independent of the coordinate of the bound electron and will therefore not excite the bound electron and contribute to $V_{eff}(t)$. The self-consistent part is therefore neglected and $\hat{V}_{xy}$ can be described by:

$$\hat{V}_{xy} = \frac{1}{|\mathbf{x}-\mathbf{y}|} \tag{6.16}$$

Second the continuum wavepackets $f_g(\mathbf{y},t)$ and $f_u(\mathbf{y},t)$ need to be calculated and a few assumptions can be made:

- $V_{eff}(t)$ is dominantly determined by the part of the continuum wave packet that has returned to the vicinity of the core at time t'.
- Due to the low laser intensity, the maximum energy of the returning electron is below the $g_x(t) \rightarrow u_x(t)$ excitation energy and therefore we assume that all the energy of the returning electron is transferred to the core.
- The laser field completes the excitation of the molecular ion.

To simplify the notation, time t is now assumed as the moment of recollision and all the assumptions are only made about the part of the wavepacket that returns to the core. At each moment t, the effective field is calculated from the part of the wave packet that has returned. The continuum wavepackets can always be written as:

$$f_{u,g}(\mathbf{y},t) = A_{u,g}(\mathbf{y},t)e^{iS_{u,g}(\mathbf{y},t)} \tag{6.17}$$

In the WKB approximation, S is the classical action of the continuum electron and A is a pre-factor [221].

The continuum wavepacket $f_g(\mathbf{y},t)$ just before recollision is written as:

$$f_g(\mathbf{y},t-0) = \sum_{\Delta\mathbf{p}} a_{\Delta\mathbf{p}}|\mathbf{p}_c + \Delta\mathbf{p}\rangle \tag{6.18}$$

$f_g(\mathbf{y},t)$ has a mean momentum $\mathbf{p}_c$ with a spread in momentum $\Delta\mathbf{p}$. In the inelastic collision all of $\mathbf{p}_c$ is transferred to the core, leaving a wavepacket with a mean momentum $\mathbf{p}_c = 0$ and spread $\Delta\mathbf{p}$. $f_g(\mathbf{y},t-0)$ undergoes a momentum kick opposite to the direction of its motion. Directly after the collision, the continuum wavepacket is given by:

$$f_u(\mathbf{y},t+0) = \sum_{\Delta\mathbf{p}} a_{\Delta\mathbf{p}}|\Delta\mathbf{p}\rangle \tag{6.19}$$

In the absence of an external laser field, the continuum wavepacket is approximated by a spherical wave that propagates away from the core, as $\Delta\mathbf{p}$ includes all directions. However in the presence of a strong laser field, the wave packet is accelerated away from the core by the field along the direction z of the field. The wavepacket after recollision $f_u(\mathbf{y},t)$ is therefore asymmetric in coordinate space and appears on one side of the core. It is assumed that in the direction perpendicular to the laser polarization, the changes in the wavepacket are small. In the direction along the laser polarization, the wavepacket is asymmetric. To model this, the wavepacket after recollision is multiplied with a function $\Theta(\mathbf{y})$ with a sharp edge. $\Theta(\mathbf{y})$ cuts the wavepacket to ensure that the wavepacket that correlates with $u_x(t)$ appears on one side of the core. Apart from this functionality the exact shape of $\Theta(\mathbf{y})$ is not exactly known. As only the sharp edge is used in the derivation a precise definition of the exact shape is not necessary.

Using equation 6.17, the continuum wavepackets $f_g(\mathbf{y},t)$ and $f_u(\mathbf{y},t)$ are described by:

$$f_g(\mathbf{y},t) \approx A_g(\mathbf{y},t)\, e^{iS_g(\mathbf{y},t)} \tag{6.20a}$$

$$f_u(\mathbf{y},t) \approx A_g(\mathbf{y},t)\, \Theta(\mathbf{y})\, e^{iS_g(\mathbf{y},t)+i\Delta S(\mathbf{y},t)} \tag{6.20b}$$

The wavepacket after collision $f_u(\mathbf{y},t)$ is thus similar to the incoming wavepacket $f_g(\mathbf{y},t)$, multiplied with $\Theta(\mathbf{y})$. The $\Delta S(\mathbf{y},t)$ in the exponential of $f_u(\mathbf{y},t)$ indicates a change in classical action as a result of the recollision. The change in the classical action ΔS is:

$$-\frac{\partial \Delta S}{\partial t} = \Delta E(t) \tag{6.21a}$$

$$\frac{\partial \Delta S}{\partial \mathbf{y}} = \mathbf{q} \tag{6.21b}$$

$\Delta E(t)$ is the transferred energy and $\mathbf{q}$ is the transferred momentum in the inelastic collision. The effective potential (eq. 6.14) can be obtained by using the expressions for $f_g(\mathbf{y},t)$ and $f_u(\mathbf{y},t)$ in equation 6.20:

$$V_{\text{eff}}(\mathbf{x},t) = \int d\mathbf{y}\, A_g^*(\mathbf{y})\Theta(\mathbf{y})e^{-iS_g(\mathbf{y},t)-i\Delta S(\mathbf{y},t)} \frac{1}{|\mathbf{x}-\mathbf{y}|} A_g(\mathbf{y})\, e^{iS_g(\mathbf{y},t)} \tag{6.22}$$

The time- and coordinate-dependent part of ΔS can be rewritten using equation 6.21:

$$e^{-i\Delta S(\mathbf{y},t)} = e^{i\int \Delta E(t) d\tau} e^{-i\int \mathbf{q} d\mathbf{y}} = e^{i\int \Delta E(t) d\tau} e^{-i\mathbf{q}\mathbf{y}} \tag{6.23}$$

Substituting this in equation 6.22 results in:

$$V_{\text{eff}}(\mathbf{x},t) = e^{+i\int^t \Delta E(\tau)\, d\tau} \int d\mathbf{y}\, \Theta(\mathbf{y}) |A_g(\mathbf{y})|^2 \frac{1}{|\mathbf{x}-\mathbf{y}|}\, e^{-i\mathbf{q}\mathbf{y}} \tag{6.24}$$

Recalling the assumptions made earlier, namely that the transferred energy ΔE is the full electron energy and the transferred momentum $\mathbf{q}$ is the full momentum of the recolliding electron at the moment of recollision:

$$\Delta E = -E_{\text{c}}(t_r) \tag{6.25a}$$

$$\mathbf{q} = -\mathbf{p}_{\text{c}}(t_r) \tag{6.25b}$$

$E_c(t_r)$ and $\mathbf{p}_c(t_r)$ are the total energy and momentum of the electron at the moment of recollision t_r. Substituting equations 6.25 into equation 6.24 results in:

$$V_{\text{eff}}(\mathbf{x},t) = e^{-i\int^t E_c(t_r)dt_r} \int d\mathbf{y}\Theta(\mathbf{y})|A_g(\mathbf{y})|^2 \frac{1}{|\mathbf{x}-\mathbf{y}|} e^{i\mathbf{p}_c\mathbf{y}}. \tag{6.26}$$

the recollision energy $E_c(t_r)$ is integrated over the recollision time and yields the phase of the interaction. Variable substitution of $\mathbf{y} - \mathbf{x} = \mathbf{r}$ leads to $e^{i\mathbf{p}_c\mathbf{y}} = e^{i\mathbf{p}_c\mathbf{x}} e^{i\mathbf{p}_c\mathbf{r}}$ and regarding the fact that the width of the wavepacket envelope is much larger than the characteristic size x of the bound electron wavefunction, equation 6.26 can be rewritten as:

$$V_{\text{eff}}(\mathbf{x},t) = e^{-i\int^t E_c(\tau)d\tau} e^{i\mathbf{p}_c\mathbf{x}} \int d\mathbf{r}\Theta(\mathbf{r})|A_g(\mathbf{r})|^2 \frac{1}{|\mathbf{r}|} e^{i\mathbf{p}_c\mathbf{r}}. \tag{6.27}$$

The expression for V_{eff} contains the operator:

$$\hat{V}(\mathbf{x}) \propto e^{-i\int^t E_c(t_r)dt_r} e^{i\mathbf{p}_c\mathbf{x}} \tag{6.28}$$

that is responsible for the transition of the bound electron by recollision The transition operator $e^{i\mathbf{q}\mathbf{x}}$ is well-known in the Born approximation in scattering theory. The $e^{-i\int^t E_c(t_r)dt_r}$ term is the phase of the effective time-dependent interaction and reflects the energy that was transmitted to the bound ion. As opposed to plane waves which are assumed in the Born approximation, the part in the integral in equation 6.26 is added to accommodate the deviation of the incoming and outgoing wavepackets from plane waves because the shape of the outgoing wavepacket is changed by the presence of the laser field.

The transition from the ground to the excited state of the ion is dipole allowed and quadrupole forbidden and the effective field is obtained by expansion of $e^{i\mathbf{p}_c\mathbf{x}}$ up to the linear term:

$$E_{\text{eff}}(t) = ie^{-i\int^t E_c(t_r)dt_r} \mathbf{p}_c \int d\mathbf{r}\Theta(\mathbf{r})|A_g(\mathbf{r})|^2 \frac{e^{i\mathbf{p}_c\mathbf{r}}}{|\mathbf{r}|}. \tag{6.29}$$

The next step is to calculate the last integral, which is the Fourier-transform of the incoming wavepacket *density* $\Theta(\mathbf{r})|A_g(\mathbf{r})|^2$ times the Coulomb interaction $\frac{1}{|\mathbf{r}|}$. The wavepacket densities in the directions transverse and along the laser polarization are assumed to have a width ρ_0 and z_0, for which expressions are given below. The wavepacket density in the direction transverse to the laser polarization is assumed to be of Gaussian shape with width $\rho_0(t)$. In the direction along the laser polarization the wavepacket density is written as $\chi(z)$ and is at this point not defined yet. The lengths of the wavepacket in the directions along z and perpendicular ρ to the laser polarization are increasing in time, reflecting the spreading of the wavepacket. As only the *density* of the wavepacket is needed and the complicated phase structure of the wavepacket is not taken into account, the following expression for the wavepacket is used:

$$|A_g(\mathbf{r})|^2\Theta(\mathbf{r}) = \frac{1}{\pi\rho_0^2} e^{-\rho^2/\rho_0^2} |\chi(z)|^2\Theta(z) \tag{6.30}$$

The $\rho-$ part of the wavepacket is normalized. For the electron density in the transverse ρ-direction a Gaussian shape is a good approximation. The wavepacket along the laser polarization direction z is however more complicated. Using equation 6.30 the expression for the effective field becomes:

$$E_{\text{eff}}(t) = ie^{-i\int^t E_c(\tau)d\tau}\mathbf{p}_c\int_{-\infty}^{+\infty} dz\Theta(z)|\chi(z)|^2 e^{ip_c z}$$
$$\times\int_0^{\infty} 2\pi\rho d\rho\frac{1}{\pi\rho_0^2}e^{-\rho^2/\rho_0^2}\frac{1}{\sqrt{\rho^2+z^2}} \tag{6.31}$$

It can be shown [220] that the last integral over ρ can be approximated by:

$$\int_0^{\infty} 2\pi\rho d\rho\frac{1}{\pi\rho_0^2}e^{-\rho^2/\rho_0^2}\frac{1}{\sqrt{\rho^2+z^2}} \sim \frac{\sqrt{\pi}}{\sqrt{\pi z^2+\rho_0^2}} \tag{6.32}$$

The last part is to estimate the wavepacket density along the laser polarization, by definition:

$$\int_{-\infty}^{+\infty} dz|\chi(z)|^2 = 1. \tag{6.33}$$

and if the characteristic size of $\chi(z)$ is z_0, the following estimate can be made: $|\chi(z)|^2 \sim 1/z_0$. Next the integral over $e^{ip_c z}$ and $\Theta(\mathbf{r})$ is calculated by a crude estimation. Writing $p_c z$ in terms of dimensionless variables: $p_c z_0 \times \frac{z}{z_0}$ and using that $p_c z_0 \gg 1$ makes $e^{ip_c z}$ a fast oscillating function on the scale of z_0. The exponential multiplied with $\Theta(z)$, which is a function with a sharp edge, allows one to estimate the integral over $e^{ip_c z}\Theta(\mathbf{r})$ by integration by parts. It can be shown that the leading term is:

$$E_{\text{eff}}(t) \sim \frac{\mathbf{p}_c}{p_c}\,e^{-i\int^t E_c(\tau)\,d\tau}\frac{1}{z_0}\frac{\sqrt{\pi}}{\sqrt{\rho_0^2+\frac{\pi}{p_c^2}}} \tag{6.34}$$

The effective field is proportional to the phase of the time-dependent interaction: $e^{-i\int^t E_c(\tau)d\tau}$ and the inverse of the size of the wavepacket: $\frac{1}{z_0}\frac{\sqrt{\pi}}{\sqrt{\rho_0^2+\frac{\pi}{p_c^2}}}$. The term $\frac{\mathbf{p}_c}{p_c}$ indicates the direction of the field.

In the last part of this section, the sizes of the wave packet ρ_0, z_0 are calculated. These are proportional to the velocity with which the wavepackets spread. The imaginary tunneling time τ_T gives uncertainties in the velocities parallel v_z and perpendicular v_ρ to the laser field.

$$\Delta v_\rho \sim \Delta v_z \sim \frac{1}{\sqrt{\tau_T}} \tag{6.35}$$

and the sizes of the wavepacket are:

$$\rho_0 = z_0 = \Delta v_{\rho,z_0}\sqrt{(t-t_b)^2+\tau_T^2} \tag{6.36}$$

t_b is the time at which the electron is 'born' in the continuum with zero velocity. The last part is to obtain the tunneling time in the multiphoton regime from the non-adiabatic tunneling time [222]. The tunneling time depends on the Keldysh parameter γ and the time of birth, related to the phase of the laser field.

$$\phi_0 = \mathrm{arccosh}(\mathrm{S}/\sqrt{\mathrm{P}}) \tag{6.37a}$$

$$S = \sin(\omega t_b) \tag{6.37b}$$

$$P = \frac{1}{2}(1+\gamma^2+S^2-\sqrt{D}) \tag{6.37c}$$

$$D = (1+\gamma^2)^2+S^4+2S^2(\gamma^2-1) \tag{6.37d}$$

γ is the Keldysh parameter: $\gamma = \sqrt{\frac{I_p}{2U_p}}$, where I_p is the ionization potential of the target. ϕ_0 is the phase in the laser field at which the electron starts it's underbarrier motion. ϕ_0 is complex and the tunneling time is defined as the imaginary part of $\tau_T = \phi_0/\omega_0$, where ω_0 is the laser frequency.

6.3.4 Calculation of effective field

Following the derivation in the previous section, we can calculate the effective field, that excites the molecular ion, using equation 6.34. We need to find the recollision momentum $\mathbf{p}_\mathrm{c}$ and energy $E_c(t_r)$ and the sizes of the wavepacket ρ_0, z_0, as a function of time. To this end, we use a standard recollision model for a few-cycle pulse, in which the classical electron trajectories in the continuum in the presence of a laser field are calculated [176]. The general equation for the position and velocity of an electron in a laser field $E_L(t)$ is given by:

$$m\ddot{z} = m\dot{v} = eE_L(t) = eE_0 f(t)\cos(\omega_0 t + \phi) \tag{6.38}$$

where E_0 is the peak field strength, ω_0 is the carrier frequency of the laser and $f(t)$ is the $\sin^2(t)$ laser envelope with pulse duration t_p. $m = 1, e = -1$ are the electron mass and charge. The magnetic field of the laser and the electric field of the ion are not considered.

The electron trajectories are started during a full half-cycle of the laser pulse, at an initial position $z_i = 0$ and initial velocity $v_i = 0$. The initial velocity is in correspondence with tunneling theory. The position and velocity of the electron during the trajectory can be calculated by analytically solving equation 6.38.

In calculating the effective field, the following assumptions are made:

- The experimental photoion spectra do not exhibit signatures of a photon structure, indicating that nuclear wavepackets ionized during different half-cycles do not interfere.

- Each half-cycle in the laser pulse can therefore be treated separately and the effective field is calculated for trajectories started during one particular half-cycle.

- Electrons coming back to the core during a 2nd and/or 3rd return have not interacted with the ion before and have not transferred momentum or energy.

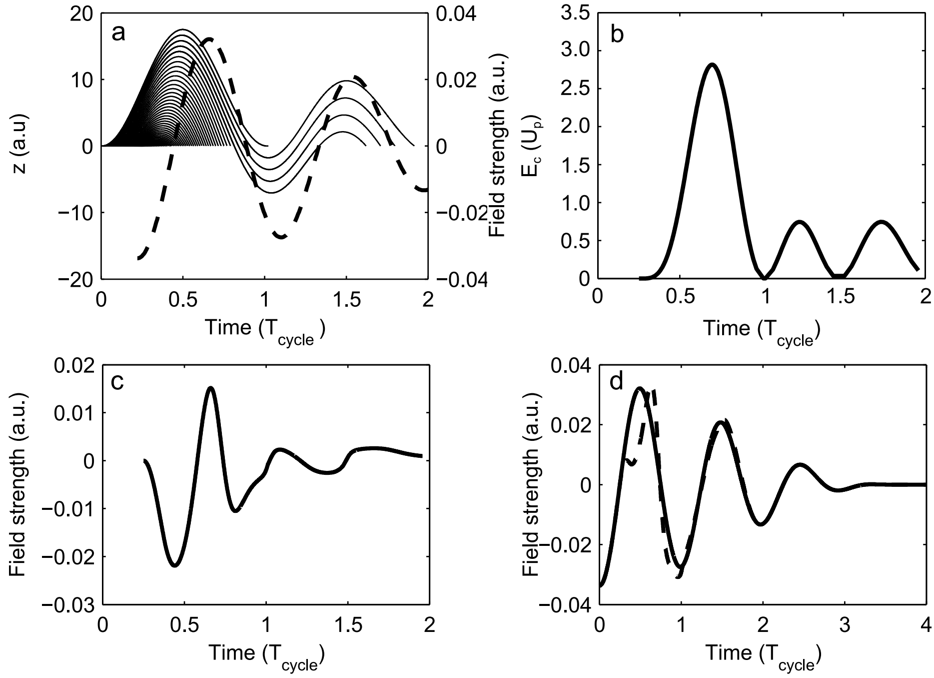

Figure 6.4: a) Classical electron trajectories (solid lines) in a few-cycle laser pulse (dotted line). The laser intensity was $I = 4 \times 10^{13}\, W/cm^2$ with $\tau_p = 7$ cycles ~ 6.4 fs FWHM. Only the trajectories of electrons that return to $z = 0$ are plotted. For clarity only a selection of the actually used trajectories is plotted. b) Recollision energy of electron as a function of the return time for all the trajectories that return to $z = 0$. The 1^{st} return has a maximum energy of $2.8\ U_p$ and the 2^{nd} and 3^{rd} return both have a maximum energy of $0.74\ U_p$. c) The effective field as calculated with equation 6.34. d) The original laser field (solid line) with the summed effective field (dotted line).

Figure 6.4 shows the result for a calculation where electron trajectories are started during a half-cycle that coincides with the maximum of the laser pulse envelope. The trajectories are plotted in Figure 6.4a, alongside with the laser field (dashed line) in which the electrons are moving. Electrons return to the core for the 1^{st} time during $t = (0 - 1)\, T_{cycle}$. Correspondingly the 2^{nd} and 3^{rd} return of the electron to the core are respectively during $t = (1.0 - 1.5)\, T_{cycle}$ and $t = (1.5 - 2)\, T_{cycle}$. Later returns are at this point not taken into account as the field-strength will have reduced significantly due to the increasing size of the wavepacket and will not significantly contribute to the $g_x \rightarrow u_x$ excitation.

The classical trajectory is sensitively dependent on the phase of the laser field at which the electron starts the trajectory in the continuum. In the absence of Coulomb potential effects, trajectories can be uniquely characterized by their time of birth and time of recollision. Only the time of births t_b, recollision time t_r, momentum $\mathbf{p}_c$

and energy E_c for electrons that return to $z = 0$ are used to construct the effective field. The recollision energy E_c is plotted for all trajectories that return to $z = 0$ as a function of the recollision time in Figure 6.4 b). The recollision energy is plotted in units of the ponderomotive potential U_p. For electron trajectories in a CW pulse, the maximum recollision energy for the 1^{st}, 2^{nd} and 3^{rd} return are respectively 3.17, 1.6 and 2.4 U_p. As opposed to the electron motion in a continuous wave (CW), the maximum recollision energy in a few-cycle pulse will depend on the half-cycle during which trajectories are started. For the trajectories plotted in Figure 6.4 b) the recollision energies for the 1^{st}, 2^{nd} and 3^{rd} return are respectively 2.8, 0.74 and 0.74 U_p and have decreased significantly due to the falling edge of the laser envelope. Recalling equation 6.34, the recollision energy of the electron is used in calculating the the phase of the effective field by integrating over the recollision energy E_c as a function of the recollision time t_r.

In the calculating the $E_{eff}(t)$, the wavepacket sizes ρ_0, z_0 are also required and are calculated by using t_b in equations 6.35, 6.36 and 6.37.

Trajectories are started during a full half-cycle of the laser field and the effective field strength needs to be weighted with a relative ionization amplitude. In the multi-photon regime, the non-adiabatic tunneling rate is used, as given in [25]:

$$\Gamma(t) \propto \exp\left(-\frac{E_0 f^2(t)}{w_0^3}\,\Phi(\gamma(t),\theta(t))\right) \tag{6.39}$$

where $\Gamma(t)$ is the ionization rate. $\Phi(\gamma(t),\theta(t))$ is [25]:

$$\begin{aligned}
\Phi(\gamma,\theta) &= (\gamma^2+\sin^2\theta+\frac{1}{2})\ln c - \frac{3\sqrt{b-a}}{2\sqrt{2}}\sin|\theta| - \frac{\sqrt{b+a}}{2\sqrt{2}}\gamma \\
a &= 1+\gamma^2-\sin^2\theta \\
b &= \sqrt{a^2+4\gamma^2\sin^2\theta} \\
c &= \sqrt{\left(\sqrt{\frac{b+a}{2}}+\gamma\right)^2+\left(\sqrt{\frac{b-a}{2}}+\sin|\theta|\right)^2}
\end{aligned} \tag{6.40}$$

where $\gamma(t) = \gamma/f(t)$ and the phase of the laser field $\theta(t) = \omega_0 t + \phi - \pi k$, where the k is chosen to let $\theta(t) \leq |\pi/2|$.

The trajectories are weighted with a relative ionization amplitude $\frac{\sqrt{\Gamma(t_b)}}{\sqrt{\Gamma(t_{HCM})}}$, where t_{HCM} corresponds to the half-cycle maximum of the laser field.

The resulting effective field is complex and is proportional to $e^{-i\phi(t)}$, where $\frac{d\phi(t)}{dt}$ is the energy of the electron at recollision. To use the effective field in the existing TDSE code, the complex conjugate of the effective field was added to it. The effective field corresponds to the co-rotating term in first order perturbation theory of a 2-level system in an oscillating electric field. The complex conjugate of the effective field is analogue to the counter-rotating term. Close to the resonance, the counter-rotating term is negligible compared to the co-rotating term. The addition of the complex conjugate of the effective field should therefore have a small effect on the excitation probability.

The resulting real effective field is shown in Figure 6.4c.
To eliminate numerical artifacts, the effective field is multiplied with a function that goes from 1 to 0 during the last $\frac{1}{4}$ laser cycle of the effective field, using a $\sin^2 t$ function. The sum of the laser field and the effective field $E_{L+E_{eff}}(t) = E_L(t) + E_{eff}(t)$ is shown in Figure 6.4d.

6.3.5 Simulations of dissociative ionization of H_2 and D_2

The time-dependent Schrödinger equation (TDSE) is solved to describe vibrations, excitations and dissociation of H_2^+ and D_2^+ molecules, after ionization at a half-cycle maximum of the laser field. The ionization step is assumed to happen instantaneously at a peak of the laser field and is modeled as a Franck-Condon projection of the vibrational ground state of H_2 and D_2 on the quasi-static ground state of H_2^+ and D_2^+.
The total molecular ion wavefunction $\Psi(x, R, t)$ is expanded in terms of the two-lowest lying field-free electronic states:

$$\Psi(x, R, t) = c_g(t)\psi_g(R, t)\phi_g(x, R) + c_u(t)\psi_u(R, t)\phi_u(x, R) \tag{6.41}$$

where R is the internuclear distance and x is the bound-electron coordinate. $\psi_{g,u}(R, t)$ are the normalized nuclear wavefunctions and $\phi_g(r, R), \phi_u(r, R)$ are the electronic wavefunctions of the electron. The two-lowest lying electronic states are considered to be the $1s\sigma_g$ and $2p\sigma_u$-state in Figure 6.2a. Note that a distinction is made between $\phi_g(x, R), \phi_u(x, R)$ and $g(x, t), u(x, t)$ in section 6.3.2. Both wavefunctions describe the bound x-electron, but $g(x, t), u(x, t)$ describe the quasi-static electronic states. The Born-Oppenheimer approximation is applied, i.e. the electronic wavefunctions are assumed to follow the nuclear dynamics adiabatically. The time-dependence of the nuclear wavepacket thus also gives the time-dependence of the electronic wavefunctions.
The molecules are assumed to be aligned along the linearly polarized laser field. The Hamiltonian that describes the interaction between the electronic states in the presence of an electric field $E(t)$ is given by:

$$\begin{aligned}\hat{H} = \hat{T}(R) + \hat{V}(R) = &-\frac{\hbar^2}{2m}\frac{\partial^2}{\partial R^2} + V(R) = \\ &\begin{pmatrix} -\frac{1}{2m_{red}}\frac{\partial^2}{\partial R^2} + V_g(R) & -\mu(R)E(t) \\ -\mu(R)E(t) & -\frac{1}{2m_{red}}\frac{\partial^2}{\partial R^2} + V_u(R) \end{pmatrix}\end{aligned} \tag{6.42}$$

where V_g and V_u are the potentials of the electronic eigenstates, m_{red} the reduced mass and $\mu(R)$ the R-dependent dipole moment. By inserting the wavefunction (6.41) into the time-dependent Schrödinger Equation: $i\hbar\frac{\partial\Psi}{\partial t} = \hat{H}\Psi$, one obtains the following coupled equations:

$$\begin{aligned}&i\frac{\partial}{\partial t}\begin{pmatrix} c_g(t)\psi_g(R, t) \\ c_u(t)\psi_u(R, t) \end{pmatrix} = \\ &\begin{pmatrix} -\frac{1}{m_{red}}\frac{\partial^2}{\partial R^2} + V_g(R) & -\mu(R)E(t) \\ -\mu(R)E(t) & -\frac{1}{m_{red}}\frac{\partial^2}{\partial R^2} + V_u(R) \end{pmatrix}\begin{pmatrix} c_g(t)\psi_g(R, t) \\ c_u(t)\psi_u(R, t) \end{pmatrix}\end{aligned} \tag{6.43}$$

Solving these coupled equations gives the time-dependence of the nuclear wavefunctions $\psi_g(R,t), \psi_u(R,t)$. A split-operator approach is applied, representing the nuclear wavepackets either in momentum $\psi_{g/u}(p,t)$ or position space $\psi_{g/u}(R,t)$. The split-operator method facilitates the application of the kinetic energy operator $\hat{T}(R) = p^2/2m$ and potential energy $\hat{V}(R)$ operator, which are respectively easier applied in momentum and the position representation of the wavefunctions.

To evaluate the localization of the eletron on the left or right proton, the wavefunction is evaluated in a basis of two localized electronic states. The $1s\sigma_g$ and $2p\sigma_u$ states are written as the bonding and antibonding combinations of the atomic wavefunctions, $\phi_{l,r}$, with the electron either on the left or right proton:

$$\begin{aligned}\phi_g(x,R) &= \frac{1}{\sqrt{2}}(\phi_l(x,R) + \phi_r(x,R))\\ \phi_u(x,R) &= \frac{1}{\sqrt{2}}(\phi_l(x,R) - \phi_r(x,R))\end{aligned} \tag{6.44}$$

It can be recognized that the localized states can be found by rewriting equations 6.44:

$$\begin{aligned}\phi_l(x,R) &= \frac{1}{\sqrt{2}}(\phi_g(x,R) + \phi_u(x,R))\\ \phi_r(x,R) &= \frac{1}{\sqrt{2}}(\phi_g(x,R) - \phi_u(x,R))\end{aligned} \tag{6.45}$$

The nuclear wavefunctions $\psi_g(R,t)$ and $\psi_u(R,t)$ are found by projecting the total wavefunction Ψ onto the localized electronic states:

$$\begin{aligned}c_l(t)\psi_l(R,t) =& \langle\phi_l(x,R)|\Psi(R,t)\rangle = \frac{1}{\sqrt{2}}(c_g(t)\psi_g(R,t) + c_u(t)\psi_u(R,t))\\ c_r(t)\psi_r(R,t) =& \langle\phi_r(x,R)|\Psi(R,t)\rangle = \frac{1}{\sqrt{2}}(c_g(t)\psi_g(R,t) + c_u(t)\psi_u(R,t))\end{aligned} \tag{6.46}$$

A linear combination of the gerade and ungerade states is created by the laser field, which results in localization of the electron on the 'left' or 'right' proton [34, 50]. The TDSE calculations yield the population in the localized states as a function of internuclear distance. A position filter is applied to remove the bound part of the localized populations and after Fourier transformation yields the photoion spectra for dissociation to the 'left' or 'right' with respect to the laser polarization.
The asymmetry parameter $A(E_k, \phi)$ for one particular ϕ is obtained by summing the populations in the localized states with a weighing factor, which reflects the relative ionization rate for the half-cycle maxima in the laser envelope. This weighing factor is $\frac{\Gamma(t_{HCM})}{\Gamma(t=0)}$, where $t = 0$ coincides with the maximum of the laser envelope. Finally, $A(E_k, \phi)$ is obtained by solving the TDSE for different values of ϕ.

6.3.6 Interference of nuclear wavepackets excited by different recollision events

In the calculation of $E_{eff}(t)$ the 1st, 2nd and 3rd return of the recollision electron to the molecular ion are included. Nuclear wavepackets excited by the 1st, 2nd and

3rd return are coherently summed and interference between these wavepackets can occur when the final kinetic energy are identical. Interference between H_2^+ nuclear wavepackets from different recollision events can occur in the case that there are two pathways leading to the same state of the total molecular system. In the TDSE calculations only the H_2^+ nuclear wavepackets are propagated and the continuum electron is consequently not described. However, the interference can only occur if the continuum electron that is correlated to the nuclear wavepacket in the $2p\sigma_u$-state, is identical for the different wavepackets. Disregarding the phase and energy of the continuum electron can thus lead to interference that is not real.

In this section it is discussed whether a description in which the continuum electron is neglected is appropiate or not. To facilitate the discussion, we rewrite the molecular ion wavefunction in equation 6.41, to include the continuum electron wavepacket. The total molecular wavefunction before recollision can be written as:

$$\Psi(x,y,R,t) = c_g(t)\psi_g(R,t)f_g(y,t)\phi_g(x,R) \tag{6.47}$$

It is assumed that $\psi_g(R,t)f_g(y,t)\phi_g(x,R)$ acts as a source for excitation to the excited state. During the 1st recollision, a part of the nuclear and electronic wavepacket $\psi_g(R,t)\phi_g(x,R)$ is excited to the $\psi_u(R,t)\phi_u(x,R)$ excited state of the ion, correlating with a continuum wavepacket $f_y(y,t)$:

$$\Psi(x,y,R,t) = c_g(t)\psi_g(R,t)f_g(y,t)\phi_g(x,R) + c_u^{(1)}(t)\psi_u^{(1)}(R,t)f_u^{(1)}(y,t)\phi_u(x,R) \tag{6.48}$$

$\psi_u^{(1)}(R,t)$ is the nuclear wavepacket, that was excited to the $2p\sigma_u$-state at the 1st return of the electron. $f_u^{(1)}(y,t)$ is the part of the continuum electron wavepacket, that transferred energy and momentum to the ion at the 1st return, indicated by the superscript (1) and $c_u^{(1)}(t)$ is the corresponding amplitude. Part of the ground nuclear wavepacket can be excited by the 2nd or 3rd return of the electron and the total wavefunction is written as:

$$\begin{aligned}\Psi(x,y,R,t) &= c_g(t)\psi_g(R,t)f_g(y,t)\phi_g(x,R) + \\ &\Big[c_u^{(1)}(t)\psi_u^{(1)}(R,t)f_u^{(1)}(y,t) + c_u^{(2)}(t)\psi_u^{(2)}(R,t)f_u^{(2)}(y,t) + c_u^{(3)}(t)\psi_u^{(3)}(R,t)f_u^{(3)}(y,t)\Big]\,\phi_u(x,R)\end{aligned} \tag{6.49}$$

where $\psi_u^{(n)}(R,t)$ is the nuclear wavepacket that is excited by the n^{th} recollision of the electron, correlating with the $f_u^{(n)}(y,t)$ continuum electron wavepacket and $c_u^{(n)}(t)$ is the corresponding amplitude.

In the current calculations, two extreme cases of wavepacket interference are presented and compared to the experimental data. The comparison to the experimental data should indicate whether interference between different wavepackets excited by different recollision events plays an import role. In case (A), it is assumed that the electron continuum wavepackets for the 1st, 2nd and 3rd return are identical:

$$f_u^{(1)}(y,t) = f_u^{(2)}(y,t) = f_u^{(3)}(y,t) \tag{6.50}$$

If equation 6.50 is correct, the nuclear wavefunctions $\psi_u^{(n)}(R,t)$ should be coherently added. In the numerical simulations, $E_{eff}(t)$ is calculated by including either the 1st, 1st+2nd, 1st+3rd or the 1st+2nd+3rd return of the continuum electron. This allows for interference between nuclear wavepackets excited by the different returns in the TDSE calculations.
In case (B), $f_u^{(n)}(y,t)$ for the 1st, 2nd and 3rd return are not identical:

$$f_u^{(1)}(y,t) \neq f_u^{(2)}(y,t) \neq f_u^{(3)}(y,t) \tag{6.51}$$

Intuitively one would expect that the electron wavepackets interacting with the ion at different returns are not identical. The difference between the electron wavepackets arises because the phase development of the electron wavepacket after recollision will probably not be identical with the phase development of an electron wavepacket that interacts with the ion at a later return. This is also supported by numerical calculations of recollision excitation of H_2^+ to simulate the H^+ kinetic energy spectra in [215]. In these calculations, the nuclear wavepackets were incoherently added and the numerical results compared well to the experimental photoion spectra.
In case (B) the nuclear wavepackets excited by the different returns should be incoherently added. In the numerical simulations, individual calculations are performed in which $E_{eff}(t)$ is nonzero only during the 1st, 2nd or 3rd return by applying appropriate Gaussian filters. The localized populations are summed after the TDSE calculations to obtain the asymmetry as a function of kinetic energy.

6.4 Numerical results

In this section the results of the TDSE calculations of H_2^+ and D_2^+ are discussed. This section is divided into three parts.
In paragraph 6.4.1, the effect of the effective field $E_{eff}(t)$ on the excitation and dissociation of H_2^+ is illustrated by plotting the time-dependent populations in the $1s\sigma_g$ and $2p\sigma_u$-states for propagation in $E_L(t)$ and $E_{L+E_{eff}}(t)$.
In paragraph 6.4.2, the dependence of the fragment kinetic energy on the time-structure of the effective field is shown by applying a filter to $E_{eff}(t)$ to include only the 1st, 2nd or 3rd return of the continuum electron.
In paragraph 6.4.3 the effect of the coherent or incoherent addition of nuclear wavepackets, excited by the different returns, on the asymmetry $A(E_k,\phi)$ is shown for H_2 and D_2. In all the calculations the following laser conditions are used: I=4×10^{13}W/cm^2, t_p=6.38 fs FWHM.

6.4.1 Recollision excitation by an effective field

Figure 6.5a,d respectively show the time-dependent energy-resolved populations in the $1s\sigma_g$ and $2p\sigma_u$ states, which is the result of solving the TDSE for H_2^+ in only the laser field $E_L(t)$. $E_L(t)$ is shown on top Figure 6.5a. The energy-resolved populations at the end of the propagation in the $1s\sigma_g$ and $2p\sigma_u$-states are respectively plotted in Figure 6.5c,f in black. The low kinetic energy fragments ($E_k < 2$ eV) are attributed to dissociation by bond-softening. The fragments observed for $E_k = 3$-10 eV is attributed to a numerical artefact in the TDSE calculations, caused by

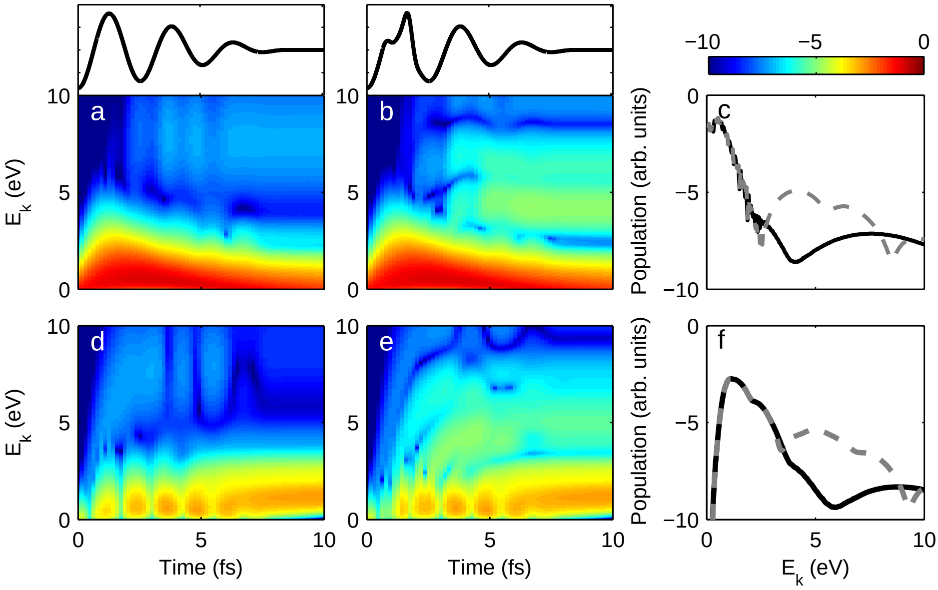

Figure 6.5: Solving the TDSE for H_2^+ in only the laser field $E_L(t)$ yield the energy-resolved populations in the a) $1s\sigma_g$ and d) $2p\sigma_u$ states, conversely the calculation using the laser field and the effective field $E_{L+E_{eff}}(t)$ yields the population in the b) $1s\sigma_g$ and e) $2p\sigma_u$ states. The populations are plotted on a logarithmic colorscale. $E_L(t)$ and $E_{L+E_{eff}}(t)$ are respectively plotted on top of panels a) and b). The populations in the c) $1s\sigma_g$ and f) $2p\sigma_u$ states at the end of the propagation are plotted for propagation in $E_L(t)$ (black) and $E_{L+E_{eff}}(t)$ (gray dashed lines). $E_{eff}(t)$ is calculated by including only the 1^{st} return of the electron to the core.

projecting the H_2 ground state wavepacket onto the quasi-static ground state of H_2^+ at the peak of the laser field.

The time-dependent populations in the $1s\sigma_g$ and $2p\sigma_u$ states for the calculation with the laser and effective field $E_{L+E_{eff}}(t)$ are respectively shown in Figure 6.5b,e. $E_{L+E_{eff}}(t)$ is shown on top of Figure 6.5b.

The effect of effective field is clearly observed in an increase in *both* the populations in the $1s\sigma_g$ and $2p\sigma_u$ states for E_k=3-8 eV. Interestingly, the dominant effect of the effective field is only observed in the laser cycle following $E_{eff}(t)$ (i.e. t > 4.5 fs). This observation supports the assumption that the recollision electron does not have enough energy on its own to excite the molecular ion to the repulsive state and needs the laser field to complete the excitation. The delay in the excitation to the repulsive state can be understood in terms of Landau-Zener tunneling [223] in which the excitation mechanism is understood by laser-induced avoided crossings. The populations in the $1s\sigma_g$ and $2p\sigma_u$ states at the end of the propagation are respectively plotted in Figure 6.5c,f in gray dashed lines. An increase of two orders of magnitude is observed for E_k = 3-9 eV, compared to the populations obtained by propagation in only the laser field $E_L(t)$ (black line). The effective field indeed induces recollision excitation resulting in the formation of ion fragments with E_k = 3-9 eV.

6.4.2 Dissociation of H_2^+ and D_2^+ by recollision excitation

The fragment kinetic energy depends on the internuclear distance R at the time of excitation to the repulsive $2p\sigma_u$-state. This dependence of the fragment kinetic energy on the time of recollision excitation was previously used in molecular clock experiments [215, 224]. This relation is schematically illustrated in Figure 6.2a. Recollision by the 1^{st}, 2^{nd} or 3^{rd} return of the electron will excite the nuclear wavepacket at larger internuclear distances, resulting in lower fragment kinetic energies. Inferring from the vibrational periods of H_2^+ and D_2^+, which are respectively $\sim$ 15 and $\sim$ 24 fs [225, 226], differences in the kinetic energy spectra can be expected between H_2^+ and D_2^+.

In this section, the effective field $E_{eff}(t)$ is only nonzero during the 1^{st}, 2^{nd} or 3^{rd} return of the continuum electron. The populations in the $1s\sigma_g$ and $2p\sigma_u$ states both illustrate the effect of the recollision electron dynamics as well as the molecular dynamics. For reasons of brevity only the population in the $2p\sigma_u$ state is shown in this section.

The population in the $2p\sigma_u$ state at the end of the propagation, calculated with the laser and effective field $E_{L+E_{eff}}(t)$ is plotted in gray dashed lines in Figure 6.6 for H_2^+ (top panels) and D_2^+ (bottom panels) and can be compared to the calculation using only the laser field $E_L(t)$ (black solid lines). The results of including only the 1^{st}, 2^{nd} and 3^{rd} return are respectively shown in Figure 6.6a,d, 6.6b,e and 6.6c,f. For all the returns an increase in the population, compared to the calculation with only the laser field $E_L(t)$ is observed. As the return time of the electron is later, the increase in the population in the $2p\sigma_u$ state is observed for increasingly smaller kinetic energies, in correspondence with the increasing internuclear distance for the later returns.

Interestingly, the increase in the population is larger for the 2^{nd} return (Figure 6.6b,e) compared to the 1^{st} return (Figure 6.6a,d). This is attributed to the larger internuclear distance at which the excitation by the 2^{nd} recollision takes place, enhancing the excitation probability.

Subtle differences between H_2^+ and D_2^+ can be observed in the relative weights of population as a function of kinetic energy. Generally, the population in the kinetic energy range E_k = 6-9 eV is larger for D_2^+ compared to H_2^+. The D_2^+ molecular ion has moved over a smaller internuclear distance compared to the H_2^+ molecular ion and excitation to the repulsive $2p\sigma_u$-state will thus result in fragments with a higher kinetic energy compared to H_2^+.

Note that the populations in the $1s\sigma_g$-state show a similar trend to the populations in the $2p\sigma_u$-state. An increase in the population with E_k = 3-9 eV is observed and is attributed to de-excitation from the $2p\sigma_u$ to the $1s\sigma_g$-state, forming fragments with E_k = 3-9 eV.

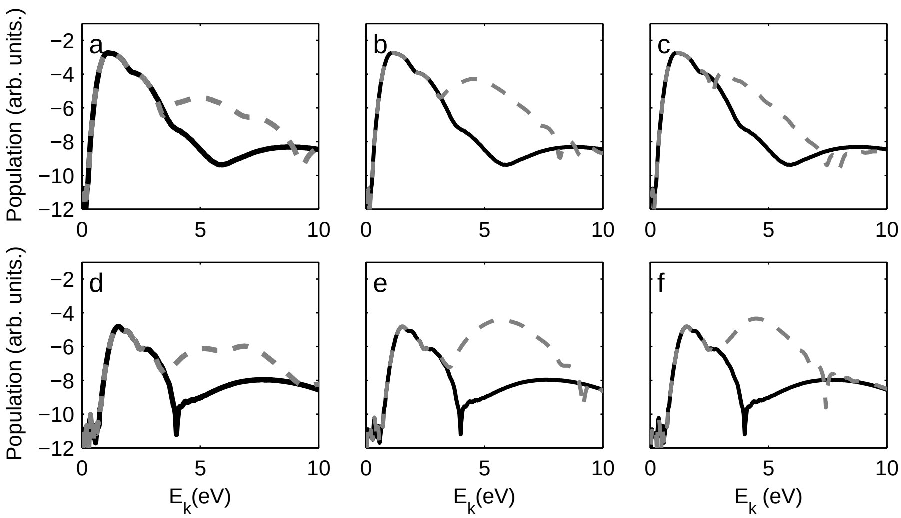

Figure 6.6: Population plotted on a logarithmic scale in the $2p\sigma_u$ state for a-c) H_2^+ and e-f) D_2^+ for propagation in the laser and effective field $E_{L+E_{eff}}(t)$ (gray dashed lines) and only the laser field $E_L(t)$ (black solid lines). $E_{eff}(t)$ includes only the a,d) 1st return b,e) 2nd return or c,f) 3rd return of the continuum electron to the core.

6.4.3 Electron localization in dissociative ionization of H_2 and D_2 as a function of CEP

Carrier-envelope-phase scans of the asymmetry: only the 1st, 2nd or 3rd return

The asymmetry parameter $A(E_k, \phi)$ calculated with only the laser field $E_L(t)$ are respectively shown for H_2 and D_2 in Figure 6.7a,e. Similar to the experimental results, regions of positive and negative asymmetry are observed for each value of ϕ. The population in the kinetic energy region E_k = 3-9 eV is negligible and the asymmetry parameter in this kinetic region is therefore not meaningful.

The effect of the 1st return of the recollision electron on the asymmetry parameter $A(E_k, \phi)$ is respectively shown for H_2 and D_2 in Figure 6.7b,f. An increase in the asymmetry in $A(E_k, \phi)$ is observed for both H_2 and D_2 for E_k = 3-9 eV. $A(E_k, \phi)$ is qualitatively similar for H_2 and D_2, apart from a π-phase difference for E_k = 6-9 eV. The asymmetry parameters $A(E_k, \phi)$, calculated by including only the 2nd return in $E_{eff}(t)$, are shown for H_2 and D_2 in Figure 6.7c,g. Interestingly the 2nd return of the continuum electron induces a clear π phase-difference between H_2 and D_2 for $E_k = 4.5 - 7$ eV. The oscillatory stripes of positive and negative $A(E_k, \phi)$ for E_k = 7-10 eV for both H_2 and D_2 are attributed to the structures observed in the energy-resolved populations in the $1s\sigma_g$ and $2p\sigma_u$ states at these energies. This might be due to interference between wavepackets that are excited by the laser pulse and by $E_{eff}(t)$. In Figure 6.7d,h the asymmetry parameter $A(E_k, \phi)$ is shown when only the 3rd return is included in calculating $E_{eff}(t)$. A π-phase difference between H_2

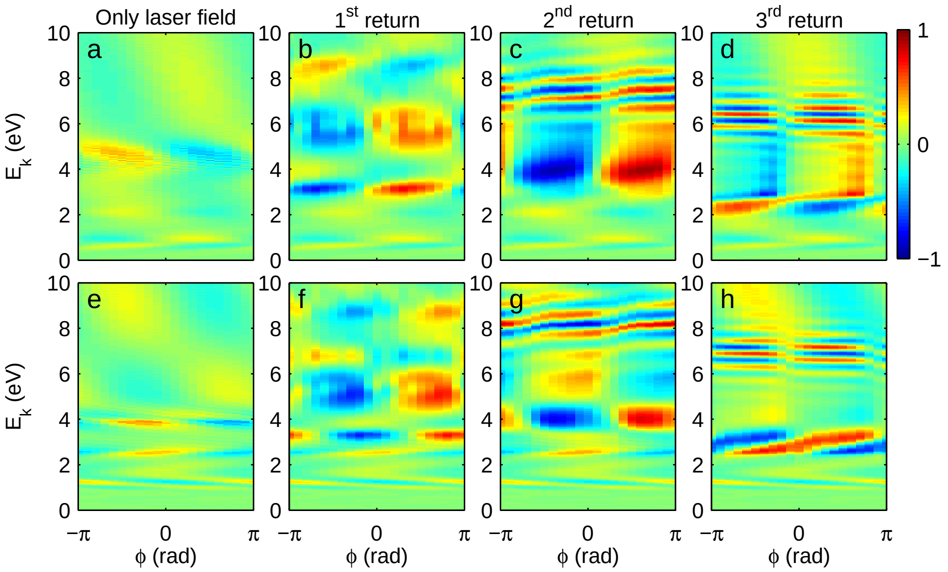

Figure 6.7: $A(E_k, \phi)$ for a-d) H_2 and e-f) D_2. The asymmetry parameter $A(E_k, \phi)$ is calculated for a,e) the laser field $E_L(t)$. The effect of the recollision dynamics on $A(E_k, \phi)$ is illustrated by adding the effective field E_{eff} to the laser field $E_L(t)$ only for times when the electron comes back to the core at the b,f) 1st return, c,g) 3rd return or d,h) 3rd return.

and D_2 is now observed for E_k = 3-6 eV.

The experimentally observed π-phase difference between H_2 and D_2 is only reproduced for excitation by the 2nd or 3rd return of the continuum electron. This suggests that multiple returns play a crucial role in the electron localization during dissociation.

Coherent addition of nuclear wave packets excited by the different returns

The nuclear wavepackets excited by the 1st, 2nd or 3rd return are coherently summed, allowing for interference excited by these wavepackets. The asymmetry parameter $A(E_k, \phi)$ is shown in Figure 6.8a-d for H_2 and 6.8e-f for D_2.

In Figure 6.8b,f the asymmetry parameter $A(E_k, \phi)$ is shown respectively for H_2 and D_2 when the 1st and 2nd return are included in $E_{eff}(t)$. A π-phase difference between H_2 and D_2 is observed over a kinetic energy range of E_k = 4.5-7 eV and can be solely attributed to recollision during the 2nd return.

The asymmetry parameter $A(E_k, \phi)$, calculated when the 1st and 3rd return are included, are shown in Figure 6.8c,g. The effect of including the 3rd return is quite dramatic on $A(E_k, \phi)$ for both H_2 and D_2, i.e. the kinetic energy dependence of $A(E_k, \phi)$ becomes more complex and is ascribed to interference between wavepackets excited by the 1st and 3rd return.

The effect of including the 1st, 2nd and 3rd return in $E_{eff}(t)$ is shown in Figure

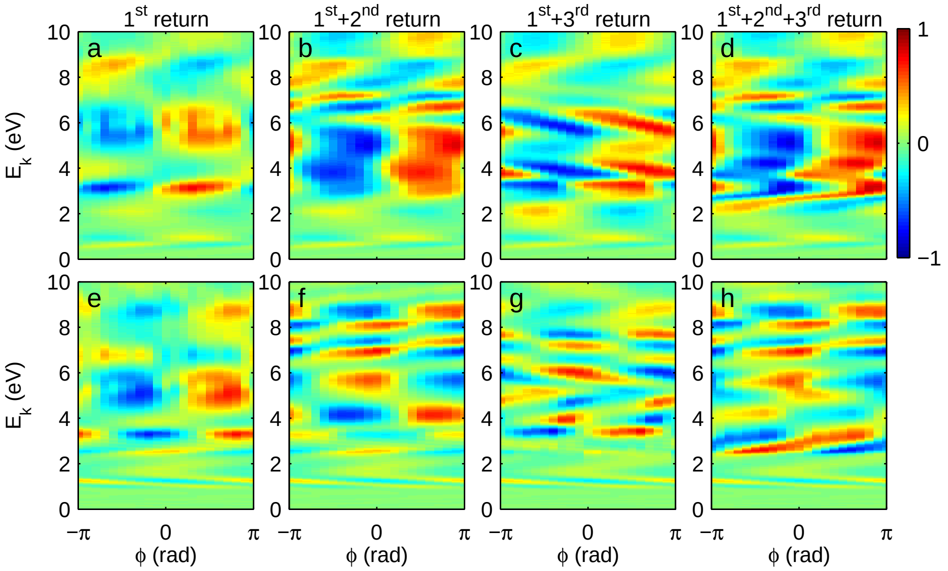

Figure 6.8: $A(E_k, \phi)$ obtained by coherent addition of nuclear wavepackets excited by the 1^{st}, 2^{nd} or 3^{rd} return of the continuum electron, allowing for wavepacket interference during dissociation. a-d) H_2 and e-f) D_2. $A(E_k, \phi)$ is obtained for including the a,e) 1^{st}st return, b,f) 1^{st} + 2^{nd} return c,g) 1^{st} + 3^{rd} and d,h) 1^{st} + 2^{nd} + 3^{rd} return of the continuum electron in calculating $E_{eff}(t)$.

6.8d,h. The π-phase difference between H_2 and D_2 extends over a kinetic energy range of E_k = 3.5-8 eV. Interestingly, Figure 6.8d shows a close resemblance to Figure 6.8b, in which only the 1^{st} and 2^{nd} return are included. The inclusion of the 3^{rd} return has mainly modified $A(E_k, \phi)$ for E_k = 2-4 eV, enhancing the asymmetry contrast.

Incoherent addition of nuclear wave packets excited by the different returns

The asymmetry parameter $A(E_k, \phi)$, calculated by incoherently adding the nuclear wavepackets excited by the 1^{st}, 2^{nd} or 3^{rd} return, is shown in 6.9a-d for H_2 and 6.9e-f D_2. The asymmetry parameter is again shown in Figure 6.9a,e when the 1^{st} return is included in calculating the effective field $E_{eff}(t)$

Figure 6.9b,f shows the asymmetry parameter $A(E_k, \phi)$ when the 1^{st}+2^{nd} return are included in calculating $E_{eff}(t)$. $A(E_k, \phi)$ for both H_2 and D_2 shows a close resemblance to the coherent wavepacket summation in Figure 6.8b,f. This illustrates that interference between wavepackets excited by the 1^{st} and 2^{nd} return does not have a large effect on $A(E_k, \phi)$.

The result of including the 1^{st}+3^{rd} return in calculating the asymmetry parameter $A(E_k, \phi)$ is shown in Figure 6.9c,g. For H_2, the effect of including the 3^{rd} return is mainly observed for E_k = 2-4 eV. The small influence of the 3^{rd} return on the fragments with $E_k > 4$ eV is attributed to the fast molecular dynamics of the H_2^+ ion.

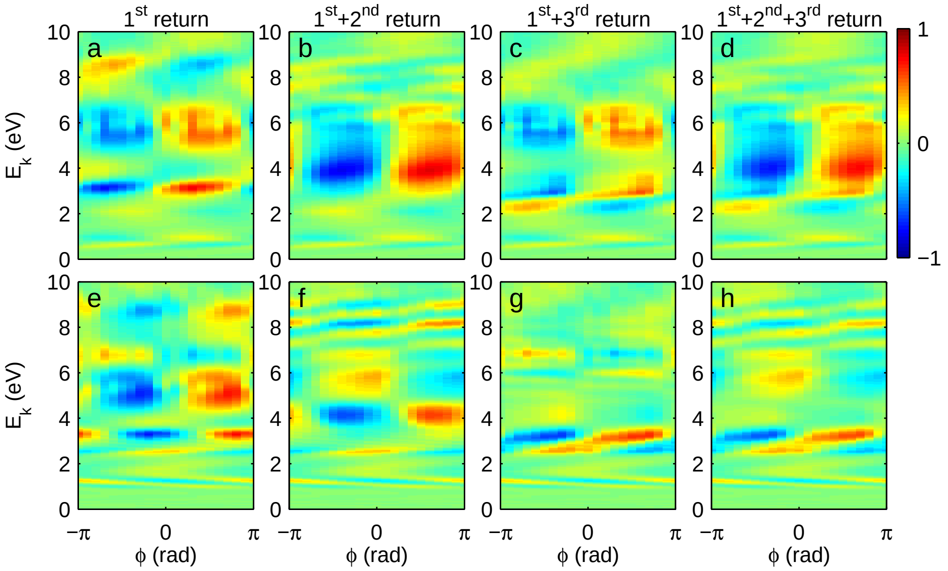

Figure 6.9: $A(E_k, \phi)$ is calculated by incoherent addition of wave packets that are excited by the 1st, 2nd or 3rd return. $A(E_k, \phi)$ is shown for a-d) H_2 e-h) D_2 when the a,e) 1st return, b,f) 1st+2nd return, c,g) 1st + 3rd and d,h) 1st + 2nd + 3rd return are included in calculating $E_{eff}(t)$.

For D_2, the effect of adding the 3rd return is more pronounced. The contrast of the asymmetry decreased significantly by including the 3rd return and the asymmetry parameter $A(E_k, \phi)$ seems to be dominated by the localized populations formed by the 3rd return. The experimentally observed π-phase difference between H_2 and D_2 is observed for E_k = 4-8 eV.

In Figure 6.9d,h $A(E_k, \phi)$ is shown for H_2 and D_2, when the 1st+2nd+3rd return are included in calculating the effective field $E_{eff}(t)$. A π-phase difference between H_2 and D_2 is observed for E_k = 4-7 eV. Regarding the fact that $A(E_k, \phi)$, calculated when only the 1st return is included, does not show a π difference between H_2 and D_2 suggests that for D_2, $A(E_k, \phi)$ is dominated by the populations excited by the 2nd and 3rd return.

6.5 Conclusion

H_2 and D_2 molecules are dissociatively ionized by a waveform-controlled few-cycle IR pulse. The fragment ion ejection shows an asymmetry with respect to the laser polarization which is attributed to an electron localization during the dissociation of the H_2^+ and D_2^+ molecular ions.

In contrast to the results in [34] the asymmetry as a function of the CEP shows a dependence on kinetic energy. Furthermore, a π-phase difference is observed between H_2 and D_2. To explain the π-phase difference between the two isotopes and the discrepancy between the two experimental results, which can be sought in the different experimental conditions, simulations of the dissociative ionization of H_2 and D_2 molecules are done. The time-dependent Schrödinger equation is solved for H_2^+ and D_2^+ in the presence of a few-cycle IR pulse.

The formation of fragments with E_k = 3-9 eV is attributed to dissociation induced by recollision excitation, which is a two-electron process that is not included in the TDSE calculations. To incorporate recollision excitation in the simulations, a semi-classical model is presented that allows one to capture the two-electron interaction into an effective field that is used in the TDSE calculation and allows one to develop a more intuitive understanding of the role of the recollision electron dynamics in the experimental results.

The numerical simulations with only the laser field $E_L(t)$ are not able to form significant populations between E_k = 3-9 eV. The laser field on its own is therefore not sufficient to qualitatively reproduce the experimental results.

The results, in which only the 1st return of the electron is included in calculating the effective field $E_{eff}(t)$, yield similar results for H_2 and D_2 and are unable to reproduce the experimentally observed π-phase difference.

Only including the 2nd return in addition to the 1st return, reproduces the aforementioned π-phase difference between the two molecules. Adding the 3rd return to the previous results, predominantly changes the kinetic energy dependence of the asymmetry parameter $A(E_k, \phi)$ only for E_k = 2-4 eV. The limited role of the 3rd recollision, which for a continuous wave has a larger recollision energy compared to the 2nd recollision is attributed to a combination of two effects. First, excitation of the H_2^+ molecule at larger internuclear distances leads to fragments with a lower kinetic energy. Second, the localized populations are predominantly formed by ionization at the three half-cycle maxima in the center of the few-cycle pulse. Due to the rapidly falling edge of the envelope, the recollision energy of the electron at the 3rd return is reduced, compared to a continuous wave, thereby decreasing the excitation probability to the $2p\sigma_u$ state.

The numerical simulations show that the 2nd return of the continuum electron is crucial in reproducing the π-phase difference between H_2 and D_2. This is remarkable in the light of previous results, where either the 1st [215] or the 3rd return [224, 227] of the electron are assigned as the dominant contribution to the photoion spectra. Furthermore, interpretation of the results in [34] included only the 1st return of the electron to the core [210].

In previous numerical simulations of recollision excitation of the H_2^+ nuclear wavepacket [215, 224], interference between nuclear wavepackets is not taken into account as these wavepackets are incoherently added.

Under which conditions should one add the nuclear wavepackets coherently or incoherently? Coherent addition of the nuclear wavepackets with their respective phases, is only appropriate when the continuum electron wavepackets, after the various recollisions, lead to the same final state of the active continuum electron.

Whereas incoherent addition is correct when the active continuum electrons, even if they end up in the same final state after the the various recollisions, their relative phases are different. In this chapter an attempt is made to investigate the importance and influence of interference between nuclear wavepackets. The coherent *and* incoherent addition of wavepackets result in qualitatively similar asymmetry

parameter$A(E_k, \phi)$. In general the coherent addition of wavepackets results in a more complicated kinetic energy dependence of asymmetry parameter $A(E_k, \phi)$. This effect is more pronounced for D_2 compared to H_2. This is attributed to the slower dynamics of D_2^+ compared to H_2^+ in the ground state, resulting in a larger phase difference between wavepackets in the ground and excited state.
In the experimental results, $A(E_k, \phi)$ is observed as tilted stripes of negative and positive asymmetry, extending from the bottom left to the top right. This tilted kinetic energy dependence of $A(E_k, \phi)$, is only to a small degree reproduced in the numerical simulations and shows a closer correspondence for the coherent addition of the wavepackets. The more uniform asymmetry parameter $A(E_k, \phi)$, i.e. the smaller kinetic energy dependence of $A(E_k, \phi)$, for the incoherent addition resembles the experimental data more than the $A(E_k, \phi)$ for the coherent addition. The physical reality will be a mixture of the two extreme cases.

A High repetition rate fast piezo valve

A.1 Motivation

In chapter 2 we described in detail the attosecond beamline at the AMOLF-institute in Amsterdam. In the experimental setup, we make use of a velocity map imaging spectrometer (VMIs) to detect the charged particles that are formed in the interaction of a gaseous medium with an attosecond pulse train and/or infrared pulse. The attosecond pulse train is a relatively weak light source, in order to increase the count rates in the experiment we have designed a VMIs in which the gas injection system is incorporated into the repeller electrode [120].

The effusive repeller described in [120] makes use of a capillary, through which the gas enters the interaction region continuously. A further increase in the signal level can therefor be obtained with a pulsed gas injection system. Towards this end, we have incorporated a pulsed piezo valve into the repeller. In this Appendix, we describe the design of the pulsed piezo valve that is the follow-up of the valve that is described in section 2.5.4. In this Appendix we discuss the new high repetition rate (> 1 kHz) fast piezo valve. The design considerations, the new mechanical design, the operation and characterization are discussed.

A.2 Design considerations

In an experimental setup that uses a pulsed laser source in the interaction with the gaseous medium, the repetition rate of the laser is an important parameter in designing pulsed valves. Various groups, amongst which the group at the AMOLF-institute, have used pulsed valves that are based on piezo disks. These valves operate by flexing a cylindrical piezo disk with a voltage pulse (200 - 1000 V) with a duration of ~ 200 μs. The disadvantage of these piezo disk valves is that they are limited to a repetition rate of 1 kHz. A growing number of femtosecond lasers with repetition rates of > 1 kHz are now being used by research groups, increasing the demand for piezo valves that can operate beyond this limit of 1 kHz. In addition, these piezo disk valves produce relatively long gas pulses, thereby increasing the gas load on the system. In a number of experiments, the rotational temperature of the molecules is an important parameter, i.e. experiments where the molecules are aligned in the laboratory frame require a cold molecular beam.

A significant decrease in the pulse duration is achieved by the magnetically activated

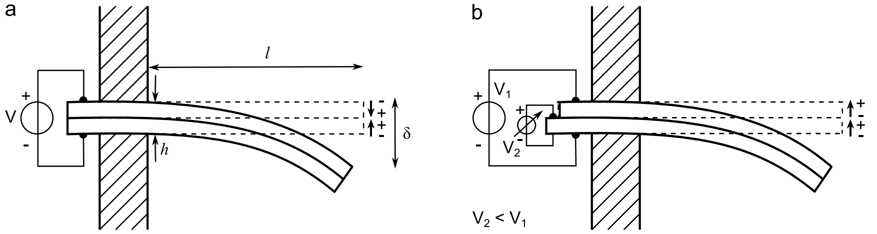

Figure A.1: a) Serial bimorph piezo with free length l and thickness h. b) Parallel bimorph piezo. Applying a bias voltage to the center contact ensures that both strips are driven in the polarization direction.

plunger valve, demonstrated by Even *et al* in 2000 operates at 1 kHz[228]. The Even-Lavie valve, as it is known amongst users, produces gas pulses with a 10 μs full-width-half-maximum (FWHM) duration, but can only operate at a maximum repetition rate of 1 kHz. A major advantage of the Even-Lavie valve is the rotational temperature of the gas molecules that can be as low as 1 K for seeded molecular beams.

For experiments that do not require such a low temperature of the molecular beam, an attractive alternative was presented about two decades ago by D. Gerlich *et al* [229]. They presented a piezo valve based on a cantilever, but this design was however never published in peer-reviewed journals. The cantilever piezo valve as presented by D. Gerlich can operate at a repetition rate of $>$ 1 kHz, producing gas pulses with a duration of 20-30 μs. Recently, a cantilever piezo valve, that is based on the design by D. Gerlich, with a repetition frequency $<$5 kHz and pulse durations of $<$10 μs was demonstrated [230].

The high repetition rate and the short pulse duration of the cantilever piezo valve are very promising. Based on the performance of this cantilever valve, we decided to build a pulsed piezo valve based on the design by D. Gerlich.

A.2.1 Piezoelectric ceramics

The operation of the valve is based on the piezoelectric effect, i.e. the piezoelectric crystal changes its shape under the influence of an electric field. By combining the piezo crystal with a material that does not change its shape under influence of the electric field, i.e. a metal in the case of the aforementioned piezo disks, a deflection of the piezo crystal is realized. Alternatively, two strips of the piezoelectric crystal with an opposite mechanical response to the electric field can be used to obtain a deflection of the piezo.

The piezo valve designed by D. Gerlich makes use of a piezoelectric ceramic that is made of a mixture of lead titanate ($PbTiO_3$) and lead zirconate ($PbZrO_3$) and is fabricated by Morgan electronics under the type name PXE 5 (new name is PZT503) [231]. Piezoelectric ceramics can be fabricated as unimorph, bimorph and multilayer stacks of the piezoelectric material. In the cantilever piezo valves, the bimorph piezoelectric ceramics proved to be the best choice. In a bimorph piezo, two strips of the piezoelectric material are bonded together and the two strips have

Table A.1: Charge constant d_{31} and thermal and electric limits of the PXE5 piezoelectric ceramic. The height and width of the PXE 5 piezo used in the current piezo valve are shown.

Charge constant	d_{31}	10^{-12} (m/V)	-215
Curie Temperature	T_c	(C°)	285
Electric field strength		(V/mm)	300
Capacity	C	(nF)	2.6
Piezo width	w	(mm)	10
Piezo height	h	(mm)	0.6

opposite (serial) or parallel polarization directions (Figures A.1a and A.1b). In a serial bimorph, the two strips are connected to a voltage source and requires only two electrical connections. Due to the opposite polarization direction of the two strips however, there is the risk of depolarization. This danger is circumvented for parallel bimorph piezos, when the strips are individually connected and both strips are driven by a voltage parallel to the polarization direction. This operation mode is actually implemented in the piezo valve presented in [230].

The piezo valve described in section 2.5.4 is based on the cantilever piezo valve design of D. Gerlich and we will therefore use the same serial PXE 5 bimorph piezo, which has proven its use in previous experiments [229, 232]. We note that in the mean time preparations were made to implement a parallel bimorph in the current piezo valve, allowing one to drive the piezo valve at higher voltages without depolarizing the piezoelectric material.

A.2.2 Deflection and resonance frequency

In designing the pulsed piezo valve we need to consider the deflection of the piezo and the resonance frequency. The deflection of the cantilever piezo is related to the piezoelectric charge constant, which is given in Table A.1 for the PXE 5 piezo. The deflection δ of a free cantilever for *static* operation is described by [230]:

$$\delta \propto \frac{l^2}{h} d_{31} E_3 \tag{A.1}$$

where d_{31} is piezoelectric charge constant, l is the free length of the cantilever and h is the total height of the cantilever (Figure A.1a). d_{31} is defined in Table A.1, together with the width and thickness of the PXE 5 piezos that are used in the current piezo valve. E_3 is the voltage applied parallel to the polarization direction of the piezo. The maximum voltage that can be applied to the PXE 5 piezo is 300 V/mm before depolarization of one of the piezoelectric layers starts to play a role.

The fundamental resonance frequency is defined as [231]:

$$\nu_1 = 400 \frac{h}{l^2} \tag{A.2}$$

The piezo valve should be operated under the fundamental resonance frequency to ensure a mechanical response that is follows the electronic driving pulse. From these equation A.1 and A.2 one can readily recognize that the deflection increases and that the resonance frequency decreases with the free length of the cantilever.

The pulsed piezo valve needs to be synchronized with the femtosecond IR laser in the experimental setup at the AMOLF-institute, which has a repetition rate of 3 kHz. The free length of the cantilever piezo was adjusted, such that the piezo valve has a fundamental resonance frequency higher than the repetition rate of the laser. Choosing $l = 6$ mm, sets the fundamental resonance frequency to 6.7 kHz. The deflection of the piezo valve in static operation is then approximately approximately 8 μm. The deflection in pulsed mode will be different due to the dynamical response of the piezo [229]. The static operation of the pulsed piezo valve, we designed at the AMOLF-institute, did not result in a considerable increase in the testing vacuum chamber ($< 10^{-6}$ mbar), pumped by a turbopump with a capacity of 200 L/s. Conversely, when operating the pulsed piezo valve at a repetition rate of 3 KHz, pressures of $\sim 10^{-4}$ mbar could be reached and indicates that the pulsed valve should not be operated too far from its resonance frequency.

A.3 Repeller with an integrated pulsed piezo valve

A.3.1 Mechanical design

The pulsed cantilever piezo valve needs to be incorporated into the repeller electrode of a VMIs. The repeller electrode incorporates a nozzle with $d = 50$ μm and $l = 200$ μm. The central part of the repeller has a 1 mm flat region, from where the electrode has a conical shape with an angle of 154° to accommodate the laser focus in front of the repeller [120].

The first design of the pulsed piezo valve that was integrated into the repeller housing, is shown in Figure 2.6. In this design, the distance of the viton disk to the nozzle was adjusted by translating the piezo with respect to the nozzle. The bimorph piezo was mounted on a translatable vespel bar and was therefore electrically and thermally isolated from the repeller housing. In the adjustment of the valve we experienced problems with the exact parallel translation of the piezo with respect to the housing. In addition, the long-term stability of the valve proved to be an issue, which was attributed to the heating of the piezo crystal and the thermal isolation by the vespel bar.

To overcome these problems we reconsidered the mechanical design of the piezo valve. The new design is shown in Figure A.2. Figure A.2a shows an expanded view of the valve and includes a short description of the individual parts. Figure A.2b shows a cut through the mounted piezo valve. In the current design, the piezo is directly clamped to the repeller housing, thereby ensuring mechanical stability and better thermal conductivity. The distance of the viton disk to the nozzle is adjusted by moving the housing that holds the piezo, with respect to the repeller housing with the nozzle.

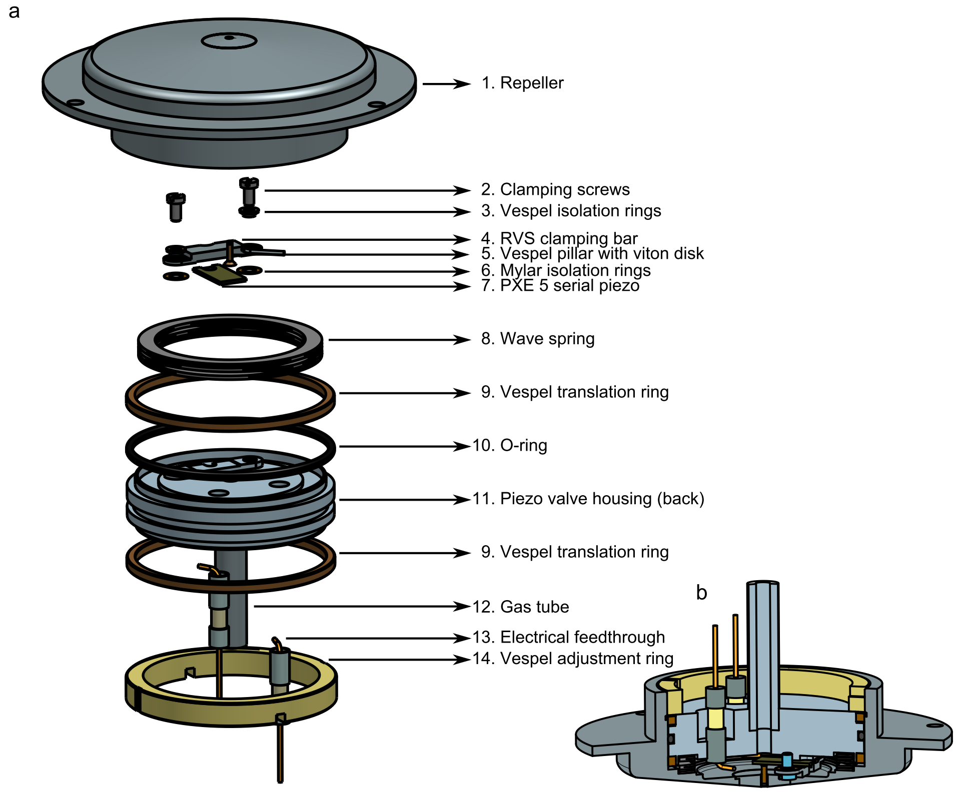

Figure A.2: a) Expanded view of the pulsed piezo valve. **1**.*Repeller*. **2**.*Clamping screws*. **3**.*Vespel isolation rings* to isolate the clamping screws (2) from (4). **4**.*RVS clamping bar* is also used to provide a positive voltage pulse. **5**.*Vespel pillar* (d = 1 mm, l = 4.4 mm) with a viton disk (d = 1 mm, h = 0.5 mm) to seal the nozzle. **6**.*Kapton rings* for isolation of the RVS bar (4) from the valve housing (11). **7**.*PXE 5 serial bimorph piezo*. **8**.*Wave spring* for pushing back the valve housing (back)(11) from the repeller (1). **9**.*Vespel translation rings* to facilitate the movement of the piezo valve housing (11) with respect to the repeller (1). **10**.*O-ring* (inner diameter d = 40 mm, ring diameter d = 1.5 mm) to seal the piezo valve. **11**.*Piezo valve housing (back)* supports the piezo and provides the floating ground potential, equal to the repeller voltage. **12**.*Gas tube* **13**.*Electrical feedthrough* for providing the positive voltage pulse. **14**.*Vespel adjustment ring* sets the distance of the viton disk with respect to the nozzle. The vespel ring has a fine thread (250 $\mu m/360°$) to ensure a precise adjustment of the valve. Two slots in the ring allow for easy adjustment with a special-made tool. b) A cut through the mounted piezo valve.

A.3.2 Expected gas density in the interaction region

The repeller with the integrated piezo valve allows one to reach a gas density that is orders of magnitude higher than can be achieved with molecular beams produced by a combination of pulsed valves and skimmers. In this paragraph, a simple calculation illustrates the expected gas densities. This calculation assumes for the first part a continuous flow from the nozzle.

In the type of experiments that are performed in our group, the charged particles arising from the interaction with the laser are detected by a combination of microchannel plates (MCPs) and a phosphor screen. The MCPs can be operated up to a pressure of 10^{-5} Torr, which in our case forms the limitation of the attainable gas density in the interaction region. Assuming this maximum pressure of 10^{-5} Torr and a turbo pump with a capacity of 500 l/s, we can introduce 5×10^{-3} Torr l/s into the vacuum chamber, corresponding to 1.5×10^{17} atoms/molecules per second. The nozzle has a diameter of 50 μm and when the atoms/molecules flow through the nozzle with a speed of 300 m/s, we obtain a flow rate of 6×10^{-4} l/s. Dividing the maximum flow rate of 5×10^{-3} Torr l/s by the flow rate of 6×10^{-4} l/s, we obtain a pressure of 8.5 Torr at the exit of the nozzle.

To obtain the expected gas density for a pulsed operation of the valve, we multiply the previously calculated gas pressure of 8.5 Torr with the inverse of the duty factor f [233]:

$$f = \Delta t \nu_{rep} = \frac{\Delta t}{T_{rep}} \tag{A.3}$$

where, ν_{rep} and T_{rep} are respectively the frequency and pulse period of the pulsed valve, related to the repetition rate of the driving laser. Δt is the duration of the gas pulse. Assuming $\Delta t = 28$ μs and a repetition rate of 3 kHz, an enhancement of a factor of 12 in the gas density can be obtained and results in an exit pressure of 102 Torr.

The laser focus is typically at a distance of $\sim$ 1 mm from the nozzle and assuming an opening angle of 1 steradian the pressure will have dropped by a a factor of 660, corresponding with a density of 0.15 Torr. The photoabsorption A is calculated using the law of Lambert-Beer and $A = \sigma l c$, where σ is the absorption cross-section, l the length of the interaction medium and c is the atom/molecule density. σ is typically 10^{-17} cm^2, $c = 7 \times 10^{-15}$ atoms or molecules/cm^3 and l is calculated using the 1 steradian opening angle and distance, giving l = 1.3 mm for d= 1 mm. The photoabsorption probability is thus 7×10^{-3}. One can compare this to the 10^{-5} photon absorption probability of a molecular beam, with a density of 10^{13} atoms/cc. The repeller with an integrated piezo valve can thus increase the countrate with 2-3 orders of magnitude. The attosecond pulse trains in our lab typically contain 10^6-10^7 photons per pulse, corresponding to 10^3-10^4 counts/laser shot.

The distance from the repeller will eventually determine the actual gas density. Increasing the distance reduces the gas density quadratically with the distance from the repeller. This is partly compensated by the increasing interaction length, which increases linearly with the distance from the repeller.

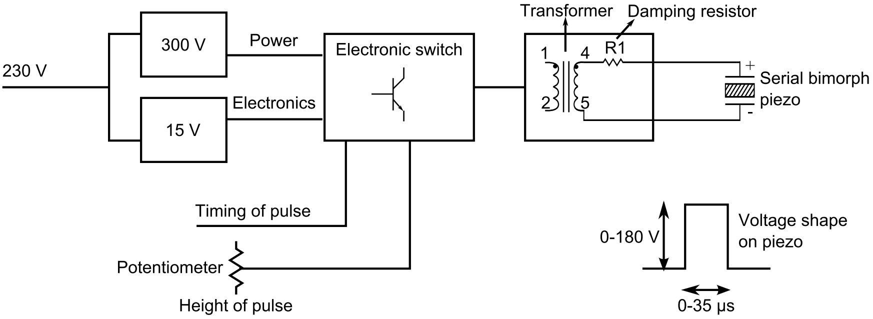

Figure A.3: Schematic diagram of the pulsed piezo valve driver. The input 230 V is used for the 300 V power supply for the voltage pulse to drive the bimorph piezo, as well as the 15 V power supply that is used for the driver electronics. The electronic switch regulates the timing as well as the height of the voltage pulse (by the potentiometer). A transformer is used to apply the voltage pulse to the serial bimorph piezo, while the ground potential is floating at the repeller voltage. A damping resistor prevents ringing in the voltage pulse due to resonances in the transformer coils. The shape of the voltage pulse on the piezo is between 0-35 μs and can have a maximum of 300 V. Due to the danger of depolarization, the piezo should not be driven above 180 V.

A.3.3 Piezo valve voltage driver

The fast pulsed piezo valve is driven by a valve driver that can generate voltage pulses at the repetition rate of the laser and with pulse durations of 0-35 μs. A complication for the valve driver is the fact that one side of the piezo is clamped to the repeller housing, which is set to a few kVs. The ground potential of the voltage pulse should therefore be equal to the repeller housing, as the piezo is in electrical contact with the repeller housing. The positive voltage pulse can be provided via an electrical feedthrough (part 13 in Figure A.2).

The piezo valve driver is home-built at AMOLF and a schematic electrical diagram is shown in Figure A.3. The valve driver uses a transformer to apply the voltage pulse to the piezo valve, to avoid that the ground of the piezo driver is set to the voltage of the repeller. The transformer transfers the electrical energy from one circuit to the other by using inductively coupled conductors, the coils. The piezo driver can deliver a maximum voltage of 300 V. A 10-turn potentiometer provides a fine adjustment of the voltage between 0-300 V. To avoid depolarization, the piezo valve should not be driven with a voltage pulse higher than 180 V. We typically use a pulse duration of t=25-35 μs.

The pulsed valve driver is triggered by a TTL pulse with a variable pulse duration and timing and which is synchronized to the driving IR laser.

A.4 Assembly and adjustment

The mounting procedure of the piezo valve is relatively easy, although there are a few points that have to be taken into account. A step-by-step description of the mounting and adjusting procedure is given.

Assembling the piezo valve

1. Clamp the piezo (7) onto the back side of the valve (11) using the RVS bar (4). The free length of the piezo should be 6 mm and is measured with a caliper.

2. Glue the vespel pillar (5) onto the piezo plate with two-component glue (i.e. Araldite 2011). The position of the vespel pillar is determined by a mounting mold that fits over the valve housing (back). The mold has a small notch for the vespel pillar. A curing time of the glue has to be taken into account, before proceeding with the following steps

3. Make an electrical connection from the electric feedthrough (13) to the RVS bar (4).

4. Mount the vespel translation rings (9) and O-ring (10) onto rim of the valve housing (back) (11) and put the wave spring (8) on the valve housing.

5. Slide the back-side (11) of the valve into the repeller housing (1). Note that the O-ring can easily be damaged during this step and lubrication of the O-ring is therefore essential.

6. First, press the back of the valve gently towards the repeller housing with your hand. The thread of the vespel ring is very fine and cannot withstand the pressure of the spring in the first few turns. Next, screw the vespel adjustment ring onto the repeller housing, by first turning the ring anti-clockwise to find the beginning of the thread. After you feel a small 'click' you can screw the ring clock-wise until the top of the ring is (almost) leveled with the rim of the repeller housing. A small tool is provided that facilitates turning the vespel ring.

7. Make an electrical connection from the valve housing (back) to provide the pulsed valve driver with the floating ground potential. There is a screwing thread in the valve for attaching the electrical connection.

Adjusting the piezo valve

The fine adjustment of the valve is most easily done by mounting the repeller with the integrated piezo valve onto the fast ion gauge test chamber, which will be described in the next section. Alternatively a small vacuum test stage would suffice. The vacuum chamber should one to translate the vespel adjustment ring without opening the vacuum chamber.

Most likely the piezo valve is not closed yet by the viton disk. When a pressure of $\sim 10^{-3}$ mbar is reached in the test chamber, you can turn the vespel ring clockwise

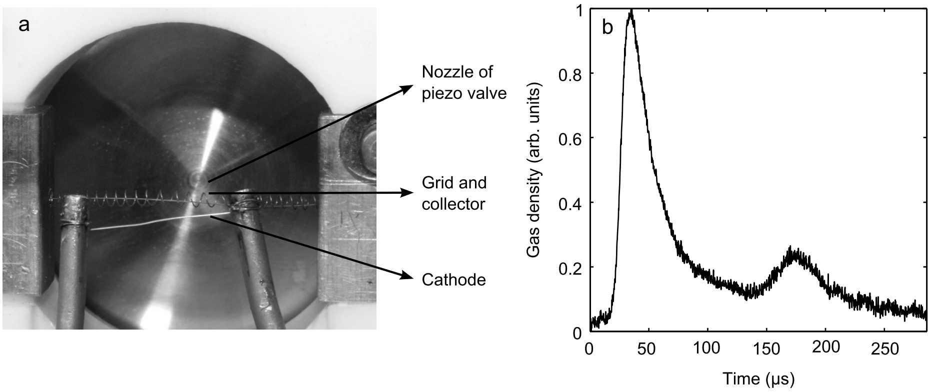

Figure A.4: a) The fast ionization gauge that was built at the AMOLF institute. The fast ionization gauge had a cathode, a grid with a diameter of 1 mm and a collector. The fast ionization gauge is mounted on a vacuum flange and the piezo valve is mounted on the outside of this flange. This configuration allows one to adjust the valve while monitoring the gas pulse with the fast ionization gauge. b) Gas pulse profile as measured with the fast ionization gauge. The fast piezo valve was operated at a repetition frequency of 3 kHz, with a pulse duration of 33 μs and voltage of 55 V and a backing pressure of 3 bar. The dominant peak corresponds to the response of the piezo to the voltage pulse, whereas the second peak is due to a bouncing of the vespel pillar onto the repeller.

until the pressure in the vacuum chamber drops. In this step, there is a potential danger of breaking the piezo when the back side of the valve is too close to the repeller housing. A good way of checking whether the piezo is broken, is to measure the capacity via the electric feedthrough. The capacity should be $\sim$ 2.6 nF.

The vespel ring should be set such that the valve produces a reasonable gas pressure in the chamber at $\sim$ 60 V and does not leak into the chamber when no voltage is applied. Typically, for the test chamber at AMOLF with a turbo pump of 200 L/s, we set the vespel ring such that the pressure reaches $\sim 10^{-5}$ mbar at a voltage of 60 V at a backing pressure of 2-3 bar and a voltage pulse duration of 25-35 μs. Note that the ring is not easily moved with a backing pressure > 1 bar and you should release the gas pressure when adjusting the valve.

Note that the current valve should not be evacuated when it is in atmospheric pressure. The spring is not strong enough to prevent the back-side of the valve collapsing into the repeller housing, thereby breaking the piezo.

A.5 Characterization of gas pulses

A.5.1 Fast ionization gauge

The output pulses from the pulsed piezo valve are characterized by a custom-made fast ionization gauge (FIG) [234]. The FIG is based on a common Bayard-Alpert type ionization gauge, comprising a grid, a cathode and an ion collector. By decreasing the grid dimension to $d = 1$ mm a time resolution of a few microseconds can be obtained. The current from the FIG is amplified by a current-to-voltage amplifier (FEMTO DHPCA-100) and read out by an oscilloscope. The AMOLF-built FIG is shown in Figure A.4a. The fast pulsed piezo valve is mounted onto the vacuum flange, which accommodates the FIG, thereby allowing an easy adjustment of the piezo valve while monitoring the output gas pulse.

A.5.2 Fast piezo valve performance

In Figure A.4b, a trace from the fast ionization gauge is shown. We observe two peaks in the trace, the dominant peak corresponds to the response of the piezo to the voltage pulse, whereas the second peak is due to a bouncing of the vespel pillar onto the repeller. This was previously observed in the piezo valve constructed by D. Gerlich [229].

The gas output of the fast piezo valve is strongly dependent on the pulse duration and voltage of the driving pulse, as well as the backing pressure and the distance of the viton disk to the nozzle. To illustrate the effect of these control parameters, we assume that the total gas output is the same.

The pulse duration of the driving pulse influences the gas pulse profile and total gas output. Increasing the gas pulse duration will in general result in a more symmetric gas pulse and a higher gas output. The gas pulse duration itself is actually not so much influenced by the driver pulse duration. The fast piezo valve at AMOLF is usually operated with a pulse duration of ~ 30 μs. The second control parameter is the voltage of the driving pulse, which influences the deflection of the piezo and thereby determines the flow through the nozzle. As one can expect, increasing the voltage will result in a higher gas throughput. There is however one complication, the bouncing of the vespel pillar onto the repeller is more pronounced for higher voltages. Therefore, increasing the voltage pulse duration will lead to a decreased ratio of the first/second peak. The third parameter that controls the gas output is the backing pressure of the gas. A higher backing pressure will result in a higher gas output and a colder molecular beam. There is however a limit of 5 bar that can be used as a backing pressure [229]. In the operation of the pulsed piezo valve we found that the viton disk should be more closely pressed onto the nozzle for increasingly high backing pressure, which increases the voltage of the driver pulse to obtain the same opening. The distance of the viton disk to the nozzle is therefore a very important parameter, which determines the maximum deflection and the maximum backing pressure that can be applied.

In the operation of the pulsed valve at AMOLF we adjust the distance of the viton disk to the nozzle such that there is no leakage of the valve with a backing pressure of 2-3 bar. The pulse valve is used with a backing pressure of 1-2 bar and driven with a pulse duration of ~ 30 μs. The desired gas output is then easily adjusted by changing the applied voltage on the piezo.

A.6 Conclusion

A high-repetition rate fast piezo valve is presented that is incorporated into the repeller electrode of a velocity map imaging spectrometer. The piezo valve is based on a cantilever design first presented by D. Gerlich [229] and allows to generate gas pulses with a frequency of 3 kHz, synchronized to the repetition rate of the HHG setup at AMOLF. The gas pulses have a pulse duration with a FWHM of 28 μs. The effusive repeller with the integrated pulsed piezo valve allows one to reach a gas density in the interaction region that is 2-3 orders of magnitude higher than with a molecular beam.

REFERENCES

[1] J. Brown and A. Carrington. *Rotational spectroscopy of diatomic molecules.* Cambridge University Press (2003).

[2] M. Diem. *Introduction into modern vibrational spectroscopy.* Wiley-Interscience (1993).

[3] F. Rouessac and A. Rouessac. *Chemical Analysis: Modern Instrumentation Methods and Techniques.* Wiley, 2nd edition ed. (2007).

[4] R. G. Gould. *The LASER, Light Amplification by Stimulated Emission of Radiation.* In P. Franken and R. E. Sands, eds., *The Ann Arbor Conference on Optical Pumping, the University of Michigan* (1959), p128.

[5] T. Maiman. *Stimulated Optical Radiation in Ruby.* Nature, **187**, 493–494 (1960).

[6] P. F. Moulton. *Spectroscopic and laser characteristics of Ti:Al_2O_3.* J. Opt. Soc. Am. B, **3**, 125–133 (1986).

[7] T. Brabec and F. Krausz. *Intense few-cycle laser fields: Frontiers of nonlinear optics.* Rev. Mod. Phys., **72**, 545 (2000).

[8] P. M. Paul, E. S. Toma, P. Breger, G. Mullot, F. Auge, P. Balcou, H. G. Muller and P. Agostini. *Observation of a train of attosecond pulses from high harmonic generation.* Science, **292**, 1689–1692 (2001).

[9] L. V. Keldysh. Zh. Eksp. Teor. Fiz., **47**, 1945 (1964). [Sov. Phys. JETP **20**, 1307 (1965)].

[10] W. Becker, F. Grasbon, R. Kopold, D. B. Milosevic, G. G. Paulus and H. Walther. *Above-threshold ionization: From classical features to quantum effects.* Adv. At. Mol. Opt. Phys., **48**, 35–98 (2002).

[11] P. Hansch, M. A. Walker and L. D. Van Woerkom. *Resonant hot-electron production in above-threshold ionization.* Phys. Rev. A, **55**, R2535–R2538 (1997).

[12] J. J. Macklin, J. D. Kmetec and C. L. Gordon. *High-order harmonic generation using intense femtosecond pulses.* Phys. Rev. Lett., **70**, 766–769 (1993).

[13] P. B. Corkum. *Plasma Perspective on Strong-Field Multiphoton Ionization.* Phys. Rev. Lett., **71**, 1994–1997 (1993).

[14] G. G. Paulus, W. Becker, W. Nicklich and H. Walther. *Rescattering Effects in above-Threshold Ionization - a Classical-Model.* J. Phys. B-At. Mol. Opt., **27**, L703–L708 (1994).

[15] D. N. Fittinghoff, P. R. Bolton, B. Chang and K. C. Kulander. *Observation of nonsequential double ionization of helium with optical tunneling.* Phys. Rev. Lett., **69**, 2642–2645 (1992).

[16] A. McPherson, G. Gibson, H. Jara, U. Johann, T. S. Luk, I. A. McIntyre, K. Boyer and C. K. Rhodes. *Studies of multiphoton production of vacuum-ultraviolet radiation in the rare gases.* J. Opt. Soc. Am. B, **4**, 595–601 (1987).

[17] M. Ferray, A. L'Huillier, X. F. Li, L. A. Lompre, G. Mainfray and C. Manus. *Multiple-harmonic conversion of 1064 nm radiation in rare gases.* J. Phys. B: At., Mol. Opt. Phys., **21**, L31 (1988).

[18] P. H. Bucksbaum, R. R. Freeman, M. Bashkansky and T. J. McIlrath. *Role of the ponderomotive potential in above-threshold ionization.* J. Opt. Soc. Am. B, **4**, 760–764 (1987).

[19] J. Zhou, J. Peatross, M. M. Murnane and H. C. Kapteyn. *Enhanced high-harmonic generation using 25 fs laser pulses.* Phys. Rev. Lett., **76**, 752–755 (1996).

[20] M. Nisoli, S. DeSilvestri and O. Svelto. *Generation of high energy 10 fs pulses by a new pulse compression technique.* Appl. Phys. Lett., **68**, 2793–2795 (1996).

[21] M. Nisoli, S. DeSilvestri, O. Svelto, R. Szipocs, K. Ferencz, C. Spielmann, S. Sartania and F. Krausz. *Compression of high-energy laser pulses below 5 fs.* Opt. Lett., **22**, 522–524 (1997).

[22] A. L. Cavalieri *et al. Intense 1.5-cycle near infrared laser waveforms and their use for the generation of ultra-broadband soft-x-ray harmonic continua.* New Journal of Physics, **9**, 242 (2007).

[23] D. J. Jones, S. A. Diddams, J. K. Ranka, A. Stentz, R. S. Windeler, J. L. Hall and S. T. Cundiff. *Carrier-envelope phase control of femtosecond mode-locked lasers and direct optical frequency synthesis.* Science, **288**, 635–639 (2000).

[24] A. Baltuska *et al. Attosecond control of electronic processes by intense light fields.* Nature, **421**, 611–615 (2003).

[25] G. L. Yudin and M. Y. Ivanov. *Nonadiabatic tunnel ionization: Looking inside a laser cycle.* Phys. Rev. A, **6401**, 013409 (2001).

[26] M. Uiberacker *et al. Attosecond real-time observation of electron tunnelling in atoms.* Nature, **446**, 627–632 (2007).

[27] F. Lindner, M. G. Schatzel, H. Walther, A. Baltuska, E. Goulielmakis, F. Krausz, D. B. Milosevic, D. Bauer, W. Becker and G. G. Paulus. *Attosecond double-slit experiment.* Phys. Rev. Lett., **95**, 040401 (2005).

[28] D. B. Milosevic, G. G. Paulus, D. Bauer and W. Becker. *Above-threshold ionization by few-cycle pulses.* J. Phys. B-At. Mol. Opt., **39**, R203–R262 (2006).

[29] G. G. Paulus, F. Lindner, H. Walther, A. Baltuska, E. Goulielmakis, M. Lezius and F. Krausz. *Measurement of the phase of few-cycle laser pulses.* Phys. Rev. Lett., **91**, 253004 (2003).

[30] M. Lewenstein and A. L'Huillier. *Strong Field Laser Physics.* Springer (2008).

[31] A. de Bohan, P. Antoine, D. B. Milošević and B. Piraux. *Phase-Dependent Harmonic Emission with Ultrashort Laser Pulses.* Phys. Rev. Lett., **81**, 1837–1840 (1998).

[32] M. Nisoli, G. Sansone, S. Stagira, S. De Silvestri, C. Vozzi, M. Pascolini, L. Poletto, P. Villoresi and G. Tondello. *Effects of Carrier-Envelope Phase Differences of Few-Optical-Cycle Light Pulses in Single-Shot High-Order-Harmonic Spectra.* Phys. Rev. Lett., **91**, 213905 (2003).

[33] C. A. Haworth, L. E. Chipperfield, J. S. Robinson, P. L. Knight, J. P. Marangos and J. W. G. Tisch. *Half-cycle cutoffs in harmonic spectra and robust carrier-envelope phase retrieval.* Nat. Phys., **3**, 52–57 (2007).

[34] M. F. Kling *et al. Control of electron localization in molecular dissociation.* Science, **312**, 246–248 (2006).

[35] A. Rundquist, C. G. Durfee, Z. H. Chang, C. Herne, S. Backus, M. M. Murnane and H. C. Kapteyn. *Phase-matched generation of coherent soft X-rays.* Science, **280**, 1412–1415 (1998).

[36] G. Sansone *et al. Isolated single-cycle attosecond pulses.* Science, **314**, 443–446 (2006).

[37] A. H. Zewail. *Femtochemistry: Atomic-scale dynamics of the chemical bond.* J. Phys. Chem. A, **104**, 5660–5694 (2000).

[38] E. Gagnon, P. Ranitovic, X. M. Tong, C. L. Cocke, M. M. Murnane, H. C. Kapteyn and A. S. Sandhu. *Soft X-ray-driven femtosecond molecular dynamics.* Science, **317**, 1374–1378 (2007).

[39] F. Kelkensberg *et al. Molecular Dissociative Ionization and Wave-Packet Dynamics Studied Using Two-Color XUV and IR Pump-Probe Spectroscopy.* Phys. Rev. Lett., **103**, 123005 (2009).

[40] A. Stolow, A. E. Bragg and D. M. Neumark. *Femtosecond time-resolved photoelectron spectroscopy.* Chem. Rev., **104**, 1719–1757 (2004).

[41] P. Wernet, M. Odelius, K. Godehusen, J. Gaudin, O. Schwarzkopf and W. Eberhardt. *Real-Time Evolution of the Valence Electronic Structure in a Dissociating Molecule.* Phys. Rev. Lett., **103**, 013001 (2009).

[42] M. Bauer, C. Lei, K. Read, R. Tobey, J. Gland, M. M. Murnane and H. C. Kapteyn. *Direct Observation of Surface Chemistry Using Ultrafast Soft-X-Ray Pulses.* Phys. Rev. Lett., **87**, 025501 (2001).

[43] F. Krausz and M. Ivanov. *Attosecond physics.* Rev. Mod. Phys., **81**, 163–234 (2009).

[44] J. Itatani, F. Quere, G. L. Yudin, M. Y. Ivanov, F. Krausz and P. B. Corkum. *Attosecond streak camera.* Phys. Rev. Lett., **88**, 173903 (2002).

[45] E. Goulielmakis *et al. Direct Measurement of Light Waves.* Science, **305**, 1267–1269 (2004).

[46] M. Schultze *et al. Delay in Photoemission.* Science, **328**, 1658–1662 (2010).

[47] A. L. Cavalieri *et al. Attosecond spectroscopy in condensed matter.* Nature, **449**, 1029–1032 (2007).

[48] E. Goulielmakis *et al. Real-time observation of valence electron motion.* Nature, **466**, 739 (2010).

[49] F. Remacle and R. D. Levine. *An electronic time scale in chemistry.* Proc. Natl. Acad. Sci. U. S. A., **103**, 6793–6798 (2006).

[50] G. Sansone *et al. Electron Localization following Attosecond Molecular Photoionization.* Nature, 763–766 (2010).

[51] W. Ackermann *et al. Operation of a free-electron laser from the extreme ultraviolet to the water window.* Nat. Photonics, **1**, 336–342 (2007).

[52] Y. Ding *et al. Measurements and Simulations of Ultralow Emittance and Ultrashort Electron Beams in the Linac Coherent Light Source.* Phys. Rev. Lett., **102**, 254801 (2009).

[53] A. A. Sorokin, S. V. Bobashev, T. Feigl, K. Tiedtke, H. Wabnitz and M. Richter. *Photoelectric effect at ultrahigh intensities.* Phys. Rev. Lett., **99**, 213002 (2007).

[54] M. G. Makris, P. Lambropoulos and A. Mihelič. *Theory of Multiphoton Multielectron Ionization of Xenon under Strong 93-eV Radiation.* Phys. Rev. Lett., **102**, 033002 (2009).

[55] L. Young *et al. Femtosecond electronic response of atoms to ultra-intense X-rays.* Nature, **466**, 56 (2010).

[56] *FLASH the free electron laser in Hamburg.* Brochure (2007).

[57] F. Krasniqi, B. Najjari, L. Struder, D. Rolles, A. Voitkiv and J. Ullrich. *Imaging molecules from within: Ultrafast angstrom-scale structure determination of molecules via photoelectron holography using free-electron lasers.* Phys. Rev. A, **81**, 033411 (2010).

[58] R. Neutze, R. Wouts, D. van der Spoel, E. Weckert and J. Hajdu. *Potential for biomolecular imaging with femtosecond X-ray pulses.* Nature, **406**, 752–757 (2000).

[59] H. N. Chapman *et al. Femtosecond diffractive imaging with a soft-X-ray free-electron laser.* Nature Phys., **2**, 839 (2006).

[60] H. N. Chapman *et al. Femtosecond X-ray protein nanocrystallography.* Nature, **470**, 73–77 (2011).

[61] A. Landers *et al. Photoelectron diffraction mapping: Molecules illuminated from within.* Phys. Rev. Lett., **8701**, 013002 (2001).

[62] R. Dorner, V. Mergel, O. Jagutzki, L. Spielberger, J. Ullrich, R. Moshammer and H. Schmidt-Bocking. *Cold Target Recoil Ion Momentum Spectroscopy: a 'momentum microscope' to view atomic collision dynamics.* Physics Reports-Review Section of Physics Letters, **330**, 95–192 (2000).

[63] A. T. J. B. Eppink and D. H. Parker. *Velocity map imaging of ions and electrons using electrostatic lenses: Application in photoelectron and photofragment ion imaging of molecular oxygen.* Rev. Sci. Instrum., **68**, 3477–3484 (1997).

[64] F. Rosca-Pruna and M. J. J. Vrakking. *Experimental observation of revival structures in picosecond laser-induced alignment of I_2.* Phys. Rev. Lett., **87**, 153902 (2001).

[65] P. Johnsson *et al. Field-free molecular alignment probed by the free electron laser in Hamburg (FLASH).* J. Phys. B-At. Mol. Opt., **42**, 134017 (2009).

[66] R. Kienberger *et al. Steering attosecond electron wave packets with light.* Science, **297**, 1144–1148 (2002).

[67] R. Kienberger *et al. Atomic transient recorder.* Nature, **427**, 817–821 (2004).

[68] J. C. Diels and W. Rudolph. *Ultrashort Laser Pulse Phenomena.* Academic Press, New York, 2nd. ed. (2006).

[69] S. Backus, C. G. Durfee, M. M. Murnane and H. C. Kapteyn. *High power ultrafast lasers.* Rev. Sci. Instrum., **69**, 1207–1223 (1998).

[70] G. Steinmeyer. *A review of ultrafast optics and optoelectronics.* J. Opt. A: Pure Appl. Opt., **5**, R1–R15 (2003).

[71] A. Shirakawa, I. Sakane, M. Takasaka and T. Kobayashi. *Sub-5-fs visible pulse generation by pulse-front-matched noncollinear optical parametric amplification.* Appl. Phys. Lett., **74**, 2268–2270 (1999).

[72] G. Cerullo and S. De Silvestri. *Ultrafast optical parametric amplifiers.* Rev. Sci. Instrum., **74**, 1–18 (2003).

[73] D. Herrmann, L. Veisz, R. Tautz, F. Tavella, K. Schmid, V. Pervak and F. Krausz. *Generation of sub-three-cycle, 16 TW light pulses by using noncollinear optical parametric chirped-pulse amplification.* Opt. Lett., **34**, 2459–2461 (2009).

[74] F. Tavella *et al. Fiber-amplifier pumped high average power few-cycle pulse non-collinear OPCPA.* Opt. Express, **18**, 4689–4694 (2010).

[75] M. Schultze, T. Binhammer, A. Steinmann, G. Palmer, M. Emons and U. Morgner. *Few-cycle OPCPA system at 143 kHz with more than 1 μJ of pulse energy.* Opt. Express, **18**, 2836–2841 (2010).

[76] G. G. Paulus, F. Grasbon, H. Walther, P. Villoresi, M. Nisoli, S. Stagira, E. Priori and S. De Silvestri. *Absolute-phase phenomena in photoionization with few-cycle laser pulses.* Nature, **414**, 182–184 (2001).

[77] C. Q. Li, E. Moon, H. Mashiko, C. M. Nakamura, P. Ranitovic, C. M. Maharjan, C. L. Cocke, Z. H. Chang and G. G. Paulus. *Precision control of carrier-envelope phase in grating based chirped pulse amplifiers.* Opt. Express, **14**, 11468–11476 (2006).

[78] L. Canova, X. W. Chen, A. Trisorio, A. Jullien, A. Assion, G. Tempea, N. Forget, T. Oksenhendler and R. Lopez-Martens. *Carrier-envelope phase stabilization and control using a transmission grating compressor and an AOPDF.* Opt. Lett., **34**, 1333–1335 (2009).

[79] T. Fordell, M. Miranda, A. Persson and A. L'Huillier. *Carrier-envelope phase stabilization of a multi-millijoule, regenerative-amplifier-based chirped-pulse amplifier system.* Opt. Express, **17**, 21091–21097 (2009).

[80] S. Koke, C. Grebing, H. Frei, A. Anderson, A. Assion and G. Steinmeyer. *Direct frequency comb synthesis with arbitrary offset and shot-noise-limited phase noise.* Nat. Photonics, **4**, 462 (2010).

[81] T. Wittmann, B. Horvath, W. Helml, M. G. Schatzel, X. Gu, A. L. Cavalieri, G. G. Paulus and R. Kienberger. *Single-shot carrier-envelope phase measurement of few-cycle laser pulses.* Nat. Phys., **5**, 357–362 (2009).

[82] S. Bohman, A. Suda, M. Kaku, M. Nurhuda, T. Kanai, S. Yamaguchi and K. Midorikawa. *Generation of 5 fs, 0.5 TW pulses focusable to relativistic intensities at 1 kHz.* Opt. Express, **16**, 10684–10689 (2008).

[83] X. Chen, L. Canova, A. Malvache, A. Jullien, R. Lopez-Martens, C. Durfee, D. Papadopoulos and F. Druon. *1-mJ, sub-5-fs carrier-envelope phase-locked pulses.* Appl. Phys. B: Lasers Opt., **99**, 149–157 (2010).

[84] C. P. Hauri, W. Kornelis, F. W. Helbing, A. Heinrich, A. Couairon, A. Mysyrowicz, J. Biegert and U. Keller. *Generation of intense, carrier-envelope phase-locked few-cycle laser pulses through filamentation.* Appl. Phys. B: Lasers Opt., **79**, 673–677 (2004).

[85] L. Gallmann, T. Pfeifer, P. M. Nagel, M. J. Abel, D. M. Neumark and S. R. Leone. *Comparison of the filamentation and the hollow-core fiber characteristics for pulse compression into the few-cycle regime.* Appl. Phys. B: Lasers Opt., **86**, 561–566 (2007).

[86] K. J. Schafer, B. Yang, L. F. Dimauro and K. C. Kulander. *Above Threshold Ionization Beyond the High Harmonic Cutoff.* Phys. Rev. Lett., **70**, 1599–1602 (1993).

[87] M. Lewenstein, P. Balcou, M. Y. Ivanov, A. L'Huillier and P. B. Corkum. *Theory of High-Harmonic Generation by Low-Frequency Laser Fields.* Phys. Rev. A, **49**, 2117–2132 (1994).

[88] P. Salieres *et al. Feynman's path-integral approach for intense-laser-atom interactions.* Science, **292**, 902–905 (2001).

[89] P. Balcou, P. Salieres, A. L'Huillier and M. Lewenstein. *Generalized phase-matching conditions for high harmonics: The role of field-gradient forces.* Phys. Rev. A, **55**, 3204–3210 (1997).

[90] M. B. Gaarde, J. L. Tate and K. J. Schafer. *Macroscopic aspects of attosecond pulse generation.* J. Phys. B-At. Mol. Opt., **41**, 132001 (2008).

[91] P. Salières and I. Christov. *Macroscopic Effects in High-Order Harmonic Generation.* In *Strong Field Laser Physics*, 261–280 (2008).

[92] P. Salieres, A. L'Huillier and M. Lewenstein. *Coherence Control of High-Order Harmonics.* Phys. Rev. Lett., **74**, 3776–3779 (1995).

[93] Y. Mairesse *et al. Attosecond synchronization of high-harmonic soft x-rays.* Science, **302**, 1540–1543 (2003).

[94] M. Bellini, C. Lynga, A. Tozzi, M. B. Gaarde, T. W. Hansch, A. L'Huillier and C. G. Wahlstrom. *Temporal coherence of ultrashort high-order harmonic pulses.* Phys. Rev. Lett., **81**, 297–300 (1998).

[95] E. Constant, D. Garzella, P. Breger, E. Mevel, C. Dorrer, C. Le Blanc, F. Salin and P. Agostini. *Optimizing high harmonic generation in absorbing gases: Model and experiment.* Phys. Rev. Lett., **82**, 1668–1671 (1999).

[96] C. G. Durfee, A. R. Rundquist, S. Backus, C. Herne, M. M. Murnane and H. C. Kapteyn. *Phase matching of high-order harmonics in hollow waveguides.* Phys. Rev. Lett., **83**, 2187–2190 (1999).

[97] A. Paul, R. A. Bartels, R. Tobey, H. Green, S. Weiman, I. P. Christov, M. M. Murnane, H. C. Kapteyn and S. Backus. *Quasi-phase-matched generation of coherent extreme-ultraviolet light.* Nature, **421**, 51–54 (2003).

[98] E. A. Gibson *et al. Coherent soft x-ray generation in the water window with quasi-phase matching.* Science, **302**, 95–98 (2003).

[99] T. Popmintchev, M. C. Chen, A. Bahabad, M. Gerrity, P. Sidorenko, O. Cohen, I. P. Christov, M. M. Murnane and H. C. Kapteyn. *Phase matching of high harmonic generation in the soft and hard X-ray regions of the spectrum.* Proc. Natl. Acad. Sci. U. S. A., **106**, 10516–10521 (2009).

[100] M. Hentschel, R. Kienberger, C. Spielmann, G. A. Reider, N. Milosevic, T. Brabec, P. Corkum, U. Heinzmann, M. Drescher and F. Krausz. *Attosecond metrology.* Nature, **414**, 509–513 (2001).

[101] I. J. Sola *et al. Controlling attosecond electron dynamics by phase-stabilized polarization gating.* Nat. Phys., **2**, 319–322 (2006).

[102] P. Tzallas, E. Skantzakis, C. Kalpouzos, E. P. Benis, G. D. Tsakiris and D. Charalambidis. *Generation of intense continuum extreme-ultraviolet radiation by many-cycle laser fields.* Nat. Phys., **3**, 846–850 (2007).

[103] Y. Oishi, M. Kaku, A. Suda, F. Kannari and K. Midorikawa. *Generation of extreme ultraviolet continuum radiation driven by a sub-10-fs two-color field.* Opt. Express, **14**, 7230–7237 (2006).

[104] X. M. Feng, S. Gilbertson, H. Mashiko, H. Wang, S. D. Khan, M. Chini, Y. Wu, K. Zhao and Z. H. Chang. *Generation of Isolated Attosecond Pulses with 20 to 28 Femtosecond Lasers.* Phys. Rev. Lett., **103**, 183901 (2009).

[105] R. Lopez-Martens *et al. Amplitude and phase control of attosecond light pulses.* Phys. Rev. Lett., **94**, 033001 (2005).

[106] S. A. Aseyev, Y. Ni, L. J. Frasinski, H. G. Muller and M. J. J. Vrakking. *Attosecond angle-resolved photoelectron spectroscopy.* Phys. Rev. Lett., **91**, 223902 (2003).

[107] I. J. Kim, C. M. Kim, H. T. Kim, G. H. Lee, Y. S. Lee, J. Y. Park, D. J. Cho and C. H. Nam. *Highly efficient high-harmonic generation in an orthogonally polarized two-color laser field.* Phys. Rev. Lett., **94**, 243901 (2005).

[108] J. Mauritsson, P. Johnsson, E. Gustafsson, A. L'Huillier, K. J. Schafer and M. B. Gaarde. *Attosecond pulse trains generated using two color laser fields.* Phys. Rev. Lett., **97**, 013001 (2006).

[109] E. Goulielmakis *et al. Single-cycle nonlinear optics.* Science, **320**, 1614–1617 (2008).

[110] P. B. Corkum, N. H. Burnett and M. Y. Ivanov. *Subfemtosecond Pulses.* Opt. Lett., **19**, 1870–1872 (1994).

[111] D. Charalambidis, P. Tzallas, E. P. Benis, E. Skantzakis, G. Maravelias, L. A. A. Nikolopoulos, A. P. Conde and G. D. Tsakiris. *Exploring intense attosecond pulses.* New Journal of Physics, **10**, 025018 (2008).

[112] H. Mashiko, S. Gilbertson, C. Q. Li, S. D. Khan, M. M. Shakya, E. Moon and Z. H. Chang. *Double optical gating of high-order harmonic generation with carrier-envelope phase stabilized lasers.* Phys. Rev. Lett., **100**, 103906 (2008).

[113] M. J. Abel, T. Pfeifer, P. M. Nagel, W. Boutu, M. J. Bell, C. P. Steiner, D. M. Neumark and S. R. Leone. *Isolated attosecond pulses from ionization gating of high-harmonic emission.* Chem. Phys., **366**, 9–14 (2009).

[114] I. Thomann, A. Bahabad, X. Liu, R. Trebino, M. M. Murnane and H. C. Kapteyn. *Characterizing isolated attosecond pulses from hollow-core waveguides using multi-cycle driving pulses.* Opt. Express, **17**, 4611–4633 (2009).

[115] M. Drescher, M. Hentschel, R. Kienberger, G. Tempea, C. Spielmann, G. A. Reider, P. B. Corkum and F. Krausz. *X-ray pulses approaching the attosecond frontier.* Science, **291**, 1923–1927 (2001).

[116] F. M. Bottcher, B. Manschwetus, H. Rottke, N. Zhavoronkov, Z. Ansari and W. Sandner. *Interferometric long-term stabilization of a delay line: a tool for pump-probe photoelectron-photoion-coincidence spectroscopy on the attosecond time scale.* Appl. Phys. B: Lasers Opt., **91**, 287–293 (2008).

[117] M. Chini, H. Mashiko, H. Wang, S. Y. Chen, C. X. Yun, S. Scott, S. Gilbertson and Z. H. Chang. *Delay control in attosecond pump-probe experiments.* Opt. Express, **17**, 21459–21464 (2009).

[118] P. Kruit and F. H. Read. *Magnetic field paralleliser for 2π electron-spectrometer and electron-image magnifier.* J. Phys. E: Sci. Instrum., **16**, 313–324 (1983).

[119] M. J. J. Vrakking. *An iterative procedure for the inversion of two-dimensional ion/photoelectron imaging experiments.* Rev. Sci. Instrum., **72**, 4084–4089 (2001).

[120] O. Ghafur, W. Siu, P. Johnsson, M. F. Kling, M. Drescher and M. J. J. Vrakking. *A velocity map imaging detector with an integrated gas injection system.* Rev. Sci. Instrum., **80**, 033110 (2009).

[121] L. Poletto and G. Tondello. *Design of a high-throughput grazing-incidence flat-field spectrometer.* Appl. Optics, **39**, 4000–4006 (2000).

[122] L. Poletto, G. Tondello and P. Villoresi. *High-order laser harmonics detection in the EUV and soft x-ray spectral regions.* Rev. Sci. Instrum., **72**, 2868–2874 (2001).

[123] *http : //henke.lbl.gov/optical_constants/.*

[124] A. S. Morlens, P. Balcou, P. Zeitoun, C. Valentin, V. Laude and S. Kazamias. *Compression of attosecond harmonic pulses by extreme-ultraviolet chirped mirrors.* Opt. Lett., **30**, 1554–1556 (2005).

[125] A. S. Morlens *et al. Design and characterization of extreme-ultraviolet broadband mirrors for attosecond science.* Opt. Lett., **31**, 1558–1560 (2006).

[126] J. H. Posthumus. *The dynamics of small molecules in intense laser fields.* Rep. Prog. Phys., **67**, 623–665 (2004).

[127] T. Kanai, S. Minemoto and H. Sakai. *Quantum interference during high-order harmonic generation from aligned molecules.* Nature, **435**, 470–474 (2005).

[128] J. Itatani, J. Levesque, D. Zeidler, H. Niikura, H. Pepin, J. C. Kieffer, P. B. Corkum and D. M. Villeneuve. *Tomographic imaging of molecular orbitals.* Nature, **432**, 867–871 (2004).

[129] T. Remetter *et al. Attosecond electron wave packet interferometry.* Nat. Phys., **2**, 323–326 (2006).

[130] A. Gijsbertsen, H. Linnartz, J. Kos and S. Stolte. *What is Wrong with the Steric Asymmetry in Atom-Molecule Collisions?* Phys. Scr., **72**, C1 (2005).

[131] A. Gijsbertsen, M. J. L. de Lange, A. E. Wiskerke, H. Linnartz, M. Drabbels, J. Klos and S. Stolte. *Sign of the state-to-state steric asymmetry of rotationally inelastic atom-molecule collisions.* Chem. Phys., **301**, 293 – 308 (2004). Stereodynamics of Molecular Reactions.

[132] M. J. L. de Lange, S. Stolte, C. A. Taatjes, J. Klos, G. C. Groenenboom and A. van der Avoird. *Steric asymmetry and lambda-doublet propensities in state-to-state rotationally inelastic scattering of NO($^2\Pi\frac{1}{2}$) with He.* J. Chem. Phys., **121**, 11691–11701 (2004).

[133] C. A. Taatjes, A. Gijsbertsen, M. J. L. de Lange and S. Stolte. *Measurements and Quasi-Quantum Modeling of the Steric Asymmetry and Parity Propensities in State-to-State Rotationally Inelastic Scattering of NO ($^2\Pi_{\frac{1}{2}}$) with D_2.* J. Phys. Chem. A, **111**, 7631–7639 (2007). PMID: 17542569.

[134] A. Hoy, J. Johns and A. R. McKellar. Can. J. Phys./Rev. Can. Phys., **53**, 2029 (1975).

[135] S. R. Langhoff, C. W. Bauschlicher and H. Partridge. *Theoretical dipole moment for the X $^2\Pi$ state of NO.* Chem. Phys. Lett., **223**, 416 – 422 (1994).

[136] S. Green. *Calculated properties for NO X $^2\Pi$ and A $^2\Sigma^+$. II. Configuration interaction.* Chem. Phys. Lett., **23**, 115 – 119 (1973).

[137] R. Sayos, R. Valero, J. M. Anglada and M. Gonzalez. *Theoretical investigation of the eight low-lying electronic states of the cis- and trans-nitric oxide dimers and its isomerization using multiconfigurational second-order perturbation theory (CASPT2).* J. Chem. Phys., **112**, 6608–6624 (2000).

[138] F. P. Billingsley II. *Multiconfiguration self-consistent-field calculation of the dipole moment function and potential curve of NO(X $^2\Pi$).* The Journal of Chemical Physics, **62**, 864–874 (1975).

[139] C. Townes and A. Schawlow. *Microwave Spectroscopy.* McGraw-Hill, New York (1955).

[140] J. M. L. J. Reinartz, W. L. Meerts and A. Dymanus. *Hyperfine structure, electric and magnetic properties of $^{14}N_2$ ^{16}O in the ground and first excited bending vibrational state.* Chem. Phys., **31**, 19 – 29 (1978).

[141] M. Drabbels and A. Wodtke. *The electric dipole moment and hyperfine structure of NO B* $^2\Pi$*: high resolution laser-induced fluorescence spectroscopy of the* $B\ ^2\Pi(\nu = 3-5) \ll X\ ^2\Pi(\nu = 0)$ *bands.* Chem. Phys. Lett., **256**, 8 – 14 (1996).

[142] K. H. Kramer and R. B. Bernstein. *Sudden Approximation Applied to Rotational Excitation of Molecules by Atoms. I. Low-Angle Scattering.* J. Chem. Phys., **40**, 200–203 (1964).

[143] M. G. Tenner, E. W. Kuipers, W. Y. Langhout, A. W. Kleyn, G. Nicolasen and S. Stolte. *Molecular beam apparatus to study interactions of oriented NO and surfaces.* Surf. Sci., **236**, 151 – 168 (1990).

[144] H. Stapelfeldt and T. Seideman. *Colloquium: Aligning molecules with strong laser pulses.* Rev. Mod. Phys., **75**, 543–557 (2003).

[145] F. Rosca-Pruna, E. Springate, H. L. Offerhaus, M. Krishnamurthy, N. Farid, C. Nicole and M. J. J. Vrakking. *Spatial alignment of diatomic molecules in intense laser fields: I. Experimental results.* J. Phys. B-At. Mol. Opt., **34**, 4919–4938 (2001).

[146] M. J. J. Vrakking and S. Stolte. *Coherent control of molecular orientation.* Chem. Phys. Lett., **271**, 209–215 (1997).

[147] F. Rosca-Pruna and M. J. J. Vrakking. *Experimental Observation of Revival Structures in Picosecond Laser-Induced Alignment of* I_2. Phys. Rev. Lett., **87**, 153902 (2001).

[148] K. F. Lee, D. M. Villeneuve, P. B. Corkum, A. Stolow and J. G. Underwood. *Field-free three-dimensional alignment of polyatomic molecules.* Phys. Rev. Lett., **97**, 173001 (2006).

[149] H. Sakai, S. Minemoto, H. Nanjo, H. Tanji and T. Suzuki. *Controlling the orientation of polar molecules with combined electrostatic and pulsed, nonresonant laser fields.* Phys. Rev. Lett., **90**, 083001 (2003).

[150] J. Breidbach and L. S. Cederbaum. *Universal Attosecond Response to the Removal of an Electron.* Phys. Rev. Lett., **94**, 033901 (2005).

[151] A. I. Kuleff and L. S. Cederbaum. *Charge migration in different conformers of glycine: The role of nuclear geometry.* Chem. Phys., **338**, 320 – 328 (2007).

[152] R. Weinkauf, P. Schanen, D. Yang, S. Sonkara and E. W. Schlag. *Elementary Processes in Peptides - Electron-Mobility and Dissociations in Peptide Cations in the Gas-Phase.* J. Phys. Chem., **99**, 11255–11265 (1995).

[153] O. Smirnova, Y. Mairesse, S. Patchkovskii, N. Dudovich, D. Villeneuve, P. Corkum and M. Y. Ivanov. *High harmonic interferometry of multi-electron dynamics in molecules.* Nature, **460**, 972–977 (2009).

[154] S. Haessler *et al. Attosecond imaging of molecular electronic wavepackets.* Nat. Phys., **6**, 200–206 (2010).

[155] M. Hoener *et al.* *Ultraintense X-Ray Induced Ionization, Dissociation, and Frustrated Absorption in Molecular Nitrogen.* Phys. Rev. Lett., **104**, 253002 (2010).

[156] A. Lafosse, J. C. Brenot, A. V. Golovin, P. M. Guyon, K. Hoejrup, J. C. Houver, M. Lebech and D. Dowek. *Vector correlations in dissociative photoionization of O_2 in the 20-28 eV range. I. Electron-ion kinetic energy correlations.* J. Chem. Phys., **114**, 6605–6617 (2001).

[157] Y. Lu, Z. X. He, J. N. Cutler, S. H. Southworth, W. C. Stolte and J. A. R. Samson. *Dissociative photoionization study of O_2.* J. Electron Spectrosc. Relat. Phenom., **94**, 135–147 (1998).

[158] P. M. Guyon, A. V. Golovin, C. J. K. Quayle, M. Vervloet and M. Richard-Viard. *Electron Emission from Aligned Superexcited O^* Atoms Produced in Photodissociation of O_2 in the 22.20–22.36 eV Region.* Phys. Rev. Lett., **76**, 600–603 (1996).

[159] P. Erman, A. Karawajczyk, E. Rachlew-Kllne, M. Stankiewicz and K. Y. Franzn. *Energy distributions of* O^+ *ions produced in photodissociation of* O_2 *in the 17 - 34 eV range.* J. Phys. B: At., Mol. Opt. Phys., **29**, 5785 (1996).

[160] J. Parker and J. C. R. Stroud. *Coherence and decay of Rydberg wave Packets.* Phys. Rev. Lett., **56**, 716–719 (1986).

[161] G. Herzberg. *Molecular spectra and molecular structure*, vol. I spectra of diatomic molecules. D. Van Nostrand, 2nd ed. (1950).

[162] A. Lafosse, J. C. Brenot, P. M. Guyon, J. C. Houver, A. V. Golovin, M. Lebech, D. Dowek, P. Lin and R. R. Lucchese. *Vector correlations in dissociative photoionization of O_2 in the 20–28 eV range. II. Polar and azimuthal dependence of the molecular frame photoelectron angular distribution.* J. Chem. Phys., **117**, 8368–8384 (2002).

[163] P. Lin and R. R. Lucchese. *Theoretical studies of cross sections and photoelectron angular distributions in the valence photoionization of molecular oxygen.* J. Chem. Phys., **116**, 8863–8875 (2002).

[164] F. Kelkensberg. *personal communication.*

[165] F. Kelkensberg, W. Siu, G. Gademann, A. Rouzee, P. Johnsson and M. Vrakking. *Attosecond control in photoionization of hydrogen molecules.* accepted (2010).

[166] W. Ackermann, G. Asova, V. Ayvazyan, A. Azima, N. Baboi, J. Bähr, V. Balandin, B. Beutner, A. Brandt and A. Bolzmann. *Operation of a free-electron laser from the extreme ultraviolet to the water window.* Nat. Photonics, **1**, 336 (2007).

[167] H. N. Chapman, A. Barty, M. J. Bogan, S. Boutet, M. Frank, S. P. Hau-Riege, S. Marchesini, B. W. Woods, S. Bajt and W. H. Benner. *Femtosecond diffractive imaging with a soft-X-ray free-electron laser.* Nature Phys., **2**, 839 (2006).

[168] A. A. Sorokin, S. V. Bobashev, K. Tiedtke and M. Richter. *Multi-photon ionization of molecular nitrogen by femtosecond soft x-ray FEL pulses.* J. Phys. B-At. Mol. Opt., **39**, L299–L304 (2006).

[169] A. T. J. B. Eppink and D. H. Parker. *Velocity map imaging of ions and electrons using electrostatic lenses: Application in photoelectron and photofragment ion imaging of molecular oxygen.* Rev. Sci. Instrum., **68**, 3477 (1997).

[170] V. Mergel *et al.* *He^{2+} on He: State-selective, scattering-angle-dependent capture cross sections measured by cold target recoil ion momentum spectroscopy (COLTRIMS).* Nucl. Instrum. Methods Phys. Res., Sect. B, **98**, 593–596 (1995).

[171] H. Wabnitz, A. R. B. de Castro, P. Gürtler, T. Laarmann, W. Laasch, J. Schulz and T. Möller. *Multiple Ionization of Rare Gas Atoms Irradiated with Intense VUV Radiation.* Phys. Rev. Lett., **94**, 023001 (2005).

[172] R. Santra and C. H. Greene. *Multiphoton ionization of xenon in the vuv regime.* Phys. Rev. A, **70**, 053401 (2004).

[173] P. M. Paul, E. S. Toma, P. Breger, G. Mullot, F. Augé, P. Balcou, H. G. Muller and P. Agostini. *Observation of a Train of Attosecond Pulses from High Harmonic Generation.* Science, **292**, 1689 (2001).

[174] M. Drescher, M. Hentschel, R. Kienberger, G. Tempea, C. Spielmann, G. A. Reider, P. B. Corkum and F. Krausz. *X-Ray Pulses Approaching the Attosecond Frontier.* Science, **291**, 1923 (2001).

[175] K. J. Schafer, B. Yang, L. F. DiMauro and K. C. Kulander. *Above threshold ionization beyond the high harmonic cutoff.* Phys. Rev. Lett., **70**, 1599 (1993).

[176] P. B. Corkum. *Plasma perspective on strong-field multiphoton ionization.* Phys. Rev. Lett., **71** (1993).

[177] B. Whitaker. *Imaging in Molecular Dynamics: Technology and Applications.* Cambridge University Press (2003).

[178] J. Mauritsson *et al.* *Attosecond Electron Spectroscopy Using a Novel Interferometric Pump-Probe Technique.* Phys. Rev. Lett., **105**, 053001 (2010).

[179] M. J. J. Vrakking. *An iterative procedure for the inversion of two-dimensional ion/photoelectron imaging experiments.* Rev. Sci. Intrum., **72**, 4084 (2001).

[180] K. Ito, R. I. Hall and M. Ukai. *Dissociative photoionization of* H_2 *and* D2 *in the energy region of 2545 eV.* J. Chem. Phys., **104**, 8449 (1996).

[181] P. Baltzer, B. Wannberg, L. Karlsson, M. C. Göthe and M. Larsson. *High-resolution inner-valence uv photoelectron spectra of the* O_2 *molecule and configuration-interaction calculations of* $^2\Pi_u$ *states between 20 and 26 eV.* Phys.Rev. A, **45**, 4374 (1992).

[182] M. Richard-Viard, O. Dutuit, M. Lavollée, T. Govers, P. M. Guyon and J. Durup. O^+ *ions dissociation studied by threshold photoelectronphotoion coincidence method.* J. Chem. Phys, **82**, 4054 (1985).

[183] Y. Lu, Z. X. He, J. N. Cutler, S. H. Southworth, W. C. Stolte and J. A. R. Samson. *Dissociative photoionization study of* O_2. J Electron spectrosc. Relat. Phenom., **94**, 135–147 (1998).

[184] T. Akahori, Y. Morioka, M. Watanabe, T. Hayaishi, K. Ito and M. Nakamura. *Dissociation processes of* O_2 *in the VUV region 500-700* **r***A.* J. Phys. B, **18**, 2219 (1985).

[185] Y. Hikosaka, T. Aoto, R. I. Hall, K. Ito, R. Hirayama, N. Yamamoto and E. Miyoshi. *Inner-valence states of* O_2^+ *and dissociation dynamics studied by threshold photoelectron spectroscopy and a configuration interaction calculation.* J. Chem. Phys., **119**, 7693 (2003).

[186] K. Ellis, R. I. Hall, L. Avaldi, G. Dawber, A. McConkey, L. Andric and G. C. King. *High resolution threshold photoelectron and photoion spectroscopy of oxygen in the 12-50 eV photon range.* J. Phys. B: At. Mol. Opt. Phys, **27**, 3415 (1994).

[187] L. G. M. Pettersson and M. Larsson. *On the character of the* O_2^{2+} $A\,^3\Sigma_u^+$ *state.* J. Chem. Phys., **94**, 818 (1991).

[188] R. I. Hall, G. Dawver, A. McConkey, M. A. MacDonald and G. C. King. *Vibrational structure of the* O_2^2+ *ground state observed by threshold photoelectron coincidence spectroscopy.* Phys. Rev. Lett., **68**, 2751 (1992).

[189] P. Bolognesi, D. B. Thompson, L. Avaldi, M. A. MacDonald, M. C. A. Lopes, D. R. Cooper and G. C. King. *Vibrationally selected* O^+-O^+ *fragmentation of* O_2 *below the adiabtic double-ionization potential studied via electron-electron coincidence spectroscopy.* Phys. Rev. Lett., **82**, 2075 (1999).

[190] R. Feifel, J. H. D. Eland and D. Edvardsson. *Valence double ionization of* O_2 *at photon energies below and above the molecular double ionization threshold.* J. Chem. Phys., **122**, 144308 (2005).

[191] E. W. Plummer, T. Gustafsson, W. Gudat and D. E. Eastman. *Partial photoionization cross sections of* N_2 *and CO using synchrotron radiation.* Phys. Rev. A, **15**, 2339 (1977).

[192] P. Baltzer, M. Larsson, L. Karlsson, B. Wannberg and M. Carlsson-Göthe. *Inner-valence states of* N_2^+ *studied by uv photoelectron spectroscopy and configuration-interaction calculations.* Phys. Rev. A, **46**, 5545 (1992).

[193] T. Aoto, K. Ito, Y. Hikosaka, A. Shibasaki, R. Hirayama, N. Yamamono and E. Miyoshi. *Inner-valence states of* N_2^{2+} *and the dissociation dynamics studied by threshold photoelectron spectroscopy and configuration interaction calculation.* J. Chem. Phys., **124**, 234306 (2006).

[194] A. Hammet, W. Stoll and C. Brion. Ibid, **8**, 367 (1976).

[195] J. H. D. Eland and E. J. Duerr. *Dissociation and electronion angular distributions in inner-valence photoionisation of CO and* N_2. Chem. Phys, **229**, 13 (1998).

[196] C. Nicolas, C. Alcaraz, R. Thissen, M. Vervloet and O. Dutuit. *Dissociative photoionization of* N_2 *in the 24−32 eV photon energy range.* J. Phys. B: At. Mol. Opt. Phys., **36**, 2239–2251 (2003).

[197] M. Besnard, L. Hellner, G. Dujardin and D. Winkoun. *Photoion-Photoion coincidence study of the fragmentation of the double charged* N_2^{2+} *cation.* J. Chem. Phys., **88**, 1732 (1988).

[198] D. W. Turner and D. P. May. *Franck-Condon factors in ionization: experimental measurement using molecular photoelectron spectroscopy.II.* J. Chem. Phys., **46**, 1156 (1967).

[199] C. E. Brion and K. H. Tan. *Partial oscillator strengths for the photoionization of* $\mathrm{N_2O}$ *and* $\mathrm{CO_2}$ *(20-60 eV).* Chem. Phys., **34**, 141 (1978).

[200] R. Locht and M. Davister. *The dissociative electroionization of carbon dioxide by low-energy electron impact. The* C^+*,*O^+ *and* CO^+ *dissociation channels.* Int. J. Mass Spectrom. Ion Process., **144**, 105 (1995).

[201] B. Kovač. *The He I photoelectron spectra of*CO_2*,*CS_2 *and OCS: vibronic coupling.* J. Chem. Phys., **78**, 1684 (1983).

[202] L.-S. Wang, J. Reutt and D. Shirley. *High resolutuion UV spectroscopy of* CO_2^+ *and* CS_2^+ *using supersonic molecular beams.* J Electron spectrosc. Relat. Phenom., **47**, 167 (1988).

[203] R. Bombach, J. Dannacher, J. P. Stadelmann and J. C. Lorquet. *Branching ratios and partition of the excess energy for the predissociation of* CO_2^+ $C\,^2\Sigma_g^+$ *molecular cations.* J. Chem. Phys., **79** (1983).

[204] J. Liu, W. Chen, M. Hochlaf, X. Qian, C. Chang and C. Ng. *Unimolecular decay pathways of state-selected* CO_2^+ *in the internal energy range of 5.2-6.2 eV: an experimental and theoretical study.* J. Chem. Phys, **118**, 149 (2003).

[205] A. W. Potts and T. A. Williams. *The observation of forbidden transistions in the He II photoelectron spectra.* J. Electron Spectrosc. Relat. Phenom., **3**, 3 (1974).

[206] A. Slattery, T. Field, M. Ahmad, R. Hall, J. Lambourne, F. Penent, P. Lablanquie and J. Eland. *Spectroscopy and metastability of* CO_2^{2+} *molecular ions.* J. Chem. Phys, **122**, 084317 (2005).

[207] T. Masuoka, E. Nakamura and A. Hiraya. *Kinetic-energy release in the dissociation of* CO_2^{2+}. J. Chem. Phys., **104**, 6200 (1996).

[208] D. M. Curtis and J. H. D. Eland. *Coincidence studies of doubly charged ions formed by 30.4 nm photoionization.* Int. J. Mass Spectrom. Ion Process., **63**, 241 (1985).

[209] S. Grafe and M. Y. Ivanov. *Effective fields in laser-driven electron recollision and charge localization.* Phys. Rev. Lett., **99**, 163603 (2007).

[210] X. M. Tong and C. D. Lin. *Dynamics of light-field control of molecular dissociation at the few-cycle limit.* Phys. Rev. Lett., **98**, 123002 (2007).

[211] A. Baltuska, T. Fuji and T. Kobayashi. *Controlling the carrier-envelope phase of ultrashort light pulses with optical parametric amplifiers.* Phys. Rev. Lett., **88**, 133901 (2002).

[212] I. Znakovskaya, P. von den Hoff, S. Zherebtsov, A. Wirth, O. Herrwerth, M. J. J. Vrakking, R. de Vivie-Riedle and M. F. Kling. *Attosecond Control of Electron Dynamics in Carbon Monoxide.* Phys. Rev. Lett., **103**, 103002 (2009).

[213] M. Kremer *et al.* *Electron Localization in Molecular Fragmentation of* H_2 *by Carrier-Envelope Phase Stabilized Laser Pulses.* Phys. Rev. Lett., **103**, 213003 (2009).

[214] H. J. Wörner, J. B. Bertrand, D. V. Kartashov, P. B. Corkum and D. M. Villeneuve. *Following a chemical reaction using high-harmonic interferometry.* Nature, **466**, 604–607 (2010).

[215] H. Niikura, F. Legare, R. Hasbani, A. D. Bandrauk, M. Y. Ivanov, D. M. Villeneuve and P. B. Corkum. *Sub-laser-cycle electron pulses for probing molecular dynamics.* Nature, **417**, 917–922 (2002).

[216] X. M. Tong, Z. X. Zhao and C. D. Lin. *Correlation dynamics between electrons and ions in the fragmentation of* D_2 *molecules by short laser pulses.* Phys. Rev. A, **68**, 043412 (2003).

[217] G. L. Yudin and M. Y. Ivanov. *Physics of correlated double ionization of atoms in intense laser fields: Quasistatic tunneling limit.* Phys. Rev. A, **63**, 033404 (2001).

[218] I. Kawata, H. Kono and Y. Fujimura. *Adiabatic and diabatic responses of* H_2^+ *to an intense femtosecond laser pulse: Dynamics of the electronic and nuclear wave packet.* J. Chem. Phys., **110**, 11152–11165 (1999).

[219] A. Becker and F. H. M. Faisal. *Intense-field many-body S-matrix theory.* J. Phys. B: At., Mol. Opt. Phys., **38**, R1 (2005).

[220] M. Ivanov. *Personal communication.*

[221] E. M. Landau, L. D. & Lifshitz. *Quantum Mechanics Non-Relativistic Theory* (1977).

[222] O. Smirnova, M. Spanner and M. Ivanov. *Analytical solutions for strong field-driven atomic and molecular one- and two-electron continua and applications to strong-field problems.* Phys. Rev. A, **77**, 033407 (2008).

[223] N. Delone and V. P. Krainov. *Atoms In Strong Light Fields.* Springer (1985).

[224] A. S. Alnaser, T. Osipov, E. P. Benis, A. Wech, C. L. Cocke, X. M. Tong and C. D. Lin. *Rescattering double ionization of D_2 and H_2 by intense laser pulses.* Phys. Rev. Lett., **91**, 163002 (2003).

[225] A. Rudenko, T. Ergler, B. Feuerstein, K. Zrost, C. D. Schroter, R. Moshammer and J. Ullrich. *Real-time observation of vibrational revival in the fastest molecular system.* Chem. Phys., **329**, 193–202 (2006).

[226] T. Ergler, A. Rudenko, B. Feuerstein, K. Zrost, C. D. Schroter, R. Moshammer and J. Ullrich. *Spatiotemporal imaging of ultrafast molecular motion: Collapse and revival of the D_2^+ nuclear wave packet.* Phys. Rev. Lett., **97**, 193001 (2006).

[227] X. M. Tong, Z. X. Zhao and C. D. Lin. *Probing molecular dynamics at attosecond resolution with femtosecond laser pulses.* Phys. Rev. Lett., **91**, 233203 (2003).

[228] U. Even, J. Jortner, D. Noy, N. Lavie and C. Cossart-Magos. *Cooling of large molecules below 1 K and He clusters formation.* The Journal of Chemical Physics, **112**, 8068–8071 (2000).

[229] D. Gerlich, G. Jerke, U. Mück and U. Person. *Schnelles Ventil zur Erzeuging serh kurzer Gasimpulse.* Tech. rep., Fakultät für Physik, Universität Freiburg, Germany.

[230] D. Irimia, D. Dobrikov, R. Kortekaas, H. Voet, D. A. van den Ende, W. A. Groen and M. H. M. Janssen. *A short pulse (7 μs FWHM) and high repetition rate (dc - 5kHz) cantilever piezovalve for pulsed atomic and molecular beams.* Rev. Sci. Instrum., **80**, 113303 (2009).

[231] *Piezoelectric ceramics.* Tech. rep., Morgan Electro Ceramics.

[232] W. G. Roeterdink and M. H. M. Janssen. *Femtosecond velocity map imaging of dissociative ionization dynamics in CF_3I.* Phys. Chem. Chem. Phys., **4**, 601–612 (2002).

[233] G. Scoles, ed. *Atomic and molecular beam methods*, vol. I. Oxford University Press (1988).

[234] W. R. Gentry and C. F. Giese. *Ten-microsecond pulsed molecular beam source and a fast ionization detector.* Rev. Sci. Instrum., **49**, 595–600 (1978).

SUMMARY

Understanding molecular dynamics has been the driving force for the work described in this thesis. Gaining insight into the physics of these dynamics can be realized by following these processes in real time. Imaging fast-moving objects requires the use of a camera with a shutter time that is short compared to the timescale at which the object moves. The motions of atoms and electrons respectively take place on the femtosecond (1 fs = 10^{-15} s) and attosecond (1 as = 10^{-18} s) timescale. In addition to the fact that atoms and electrons are too small to be imaged by conventional cameras, the motions of these particles are too fast. Therefore, novel experimental techniques needed to be developed that can follow these molecular dynamics in a time-resolved way.

The availability of light sources with femtosecond pulse durations, spurred the development of a novel experimental technique that allowed one to investigate the mechanisms of chemical reactions. In femtochemistry, one uses a femtosecond pulse to initiate the dynamics under investigation and employs a second pulse to probe the progress of the dynamics. Femtosecond pump-probe spectroscopy has enabled a whole new research field and was awarded with the Nobel prize in 1999.

The last decade has seen the emergence of a number of novel light sources that have greatly impacted the field of atomic and molecular physics. In this thesis we explored applications of three light sources in probing nuclear and electron dynamics in molecules. We describe experiments, in which these sources have been used to study molecular dynamics, or experiments that have formed an important step towards this goal. The first light source is based on high harmonic generation, producing extreme-ultraviolet (XUV) light pulses with pulse durations in the attosecond time-domain. These table-top XUV light sources are complemented by the (soft) X-ray free electron lasers (FELs), providing pulses with femtosecond durations at unprecedented intensities. Finally, we used femtosecond IR laser pulses that comprise only a few oscillations of the optical cycle and of which the carrier-envelope-phase (CEP) is stabilized.

XUV attosecond light pulses by HHG

Strong-field interaction with an atomic medium has led to the discovery of high harmonic generation as a source for light pulses with energies in the XUV regime and, under certain conditions, with pulse durations in the attosecond time-domain, thereby entering the natural timescale of electron motion. Inspired by the experimental methods employed in femtochemistry, these short and energetic pulses form the basis of a new type of pump-probe spectroscopy to study nuclear and electron dynamics in real-time. This is the topic of the first part of this thesis.

The experimental techniques that are required to perform a successful attosecond pump-probe experiment are described in **Chapter 2**, together with a detailed description of the attosecond experimental setup at the AMOLF-institute in Amsterdam, where the experiments were performed that are presented in chapter 4.

In experiments where structural and dynamical information is obtained by using diffraction, it is a prerequisite to measure the diffracted photons or electrons in a frame that is defined by the molecular axes. One possibility is to align (and orient) the molecules in the laboratory frame and measure the photons or photoelectrons with a velocity map imaging spectrometer. In **Chapter 3**, as a first step to realize such an experiment, we oriented NO molecules in the laboratory frame by using a combination of hexapole state-selection and orientation in a strong dc electric field. The orientation was subsequently probed by dissociative ionization by XUV light pulses generated by HHG, 800 nm or 400 nm pulses.

The experiment was an attempt to resolve a sign discrepancy between measurements and calculations of the steric asymmetry of rotationally inelastic collisions of He-NO, Ar-NO and D_2-NO molecules. The discrepancy would be resolved if the sign of the NO dipole moment would be opposite to theoretical predictions. The orientation of the state-selected NO molecules in the electric field is such that the negative (positive) end of the molecule is oriented towards the negative (positive) electrode. By probing the orientation of the NO molecules, we determined that the sign of the NO dipole moment was negative (N^-O^+) in correspondence with theoretical predictions. A possible error in the sign of the dipole moment was therefore excluded as the reason for the aforementioned discrepancy.

The excitement about attosecond pulses is motivated by the prospect of resolving electron dynamics in atoms, molecules and condensed matter. In **Chapter 4** we explore the use of attosecond pulses as a probe for electron dynamics in molecules. We exposed O_2 molecules to a moderately strong IR field, thereby inducing a time-dependent polarization in these molecules. This polarization was probed by an attosecond pulse train (APT). The yield and angular distribution of ion fragments that resulted from the interaction with the APT + IR field, showed a dependence on the XUV - IR delay. The oscillations in the ion yield can be explained by an interference of two XUV + IR ionization pathways that involve two ionization continua, which are coupled to each other by the IR-field. The combined information of the delay-dependent ion yield and angular distributions allowed us to extract the electronic states that are involved in the coupling. The experiment shows that attosecond pulses can be used to probe IR-induced electron dynamics.

Soft x-ray free electron lasers

Femtosecond XUV pulses can nowadays routinely be generated in table-top setups. A complementary light source are the facility-scale (soft) X-ray free electron lasers, providing femtosecond light pulses at unprecedented intensities. The interest in these light sources is also based on the prospect of developing a novel experimental method that follows nuclear dynamics based on diffraction principles.

In **Chapter 5** we successfully implemented a velocity map imaging spectrometer (VMIs) at the soft X-ray free electron laser in Hamburg (FLASH). We used FLASH to ionize a range of noble gases and molecules and have characterized the electronic states and dissociative ionization pathways that were accessed via single photon absorption. The experiment was the first VMIS experiment at a free electron laser and was an important step in developing a novel method to follow nuclear motion that is based on 'illuminating the molecule from within'. In this method one measures the photoelectron angular distribution of aligned molecules, which contains signatures of intramolecular diffraction and can be used to follow nuclear dynamics in time. Following the experiment described in chapter 5, we have meanwhile performed follow-up experiments that induced molecular dynamics by a synchronized Ti:Sa laser and probed these dynamics with FLASH.

Carrier-envelope-phase stabilized few-cycle IR pulses

Control over the CEP of few-cycle laser pulses has introduced a new control parameter in the interaction of light with matter. It has revealed that strong-field processes can be sensitive to the instantaneous electric field, rather than the envelope, of the laser pulse.

In **Chapter 6** we used these light pulses to dissociatively ionize H_2 and D_2 molecules and studied the electron localization that takes place during the dissociation of H_2^+ and D_2^+ molecular ions. The electron localization, observed as an asymmetry in the fragment ion ejection, shows a dependence on the CEP. It demonstrates that control over the CEP of few-cycle pulses can be used to steer the electron to the 'right' or 'left' nucleus during the dissociation. The current experiment was carried out using slightly longer laser pulses and at lower intensities than a previous experiment.

Interestingly, the asymmetry in the fragment ion ejection shows a dependence on the kinetic energy, not observed earlier. In addition a π-phase difference is observed between the results for H_2 and D_2. To understand this kinetic energy dependence of the asymmetry in fragment ejection and the π-phase difference between H_2 and D_2, we performed numerical simulations in which the time-dependent Schrödinger equation (TDSE) was solved for H_2^+ and D_2^+ in the presence of a few-cycle IR pulse. However a crucial element in the experiment was excitation of the molecular ion induced by recollision of the continuum electron, which was mediated by the IR field. Recollision excitation is a two-electron phenomenon. Currently, exact calculations of such processes are unfeasible. A semiclassical approximation was developed, that allowed us to capture the electron-electron interaction into an effective field that can be used in the TDSE calculations. In addition, the semiclassical approximation provided an intuitive understanding of the role of the recollision electron dynamics in the experiment. In the numerical results, the second return of the recollision electron to the molecular ion was elemental in reproducing the observed π-phase difference between H_2 and D_2. This was quite a surprising result in light of earlier numerical calculations of recollision excitation of H_2^+, in which the first and third return of the continuum electron to the parent ion were considered to be most important.

SAMENVATTING

De doelstelling van het onderzoek dat is beschreven in dit proefschrift is het bestuderen van de dynamica van moleculen. Door experimenten te doen waarin we deze dynamica in de tijd volgen, kunnen we hier meer inzicht in verkrijgen.

Een scherpe foto maken van snel bewegende objecten vereist een sluitertijd die kort is in vergelijking met de tijdschaal waarop het object zich beweegt. Naast het feit dat atomen en elektronen te klein zijn om vast te leggen met een gewone camera, zijn de bewegingen van deze deeltjes ook veel te snel. De bewegingen van atomen en elektronen vinden namelijk plaats op respectievelijk de femtoseconde (1 fs $= 10^{-15}$ s) en de attoseconde (1 as $= 10^{-18}$ s) tijdschaal.Om deze processen in de tijd te kunnen volgen moeten er nieuwe experimentele technieken ontwikkeld worden die deze moleculaire dynamica tijdopgelost kunnen meten.

De beschikbaarheid van lichtbronnen met pulsen die slechts tientallen femtoseconden lang zijn, heeft geleid tot de ontwikkeling van een nieuw onderzoeksveld: de femtochemie. . De femtochemie heeft men in staat gesteld om de moleculaire dynamica tijdenschemische reacties te volgen op de femtoseconde tijdschaal. In deze experimenten gebruikt men een femtoseconde laserpuls ('pump' puls) om de chemische reactie te starten waarna een tweede laserpuls ('probe' puls) wordt gebruikt om de voortgang van de reactiedynamica te volgen. Femtoseconde 'pump-probe' spectroscopie heeft zich tot een geheel nieuw onderzoeksveld ontwikkeld en werd in 1999 met een Nobelprijs onderscheiden.

Het ontstaan van nieuwe lichtbronnen heeft vaak een grote invloed gehad op het onderzoek in de molecuul fysica. In het onderzoek, dat we in dit proefschrift beschrijven, hebben we gekeken hoe drie nieuwe lichtbronnen gebruikt kunnen worden om nucleaire en elektron dynamica in moleculen te volgen. Enerzijds beschrijven we experimenten waarin deze lichtbronnen zijn gebruikt om moleculaire dynamica te bestuderen. Anderzijds beschrijven we experimenten waarin weliswaar geen dynamica wordt onderzocht maar die desondanks een belangrijke stap zijn geweest in de ontwikkeling van methoden om dit doel te realiseren. De eerste lichtbron die in dit proefschrift wordt gebruikt is gebaseerd op hogere harmonische generatie (HHG). In HHG worden extreem-ultraviolet (XUV) lichtpulsen geproduceerd die tientallen tot honderden attoseconden lang zijn. De tweede lichtbron is de (zachte) röntgen vrije elektronen laser (VEL). Deze VELs genereren lichtpulsen die tientallen femtoseconden lang zijn en kunnen ongeëvenaarde intensiteiten bereiken. De laatste lichtbron is de femtoseconde infrarood (IR) laser die pulsen genereert met maar een paar oscillaties van de optische periode. Daarnaast is de fase, tussen de oscillaties van het elektrische veld ('carrier') en de pulsomhullende ('envelope'), de zogenaamde 'carrier-envelope-phase' (CEP), gestabiliseerd.

XUV lichtpulsen gebaseerd op HHG

Hogere harmonische generatie vindt plaats door de interactie van een intens laserveld met een atomair medium. Met HHG kunnen lichtpulsen worden gemaakt in het XUV golflengte gebied. Onder bepaalde omstandigheden, hebben deze lichtpulsen een pulsduur die in het attoseconde domein valt, de tijdschaal waarop de bewegingen van elektronen plaatsvinden. Geïnspireerd door de experimentele methodes die in de femtochemie gebruikt worden, leggen deze zeer korte en energieke lichtpulsen de basis voor een nieuwe vorm van 'pump-probe' spectroscopie om nucleaire en elektron dynamica op een tijdopgeloste manier te bestuderen. Dit is het onderwerp van het eerste deel van dit proefschrift.

De experimentele technieken die nodig zijn om een succesvol attoseconde 'pump-probe' experiment uit te voeren, worden in hoofdstuk 2 beschreven. In dit hoofdstuk wordt ook een gedetailleerde beschrijving van de attoseconde experimentele opstelling op het AMOLF-instituut in Amsterdam gegeven. De experimenten die in hoofdstuk 4 gepresenteerd worden, zijn op deze opstelling uitgevoerd.

Een belangrijk doel van het onderzoek is het ontwikkelen van methoden waarmee de (tijdsafhankelijke) structuur van een molecuul gemeten kan worden. In één methode, waar we ons specifiek op hebben gericht, wordt de moleculaire structuur bepaald door de verstrooiing van fotoelektronen op de nuclei te meten. Hierdoor ontstaat een diffractiepatroon wat de structuur van het molecuul. In dergelijke experimenten is het een voorwaarde om de verstrooide fotoelektronen in een frame te meten dat bepaald wordt door de oriëntatie van het molecuul (moleculair frame). Eén mogelijkheid is om de moleculen uit te lijnen (en te oriënteren) in het frame van het laboratorium en vervolgens de energie en hoekverdeling van de fotoelektronen, te meten met een zogenaamde 'velocity map imaging spectrometer' (VMIS).

Als eerste stap om zo'n experiment te realiseren hebben we NO moleculen in het laboratoriumframe georiënteerd met. Met andere woorden, we hebben de NO moleculen, die in eerste instantie willekeurig georienteerd waren, zo gericht dat de N- of O-atomen voornamelijk naar één richting wijzen. Dit hebben we gedaan door eerst een bepaalde kwantumtoestand van de NO moleculen te selecteren met behulp van een 'hexapool'. Vervolgens hebben we deze moleculen georiënteerd met een sterk statisch elektrisch veld. De NO moleculen in de geselecteerde kwantumtoestand willen zich zo oriënteren dat de meer negatieve kant van het molecuul, gericht is naar de meer negatieve elektrode. Vervolgens hebben we de oriëntatie bepaald door de moleculen op te breken (dissociëren) in een N- en een O-atoom en te meten in welke richting het N/O atoom vliegt ten op zichte van het statisch elektrisch veld. We hebben de moleculen gedissocieerd, door de NO moleculen te ioniseren met XUV HHG lichtpulsen, met de fundamentele of de tweede harmonische van een Ti:Sa laser.

Het experiment was een poging de oorzaak te vinden voor een discrepantie in het teken tussen berekeningen en metingen van de sterische asymmetrie van rotationele inelastische botsingen van NO-He, NO-Ar en D_2-NO. In deze berekeningen is aangenomen dat het dipoolmoment van NO negatief is, in overeenstemming met een andere theoretische berekening. De discrepantie in het teken van de sterische asymmetrie zou opgelost zijn, wanneer het teken van het NO dipoolmoment positief zou zijn.

Door de oriëntatie van de NO moleculen in het statisch elektrisch veld te meten, hebben we vastgesteld dat het teken van het NO dipoolmoment negatief is (N^-O^+). Een fout in het teken van het NO dipoolmoment in de theoretische berekeningen, over de sterische asymmetrie, is daarom uitgesloten als oorzaak voor de zojuist genoemde discrepantie.

Er is veel interesse in attoseconde pulsen omdat de korte pulsduur van deze lichtbronnen het mogelijk maakt elektron dynamica in atomen, moleculen en gecondenseerde materie, tijdopgelost te meten. In hoofdstuk 4 verkennen we het gebruik van attoseconde pulsen als een 'probe' voor elektron dynamica in moleculen. We hebben O_2 moleculen blootgesteld aan een gematigd sterk IR-veld, waardoor we een tijdsafhankelijke polarisatie in deze moleculen teweegbrengen. Deze polarisatie is gemeten met een attoseconde puls trein (APT). De opbrengsten en hoekverdelingen van ionfragmenten, die het resultaat zijn van de interactie van de moleculen met de XUV + IR pulsen, vertoonden een afhankelijkheid van de tijdsvertraging tussen de twee pulsen. Het experiment demonstreert dat attoseconde pulsen gebruikt kunnen worden om elektrondynamica, die door een IR-veld worden geïnduceerd, te volgen.

Zachte röntgen vrije elektronen lasers.

HHG stelt ons in staat om femtoseconde XUV pulsen te produceren in experimentele opstellingen ter grootte van een lasertafel. De opbrengst van deze bronnen is echter beperkt. XUV/(zachte) röntgen VELs, met een lengte van een paar honderd meter, kunnen femtoseconde pulsen genereren met een ongeëvenaarde hoeveelheid fotonen per puls.

Deze VELs, zijn onder andere, interessante lichbronnen omdat ze gebruikt kunnen worden in de eerder genoemde fotoelektron diffractie techniek. In hoofdstuk 5 hebben we met succes een 'velocity map imaging spectrometer' op de VEL in Hamburg (FLASH) geïnstalleerd. We hebben FLASH gebruikt om een reeks edelgassen en moleculen te ioniseren en we hebben de elektronische toestanden en dissociatieve ionisatiekanalen, die via de absorptie van één foton werden bereikt, gekarakteriseerd. Het experiment was het eerste VMI experiment op een vrije elektronen laser. De VMI is de detector waarmee we in een later stadium het fotoelektron diffractiepatroon willen meten. Inmiddels zijn er een aantal vervolgexperimenten succesvol uitgevoerd op basis van de VMI implementatie van hoofdstuk 5. In deze experimenten hebben we moleculaire dynamica geïnduceerd met een Ti:Sa laser, die gesynchroniseerd is met de VEL, en deze dynamica gevolgd met FLASH.

'Carrier-envelope-phase stabilized few-cycle' femtoseconde pulsen

De controle over de CEP van femtoseconde pulsen met een pulsduur van slecht een paar optische periodes, heeft een extra controle parameter geïntroduceerd in de interactie van licht met materie. Deze 'CEP-stabilized few-cycle' lichtpulsen hebben gedemonstreerd dat bepaalde processen, die plaats vinden in een heel sterk laserveld, gevoeligzijn voor het instantane elektrische veld waar normaal gesproken alleen effecten van de pulsomhullende merkbaar zijn.

In hoofdstuk 6 hebben we deze CEP-gestabiliseerde lichtpulsen gebruikt om H_2 en D_2 te ioniseren en te dissociëren. Tijdens de dissociatie zal het overgebleven gebonden elektron zich op één van de nuclei lokaliseren. We hebben gedemonstreerd dat we de uitkomst van deze lokalisatie (op de 'linker' of 'rechter' nucleus) kunnen 'sturen' door de CEP te veranderen.

In het experiment vertaalde de controle over de elektronlokalisatie zich in een asymmetrie in het aantal H^+ of D^+ fragmenten dat aan de 'linker'- en de 'rechter'-kant - ten opzichte van de laserpolarisatie - op de detector valt. Controle over de CEP van 'few-cycle' laserpulsen kan dus gebruikt worden om intramoleculaire elektronbeweging te sturen.

Het huidige experiment is uitgevoerd met een iets langere laserpuls en bij een lagere laser intensiteit dan een eerder experiment. In ons nieuwe experiment zagen we dat de asymmetrie afhankelijk was van de kinetische energie, in tegenstelling tot wat eerder gemeten is. Daarnaast hebben we waargenomen dat de CEP-afhankelijkheid van de asymmetrie voor H_2 en D_2 een π-fase verschil vertoont. Om de kinetische energie afhankelijkheid van de asymmetrie en het π-fase verschil tussen H_2 en D_2 te begrijpen, hebben we numerieke simulaties uitgevoerd. Hierbij hebben we de tijdsafhankelijke Schrödinger vergelijking (TASV) opgelost voor H_2^+ en D_2^+ moleculen in aanwezigheid van de 'few-cycle' femtoseconde laserpuls. Een cruciaal element in het experiment is echter de excitatie van H_2^+/D_2^+ naar de dissociatieve toestand, als gevolg van recollisie van het continuumelektron met het moleculaire ion. Recollisie-excitatie is een twee-elektronen fenomeen en vindt plaats onder invloed van het oscillerende laser veld en kan niet in het TASV model worden gesimuleerd. Daarom hebben we een semiklassiek model ontwikkeld, dat ons in staat heeft gesteld om de elektron-elektron interactie te beschrijven met een effectief optisch veld, dat weer gebruikt kan worden in de TASV berekeningen.

In de numerieke resultaten was de tweede recollisie van het continum-elektron met het moleculaire ion cruciaal om het π-fase verschil tussen H_2 en D_2, dat we in het experiment hebben gezien, te reproduceren. Dit was een verassend resultaat in het licht van eerdere numerieke berekeningen van de recollisie excitatie van H_2^+, waarin de eerste en derde recollisie van het continuüm-elektron met het moleculaire ion, als meest belangrijk werden beschouwd.

DANKWOORD

"Dankbaar zijn maakt gelukkig" en zo heb ik het schrijven ook ervaren. Het dankwoord schrijven is het afronden van een memorabele en bijzondere periode. Promoveren is een leerzame reis voor mij geweest en ik heb op deze reis ontzettend veel leuke, lieve en interessante mensen als reisgenoten gehad. Ik ben dankbaar voor alle mensen die me hebben geholpen, steun en vertrouwen hebben gegeven en me de nodige ontspanning hebben bezorgd!

Ik wil allereerst mijn promotor Marc Vrakking bedanken voor het bieden van een uitdagende omgeving, waarin ik ontzettend veel heb geleerd, niet alleen over de natuurkunde, maar ook over mezelf. Marc, ik bewonder jouw kennis van de natuurkunde en vooral de intuïtieve manier waarmee je dit op mij wist over te brengen. Daarnaast wil ik je bedanken dat jouw deur altijd open stond voor vragen en voor jouw oprechte interesse in de experimenten. Bedankt voor de mogelijkheid om op allerlei plekken in Europa met mensen samen te werken en mooie metingen te verrichten.

The work described in this thesis would not have been possible without the help of a number of great people, with whom I had the pleasure to work.
I would like to acknowledge Misha Ivanov from Imperial College, London for developing the semiclassical approximation that formed the theoretical basis for the work on H_2 and D_2. Misha, I am really thankful for the discussions we have had and for your inspiring and energizing enthusiasm. I always came back very motivated from my visits to you! Thank you for reading my thesis so carefully and for being a member of my PhD-committee.
The work on H_2 and D_2 was performed at the Politecnico in Milano, as part of a collaboration of the groups of Mauro Nisoli (Politecnico Milano) and Anne L'Huillier (Lund University). I am grateful for the opportunity, that you provided, to work with a unique experimental setup. I would like to acknowledge Giuseppe and Mauro for their hospitality at the Politecnico Milano. Giuseppe, special thanks to you for the extensive efforts in the lab and for your 'fingerspitzengefühl' with the laser. I would like to thank Matthias, Enrico, Federico, Thomas, Marko, Sergey and Franck for our joint efforts in the lab.
The work on O_2 benefited a lot from the collaboration with Danielle Dowek from the Universiteé Paris-Sud. Danielle, thank you for the fruitful discussions we have had. I also want to thank you for being a member of my PhD-committee. I would like to acknowledge Robert Lucchese from Texas A&M University for his contributions to the work on O_2.
I would like to thank Umberto de Giovannini and Angel Rubio from the University of the Basque Country, San Sebastian, Spain for their ongoing efforts in developing TDDFT calculations to support the experimental results on O_2 and for their hos-

pitality during my visit there.
Ik wil Huib en Wim bedanken voor het plaatsnemen in de manuscriptcommissie en voor hun suggesties ter verbetering van het proefschrift. Wim, bedankt voor het regelen van alle formele procedures omtrent de promotie. Ronnie, bedankt voor het plaatsnemen in mijn promotiecommissie.

De interesse in onderzoek doen en willen weten hoe dingen werken heb ik tijdens mijn afstudeeronderzoek meegekregen in de groep van Mark Golden. Mark, en Jeroen, veel dank voor het aanwakkeren van mijn eigen enthousiasme.

Promovendi op AMOLF mogen zich gelukkig prijzen met de aanwezigheid van de fantastische ondersteunende afdelingen. Mijn promotie heeft veel baat gehad bij de kundigheid van deze mensen.
Ik wil Iliya en Dirk-Jan van het ontwerpbureau bedanken voor het ontwerpen van de gepulste gasklep. Ik heb de manier, waarop jullie altijd meedenken over de beste en tegelijkertijd werkbare oplossing, ontzettend gewaardeerd. Het maken van deze mooie ontwerpen ligt in de vakkundinge handen van de mechanische workshop. Wim, Jan, Wouter, Henk en Menno, bedankt voor alle onderdelen die jullie de afgelopen jaren voor ons hebben gemaakt en voor het doen van allerlei haastklusjes. Ik wil Ricardo en Niels speciaal bedanken voor het maken van de gepulste klep, met alle priegelonderdeeltjes die jullie zo 'leuk' vonden.
Ik wil Duncan, Ronald en Idsart van Elektronica bedanken voor de onderdelen die ze hebben gemaakt en voor hun hulp als er weer eens een probleempje (met hoge voltages) in het lab was. Idsart, bedankt voor je geduld en het beantwoorden van al mijn vragen over elektronica.

Ik ben heel dankbaar voor de aanwezigheid van Rob in onze groep. Rob, dank je wel voor alle steun in het lab, maar nog meer bedankt voor jouw interesse hoe het met mij ging. Je had altijd tijd voor een aantal lieve woorden van aanmoediging. Ik heb dit heel erg gewaardeerd! Ik wens je veel goeds in het leven. Ik ben ook dank verschuldigd aan excellente technische ondersteuning van Hinco en Ad. Dank jullie voor de tijd die jullie altijd hadden om me ergens mee te helpen of gaatjes te boren.

During my PhD at AMOLF, I have had the pleasure to work with many people that came to visit us in Amsterdam. In particular I would like to thank Francesca, Matteo and Kyungseung from the Politecnico Milano for contributing to the experiments we did and the fun, laughter and sushi we had together.

In the past years, I enjoyed working with the many people that were and currently are in the XUV-physics group and I consider myself lucky with the great atmosphere in the group. I want to thank you for all the jokes we made, the sailing trips and the tapas and many beers we have had together.
Toen ik in de groep kwam, was Arjan de eerste die me de kneepjes van de experimentele natuurkunde in de groep bijbracht. Arjan, ik wil je bedanken voor je intensieve begeleiding gedurende deze periode in de groep, ik heb daar veel aan gehad. Veel geluk gewenst aan jou, Ingrid en Johannes. Per, you were a great sup-

port in understanding strong-field physics. I want to thank you so much for your infinite patience and answering all my silly questions in a very clear way. Thank you for inviting us to spend midsummer at your parent's home in Sweden, it was a great experience! All the best to you, Maria, Hannes and Elin. Arnaud, thank you for bringing your Frenchness to the group and sharing your excellent taste of French wine with us! Omair, I really appreciated your british black humor and thank you for bringing a good laughter to the group. I wish both of you all the best.

Freek, Georg en Ymkje, we zijn allemaal binnen een jaar op AMOLF begonnen en ik wil jullie bedanken voor de vriendschap die we de afgelopen 4 jaar hebben opgebouwd.
Freek, in de afgelopen jaren heb ik veel met je samengewerkt en ik heb veel van je geleerd door onze discussies en van je heldere en intuïtive uitleg van de natuurkunde. Ik wil je bedanken voor de zovele uren die we samen in het lab hebben doorgebracht (hopend dat deze scan nu wel goed zou zijn). Dank je voor je hulp bij de interpretatie van de resultaten en je kritische blik naar bijna alles wat er in dit proefschrift staat. Je steun tijdens het schrijven en het afronden van dit boekwerk heb ik heel erg gewaardeerd, net zoals onze gedeelde obsessie voor espresso, opgedaan in Milano. In het afgelopen jaar hebben we een mooie vriendschap opgebouwd die me dierbaar is, dank je daarvoor.
Ymkje ik wil jou bedanken voor de mentale support en alle kopjes thee die we samen gedronken hebben. Het was heel fijn om iemand in de groep te hebben die de mindere momenten van een promotie goed snapte en daarmee te kunnen praten.
Georg, ik wil je bedanken voor de leuke samenwerking in het lab en jouw zorg voor de laser waarmee we veel experimenten hebben gedaan. Dank je voor alle lol die we hebben gehad en voor onze gedeelde liefde voor goed eten. Ondanks alle grapjes over duits brood ben ik je toch dankbaar voor jouw invloed hierop!
Julia en Aneta, thank you for being in our group and bringing more female influence! I appreciated our teabreaks in the afternoon, together with the chocolate and cakes! I thank you for your many kind words you said and the mental support you gave.
Federico, thank you for bringing your Argentinian coolness, your humor (and South Park) to our group! Thank you for inviting us to your wedding, I was honored to be part of this day and I wish you and Nayra lots of love and happiness together.
I want to thank the new people in the group, Axel, Christian, Chung-Hsin, Jesse, Truong and Florian for taking over the setup and your drive to measure beautiful physics. I wish you all the best and good luck in Berlin!

Ik heb AMOLF als een warme en welkome omgeving ervaren en dit is mede mogelijk gemaakt door mensen zoals Ernst-Jan, Ruben, Gianluca en Klaas-Jan, dank jullie wel! Maaike, Nienke en Marjon, bedankt voor onze meidenavondjes! Nienke ik vond het erg leuk om met je naar San Francisco te gaan!
Ik wil mensen die ik tijdens mijn studie heb leren kennen, Sanne, Alex, Nienke, Peter H, Peter D, Rachel en Johanneke bedanken voor de vele uurtjes samen studeren, de gezelligheid op de UvA, de biertjes in de RTTR en de gezamelijke etentjes.

Ik ben daarnaast heel dankbaar voor de lieve en leuke mensen om mij heen. Ik wil Anne, Kaspar, Niels, Tim, Klara, Guusje, Martijn, Janneke, Joram, Hannah Kay, Daan, Nienke en Ton bedanken voor de leuke feestjes en lekkere etentjes die we hebben gehad. Ik vond de weekendjes weg super!

Anne, je kent mij al meer dan de helft van mijn leven en we hebben samen heel wat meegemaakt. Bedankt voor je onvoorwaardelijke steun en vriendschap en voor de mooie paardrijreizen die we hebben gemaakt en gaan maken! Niels, ik ben ook jou dankbaar voor de steun die je me hebt gegeven.

Huib, ik wil je bedanken voor jouw liefdevolle en inspirerende reisgezelschap in de afgelopen paar jaar en voor je vertrouwen in mij. Bedankt voor het verrijken van mijn leven door mijn ogen te openen voor nieuwe facetten van het leven.

Marjon, ik wil jou bedanken voor onze fijne en bijzondere vriendschap. Ik ben elke keer weer verwonderd over de dingen de we (apart en toch samen) meemaken. Ik ben ontzettend dankbaar voor en blij met jouw liefdevolle en energieke aanwezigheid in mijn leven. Dank dat je mijn paranimf wilt zijn!

親愛的爸爸和媽媽，我誠心地感謝您們的支持。我非常感謝您們耐心地傾聽我的故事，讓我們親子之間的關係更緊密。我再一次感謝您們對我經濟上的支持,因為您們的支持讓我無後顧之憂地從事許多能讓我放鬆和幫助我度過艱難時期的事。

Mom and Dad, I want to thank you for your support and I am grateful for our deepened relationship. I also want to thank you for your financial support, which enabled me to do things that made me relax or supported me in a challenging period.

Joe, Jeremy, Makayla and Ethan I am thankful for having you as my family. Living so far apart I am grateful for the time we have spent together.

Ik prijs mezelf gelukkig met de lieve en warme mensen in mijn andere grote, bijzondere en bonte familie (Marten, Nel, Freek, Esther, Eran, Boaz, Lauren, Marije, Arnold, Marten, Allard, Lotte, Joanne, Brenda (+1), Jasper, Ingeborg, Ossama en Hugo). Ik wil jullie bedanken voor jullie acceptatie, steun, warmte en liefde.

Ik wil Marten en Nel bedanken voor jullie grote hart en dat jullie mij een liefdevol thuis hebben gegeven. Bedankt voor jullie wijze levenslessen en jullie steun en liefde. Ik had dit niet zonder jullie kunnen bereiken.

Joanne, ik wil jou bedanken dat je mijn paranimf wilt zijn! Ik ben ook heel dankbaar voor onze relatie van de afgelopen tijd. De weekendjes bij jullie vind ik heerlijk.

Ton ik ben zo dankbaar voor jou in mijn leven. Ik wil je bedanken voor de mooie, soms moeilijke en bijzondere reis die we samen hebben gemaakt. Jouw onvoorwaardelijke liefde en vertrouwen hebben me rust en een thuis gegeven, dank je daarvoor. Ik ben blij met wat we samen geleerd en ontdekt hebben en ik kijk uit naar de reis in de toekomst. Ik wens ons veel liefde, moed en wonderlijke verbazing toe in het leven.

Wing Kiu
11 Mei 2011, Amsterdam

About the author

Wing Kiu Siu was born on August 27, 1982 in Hong Kong. She moved to the Netherlands at the age of 4 and spent major part of her childhood in Sleeuwijk. She went to secondary school in Gorinchem at the Gymnasium Camphusianum. After obtaining her diploma in 2000, she started her studies of chemistry at the University of Amsterdam. In 2003 she obtained her Bachelor of Science degree and started specializing in the field of condensed matter physics. Her masters research project concerned the angle-resolved photoemission on layered colossal magnetoresistant manganites and was carried out at the 'Van der Waals-Zeeman institute' in Amsterdam. She obtained her masters degree with honors in 2006 and went to Shanghai to study Chinese mandarin at the Jiao Tong University for 6 months. Upon returning to the Netherlands, she started her PhD research in the group of Marc Vrakking at the FOM-institute for Atomic and Molecular Physics (AMOLF) in Amsterdam. The results of this research are presented in this thesis.

LIST OF PUBLICATIONS

Publications covered in this thesis:

Attosecond Molecular Science, F. Kelkensberg, W. Siu, P. Johnsson, and M. J. J. Vrakking, in: Dynamical Processes in Atomic and Molecular Physics, Bentham e-books (2011) (*Chapter 2*)

Direct Determination of the Sign of the NO Dipole Moment, A. Gijsbertsen, W. Siu, M. F. Kling, P. Johnsson, P. Jansen, S. Stolte, and M. J. J. Vrakking, Phys. Rev. Lett. **99**, 213003 (2007) (*Chapter 3*)

Attosecond ionization of O_2 molecules in the presence of an IR laser Field, W. Siu, F. Kelkensberg, G. Gademann, A. Rouzée, P. Johnsson, D. Dowek, M. Lucchini, F. Calegari, U. Giovanni, A. Rubio, R. Lucchese, H. Kono, F.Lépine, M. J. J. Vrakking, *manuscript in preparation* (*Chapter 4*)

Velocity map imaging of atomic and molecular processes at the free electron laser in Hamburg (FLASH), P. Johnsson, W. Siu, A. Gijsbertsen, J. Verhoeven, A. S. Meijer, W. van der Zande, and M. J. J. Vrakking, J. Mod. Opt. **55**, 2693 (2008) (*Chapter 5*)

Electron localization in recollision excitation induced dissociation of H_2^+ and D_2^+ molecules, W. Siu, F. Kelkensberg, G. Sansone, M. F. Kling, O. Ghafur, P. Johnsson, M. Swoboda, E. Benedetti, F. Ferrari, F. Lépine, S. Zherebtsov, I. Znakovskaya, A. L'Huillier, M. Nisoli, M. Yu. Ivanov & M. J. J. Vrakking, *manuscript in preparation* (*Chapter 6*)

Other related publications:

A velocity map imaging detector with an integrated gas injection system, O. Ghafur, W. Siu, P. Johnsson, M. F. Kling, M. Drescher and M. J. J. Vrakking, Rev. Sci. Instr. **80**, 033110 (2009)

Attosecond control in photoionization of hydrogen molecules, F. Kelkensberg W. Siu, J. F. Pérez-Torres, F. Morales, G. Gademann, A. Rouzée, P. Johnsson, M. Lucchini, F. Calegari, J. L. Sanz-Vicario, F. Martín, and M. J. J. Vrakking, Phys. Rev. Lett. *accepted*

Molecular Dissociative Ionization and Wave-Packet Dynamics Studied Using Two-Color XUV and IR Pump-Probe Spectroscopy, F. Kelkensberg, C. Lefebvre, W. Siu, O. Ghafur, T. T. Nguyen-Dang, O. Atabek, A. Keller, V. Serov, P. Johnsson, M. Swoboda, T. Remetter, A. L'Huillier, S. Zherebtsov, G. Sansone, E. Benedetti, F. Ferrari, M. Nisoli, F. Lépine, M. F. Kling, & M. J. J. Vrakking, Phys. Rev. Lett. **103**, 123005 (2009)

Field-free molecular alignment probed by the free electron laser in Hamburg (FLASH), P. Johnsson, A. Rouzée, W. Siu, Y. Huismans, F. Lépine, T. Marchenko, S. Düsterer, F. Tavella, N. Stojanovic, A. Azima, R. Treusch, M. F. Kling and M. J. J. Vrakking, J. Phys. B **42**, 134017 (2009)

Characterization of a two-color pumpprobe setup at FLASH using a velocity map imaging spectrometer, P. Johnsson, A. Rouzée, W. Siu, Y. Huismans, F. Lépine, T. Marchenko, S. Düsterer, F. Tavella, N. Stojanovic, H. Redlin, A. Azima, and M. J. J. Vrakking, Optics Lett. **35**, 4163 (2010)

Attosecond control of electronion recollision in high harmonic generation, G. Gademann, F. Kelkensberg, W. K. Siu, P. Johnsson, M. B. Gaarde, K. J. Schafer & M. J. J. Vrakking, New J. Phys. **13**, 033002 (2011)

Molecular frame photoelectron angular distributions from EUV ionization of aligned molecules, F. Kelkensberg, A. Rouzée, W. Siu, G. Gademann, P. Johnsson, M. Lucchini, R. R. Lucchese, & M. J. J. Vrakking, *submitted*

Impulsive orientation and alignment of quantum-state-selected NO molecules , O. Ghafur, A. Rouzée, A. Gijsbertsen, W. Siu, S. Stolte, M. J. J. Vrakking , Nat. Phys. **5**, 289 (2009)

Electron localization following attosecond molecular photoionization, G. Sansone, F. Kelkensberg, J. F. Pérez-Torres, F. Morales, M. F. Kling, W. Siu, O. Ghafur, P. Johnsson, M. Swoboda, E. Benedetti, F. Ferrari, F. Lépine, J. L. Sanz-Vicario, S. Zherebtsov, I. Znakovskaya, A. L'Huillier, M. Yu. Ivanov, M. Nisoli, F. Martín & M. J. J. Vrakking, Nature **465**, 763 (2010)

Angle-resolved photoelectron spectroscopy of sequential three-photon triple ionization of neon at 90.5 eV photon energy, A. Rouzée, P. Johnsson, E. V. Gryzlova, H. Fukuzawa, A. Yamada, W. Siu, Y. Huismans, E. Louis, F. Bijkerk, D. M. P. Holland, A. N. Grum-Grzhimailo, N. M. Kabachnik, M. J. J. Vrakking, and K. Ueda, Phys. Rev. A **83**, 031401 (2011)

Attosecond Electron Spectroscopy Using a Novel Interferometric Pump-Probe Technique, J. Mauritsson, T. Remetter, M. Swoboda, K. Klünder, A. L'Huillier, K. J. Schafer, O. Ghafur, F. Kelkensberg, W. Siu, P. Johnsson, M. J. J. Vrakking, I. Znakovskaya, T. Uphues, S. Zherebtsov, M. F. Kling, F. Lépine, E. Benedetti, F. Ferrari, G. Sansone & M. Nisoli, Phys. Rev. Lett. **105**, 053001 (2010)